University of Kent

Doctoral Thesis

A study of the application of adaptive optics (AO) in optical coherence tomography (OCT) and confocal microscopy for the purpose of high resolution imaging

Author:
Christopher Costa

Supervisor:
Prof. Adrian Podoleanu

A thesis submitted in fulfilment of the requirements for the degree of Doctor of Philosophy

in the

Applied Optics Group
School of Physical Sciences

May 2016

Declaration of Authorship

I, Christopher Costa, declare that this thesis titled, 'A study of the application of adaptive optics (AO) in optical coherence tomography (OCT) and confocal microscopy for the purpose of high resolution imaging' and the work presented in it are my own. I confirm that:

- This work was done wholly or mainly while in candidature for a research degree at this University.
- Where any part of this thesis has previously been submitted for a degree or any other qualification at this University or any other institution, this has been clearly stated.
- Where I have consulted the published work of others, this is always clearly attributed.
- Where I have quoted from the work of others, the source is always given. With the exception of such quotations, this thesis is entirely my own work.
- I have acknowledged all main sources of help.
- Where the thesis is based on work done by myself jointly with others, I have made clear exactly what was done by others and what I have contributed myself.

Signed: _____

Date: _____

"It is in the admission of ignorance and the admission of uncertainty that there is a hope for the continuous motion of human beings in some direction that doesn't get confined, permanently blocked, as it has so many times before in the history of man."

Richard Feynman

UNIVERSITY OF KENT

Abstract

Faculty Name
School of Physical Sciences

Doctor of Philosophy

A study of the application of adaptive optics (AO) in optical coherence tomography (OCT) and confocal microscopy for the purpose of high resolution imaging

by Christopher Costa

A problem is presented when imaging the eye in that optical aberrations are introduced by tissues of the anterior eye such as the cornea and lens. Adaptive optics (AO) and scanning laser ophthalmoscopy (SLO) have been combined to detect and compensate for these aberrations through the use of one or more correcting devices. Different corrector options exist, such as a liquid crystal lens or a deformable mirror (DM), such as that used in this thesis. This study seeks to use the ability of the DM to add focus/defocus aberrations to the closed loop AO system. This procedure could allow for dynamic focus control during generation of B-scan images using spectral domain optical coherence tomography (SD-OCT), where typically this is only possible using slower time domain techniques. The confocal gate scanning is controlled using the focus altering aberrations created by changing the shape of the deformable mirror.

Using the novel master-slave interferometry method, multiple live *en-face* images can be acquired simultaneously. In this thesis, application of this method to an AO system is presented whereby *en-face* images may be acquired at multiple depths simultaneously. As an extension to this research, an OCT despeckle method is demonstrated. Further to this work is the investigation of the role in AO for optimisation of optical systems without the requirement for direct aberration measurement. Towards this end, genetic algorithms (GA) may be employed to control the DM in an iterative process to improve the coupling of light into fibre.

Acknowledgements

Completing this PhD was one of the hardest things I've had to do and would not have been possible without the support of some incredible people. I would first like to thank Professor Adrian Podoleanu for his tireless dedication and invaluable mentorship during my time at Kent. Adrian's enthusiasm for the science is a constant inspiration and I really could not have asked for a finer supervisor.

It has been a pleasure to work with the other members of the Applied Optics Group; I'm so grateful to have found so many friends amongst my colleagues, which can be a rare thing. The close relationships we formed as a group made for such an enjoyable work environment that it often didn't seem like work at all.

This work would not have been possible without the support of the University of Kent. I would also like to thank the technical and administration teams that form the backbone of our group, and without them we simply cease to function.

When things got tough I was able to lean heavily on my closest friends, who were always there to support and encourage me. In particular I would like to thank Radu Stancu, Manuel Marques, Nadia Yiannaki, James Gilbert, Wesley Naeimi, Deji Ajisebutu and Katie Hawcutt. A fantastic group of friends that I feel so privileged to know.

Though they probably never fully understood my work, or even my motivation, my parents have been behind me the whole way and I'll always be grateful for their endless generosity and invaluable advice.

Lastly I would like to thank Hannah Irons, the love of my life. Without you I would have been truly lost, and even that sounds like a gross understatement. I hope that I can be just as supportive for the remainder of your PhD as you were for me.

Contents

Declaration of Authorship i

Abstract iii

Acknowledgements iv

Contents v

List of Figures x

List of Tables xvii

Abbreviations xviii

Symbols xix

1 Introduction 1
- 1.1 The anatomy of the eye . . . 1
- 1.2 Motivation . . . 4
- 1.3 Chapter Summary . . . 5

2 Microscopy 8
- 2.1 Introduction . . . 8
- 2.2 Conventional microscopy . . . 8
  - 2.2.1 Description . . . 8
  - 2.2.2 Limitations . . . 10
- 2.3 Scanning microscopy . . . 11
  - 2.3.1 Description . . . 11
  - 2.3.2 Limitations . . . 13
- 2.4 Confocal microscopy . . . 14
  - 2.4.1 Description . . . 14
  - 2.4.2 Limitations . . . 16
  - 2.4.3 Transversal scanning . . . 17
- 2.5 Scanning laser ophthalmology (SLO) . . . 17
  - 2.5.1 Description . . . 18

2.5.2 Transversal scanning . . . 18
2.5.3 Limitations . . . 19
2.6 Resolution and the effect of pinhole size . . . 20

3 Optical coherence tomography (OCT) 24
3.1 Introduction . . . 24
3.2 White Light Interferometry . . . 27
3.2.1 Resolution . . . 31
3.2.2 Sensitivity . . . 34
3.3 Time-Domain Optical Coherence Tomography (TD-OCT) . . . 35
3.3.0.1 Advantages . . . 37
3.3.0.2 Limitations . . . 38
3.4 Spectral-Domain Optical Coherence Tomography (SD-OCT) . . . 38
3.4.1 Advantages of SD-OCT over TD-OCT . . . 39
3.4.2 Limitations . . . 39
3.4.2.1 *En-face* imaging . . . 39
3.4.2.2 Hardware limitations . . . 39
3.4.2.3 Mirror terms . . . 41
3.5 Swept-Source Optical Coherence Tomography (SS-OCT) . . . 41
3.6 Summary of modalities . . . 42
3.7 Noise . . . 42
3.7.1 Shot noise . . . 45
3.7.2 Excess photon noise . . . 46
3.7.3 SNR . . . 47

4 Adaptive optics 49
4.1 Introduction . . . 49
4.2 Wavefront measurement . . . 50
4.3 Wavefront manipulation . . . 55
4.4 Open and closed loop correction . . . 58

5 AO-SLO/OCT for eye imaging and high resolution microscopy 60
5.1 Introduction . . . 60
5.1.1 Legacy AO-SLO/OCT . . . 61
5.1.1.1 Design . . . 61
5.1.1.2 Achievements . . . 63
5.1.1.3 Limitations . . . 64
5.1.2 Objectives . . . 65
5.2 Methodology . . . 66
5.2.1 Fibre array . . . 66
5.2.1.1 Design . . . 67
5.2.1.2 Achievements . . . 68
5.2.1.3 Limitations . . . 69
5.2.2 Improved design with non-planar mirror arrangement . . . 69
5.2.3 Considerations . . . 70
5.2.3.1 Beam size . . . 71
5.2.3.2 System induced aberrations . . . 72

5.2.3.3 Conjugate planes . . . 72
5.2.3.4 Removal of lenses due to back reflections . . . 72
5.2.4 Optical design . . . 73
5.2.5 Wavefront optimisation . . . 74
5.2.5.1 Initialisation of adaptive optics . . . 76
5.2.5.2 Closed loop correction . . . 80
5.2.6 Image acquisition and processing . . . 80
5.2.6.1 Synchronised analogue input/output . . . 81
5.2.6.2 Image reconstruction . . . 81
5.3 Results . . . 82
5.3.1 Wavefront characterisation . . . 82
5.3.2 Experimental analysis of transversal resolution . . . 86
5.3.3 Microscopy of thumb and skin *in-vivo* . . . 87
5.3.4 *In-vivo* human eye imaging . . . 88
5.4 Conclusions . . . 96
5.5 Evaluation . . . 97

6 Swept source optical coherence tomography Gabor fusion splicing technique for microscopy of thick samples using a deformable mirror 99
6.1 Preface . . . 99
6.2 Introduction . . . 100
6.2.1 Problems presented with AO/SS-OCT . . . 100
6.2.2 Possible solution . . . 100
6.3 Methodology . . . 101
6.3.1 Concept . . . 101
6.3.2 Optical design for minimizing system-induced aberrations . . . 102
6.3.3 Active aberration compensation using deformable mirror . . . 103
6.3.4 Shifting the confocal gate . . . 104
6.3.5 Analysis of the confocal profile and signal strength during focus sweep . . . 105
6.3.6 Assessment of the transversal resolution . . . 107
6.3.7 Effect upon wavefront when manipulating focus . . . 110
6.3.8 Test procedure . . . 112
6.4 Results . . . 112
6.5 Conclusions . . . 117
6.6 Evaluation . . . 117
6.7 Acknowledgments . . . 118

7 AO/SS-OCT Master/Slave interferometry for simultaneous live *en-face* imaging at different depths 119
7.1 Introduction . . . 119
7.2 Methodology . . . 123
7.2.1 System design . . . 123
7.2.2 Signal acquisition and processing . . . 125
7.3 Results . . . 125
7.3.1 Elimination of fringes in images of specular targets . . . 125
7.3.2 Imaging the thumb at different depths simultaneously . . . 126

7.3.3 Sectioning of sweat duct in thumb . . . 127
7.3.4 Imaging the retina and photorecptors *in-vivo* . . . 129
7.4 Conclusions . . . 131
7.5 Evaluation . . . 132

8 Genetic programming technique for sensor-less wavefront optimisation 134
8.1 Introduction . . . 134
8.1.1 Particle Swarm Optimisation (PSO) . . . 135
8.1.2 Genetic Algorithm (GA) . . . 136
8.1.2.1 Genes and the gene pool . . . 137
8.1.2.2 Chromosome . . . 137
8.1.2.3 Individuals, populations and generations . . . 138
8.1.2.4 Fitness . . . 139
Gold standard . . . 139
8.1.2.5 Creating a new generation . . . 140
8.1.2.6 Parent selection . . . 141
Random selection . . . 142
Truncation selection . . . 143
Roulette wheel selection . . . 144
Rank selection . . . 144
Tournament selection . . . 146
8.1.2.7 Reproduction . . . 147
8.1.2.8 Iteration and evolution . . . 153
8.1.2.9 Termination of the GA . . . 157
8.2 Methodology . . . 159
8.2.1 Overview . . . 159
8.2.2 Optical system . . . 160
8.2.3 GA structure . . . 160
8.2.3.1 Genes and the gene pool . . . 161
8.2.3.2 Chromosome . . . 161
8.2.4 Fitness function . . . 162
8.2.5 Reproduction . . . 162
8.2.6 Calibration . . . 163
8.2.6.1 Population size . . . 163
8.2.6.2 Crossover/mutation chance . . . 164
8.2.6.3 Injection frequency . . . 164
8.2.7 Monitoring . . . 165
8.3 Results . . . 166
8.3.1 Calibration . . . 166
8.3.1.1 Population size . . . 166
8.3.1.2 Crossover/mutation chance . . . 167
8.3.1.3 Injection frequency . . . 167
8.3.2 Experiment without injection . . . 170
8.3.3 Experiment with injection . . . 170
8.3.4 Sensitivity . . . 175
8.3.5 Robustness . . . 177
8.3.6 Experiment at 1060 nm . . . 179

8.3.7 Resolution 180
8.4 Conclusions 183
8.5 Evaluation 184

9 Conclusions **185**
9.1 Summary 185
9.2 Achievements 186
9.3 Evaluation 187
9.4 Future work 188

A Mirao 52-E specifications **209**

B SLD data sheet **211**

C LabVIEW implementation of the genetic algorithm **212**

List of Figures

1.1 Diagram showing the anatomy of the human eye (http://www.depure.org/anatomy-of-human-and-its-explanation/anatomy-of-human-eye). 1
1.2 Diagram showing the anatomy of the retina, with a distribution of rods and cones (https://classconnection.s3.amazonaws.com/32/flashcards/806032/png/retina1318520689618.png) 2

2.1 Diagram of a conventional microscope in transmission. 9
2.2 Diagram of a conventional microscope in reflection. 9
2.3 Diagram showing light scattering from different depth interfaces in an object. 10
2.4 Diagram of a scanning microscope in transmission. 11
2.5 Diagram of a scanning microscope in transmission at different transversal position. 11
2.6 Diagram of a scanning microscope in reflection. 12
2.7 Diagram of a scanning microscope in transmission with contributions from out of focus region D' and stray light contribution from different transversal positions A' and B'. 13
2.8 Diagram showing scattered light from different transversal positions in the focal plane contributing to the image seen by the detector. 13
2.9 Diagram of a confocal microscope in transmission. 14
2.10 Diagram of a confocal microscope in reflection. 15
2.11 Diagram showing the imperfect rejection of reflectors that are out of the focal plane. 16
2.12 Simplified diagram demonstrating the use of a galvoscanner to sweep a collimated beam transversally across an objective lens. This has the effect of focussing the beam at different transversal positions on the object by altering the reflected angle of the beam. 17
2.13 Diagram demonstrating the adaptation of a microscope system to cater for transversal scanning of the retina. The lens of the eye is used to change the angle of incidence of light focussed on the retina. 19

3.1 Diagram showing scanning regimes for OCT. 25
3.2 Diagram showing the penetration depth and resolution of OCT in comparison with confocal microscopy and ultrasound. 26
3.3 Diagram showing a Michelson interferometer. 27
3.4 Diagram demonstrating the process that produces a spatially coherent and chromatically coherent light source. 31
3.5 Diagram showing the difference between long and short coherence length. 32

3.6 Diagram showing the difference between low and high NA and the effect on the confocal parameter b. OCT imaging is usually performed with low NA to increase depth of focus, though transversal resolution is compromised. 33
3.7 Diagram showing TD-OCT concept. 35
3.8 Diagram showing TD-OCT system. 36
3.9 Diagram showing dynamic focus in a TD-OCT system. 37
3.10 Diagram showing a non-balanced detection system, where α denotes the splitting ratio of the coupler. 45
3.11 Diagram showing a balanced detection system, where $\alpha 1$ and $\alpha 2$ denote the splitting ratio of the two couplers. 45

4.1 Diagram demonstrating the effect of irregular optical interfaces on the quality (flatness) of the wavefront. 50
4.2 Diagram representing a Shack-Hartmann wavefront sensor. An unaberrated beam of light presents a flat wavefront. The beam is decomposed by the lenslet array into a spot pattern on the CCD camera. 51
4.3 Diagram representing a Shack-Hartmann wavefront sensor. In this case, the wavefront has aberrations and causes displacement of the spots on the CCD camera 51
4.4 Image showing Zernike polynomials up to the 6th order. Higher order abberations are towards the base of the pyramid and low order aberrations are at the tip of the pyramid. (http://bme240.eng.uci.edu/students/08s/ticenogl/ Wavefront-Guided%20LASIK/Wavefront.html) 53
4.5 A diagrammatic representation of wavefront correction in transmission using a liquid-crystal spatial light modulator (SLM) 55
4.6 A deformable mirror is used as a wavefront corrector, applying the inverse function of the combined detected aberrations. The result is a flat wavefront in reflection. 55
4.7 Diagram presenting the structure of a deformable mirror with a segmented surface. 56
4.8 Diagram presenting the structure of a deformable mirror with a continuous surface. 57

5.1 Diagram showing the legacy AO-SLO/OCT system. 61
5.2 Diagram showing the resizing of imaging beam in an AO-SLO system. . . 62
5.3 Diagram showing an AO-SLO/OCT system using a fibre array. 67
5.4 Schematic of wavefront sensing system. The lens L1 is representative of the eye lens, with the object O representing the retina. 73
5.5 DM in random phase 74
5.6 Spot pattern pre-correction 75
5.7 Wavefront pattern pre-correction 76
5.8 Building interaction matrix 77
5.9 Images of wavefront during 4 of the 105 stages of IM acquisition. 78
5.10 Calculated Eigenmode influence on wavefront. 79
5.11 Spot patterns detected by WFS before and after closed loop correction . . 83
5.12 Wavefront error calculated from spot pattern pre- and post-correction. . . 84
5.13 3D Wavefront error calculated from spot pattern pre- and post-correction. 84
5.14 Pixel intensity distribution pre- and post-correction. 84

5.15 Calculated slopes post-correction. Image 5.15b shows the slopes extended to emphasize the shape of the wavefront. 85
5.16 Confocal image of USAF target displaying the smallest bars 2 μm apart. . 86
5.17 Images of the thumb acquired using a 25 mm lens as the objective. The DM was used to shift the focus to three different depths during imaging. Image size is 1 mm by 1 mm. 87
5.18 Image of the skin showing the stratum corneum and hair. Image size is 1 mm by 1 mm. 88
5.19 Images of retina acquired from human eye *in-vivo* with 1.5 V to scanners. Image size is 1 mm by 1 mm. 89
5.20 Images of retina acquired from human eye *in-vivo* with 1.0 V to scanners. Image size is 700 μm by 700 μm. 90
5.21 Images of retina acquired from human eye *in-vivo* with 1.0 V to scanners. Image size is 700 μm by 700 μm. 92
5.22 Images of retina acquired from human eye *in-vivo* with 0.5 V to scanners. Image size is 350 μm by 350 μm. 94
5.23 Image showing intensity profile taken from Fig. 5.22a running vertically down the centre of the image. 95
5.24 Images of retina acquired from human eye *in-vivo* with 0.25 V to scanners. Image size is 175 μm by 175 μm. 96

6.1 Schematic of the AO/SS-OCT system with imaging at 1060 nm and wavefront sensing plus confocal microscopy at 830 nm. 102
6.2 Chart showing how the confocal profile shifts in depth and changes shape as we add 1 and 2 μm RMS focus. 105
6.3 Chart showing decay in signal intensity with added focus 106
6.4 High contrast confocal image of the USAF target showing the smallest 2 μm bars at the bottom. Two sets of three bars are shown oriented horizontally and vertically. Image size is 250 x 250 pixels covering an actual area of 70 x 70 μm^2 on the target. 107
6.5 Effect of defocus on the image acquired from the USAF target, using the same area as in Fig. 4. The original image (C) is repeated in (D) and placed alongside images taken with -2 (A), -1 (B), 1 (E) and 2 (F) μm RMS focus added to the DM. 108
6.6 Images of the USAF target obtained using the DM deformed to create 3 μm (B) and 4 μm (C) RMS defocus, with the original 0 μm focus image (A) for comparison. 109
6.7 RMS wavefront error as focus is manipulated. Total error: green region. Error excluding focus: blue region. Error excluding tilts and focus: red region. 110
6.8 Effect of focus manipulation on defocus aberration (green) and on seven other high-order aberrations (according to colour in the inset). 111
6.9 Magnified view of WFS RMS error showing effect of focus on wavefront excluding tilts and focus aberrations. 111
6.10 Images acquired of a phantom constructed from ten 0.17 mm thick glass slides (bound top and bottom with sellotape of similar thickness) with focus set to -4 (A), 0 (B) and 4 (C) covering a total range of 2 mm. Final image (D) is synthesized through extraction of in-focus regions from a stack of images acquired with focus shifted incrementally. 113

6.11 OCT B-scan images of an infra-red card, with focus set to -1.5 (A), 0 (B), and 1.5 (C) covering a range of 0.75 mm. The final image (D) is the composite Gabor image. 114
6.12 B-scan-OCT images of *in-vivo Drosophila* with focus at -1 (A), 0 (B), and 1 (C) covering a total range of 1 mm axial range measured in air. Final image (D) is synthesized through extraction of in-focus regions from a stack of images acquired with focus shifted incrementally. 115
6.13 *In-vivo* OCT B-scan images acquired of thumb with fixed focus (A) at the surface and after Gabor splicing (B). Visible are the distinctive spiral structures of the sweat ducts, and the deeper tissues are enhanced in (B) due to focus sweep. Image size is 1 mm (horizontal) by 2 mm (vertical) measured in air. 116

7.1 Diagram showing master-slave interferometry configuration. Both interferometers operate in Fourier domain, however the master interferometer acts as a reference for axial selection as in TD-OCT. The electrical signal proportional to the shape of the channelled spectrum from the slave interferometer is cross-correlated with the electrical signal proportional to the shape of the channelled spectrum from the master. 121
7.2 Diagram showing alternate MSI configuration where a single interferometer is used. The object can be replaced with a mirror to switch the system to master mode for mask acquisition. 122
7.3 Schematic of the AO/MSI-OCT system with imaging at 1060 nm and wavefront sensing at 830 nm. 124
7.4 Images of USAF target at three values of p. 126
7.5 Averaged image over $p = 1$ to $p = 20$. Large horizontal black bars indicating fringes have been eliminated. 126
7.6 Images of the thumb acquired simultaneously using MSI with $p = 1$ to $p = 100$. 127
7.7 Images of a sweat duct in the thumb at three values of p. 127
7.8 3D volume images of the sweat duct in thumb at two orientations. 128
7.9 Cross-sectional image of the sweat duct in the thumb extracted from a volume produced by MSI method. Fire LUT has been applied to increase clarity of the image. 129
7.10 Images acquired from the retina *in-vivo* using MSI. 130

8.1 Diagram showing structure of a GA, with generations progressing from left to right. 136
8.2 Diagram showing the composition of a generation. A portion of a created generation will be the best performing individuals from the previous generation, with the remaining slots filled by children produced during the reproduction cycle. 140
8.3 Diagram demonstrating local and global maxima in the search space for a GA. 142
8.4 Diagram depicting the injection of random individuals into the next generation to revitalise a stagnant GA. 143
8.5 Diagram representing roulette wheel selection. Each individual has a percentage chance to be selected for reproduction derived from its fitness as a fraction of the average fitness of the generation. 145

8.6 Diagram demonstrating rank based selection. Similar to roulette wheel selection, though selection chance is based upon individuals fitness rank in their generation rather than their actual fitness value. 146
8.7 Diagram showing two parents undergoing crossover reproduction. The red dashed line indicates a mutually shared crossover point. Genetic material up to this point is extracted from parent 1 and added to the child. The genetic data after the crossover point is extracted from parent 2 and added to the child. The result is a child with shared genetic data from both parents; all chromosomes maintain the same length. Child 2 is optionally used by some GAs, formed from the remaining segments. . . . 147
8.8 Diagram showing two parents undergoing crossover reproduction. The red arrows show randomly determined crossover points for both parents. Genetic material up to this point is extracted from parent 1 and added to the child. The genetic data after the crossover point is extracted from parent 2 and added to the child. The result is a child with shared genetic data from both parents; in this case both children have variable length chromosomes. 148
8.9 Diagram showing two parents undergoing crossover reproduction. The red dashed lines indicate mutually shared crossover points. Genetic material up to the first crossover point is extracted from parent 1 and added to the child. The genetic data after the first crossover point is extracted from parent 2 and added to the child. Finally, the data after the second crossover point is taken from parent 1 to add to the child. Chromosome length here is preserved. Child 2 is optionally used. 149
8.10 Diagram showing two parents undergoing crossover reproduction. The red arrows indicate random crossover points. Chromosome length here is variable. Child 2 is optionally used. 149
8.11 Diagram showing uniform crossover with $p = 0.5$. Each gene has a 50% chance of being taken from either parent. Child 2 is optionally used. . . . 150
8.12 Diagram showing uniform crossover with $p = 1$. This guarantees that crossover occurs after every gene, ensuring an equal contribute to the child by both parents. Child is formed by taking every second gene from both parents and interweaving them together. Child 2 is optionally used. 150
8.13 Diagram showing 1-point mutation, resulting in a single gene being swapped for another in the gene pool. Chromosome length is preserved. 151
8.14 Diagram showing 1-point mutation, resulting in two genes being swapped for another in the gene pool. Chromosome length is preserved. 151
8.15 Diagram showing 1-point mutation, resulting in a single gene being destroyed. Chromosome length is shortened. 152
8.16 Diagram showing 2-point mutation, resulting in two genes being destroyed. Chromosome length is shortened. 152
8.17 Diagram showing 1-point mutation, resulting in a single gene B being created and placed between D and E. Chromosome is lengthened. 153
8.18 Diagram showing 2-point mutation, resulting in two genes F and A being created. Chromosome is lengthened. 153
8.19 Diagram summarising the processes of a GA. 154
8.20 Pseudocode for genetic algorithm 155
8.21 Diagram showing an AO/SLO system without the WFS. 160

8.22 Diagram showing the workflow of a fitness measurement for a single individual. 161
8.23 Diagram showing population composition prediction of new generation after reproduction phase. Presented is the composition of a standard population (left) and a population with injection of random individuals (right). 163
8.24 Graph showing results from calibration test. Presented are the progression of fittest individuals over 100 generations for five population sizes. . . 168
8.25 Graph displaying the effect of mutation chance on peak fitness over 100 generations. 169
8.26 Graph displaying the effect of modifying the frequency of the injection of random individuals into the population over 100 generations. 169
8.27 Graphs showing the results of running the GA with a population size of 100 for a total of 10 times. The GA achieves saturation of the photodetector 8 times. 171
8.28 Graph showing fittest values of each generation for population size of 100. Experiment was run 10 times, each represented by a single line in the chart. 172
8.29 Graphs showing the results of running the GA with a population size of 100 for a total of 10 times. In these experiments, an injection of random individuals occurs every 10 generations and the average fitness is displayed in red. A sharp drop in average fitness occurs immediately after an injection. 173
8.30 Graph showing peak fitness of 10 iterations of the GA with population size of 100 with injection enabled. 174
8.31 Graph showing a comparison of GA experiment with and without injection. The blue and yellow regions represent the peak and average fitness of the GA with injection enabled, respectively. The green and red regions represent the peak and average fitness of the GA without injection enabled, respectively. 175
8.32 Graph showing the results of the sensitivity experiment with the SLD power halved. 176
8.33 Graph showing the results of the sensitivity experiment with the SLD power quartered. 176
8.34 Graph showing the results of the robustness experiment. At the three points indicated on the graph, the object was physically moved out of focus of the objective lens and the results observed. 178
8.35 This diagram displays the results of the genetic algorithm as it achieves optimisation of the wavefront through measurement of 1060 nm light using a low-gain photo-detector. The blue region describes peak fitness levels per generation, and the red region is the average fitness. 179
8.36 Image of the USAF resolution target acquired using 830 nm SLO. This image was acquired after bringing the system to a corrected state using CASAO's closed loop. 180
8.37 Image of USAF resolution target acquired using 830 nm SLO. This image was acquired after bringing the system to a corrected state using the GA. 180
8.38 Figure demonstrating the location of the profiles seen in Fig. 8.39 and 8.40 from the images in Fig. 8.36 and 8.37. 181
8.39 Intensity profile of the USAF target after normal closed loop acquisition. . 181
8.40 Intensity profile of the USAF target after GA correction. 182

B.1 Specifications of SLD emitting light with central wavelength 830 nm. . . . 211

C.1 Start Evolution.VI is the primary VI to execute when running the GA. This VI is responsible for setting the starting parameters of the GA, opening communications with the DM, creating log files and the random starting population from a seed file. 213
C.2 Generate Random Population From Seed.VI will import an XML file acquired from CASAO. This file contains a set of command values that determine the voltages applied to each actuator in the DM. The VI will generate a number of 52-length 1D arrays equal to Population Size by adding random numbers to the seed file. 214
C.3 Main Loop.VI is where the majority of the GA functionality occurs. This VI will remain active until the GA terminates. In this VI there are calls to various sub VIs that determine the fitness of a solution and initialise the reproduction cycle. Also seen in this VI are the various code fragments used to generate logs and reports during GA execution. 215
C.4 Generate Random Population.VI is similar to Fig. C.2 though it does not require a seed file to generate a random set of individuals. 216
C.5 Random Number.VI generates a random number between two given limits and is used for many functions in the GA. 216
C.6 Read CASAO Command Values.VI is responsible for reading the XML files output by the CASAO software. This VI reads through the file to find the tags for the command values, and exports them as an array of doubles. 217
C.7 Get individual fitness.VI calculates the fitness value of a given individual. 218
C.8 Get Fittest Individual.VI will sort through the population of individuals and select the one with the highest fitness. 218
C.9 Log Entry.VI will create an entry in the log file for the current individual with all its relevant information, including values and fitness level. 218
C.10 Select Fittest N Individuals.VI will sort through the population and select the top N fittest individuals. 218
C.11 Rank Selection.VI is the method used to select two parents for breeding. . 219
C.12 Crossover 1 Point.VI takes two parent individuals, randomly determines a crossover point and then cuts these parents, splicing them together to create a child. 220
C.13 Mutate 1 Point.VI takes a single parent individual and selects a single value in the array to change. 220
C.14 Generation Report.VI provides information for each generation such as time stamp, highest fitness and average fitness. 221

List of Tables

3.1 Table summarising the differences between the OCT modalities. 43

5.1 Beam parameters for the chief ray pre- and post-correction as measured by the WFS. 85

8.1 Sample selection chances for rank based selection. 146
8.2 Table showing the parameters of the GA while testing the effect of population size on execution speed of the algorithm. 164
8.3 Table showing the parameters of the GA while testing the effect of crossover and mutation probability. 164
8.4 Table showing the parameters of the GA while testing the effect of injection frequency. 165
8.5 This table describes the content of the two output logs. Population log is a comprehensive report of the creation and testing of every individual throughout the life cycle of the GA. Generation log records a single line for each generation, detailing the fittest individual and average fitness for that generation. 165
8.6 This table shows the run time for 100 generations with various population sizes. Also displayed is the total gain in fitness from the initial value to the final value, and a measure of fitness gained per minute of running time. 166
8.7 Table showing GA parameters for a experimentation with population size of 100. For these experiments, the periodic injection of random individuals has been disabled. 170
8.8 Table showing GA parameters for a experimentation with population size of 100. Injection of randomised individuals occur every 10 generations and comprise approximately 50% of the total population after reproduction. . 171

A.1 Specifications of the Mirao-52e 209
A.2 Specifications of the electronic control unit for Mirao-52e 209
A.3 Actuator layout of the Mirao-52e 210

Abbreviations

AO	**A**daptive **O**ptics
APD	**A**valance **P**hoto**d**iode
CM	**C**onfocal **M**icroscopy
DM	**D**eformable **M**irror
EPN	**E**xcess **P**hoton **N**oise
FD	**F**ourier **D**omain
FFT	**F**ast **F**ourier **T**ransform
FWHM	**F**ull **W**idth **H**alf **M**aximum
GA	**G**enetic **A**lgorithm
MEMS	**M**icro-**e**lectro **M**echanical **S**ystem
NA	**N**umerical **A**perture
NI	**N**ational **I**nstruments
OCT	**O**ptical **C**oherence **T**omography
OPD	**O**ptical **P**ath **D**ifference
PSF	**P**oint **S**pread **F**unction
RMS	**R**oot **M**ean **S**quared
SLD	**S**uper **L**uminescent **D**iode
SLM	**S**patial **L**ight **M**odulator
SLO	**S**canning **L**aser **O**phthalmoscope
SNR	**S**ignal to **N**oise **R**atio
SS	**S**wept **S**ource
TD	**T**ime **D**omain
USAF	**U**nited **S**tates **A**ir **F**orce
WFS	**W**ave**f**ront **S**ensor

Symbols

c	Speed of light
x, y, z	Spatial coordinates
r	Radial distance
p	Normalised radial distance
λ	Wavelength
NA	Numerical aperture
ω	Angular frequency
θ	Angle
f	Focal length
I	Intensity
D	Diameter
l	Length
ϕ	Phase
n	Index of refraction
σ	Noise
t	Time
E	Electric field
α	Photodetector response
Z	Zernike coefficient
Π	Degree of polarisation
B	Electrical bandwidth

Chapter 1

Introduction

1.1 The anatomy of the eye

Before the construction of man-made optical systems there existed a complex biological imaging device - the eye. Eyes can be loosely defined as any biological organ that is capable of detecting light to create some causal effect, such as electro-chemical impulses in the brain or, in the case of basic organisms, a simple determination of ambient light intensity. The first proto-eyes evolved in animals during the Cambrian period, and rapidly diversified and evolved into the wide range of eyes we know today [1].

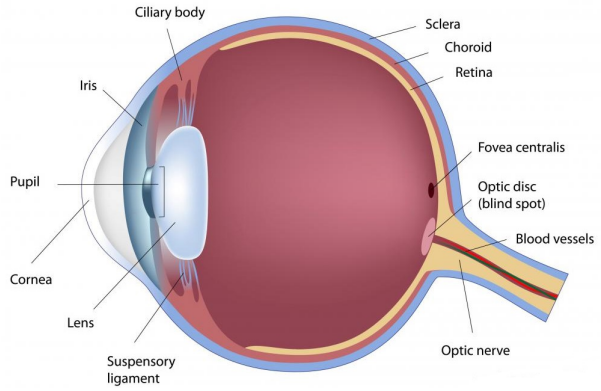

FIGURE 1.1: Diagram showing the anatomy of the human eye (http://www.depure.org/anatomy-of-human-and-its-explanation/anatomy-of-human-eye).

Fig. 1.1 shows a diagrammatic representation of the anatomy of the human eye. Light enters the eye through the pupil and is focused by the lens onto the retina. The lens itself has a graded refractive index, and may be stretched by the conjoined ligaments to change the focal length of the eye. This allows for the eye to focus at varying

distances, allowing for a longer range of vision. The retina itself contains over 120 million photoreceptors, which are light-sensitive cells that produce electro-chemical impulses as they are stimulated by light [2]. These neural signals are transmitted through the optic nerve to a region of the brain called the primary visual cortex, which is responsible for the reconstruction of the image [3]. The region where the optic nerve connects to the main chamber of the eye is called the optic disc and lacks photoreceptors, creating a blind spot. To compensate for this blind spot, the eye rapidly moves and integrates the captured information so the brain may fill in the blind spot. This is called microsaccade [4].

The iris is responsible for moderating the amount of light that is transmitted into the eye. It is capable of expanding and contracting dynamically in response to ambient and directed light levels, in a range between 2 and 8 mm diameter [5][6]. For low light situations, the iris will expand to dilate the pupil, allowing for more light to enter the eye. When the environment is bright, the iris will contract to block light until the photoreceptors on the retina are no longer bleached [7]. The anterior chamber of the eye is filled with a transparent gel medium called the vitreous humour, which presses against the retina and helps to maintain the structure of the eye [8]. The composition of the vitreous is over 98% water, with additional salts, sugars, proteins and a network of collagen type II fibres. It has a refractive index of 1.337, which increases the numerical aperture of the eye [9].

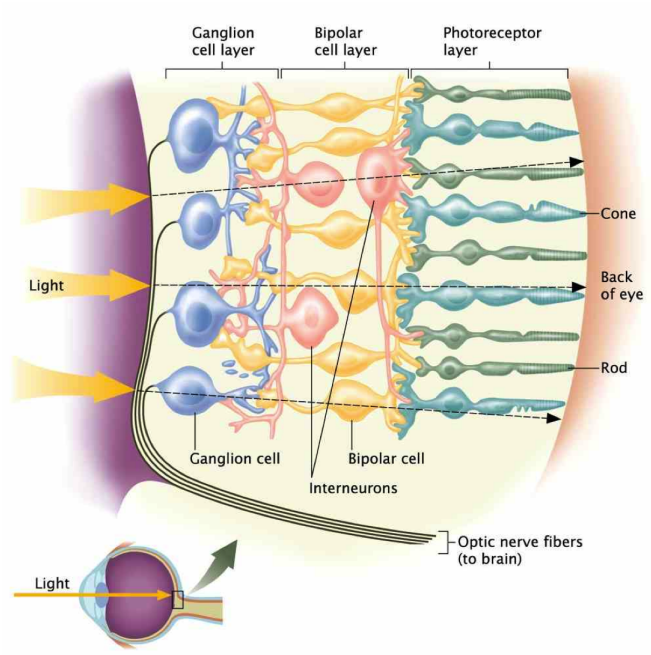

FIGURE 1.2: Diagram showing the anatomy of the retina, with a distribution of rods and cones (https://classconnection.s3.amazonaws.com/32/flashcards/806032/png/retina1318520689618.png)

There are two main types of photoreceptors, rods and cones, with approximately 125 million photoreceptors distributed non-uniformly over the majority of the surface of the retina [10]. Rods are approximately 2 μm in diameter and cannot distinguish colour or fine detail, only light intensity. These rod cells are exceptionally sensitive to light and provide some vision in grey scale in low-light environments. These cells are distributed across most of the retina except the fovea and the optic disc, with a higher density in the peripheries of the retina than the central area. A single nerve fibre may be connected to hundreds of rod cells [11].

Cones (with a size of 6 μm at the widest point) are far less populous than rods, in the range of 6 to 7 million cells, and are responsible for colour vision and fine detail determination [12]. These cells are far less sensitive than rods, and require more light to function and will not operate in low-light environments. Cones can be further divided into three subcategories, those sensitive to short, medium and long wavelength light. These equate as sensitivity to blue, green and red portions of the visible spectrum, respectively [13]. Cone cells are most concentrated at the fovea, with a sparse distribution of cones towards the periphery of the retina. In this region nearer the optic nerve, called the *fovea centralis*, the cones are much smaller with diameters of 1 to 3 μm. An image of the highest detail is provided when looking directly at an object, stimulating the central region of the retina and activating the most cones. The peripheral vision lacks detail and the capability to accurately distinguish colour [14].

Like any organic or inorganic system, the eye is not perfect. There are many factors that negatively impact the performance of the eye and degrade the perceived image. *Myopia*, or near-sightedness, is the condition whereby the lens focuses the rays of light to a point in front of the retina, due to the equivalent power of the lens being too great for the axial length of the eye [15]. The resultant effect is that images of distant objects are focussed in front of the photoreceptors, resulting in a blurred image, though nearby objects are significantly less affected [16]. Typical treatment involves the use of spectacles to compensate this effect [17]. Conversely, *hyperopia* is a defect whereby the light entering the eye is focussed at a point behind the retina, also resulting in the formation of a defocussed image. This results in an effect called farsightedness, negatively impacting the imaging of close objects whilst distant objects are significantly less affected [18]. It is possible to treat this condition with surgery [19].

Accommodation is the term given to the eye's ability to perform macro and fine focussing [20]. The eye uses a crystalline lens supported by ciliary ligaments, which may relax and contract to stretch or compress the lens. When the muscles are relaxed, they pull on the rim of the lens, drawing it into a relatively flat configuration. This increases its radii and focal length [21]. *Presbyopia* is the term given to the defect whereby the range

of accommodation is reduced, inhibiting the ability to focus on near objects [22][23]. *Astigmatism* is arguably the most common form of eye defect, caused by an irregular curvature of the cornea. This causes variation in the equivalent power of light across the surface of the cornea due to differing refractive indices. Astigmatism may be related to myopia and hyperopia in various degrees.

Physical damage, disease and age are key factors in eye performance degradation. As the eye ages there is a progressive reduction in the visual quality produced by the eye. These defects occur most dramatically in the lens, where its shape, mass and size may change significantly, affecting the diameter of focussed spots on the retina [24]. Presbyopia occurs typically in adults aged over 40, with accommodation severely compromised in adults over 50 years old. Transmission of light is reduced in aged lenses as they become 'cloudy' with age [25].

Aside from damage and degeneration, the eye itself is a flawed design [26]. The layer of photoreceptors is located at the back of the retina behind the nerve fibres and blood vessels, causing attenuation of light. Further, the photoreceptors themselves will bleach (saturate) at comparatively low light levels (considering available ambient light, e.g. on a sunny day), necessitating the use of the pupil as a pinhole.

1.2 Motivation

The eye as an imaging system is imperfect and prone to progressive error with age. Degradation of vision leads to a lower quality of life for an individual, and great progress has been made in identifying the causes and effects of eye defects. Poor visual acuity may result from conditions such as glaucoma [27][28] and macular degeneration [29][30][31], but also be symptomatic of direct damage or greater conditions such as diabetes [32][33]. High definition cameras and microscopes may be used to image the surface of the eye to visually determine damage or degeneration [34]. Microscopic images of the surface of the eye have also been compared to histological studies for accuracy measurements [35].

In-vivo imaging of the retina is problematic when the eye itself is flawed. The lens of the eye, with all its defects, must be considered a part of the optical system when imaging the retina. Performance of the retinal imaging system is determined largely by the quality of the eye - namely the condition of the lens, the range of accommodation and the length of the anterior chamber. Imaging resolution on the retina is contingent on the pupil size, which is limited by the biological constraints of the organ. The retinal tissues are very sensitive to light and may be damaged when the illuminating source is too bright [36]. This limits the maximum light permissible into the eye when imaging

the retina as care must be taken to avoid damaging the tissues with high optical power. For safety, emission power of light sources must be reduced, though that also reduces overall sensitivity of the imaging system as less light is backscattered to the detector. Factors outside the optical imaging system itself must also be considered; in particular, the quality of the patient's eye will have an effect on performance. A degenerated eye will reduce the light backscattered from the retina resulting in lower intensity, even before aberrations are considered.

The motivation for this work is to progress technologies that enable safe imaging of the eye *in-vivo* for the early diagnosis of retinal defects or other diseases. This research focusses on non- or minimally-invasive imaging techniques such as scanning laser ophthalmoscopy (SLO) and optical coherence tomography (OCT). These techniques are also useful for imaging other tissues such as skin, and this application will also be investigated. The effects of eye degeneration on vision may be measured and corrected using adaptive optics (AO) technologies. Adaptive optics - the process of detecting optical aberrations and using a control mechanism to compensate - is the core of this research. As described previously, there are many possible defects that may occur in the eye and adaptive optics is a critical technology that allows for high resolution imaging of the retina. There are additional uses for adaptive optics aside from eye imaging. The mechanisms involved in this technology afford great dynamic control over the optical properties of the system, and this control may be exploited to enhance its imaging capabilities.

1.3 Chapter Summary

This section provides a brief description of the contents of each chapter and its relevance to the thesis as a whole. Chapter 1 serves as an introduction to the thesis, discussing the anatomy of the eye and the state of technologies related to microscopy and OCT. In addition, the introductory chapter will provide the author's motivation for research into this field, specific to the use of confocal microscopy and OCT in application to eye imaging.

Chapter 2 introduces the field of microscopy and provides a detailed description of the core theories that support the techniques discussed in this thesis. Special mention is made of the SLO technology, which provides the basis for the research conducted over the course of this PhD. The capabilities and limitations of several microscopy techniques are explored, as are their various practical implementations and applications.

The next chapter develops upon the content of chapter 2 through the introduction of optical coherence tomography (OCT). The theory of white light interferometry, upon

which OCT is based, is explained in detail before its imaging applications are discussed. Also detailed are the various optical sources that make OCT possible, along with a comparison of the different imaging modalities.

The fourth chapter focusses the thesis in one particular area of research, that of AO and its role in modern optical systems. Having been applied first to astronomy, this chapter details the miniaturisation and application of AO to microscopy. The discussion of adaptive optics continues with an explanation of the various optical aberrations. The cause and compound effect of aberrations are a core component to the research conducted in this PhD. Through the detection and management of aberrations, adaptive optics are capable of greatly improving system resolution, particularly when applied to eye imaging as demonstrated in this chapter.

Chapter 5 is the first experimental chapter in this thesis. Contained within are details of a project aiming to implement AO in a combined SLO/OCT imaging system. The content of this chapter forms the basis for all further experimental chapters as it explores the capabilities of AO in improving the wavefront error to enhance system resolution. Explored are the properties of the deformable mirror (DM) and wavefront sensor (WFS), and the design philosophy of an effective AO-SLO/OCT system. Though the primary objective of the work was for eye imaging, the system was also used as a high resolution microscope to image other objects. The project is characterised experimentally by imaging phantoms and resolution targets before acquiring images from biological samples such as the eye *in-vivo*.

Chapter 6 expands upon the work detailed in the previous experimental chapter. With the AO-SLO/OCT system characterised and the performance of the AO assessed, the next step is to assert control over the wavefront using the deformable mirror. The broadband optical source is exchanged for a swept source to facilitate higher imaging speeds. A natural drawback of imaging in the spectral domain (SD) is the decay of sensitivity with depth and the impossibility to perform dynamic focussing. Time domain (TD) OCT systems are able to be configured with dynamic focus such that the confocal gate shifts in synchronism with the coherence gate, achieving good contrast throughout an axial scan. This is not possible with SD-OCT, so this project seeks to manipulate the confocal gate using the deformable mirror to simulate the same effect.

Chapter 7 shows preliminary works into the combination of AO with a novel method, invented in the Applied Optics Group at Kent, termed as master-slave interferometry (MSI). AO-SLO/OCT provides the capability for high resolution images through the reduction of voxel size, and MSI allows for live *en-face* imaging at multiple depths simultaneously using a swept source (SS). This chapter demonstrates a novel application of the MSI in attenuating the speckle effect present in OCT images. Results show

that the system is capable of producing *en-face* images of specular targets wherein the speckle, seen as regular fringes over the target, are removed through averaging of several adjacent *en-face* images at fractions of the probing wavelength. Also presented are images acquired of biological tissue *in-vivo*, demonstrating real-time *en-face* sectioning of the thumb and the retina.

The final experimental chapter of this thesis takes a different approach to optimising an optical system using AO. Wavefront optimisation is typically achieved through repeated measurement and compensation of the wavefront error using a closed loop connecting a wavefront sensor and a deformable mirror. There are several factors that must be considered when designing an AO-SLO/OCT system as detailed in chapter 5. This project aims to eliminate the dependence of the correction algorithm on the wavefront sensor, thereby allowing wavefront optimisation to be performed with a more compact system. This would also allow for wavefront correction using a highly reflective object, and may negate the disadvantage of the back-reflections incurred when using lenses. Additionally, the path of the imaging beam may contain some elements that are not common with the wavefront sensing arm, leaving the AO closed loop blind to the effects of aberrations induced by these elements. The approach described in this chapter involves the use of a genetic algorithm (GA) to iteratively explore the search space of solutions to reach an optimal configuration of the deformable mirror to reach maximum detected irradiance. The GA solution avoids the problem of non-common elements between the sensing and imaging paths as it uses the imaging path for sensing also.

Chapter 9 provides an overall summary of the work presented in this thesis, and contains a final discussion and evaluation. Additionally, suggestions for future work are presented in this chapter.

Chapter 2

Microscopy

2.1 Introduction

This chapter summarises the evolution of microscopy techniques into the modern systems used today. Presented are the core principles of optics and microscopy, including image magnification and image formation through scanning and detection.

2.2 Conventional microscopy

Though the earliest magnifying glasses were invented in the 13th century, it wasn't until the 1590's when experimentation with multiple lenses were conducted. Two Dutch spectacle makers, Zacharias Jansen and his father Hans, created a configuration with several lenses mounted in a tube, and observed that the object at the end of the tube was magnified significantly beyond the capabilities of a single lens. For many years the device remained only a novelty until Antoni van Leeuwenhoek created the first true compound microscope in the late 17th century. Technologies to create improved lenses through grinding and polishing aided Antoni in creating a microscope with greater than 270x magnification power [37]. Using his microscopes, Antoni was able to make many important discoveries in microbiology and is today considered the father of microbiology.

2.2.1 Description

Conventional or 'full-field' microscopes operate by illuminating a sample and observing backscattered light through a set of optical elements that magnify the image using lenses. Backscattered light refers to all light that is returned from the sample and captured by

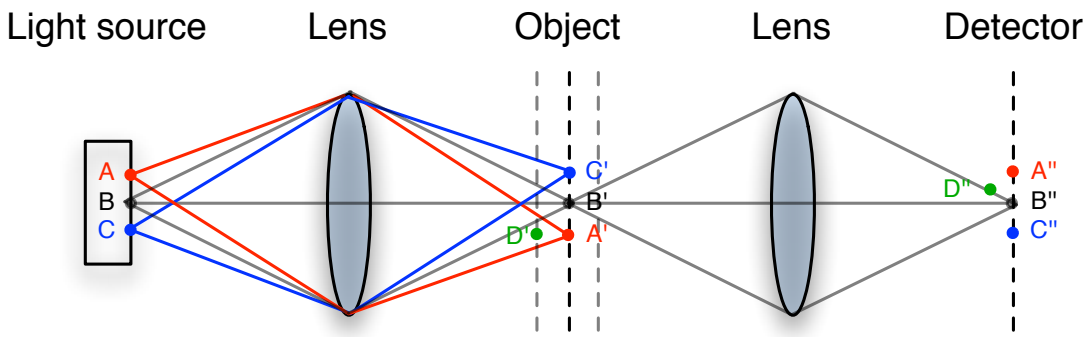

FIGURE 2.1: Diagram of a conventional microscope in transmission.

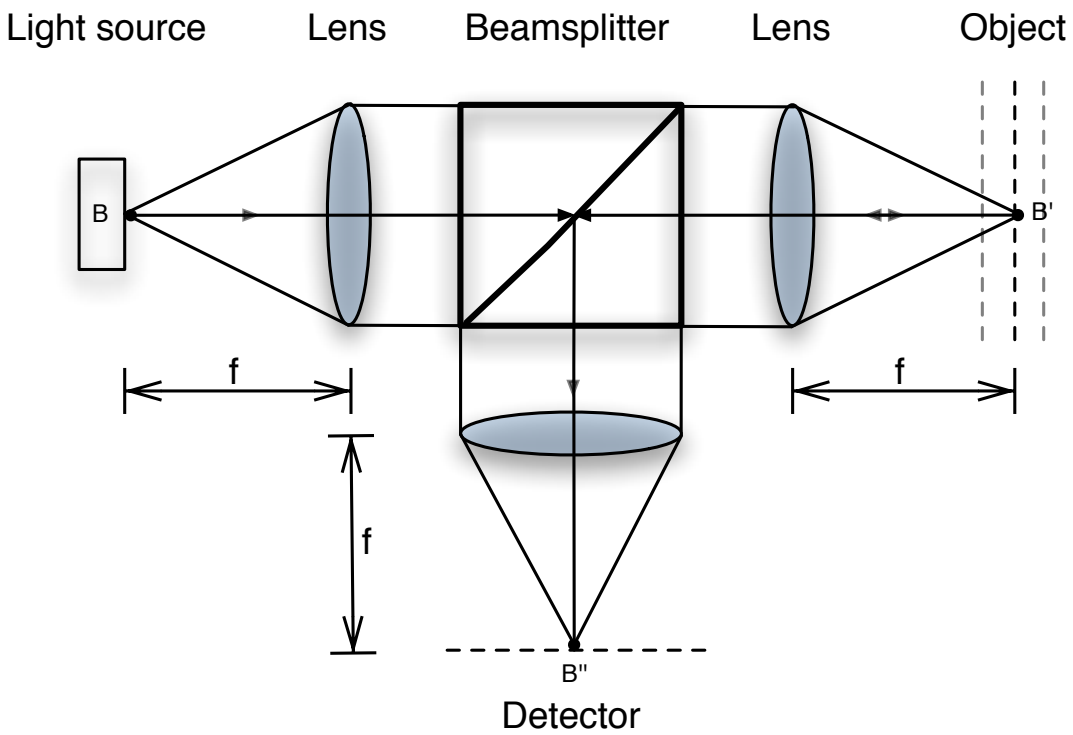

FIGURE 2.2: Diagram of a conventional microscope in reflection.

the objective lens, contributing to the image seen by an observer. Fig. 2.1 shows a conventional microscope in transmission. A light source broadly illuminates the lens and is focussed onto the object at f. The central point of emission B can be seen to focus at position B' and then transmit through the object. The ray then diverges and is focussed onto the detector at position B'' by a second lens. Light emitted from transversal positions A and C from the optical source will also contribute to the detected image as seen by points A'' and C''. Additionally, light from out-of-focus regions D within the convergent beam may also contribute to the image D'' if captured by the

focussing lens. When the object is highly attenuating, the microscope may be configured to function in reflection.

Fig. 2.2 shows a conventional full-field microscope in reflection. In this case, a beamsplitter is used. In this example, light from the source B is collimated by a lens and transmitted through a beamsplitter to be focussed onto the object at B' using an objective lens. Light backscattered from this position is captured by the objective lens, collimated and reflected to an additional lens that focusses the light onto the detector at position B''. This arrangement causes a loss of detected optical power due to the beamsplitter, however it allows for imaging of objects that are highly attenuating, as most thick samples are.

2.2.2 Limitations

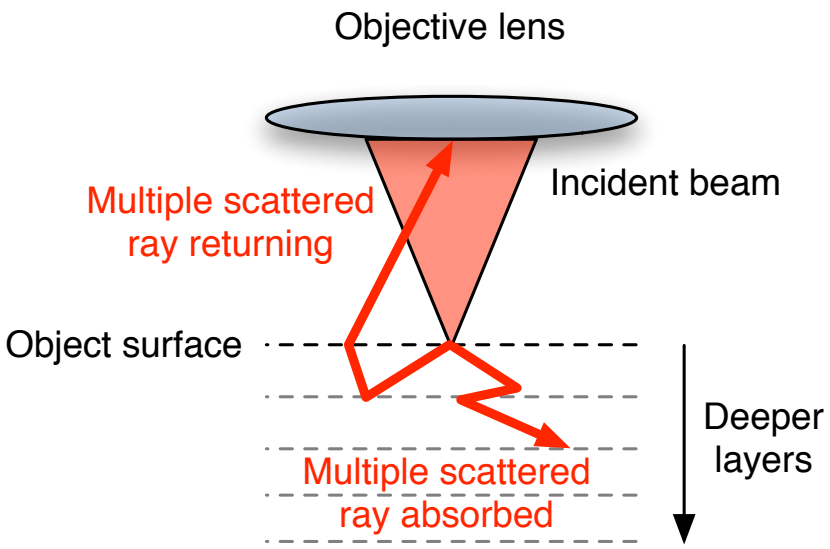

FIGURE 2.3: Diagram showing light scattering from different depth interfaces in an object.

As photons travel trough a medium they may experience multiple scattering events upon contact with similarly or larger sized particles, before being absorbed or backscattered. These photons may be captured by the objective and return information from out of focus regions, resulting in loss of image resolution and contrast. This effect can be seen in Fig. 2.3 where light backscattered from out of focus regions is captured by the objective lens.

Additionally, the use of a lamp broadly emitting white light can have a similar effect. Ideally, a microscope would allow for examination of returned light from a single point

on the sample at any given time. Use of a lamp will illuminate all points of the sample simultaneously, introducing cross-talk between points; the desired imaging point will be distorted by rays of scattered light from neighbouring points.

2.3 Scanning microscopy

2.3.1 Description

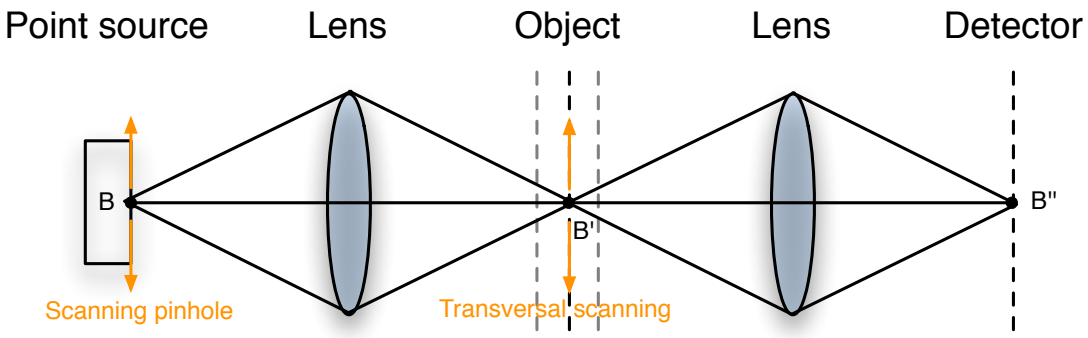

FIGURE 2.4: Diagram of a scanning microscope in transmission.

A scanning microscope improves upon the design of the full-field microscope by using a point light source to illuminate a single point on the sample. Figure 2.4 shows a schematic of a scanning microscope in transmission, demonstrating how the single point of emission B illuminates a single point B' in the focal plane on the sample. Light transmitted from point B' is then focused by a lens to a single point B'' on the detector.

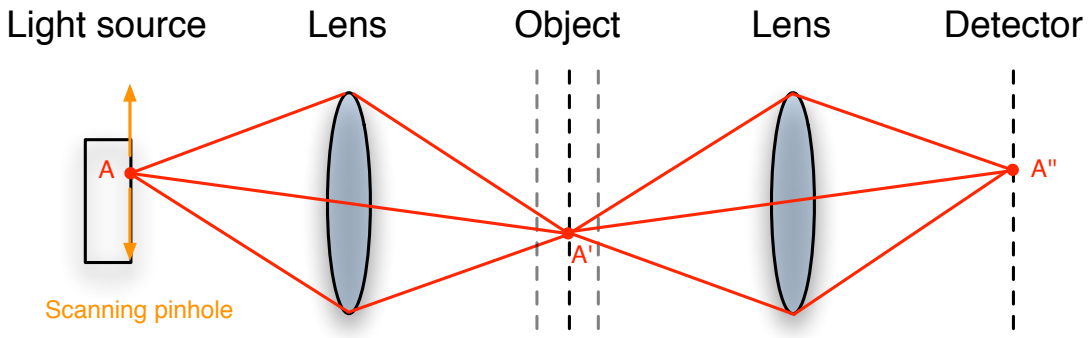

FIGURE 2.5: Diagram of a scanning microscope in transmission at different transversal position.

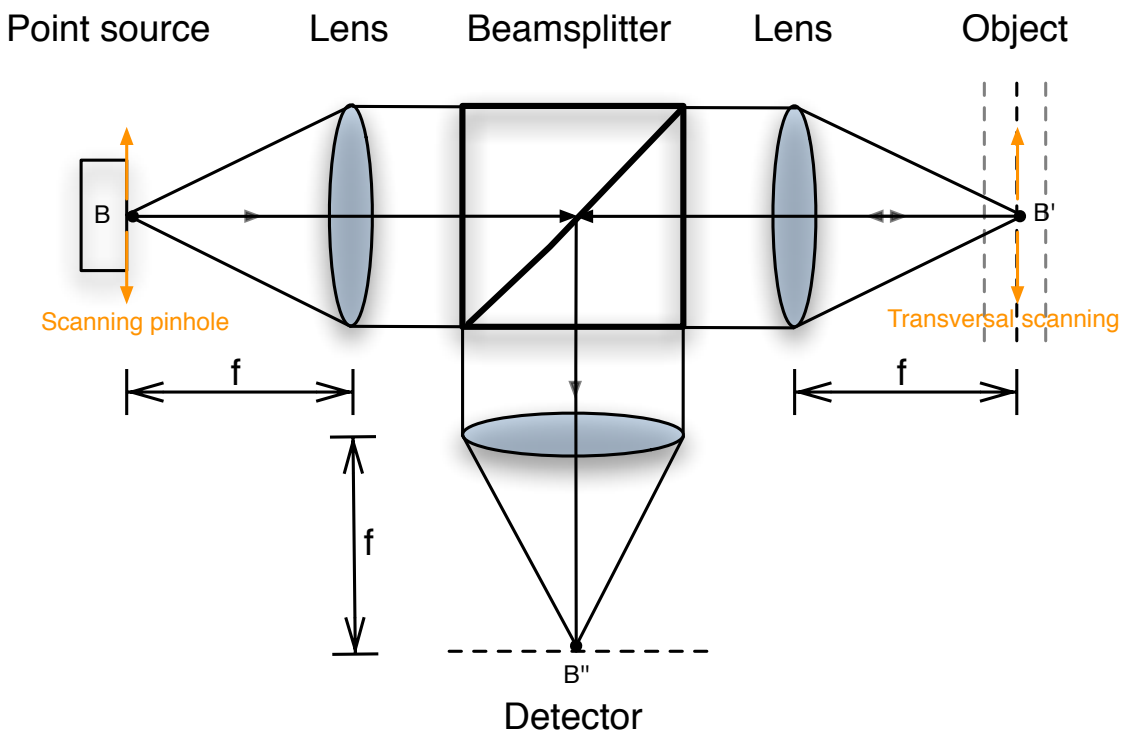

FIGURE 2.6: Diagram of a scanning microscope in reflection.

Other points in the focal plane are not directly illuminated by the point source until it is scanned transversally across the surface of the sample. Fig. 2.5 shows the same scanning microscope wherein the light source pinhole has been repositioned, in a sense this shifts the point source to position A. The light propagates through the system and is focussed on a different transversal position on the object A' in the same focal plane. The light from this position is then focused onto the detector at position A''. A complete image may be formed by sweeping the pinhole across the aperture of the light source. As the point source is moved, the spot on the sample illuminates each point in the object sequentially and an image may be formed. In this way there is no direct contribution of neighbouring points to the desired imaging point. When the scanning microscope is positioned to image point B', the contribution from a neighbouring point A' is minimal, though not completely eliminated. Fig. 2.7 shows how the point source at B illuminates only transversal position B' on the object, and A' and C' are rejected.

Fig. 2.6 shows the configuration of a scanning microscope in reflection. This operates functionally the same as shown in Fig. 2.2, with the exception that a point source is used instead of a broad light source.

2.3.2 Limitations

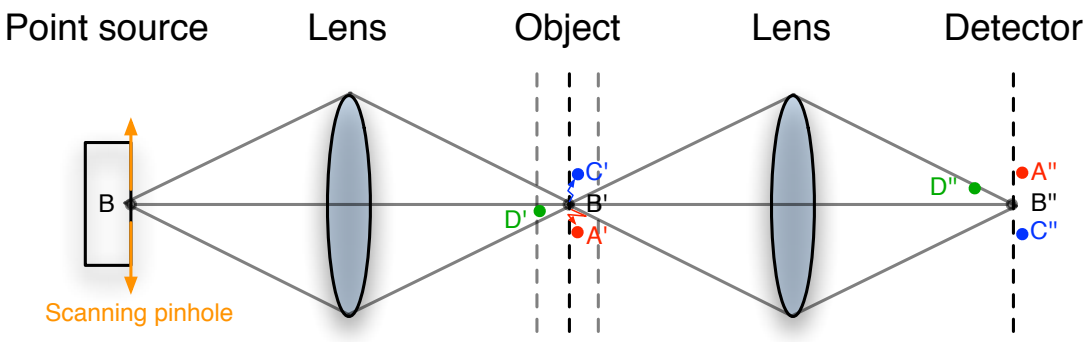

FIGURE 2.7: Diagram of a scanning microscope in transmission with contributions from out of focus region D' and stray light contribution from different transversal positions A' and B'.

Fig. 2.7 also shows that the scanning microscope shares one of the limitations of the conventional full-field microscope described in Fig. 2.1. When the pinhole is positioned such that B is the point source, it is expected that only information from B' should reach the detector at position B''. Though there is no direct contribution to the image from points A' and C', it can be seen that light from an out-of-focus region D' is captured by the focussing lens and reaches contributes to the image, causing a defocussed image of D' to overlay the image of B'.

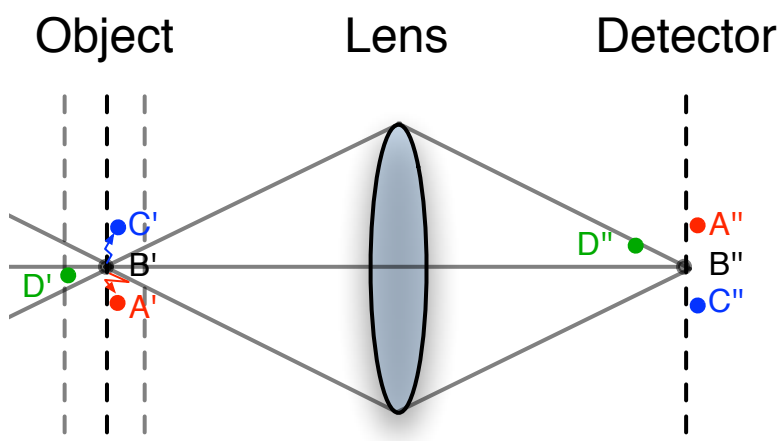

FIGURE 2.8: Diagram showing scattered light from different transversal positions in the focal plane contributing to the image seen by the detector.

In addition, there may be some slight contribution of points A' and B' to the final image. Fig. 2.8 shows a closer look at the scattering within the object. Some light that is focussed at point B' may scatter to neighbouring positions A' and C' and be captured

by the lens to form an image on the detector at A'' and C''. This contribution of light from neighbouring transversal positions will cause a loss in resolution as the ability to discriminate points is diminished.

2.4 Confocal microscopy

The first reported confocal scanning microscope was built by Marvin Minsky in 1955, who went on to file a patent in 1957 [38]. In this configuration, the point source was stationary and the object fixed to a translation stage that scanned the object under the probing beam. In 1971, two scientists from Yale University published papers describing the first confocal scanning microscope using a laser [39]. This system achieved scanning by moving the lens and the cathode ray rather than the object. Later in 1977, scientists from Oxford University published a paper that discusses theoretical analysis of confocal laser scanning microscopes [40]. In the late 1980's, Amos and White from Cambridge University built the first confocal scanning microscope utilising a flying spot [41][42].

2.4.1 Description

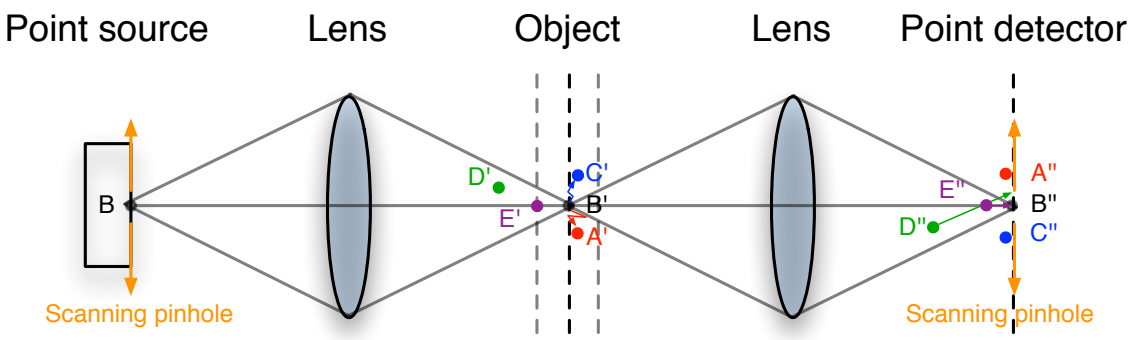

FIGURE 2.9: Diagram of a confocal microscope in transmission.

The confocal microscope was designed to address the problems of the scanning microscope with regards to acceptance of rays from out of focus positions. In combination with a point source, a pinhole is placed at a conjugate point in the system prior to the detector. As the point source is in position B, the point B' is illuminated on the sample, as seen in Fig. 2.9. As with the scanning microscope, the cone of rays illuminates points outside of the focal plane D' and E', while scattered light illuminates neighbouring points within the focal plane A' and C'.

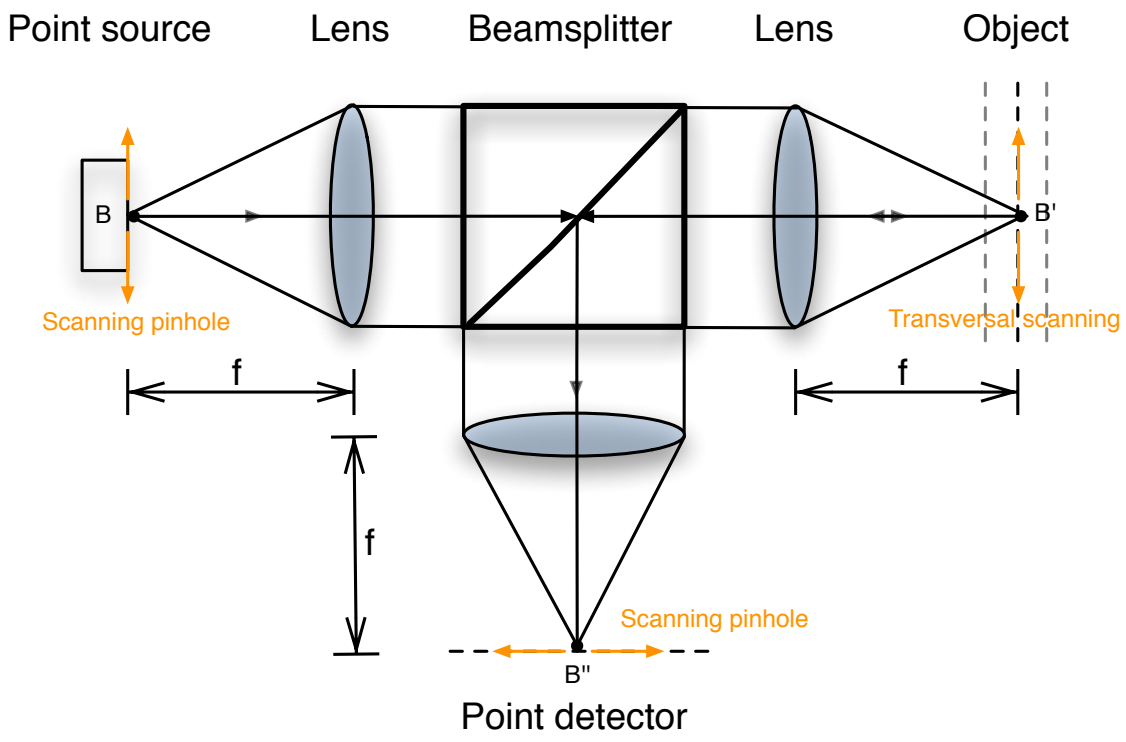

FIGURE 2.10: Diagram of a confocal microscope in reflection.

A pinhole is placed in front of the aperture of the detector, creating a point detector. The role of this pinhole is to block the light returning from out-of-focus points on the sample. Rays returning from points A', C' and D' are blocked by the pinhole and not collected by the point detector. In this way, the confocal microscope is able to illuminate a single point on the sample at any given time and also eliminate most of the stray reflections that might otherwise reach the detector and degrade the image. To form a complete image the point source must be translated in synchronism with the point detector.

Fig. 2.10 shows the configuration of a confocal microscope in reflection. This configuration serves as the basis for more advanced imaging techniques such as SLO and OCT. Since transmissive light cannot be collected in the case of eye imaging, a configuration where light is collected in reflection is important.

In practice, it may be difficult to arrange a confocal microscope with multiple moving pinholes as described in Fig. 2.9. Light from an optical source may be emitted from a fibre, with the fibre tip acting as a point source, with an effective pinhole size equal to the fibre core. Likewise, light returned from the object may be collected by a lens and focussed onto a fibre tip and then propagated to a detector, effectively creating a point detector.

2.4.2 Limitations

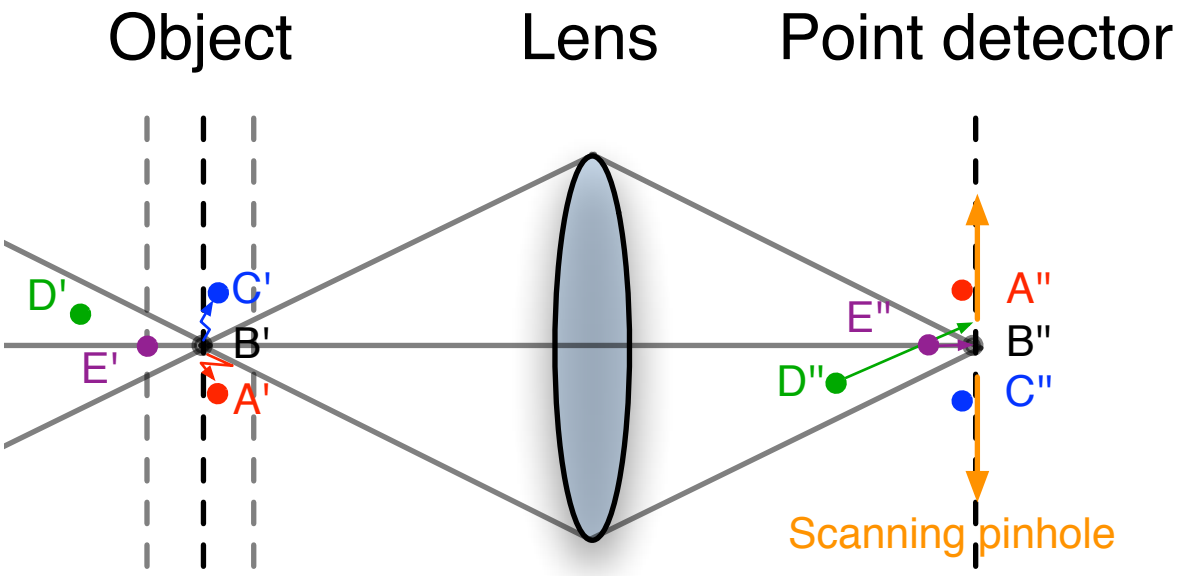

FIGURE 2.11: Diagram showing the imperfect rejection of reflectors that are out of the focal plane.

Confocal microscopes are not perfect in rejecting light from out of focus points. Fig. 2.11 shows a closer look at the interaction between the light focussed on the object and the signal that reaches the point detector. It can be seen that an improvement is made over the scanning microscope with regards to rejection of scattered light from adjacent regions in the focal plane. Scattered light from A' and C' are blocked by the pinhole detector at A'' and C''.

A problem remains, however, in that the cone of rays focussed on B' is also seen to illuminate points D' and E'. Light returning from these points are not completely blocked by the pinhole detector; there is a direct contribution of E' to the image at E'', and scattered light from D' may still be accepted by the pinhole detector at D''. These points will contribute to the image resulting in a loss of resolution, particularly in depth. Reducing the size of the pinholes allows for higher rejection rates for points outside the focus, though this will also reduce the amount of light that reaches the detector. Sufficiently bright light sources such as super luminescent diodes (SLDs) and lasers should be used to compensate for this loss.

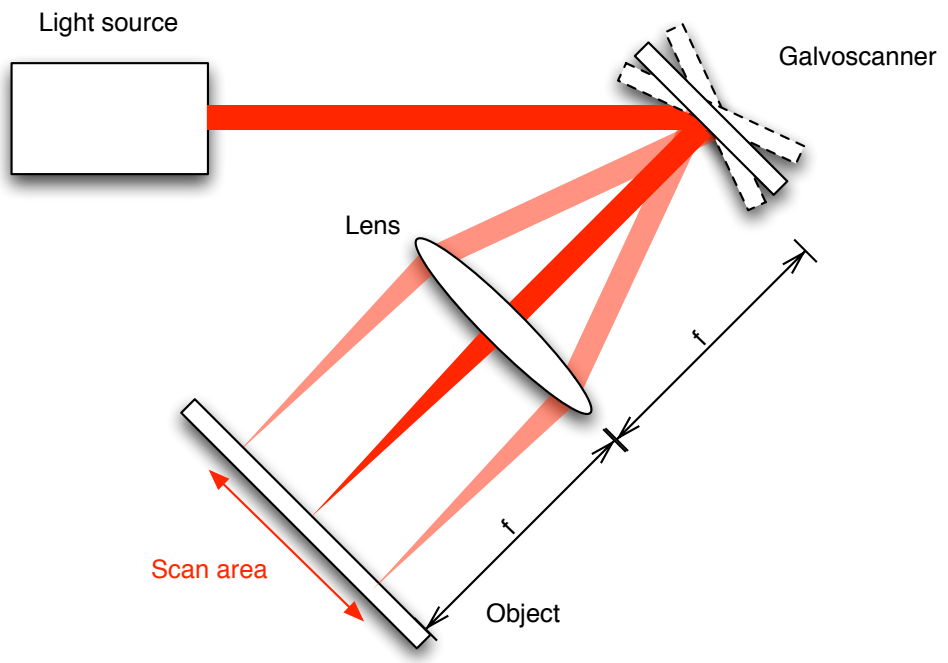

FIGURE 2.12: Simplified diagram demonstrating the use of a galvoscanner to sweep a collimated beam transversally across an objective lens. This has the effect of focussing the beam at different transversal positions on the object by altering the reflected angle of the beam.

2.4.3 Transversal scanning

For the purpose of transversal scanning, motorised stages or mirrors may be used to modify the beam position in free space. Fig. 2.12 shows a simplified configuration of interface optics where collimated light emitted from a point source (using a lens to collimate the divergent emission from the fibre) is reflected by a galvoscanner, which scans the beam across the surface of the objective lens. The beam is focussed to a point on the object and may be scanned across the surface by modulating the voltage to the scanner.

2.5 Scanning laser ophthalmology (SLO)

The adaptation and use of a confocal microscope for eye imaging was reported in 1987 by Webb and Hughes [43]. This configuration rasters a probing beam across the retina and uses an avalanche photodiode (APD) detector to generate an image from the collected backscattered light.

2.5.1 Description

Confocal microscopes use an objective lens to focus the beam upon the imaging sample. Though a confocal microscope can produce high resolution images, some modifications are required before it becomes suitable for imaging an eye. Using an eye as a sample introduces an additional optical element - the lens of the eye itself. In the case of retinal imaging, it is required for the system to produce a collimated imaging beam, which may then be focussed by the eye lens to a small spot upon the retina.

The confocal microscope must be modified such that the optical path is not terminated with an objective lens, and that the beam is collimated when it meets the eye. In addition, careful consideration must be made with regards to beam diameter at this point. The pupil of the eye dynamically reacts to ambient light levels, contracting in bright environments and dilating in dark environments to, in effect, modify the sensitivity of the eye. Since an SLO system must exploit the eye lens, it is restricted by the size of the pupil. As an example, the pupil of the human eye may have a diameter of 4 to 9 mm in low light, and between 3 to 5 mm in brighter environments.

This presents a problem when imaging the retina; should the system be calibrated for the maximum pupil size, the minimum or somewhere in between? To maximise the potential for an SLO system, one might wish to consider the best case scenario; namely, the largest pupil size that may be achievable. Increasing the available pupil size will have a positive effect on the imaging resolution as the NA is increased, given a perfect lens. Conceivably a drug such as Tropicamine may be administered to the eye to dilate the pupil, allowing for transmission of a larger diameter beam and producing higher resolution images. When the lens is imperfect, increasing the pupil diameter may in fact degrade the image, which is where wavefront correction methods such as those discussed in chapter 4 are necessary.

2.5.2 Transversal scanning

A major difference between a confocal microscope and an SLO system is the effect on the scanning regime. Fig. 2.13 demonstrates a variation of the configuration shown in Fig. 2.12, wherein the system has been modified from microscopy of tissue to retinal imaging. Eye imaging involves an extra lens (the lens of the eye itself) positioned immediately prior to the sample, so the system must be adjusted to ensure the spot is focussed upon the retina. This is done by constructing a telescope comprised of two lenses separated by $f_1 + f_2$, where these values denote the focal length of the first and second lenses.

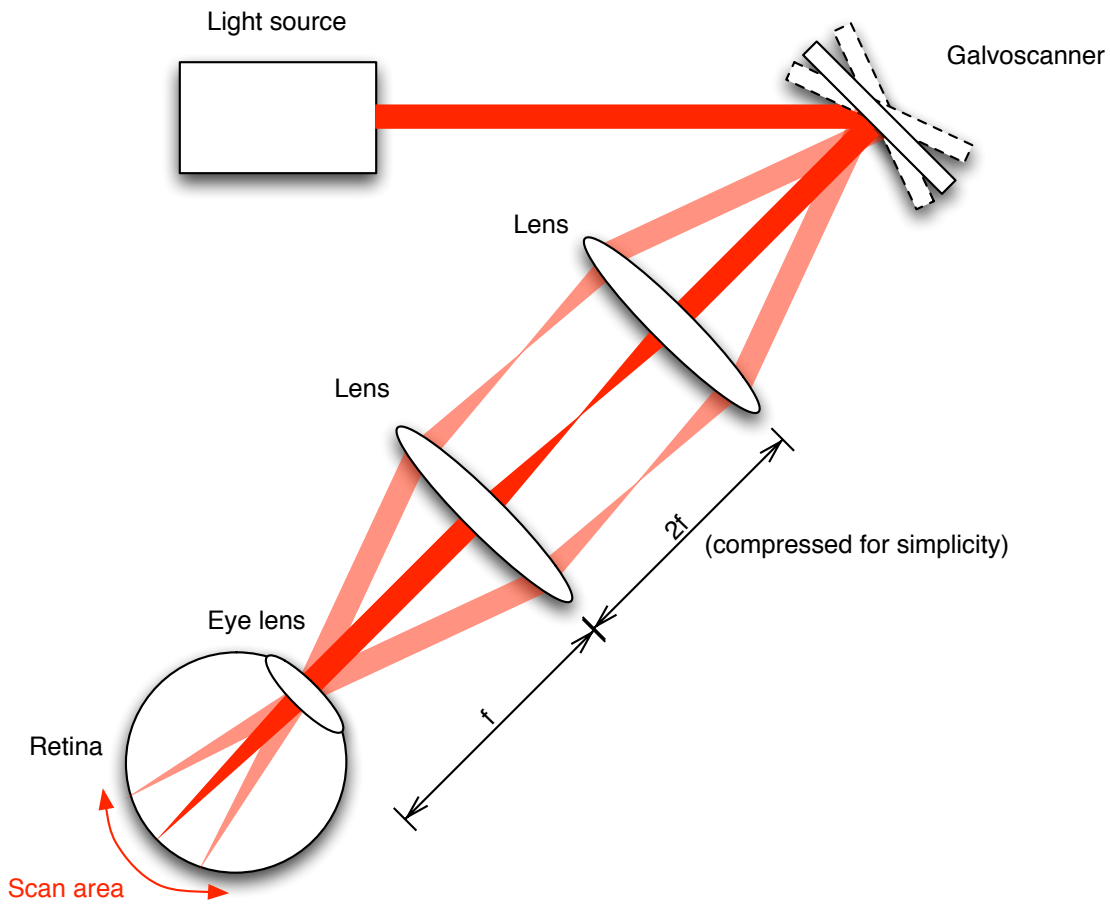

FIGURE 2.13: Diagram demonstrating the adaptation of a microscope system to cater for transversal scanning of the retina. The lens of the eye is used to change the angle of incidence of light focussed on the retina.

When imaging tissue, Fig. 2.12 shows that the object is placed at f from the lens. Placing the eye at this position will create an image of the surface of the cornea, as the beam is scanned across its surface. To image the retina, the beam is required to enter the pupil at all transversal positions of the galvoscanner. In Fig. 2.13 it can be seen that a second identical lens is placed at $2f$ from the first, and then the eye is positioned at f from this objective. The beam is collimated as it transmits through the eye lens, and the spot on the cornea is stationary as the galvoscanner is moved. This off-axis configuration is what allows for transversal imaging of the retina.

2.5.3 Limitations

SLO is still subject to several limitations that reduce the quality of images. The system resolution and sensitivity is at the mercy of the eye being imaged, which proves to be a

problematic target. Reflections from the cornea may distort the image, and aberrations caused by imperfections in the lens will lower resolution and sensitivity. An old, diseased or damaged eye may be so aberrant and lowly transmissive that the image provides little diagnostic information.

With a possible requirement of drug administration to dilate the pupil, SLO moves from a non-invasive to a minimally-invasive medical imaging technique. This introduces more ethics procedures for clinicians, and also imposes limitations on the frequency of imaging sessions as the eye recovers. Additionally, human patients may find the procedure uncomfortable or refuse it outright.

SLO offers high resolution and is able to determine individual photoreceptors within a narrow field of view. The small imaging angles prove problematic when the target is a conscious, living organism. The eye is never static; microsaccades keep the eye moving very fast even when the patient is fixated upon a point. In addition, respiration and vascular activity will cause tissues in the eye to move or change properties. To compound this problem, the patient's head or body may move over time even with the use of a headrest. The combination of these factors will produce motion artefacts in the images or lower resolution. There are several ways to compensate for this motion reported in literature, though they involve additional elements that raise the complexity of the system design [44][45].

There is also the concern of low axial resolution. SLO provides high transversal resolution images, making it ideally suited for *en-face* imaging of the retina, however attempting to image deeper into tissue is problematic. Using longer wavelength light sources will allow for deeper penetration into tissue, however there is still the issue of light backscattered from all axial positions relative to the beam contributing to the image. It is not possible to acquire an *en-face* slice at a particular depth without contribution from reflectors at different depths. A technique called optical coherence tomography (OCT) is described in chapter 3 which reduces the voxel size, allowing for better discrimination in depth.

2.6 Resolution and the effect of pinhole size

The resolution of a microscope can be determined by considering the focussed point on the object as a diffraction-limited spot. The amplitude of the light on the object as detected is given by the point spread function (PSF) of the objective lens h(v):

$$h(v) = \frac{2J_1(v)}{v} \tag{2.1}$$

where

$$v = \frac{2\pi\rho}{\lambda}\eta \sin\alpha \tag{2.2}$$

where ρ is the radial distance from the optical axis, η is the index of refraction for the imaging medium, J_1 is a first-order Bessel function of the first kind and α is the half angle of incidence of light on the objective lens. The term $\eta \sin\alpha$ is the numerical aperture of the objective lens, its value given by the expression

$$NA = \eta \sin\alpha = \eta \sin\left[\arctan\left(\frac{D}{2f}\right)\right] \tag{2.3}$$

and can be approximated to

$$NA \approx \eta\frac{D}{2f} \tag{2.4}$$

where D is the diameter of the objective lens.

For microscopy we operate in terms of intensities and not with electric fields since the waves for two neighbouring fields do not interact, however their intensities are cumulative. The intensity PSF for a standard microscope operating with incoherent illumination is given by the square of the modulus of the electric field PSF:

$$I(v) = |h(v)|^2 = \left(\frac{2J_1(v)}{v}\right)^2 \tag{2.5}$$

This function describes the Airy disc around the central lobe at v_0. As $\sin\alpha$ increases, the transversal size of the spot becomes smaller, increasing resolution. Given $v_0 = 1.22\pi$, the transversal resolution can be calculated as

$$\rho_0 = \frac{\lambda}{2\pi \sin\alpha} \cdot 1.22\pi = 0.61\frac{\lambda}{\eta \sin\alpha} \tag{2.6}$$

The intensity of a given point in the image is given by the convolution

$$I(v) = |h|^2 * |r|^2 \tag{2.7}$$

where $|h^2|$ denotes the intensity of the PSF and $|r^2|$ denotes the intensity of the point in the image. It can be seen that the intensity PSF of a standard microscope is linear.

In the case of a confocal microscope in reflection, the objective lens is used twice. Since the waves in a confocal microscope are spatially coherent and the intensities are not cumulative, the intensity PSF is given by the convolution

$$I(v) = |h^2 * r|^2 \tag{2.8}$$

assuming that the point on the detector is infinitesimally small. For a confocal microscope, the intensity PSF is given by

$$I(v) = \left(\frac{2J_1(v)}{v}\right)^4 \tag{2.9}$$

From this expression it can be seen that for a confocal microscope, the intensity PSF is equal to the square of the standard microscope PSF. This introduces a non-linearity that improves the transversal resolution over the standard microscope. The size of the Airy disc has not changed but it has the effect of reducing the side lobes that can cause speckle [46]. Speckle noise is caused by the contribution of the side lobes to the image as seen by the point detector. In a standard microscope, the first side lobe is reduced by 18 dB from the peak of the central lobe. For a confocal microscope this value increases to 36 dB, causing a sharpening of the FWHM of the PSF.

A confocal microscope also allows for discrimination in depth, which is not possible with a standard microscope [47][48]. To assess depth resolution, the object may be exchanged with a plane mirror. The intensity of detected light from the mirror given an infinitesimally small pinhole is expressed as

$$I(u) = \left(\frac{\sin(\frac{u}{2})}{\frac{u}{2}}\right)^2 \tag{2.10}$$

where

$$u = \frac{8\pi}{\lambda} z\eta \sin^2\frac{\alpha}{2} \approx 2z\frac{\pi}{\lambda}NA^2 \tag{2.11}$$

Axial resolution for a confocal microscope is commonly expressed as

$$\rho_{axial} = 1.4\lambda\frac{\eta}{NA^2} \tag{2.12}$$

Though the improvement in axial resolution over a standard microscope is modest, there is a significant axial resolution advantage when performing depth sectioning of thick samples with a confocal microscope [49].

These expressions work under the assumption of infinitesimally small pinholes. In practice, the pinholes have a finite size with resolution (transversal and axial) becoming poorer as the pinhole size increases, though more signal is collected [50]. The configuration of a confocal microscope is a compromise between transversal resolution, axial resolution and the efficiency of light coupled back to the detector, with a dependency on pinhole size and is represented by the normalised expression v_p:

$$v_p = \frac{2\pi}{\lambda} r_p \eta \sin \alpha_p \tag{2.13}$$

where r_p denotes the radius of the pinhole and $\eta \sin \alpha_p$ is the NA of the lens in front of the pinhole. As the pinhole size increases from zero, the axial resolution is practically constant up to $v_p = 2$ and increases continuously from $v_p = 4$. Transversal resolution immediately worsens as v_p increases from 0.5 and then stays constant for $v_p > 4$. It can be determined that the ideal case for a confocal microscope is $v_p \leq 0.5$.

Chapter 3

Optical coherence tomography (OCT)

3.1 Introduction

Optical coherence tomography (OCT) is an evolution of confocal microscopy that has found a niche as an optical imaging modality for medicine and biomedical optics [51][52]. Confocal microscopes facilitate the imaging of objects at high transversal resolution by eliminating rays that are out of focus (see section 2.4). OCT systems are able to acquire high resolution cross-sections of biological tissues by measuring light that is backscattered, with fine discrimination in depth as determined by the coherence gate [53][54]. An OCT system is capable of distinguishing layers in depth and resolving micro-structures within the biological sample. The key benefit of OCT is that imaging is able to be performed *in-vivo* and in real time [55][56]. OCT is able to perform non- or minimally-invasive optical biopsy of living tissue, presenting tissue pathology to a clinician without the requirement of its removal from the host.

Transversal and depth resolution of confocal imaging systems are determined by the numerical aperture (NA) of the objective used to focus the light upon a sample. This is problematic when imaging some tissues where lenses must be pressed close the sample with an interface of oil. This procedure is unsuitable for *in-vivo* eye imaging, where the imaging objective is the lens of the eye itself and the NA cannot be increased. OCT is able to achieve such high depth resolution by decoupling it from the NA of the objective. The depth resolution of an OCT system is determined mainly by the optical source used, and not by the objective. It is for this reason that OCT is able to achieve a depth resolution several orders of magnitude higher than confocal microscopy when

imaging the eye. OCT systems have been reported to achieve depth resolution of 1 μm, or 2 μm in the eye [57].

Light is transmitted into the sample and reference arms, and the intensity of the interference signal of backscattered light from both arms is captured. A cross-sectional image is acquired by taking these measurements while using a scanning mirror to sweep the imaging beam across the sample, similarly to Fig. 2.12. In this way, multiple axial scans (A-scans) are acquired transversally, forming a 2D data set. This 2D data set represents the information gained from backscattered light in a cross-sectional plane through the tissue. These cross-sectional OCT images are often referred to as B-scans.

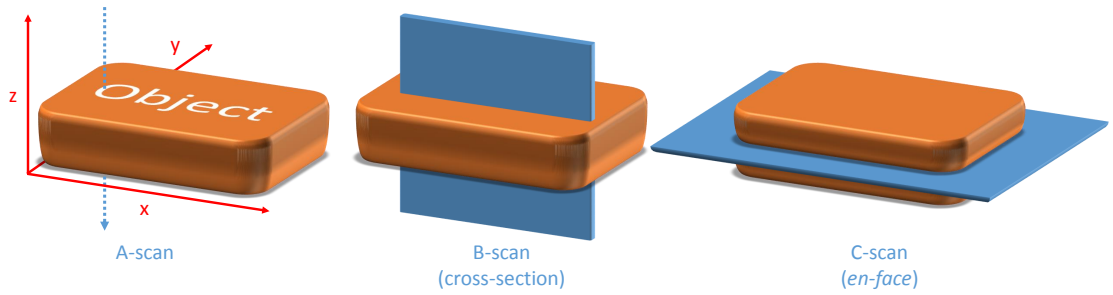

FIGURE 3.1: Diagram showing scanning regimes for OCT.

With the employment of an additional scanning mirror, the beam may be rastered in two dimensions across the sample whilst acquiring OCT A-scans. This allows for acquisition of 3D data sets, representing a 3D image of the scanned sample volume. This 3D data is then manipulated to provide images from different planes, most notably presenting *en-face* (top-down, or C-scan) images. Fig. 3.1 visualises the differences between an axial reflectivity profile (A-scan), a cross-section (B-scan) and an *en-face* transversal scan (C-scan).

There are many imaging techniques that use a range of technologies such as microscopy, ultrasound, magnetic resonance imaging (MRI) and more. The common element among these modalities is that they are all non-invasive, making them ideal for biomedical imaging. A comparison of these imaging techniques emphasizes the importance of OCT, as seen in Fig. 3.2. Confocal microscopy is able to achieve high transversal resolution, though the penetration depth is low ($<$ 1 mm) [58]. Microscopy is typically performed *en-face* to take advantage of the high transversal resolution. The imaging depth of microscopes are limited due to the attenuation of light within the object, which has been modelled extensively [59][60][61][62][63]. Scattering and absorption of light within the object significantly degrade its maximum imaging depth to a few hundred micrometres, and scattering also reduces depth resolution.

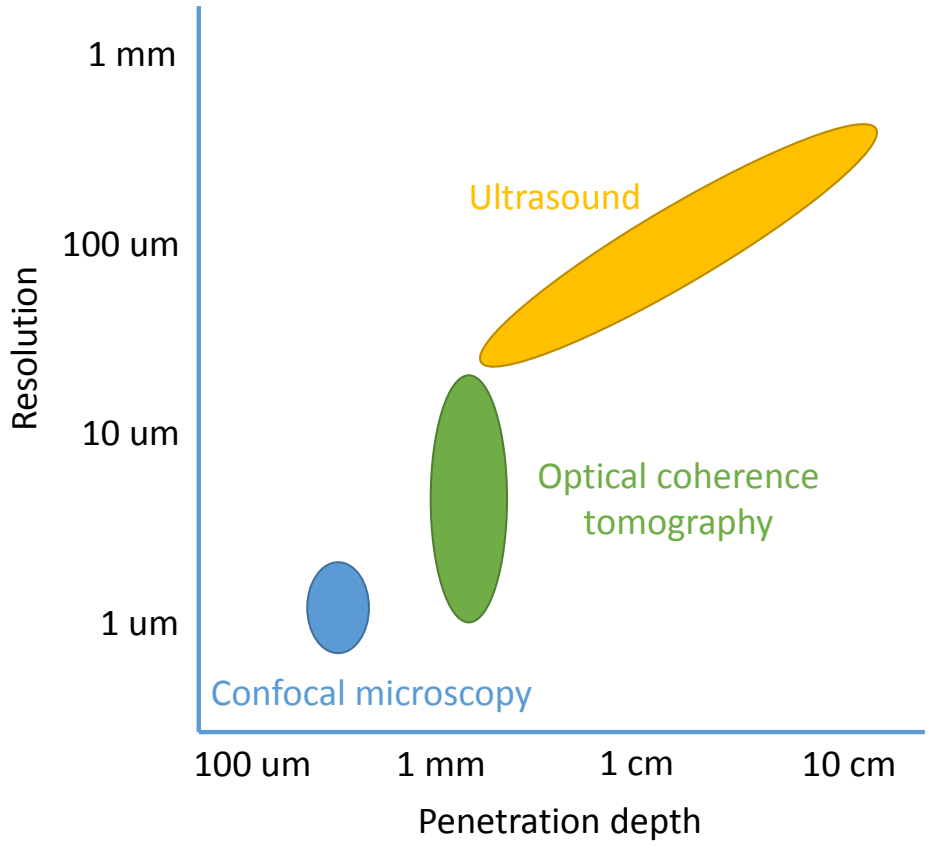

FIGURE 3.2: Diagram showing the penetration depth and resolution of OCT in comparison with confocal microscopy and ultrasound.

Ultrasonic imaging (sonography) is typically capable of achieving a resolution of 0.1 to 1 mm, depending on the frequency used in the range 3 to 40 MHz [64][65]. The principal benefit of ultrasound is the penetration depth, enabling imaging deep in the body [66][67]. Some ultrasound imaging systems have been configured to emit higher frequencies (over 100 MHz) for increased resolution of approximately 20 μm at the cost of penetration depth, restricting them to less than a centimetre in tissue due to the increased attenuation of highest frequencies by biological matter [68].

There exists a gap between microscopy and ultrasound that is neatly filled by the capabilities of OCT as an imaging modality. OCT can achieve high transversal and axial resolution, and offers an increased maximum imaging depth of several millimetres when compared with standard microscopy. When compared with ultrasound, modern OCT systems offer an axial resolution improvement of several orders of magnitude.

Being an optical imaging technique, OCT suffers from a low penetration depth due to high scattering of light by most biological tissues. Confocal microscopy can typically penetrate 350 μm in the skin, whereas OCT may reach 1.5 μm in skin. Internal tissues

can still be imaging by using specially designed instruments that convey the light through a suitable delivery tool such as an endoscope or catheter [69][70][71]. This enables imaging of certain regions of the body such as the larynx *in-vivo*, using a compact hand-held tool that is convenient for clinical use [72][73][74].

3.2 White Light Interferometry

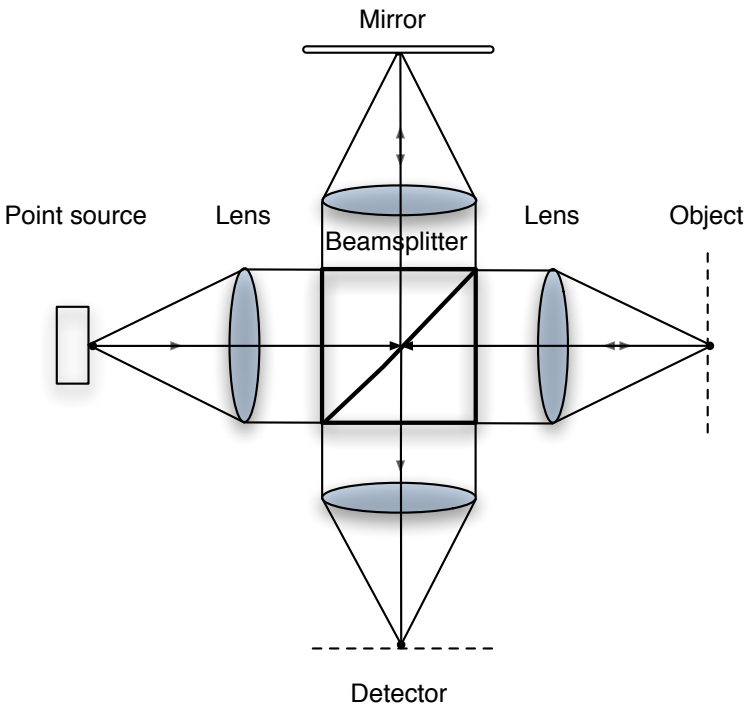

FIGURE 3.3: Diagram showing a Michelson interferometer.

Several parallels can be drawn between ultrasound and OCT imaging. Both technologies emit waves of radiation and measure the backscattered signal from an object. As the sound or light travels through an object, it is backscattered differently from internal layers with varying acoustic or optical properties. This procedure allows for imaging of interfaces within the object.

The key difference is the speed of the emitted radiation used for imaging. Sound waves propagate through soft tissue at a speed of $\backsim 1.5 \text{ x } 10^3$ m/s in comparison with much larger $c = 3 \text{ x } 10^8$ m/s.

White light interferometry (also referred to as low coherence interferometry) is the optical measurement technique upon which OCT is founded.

Fig. 3.3 shows a diagram of a Michelson interferometer in bulk (air). Light emitted from a point source is collimated by a lens and then divided into two arms by an optical beamsplitter. One path, called the reference arm, is focussed by a lens and terminated by a mirror that is oriented orthogonal to the incident beam, sending light directly back to the beamsplitter. The remaining light is directed into the object arm towards an objective lens that focusses the light on an imaging sample. Light that is backscattered from the object and is collected by the objective lens will pass back through the beamsplitter.

Light returned from both arms is recombined here and travels to a detector. When the optical path difference (OPD) between the arms is less than the coherence length of the source, an interference signal is obtained when the beams are recombined [75].

The electric field intensity E at a given point in space is given by the sum of separate contributing fields E_1, E_2 (shown in Eq 3.1), in this case E_1 and E_2 represent light returning from the reference and object arm, though the same is true of two independent sources.

$$E = E_1 + E_2 \tag{3.1}$$

Since measurement of the electric field is an impractical quantity to detect due to instrument limitations (as there simply is not a device fast enough to measure this quantity), the irradiance I is measured directly using a photodetector. Irradiance (often referred to as intensity) is the average energy per unit area per unit time. Any photodetector has a light-admitting aperture of fixed area A with an integration time average of T, causing the measurement of I to vary between instruments. This can be made a practical comparable measurement by dividing the value by the area A and by time T, producing a quantity unaffected by variations of these two factors. Within a medium that is homogeneous and isotropic, irradiance can be expressed as

$$I = \epsilon\nu\langle E^2\rangle_\tau \tag{3.2}$$

where $\langle E^2\rangle_\tau$ is the time average of the magnitude of the electric field intensity squared $\langle E \cdot E\rangle_\tau$. For consideration of an identical medium for both fields, the constants can be removed and irradiance can be simplified to

$$I = \langle E^2\rangle_\tau \tag{3.3}$$

Given that

$$E^2 = E \cdot E \tag{3.4}$$

for the case of two contributing fields

$$E^2 = (E_1 + E_2) \cdot (E_1 + E_2) \tag{3.5}$$

therefore

$$E^2 = E_1^2 + E_2^2 + 2E_1 \cdot E_2 \tag{3.6}$$

Taking the time average of this equation determines that irradiance becomes

$$I = I_1 + I_2 + I_{12} \tag{3.7}$$

and can be expanded as follows

$$I = \langle E_1^2 \rangle_\tau + \langle E_2^2 \rangle_\tau + 2\langle E_1 \cdot E_2 \rangle_\tau \tag{3.8}$$

Within this equation we have the sum detected irradiance from two sources

$$I_1 = \langle E_1^2 \rangle_\tau \tag{3.9}$$

$$I_2 = \langle E_2^2 \rangle_\tau \tag{3.10}$$

and a third expression

$$I_{12} = 2\langle E_1 \cdot E_2 \rangle_\tau \tag{3.11}$$

called the **interference** term.

The electric field output of the detector in the interferometer is the sum of the signal from the object arm $E_o(t)$ and the reference arm $E_r(t)$:

$$I_o \backsim E_r + E_o \tag{3.12}$$

Consider now only the case of monochromatic, linearly polarised light. The electric field component of light returned from the object and reference arms can be expressed as:

$$E_o(t) = E_{o0} cos(knz_o - \omega t) \tag{3.13}$$

$$E_r(t) = E_{r0} cos(knz_r - \omega t) \tag{3.14}$$

Where Eq. 3.13 and 3.14 represent the object and reference arms respectively. In these equations, k is the wavenumber, z is the optical path distance, n is the refractive index of the object media, ω is the angular frequency of the light and t is time. Here, the term knz is the phase ϕ accumulated by the wave though its propagation through the interferometer.

$$\phi = knz \tag{3.15}$$

Eq. 3.13 and 3.14 can be substituted into Eq. 3.8 using 3.15:

$$I_d \backsim \langle E_r \rangle^2 + \langle E_o \rangle^2 + 2E_r E_o cos(\Delta\phi) \tag{3.16}$$

where

$$\Delta\phi = \phi_o - \phi_r \tag{3.17}$$

$\Delta\phi$ can be expressed in terms of summed object and reference paths lengths (l_o and l_r respectively) rather than the total round trip z:

$$\Delta\phi = kn\Delta z = \frac{2\pi}{\lambda} n(2l_o - 2l_r) = \frac{4\pi}{\lambda} n\Delta l \tag{3.18}$$

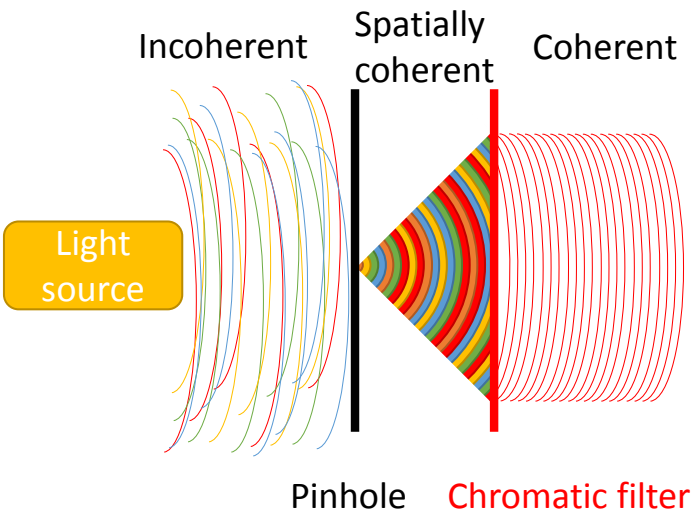

FIGURE 3.4: Diagram demonstrating the process that produces a spatially coherent and chromatically coherent light source.

3.2.1 Resolution

Fig. 3.4 shows a light source that is made coherent through use of a pinhole and a chromatic filter. In cases where the light is monochromatic and **highly** coherent (narrow linewidth) or has a long coherence length, interference fringes can be seen across large values of Δl, that is, for longer OPD.

For the determination of reflectors in depth, it is necessary to measure absolute distance and dimensions of structures within the object. To do this, low coherence (broad bandwidth) light is used. The superposition of electromagnetic fields will have slight differences in phase as a function of time. The coherence length l_c is a key characteristic of low coherence light, and it is inversely proportional to the bandwidth. Using a broadband, low coherence source with an interferometer will produce interference fringes only when the OPD between the object and reference arms is within the coherence length l_c.

The value of l_c determines the depth resolution when imaging with an OCT system - shorter coherence length is more discriminating and produces higher resolution axial scans when scanning the reference mirror [76]. It is this property that differentiates OCT from confocal microscopy systems, where the resolution is determined by the focussing lens parameters for the latter [77][78]. Fig. 3.5 visualises the difference between long and short coherence length light, illustrating the axial resolution advantage of short coherence length for OCT. For a source with Gaussian distribution, the axial resolution is given by Eq. 3.19:

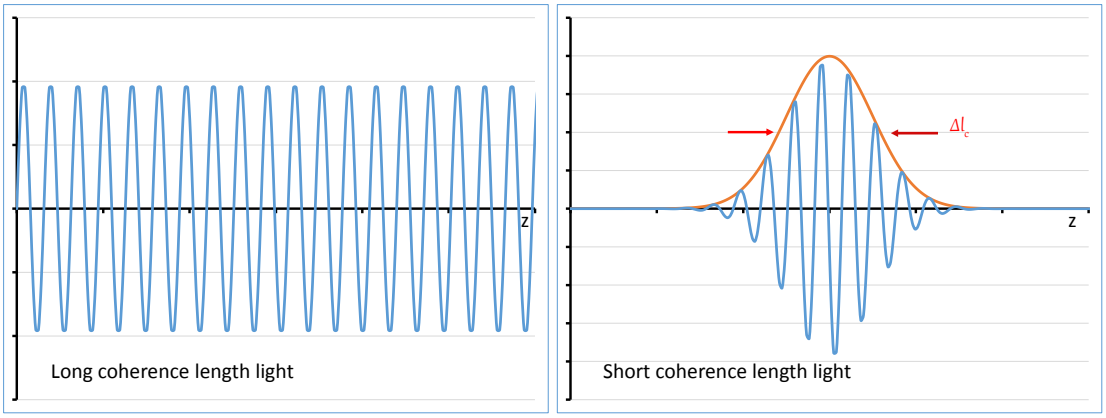

FIGURE 3.5: Diagram showing the difference between long and short coherence length.

$$\Delta z = \frac{2ln2}{\pi}\left(\frac{\lambda^2}{\Delta\lambda}\right) \tag{3.19}$$

where Δz is the FWHM of the autocorrelation function, $\Delta\lambda$ is the FWHM of the power spectrum and λ is the central emission wavelength of the optical source. It is evident that broad bandwidth sources are desirable for high axial resolution in OCT [79][80].

Lateral resolution of an OCT system is determined by the confocal microscope at the core of the system. The properties of the focussing lens and the incident beam determine the diameter of the focussed spot on the object. The minimum spot size that a beam can be focussed to is inversely proportional to the NA. The transverse resolution Δx is given by

$$\Delta x = \frac{4\lambda}{\pi}\left(\frac{f}{d}\right) \tag{3.20}$$

where d is the incident beam diameter on the focussing lens and f is its focal length. It can be seen from Eq. 3.20 that higher lateral resolution may be obtained by maximising the incident beam diameter d and shortening the focal length of the objective lens f. These are factors that may be configured for microscopy, however these parameters are fixed when imaging the eye where d is limited by the maximum pupil dilation and f is the length of the patient's eye.

Additionally, lateral resolution has a relationship with the depth of focus, which is twice the Rayleigh range $2Z_R$ as shown by Eq. 3.21

$$2z_R = \frac{\pi\Delta x^2}{2\lambda} \tag{3.21}$$

Therefore, a higher NA narrows the waist of the confocal profile, increasing the lateral resolution but reducing the depth of focus as shown in Fig. 3.6. For confocal microscopy it is important to increase NA as high as possible to both increase lateral resolution and to limit the contributions of out-of-focus regions in depth to the image. With OCT, a lower NA can be used since the coherence gate allows rejection of these out-of-focus rays. The additional benefit of having a lower NA for OCT is the increased depth of field, allowing for a greater axial scan range wherein reflectors in depth are in focus [81]. In this case, the low coherence interferometry provides the axial resolution and the lateral resolution is maintained for a wider axial range as the coherence gate is shifted along the axis.

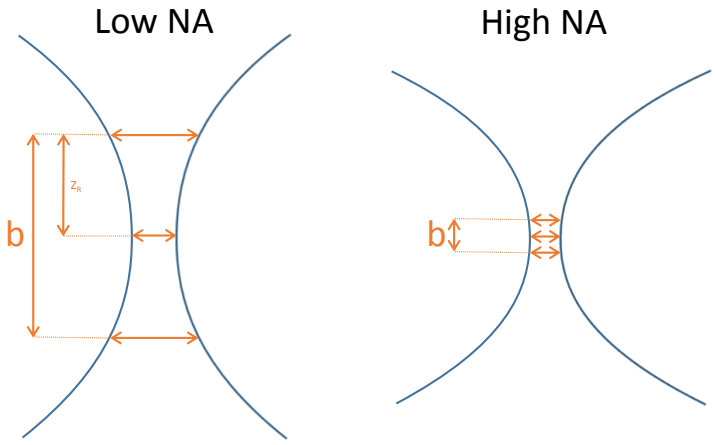

FIGURE 3.6: Diagram showing the difference between low and high NA and the effect on the confocal parameter b. OCT imaging is usually performed with low NA to increase depth of focus, though transversal resolution is compromised.

An imaging regime exists called optical coherence microscopy (OCM) where high NA is used with low coherence interferometry to create a high lateral and axial resolution images [82][83][84]. This operates essentially as a high resolution confocal microscope with high axial discrimination, reducing the contribution of backscattered light from different lateral positions and depths.

The compromise between depth of field and lateral resolution for OCT can somewhat be alleviated by dynamic focus techniques. Using an objective lens with a high NA, images may be acquired where the lens is shifted in synchronism with the coherence gate. This shifts the waist of the confocal profile together with the coherence gate, essentially creating a depth scanning OCM [85]. This is covered in section 3.3.

3.2.2 Sensitivity

Since OCT measures electric field interaction using optical homodyne detection rather than intensity of reflected light it is capable of high sensitivity [86]. As seen with Eq. 3.16, the oscillating interference term is the result of signal reflected from the object arm of the interferometer multiplied by the electric field contribution from the reference arm. Even if the signal from the object arm is weak, given high amplitude reference arm signal, the magnitude of the oscillating term produced by the detector is increased. This is particularly important when imaging an object with low reflectance or for objects that limit maximum permissible irradiance such as living tissue samples.

The SNR of optical systems are characterised by the expression

$$SNR = 10log\left(\frac{nP}{2hvB_{NE}}\right) \tag{3.22}$$

[86]

where n is the quantum efficiency of the detector, hv is the photon energy, P is the signal power and B_{NE} is the noise equivalent bandwidth of the demodulating electronic filter. From Eq. 3.22 it can be deduced that the SNR scales as detected power divided by the noise equivalent bandwidth of the detection. The effect is that higher image resolution and acquisition speed results in a loss of SNR, so more optical power is needed to rebalance a given SNR. OCT systems typically have sensitivities measured in the range of 90 to 100 dB. In summary, the sensitivity limit of OCT is limited by the maximum achievable optical power incident on the object. In the case of eye imaging, this is dictated by the ANSI standard.

In addition, detection sensitivity may be hindered by highly scattering object media such as biological tissues. This can be compensated by selecting an optical source with a longer wavelength to reduce scattering and increase penetration depth.

The most commonly used optical sources for TD-OCT and SD-OCT are superluminescent diodes (SLDs) due to their relatively low cost and small physical profile. Modern SLDs use multiplexed diodes to achieve bandwidths in excess of 150 nm, translating to high axial resolution in the range of 3 to 5 μm.

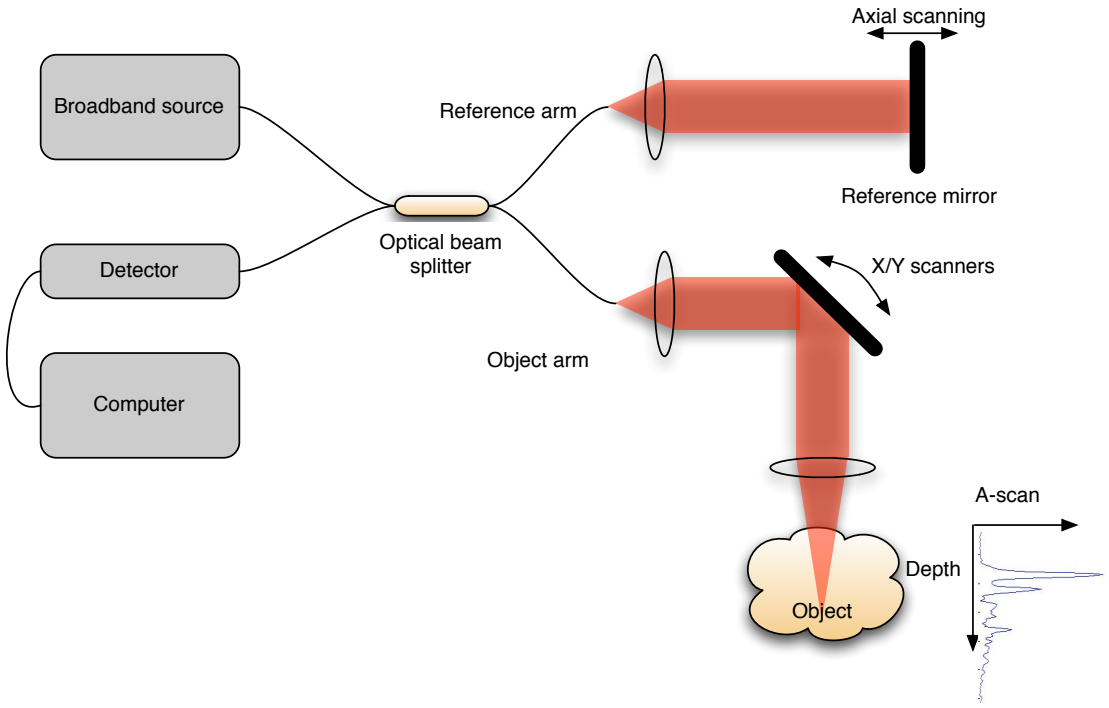

FIGURE 3.7: Diagram showing TD-OCT concept.

3.3 Time-Domain Optical Coherence Tomography (TD-OCT)

Early OCT systems operated in the time domain (TD-OCT) using a broadband light source, interferometer, photodetector and a translation stage. Fig. 3.7 shows a simplified diagram of a TD-OCT system, where light emitted from a broadband source is split into two arms, the reference and object arm, which are later recombined using a fibre coupler and sent to a detector.

The reference arm is terminated by a mirror mounted upon a one dimensional translation stage. Actuating this stage causes the length of the reference arm to change, which shifts the coherence gate in the object arm axially. The resultant effect is the probing region shifts to a different depth in the object.

Fig. 3.8 shows a more detailed schematic of a simple TD-OCT system. Light from a point source is first collimated by a lens and then divided by an optical beamsplitter. Light transmitted to both arms is then focussed by an additional lens in each arm. As the reference stage is shifted, the coherence gate is shifted by an equal distance in the object arm. Light backscatterd from both arms is recombined at the beamsplitter and transmitted to a detector.

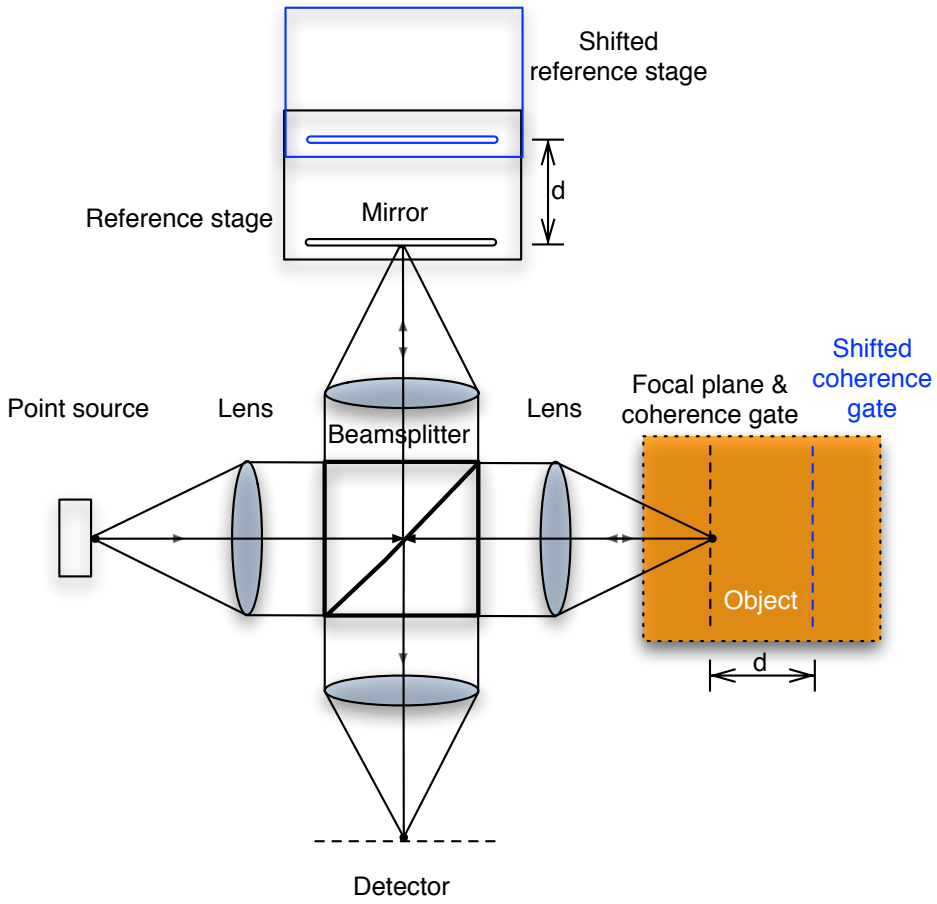

FIGURE 3.8: Diagram showing TD-OCT system.

An OCT image is formed by rapidly actuating the reference stage to acquire a succession of axial measurements of backreflected light using a photodetector. There are several scanning regimes that modify the way the TD-OCT system acquires data sets. Most commonly with TD-OCT is the priority of a depth (A-scan) measurement. In this manner, a full actuation of the translation stage between its limits interrogates the axial z profile of the object in a single transverse position x before the beam is moved to the next transversal position. Therefore, a cross-sectional image (B-scan) may be acquired by performing a series of A-scans whilst transversally scanning the beam across the object in x. Alternatively, the TD-OCT can operate with transverse priority whereby the reference mirror remains static and the beam is moved transversally across the object in x (T-scan). By rastering the beam in two dimensions using XY galvoscanners, this allows for a complete two dimensional *en-face* image (C-scan) to be acquired at a single depth position in the object. This mode produces an image in the same plane as that produced by conventional confocal microscopy.

3.3.0.1 Advantages

Though there is a speed disadvantage when using TD-OCT for cross-sectional imaging, there is benefit when acquiring C-scans (*en-face*) compared to newer methods. Using two galvoscanners, the beam can be rastered across the surface of an object much like an SLO system. For the duration of this raster, the reference mirror's axial position remains static, ensuring only light backscattered from the object at one depth is imaged.

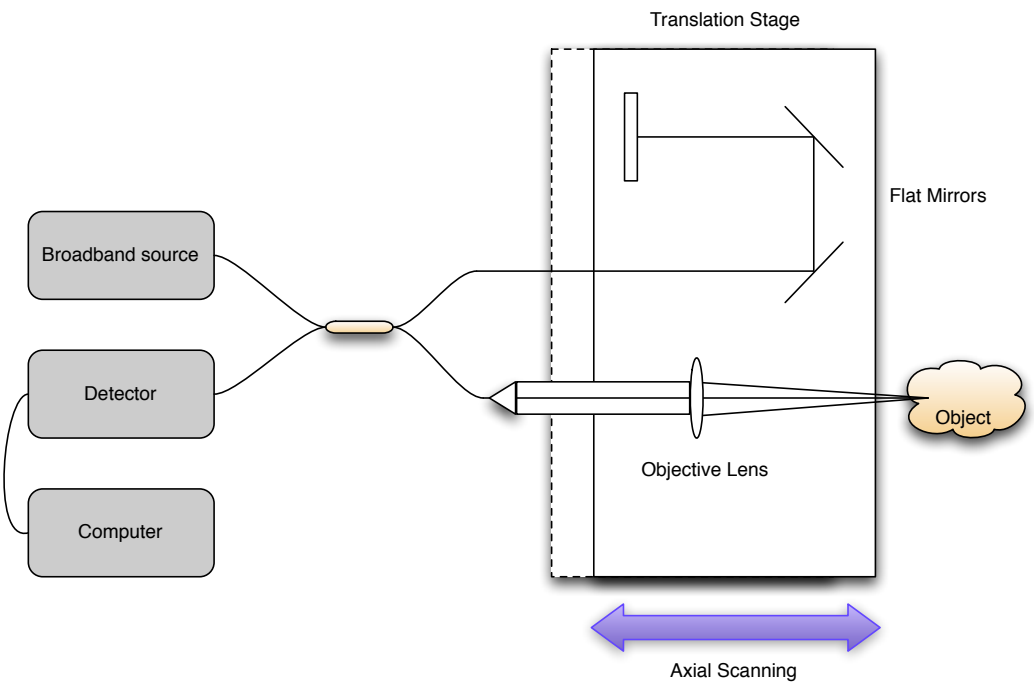

FIGURE 3.9: Diagram showing dynamic focus in a TD-OCT system.

Fig. 3.9 shows a TD-OCT configuration improved with dynamic focus. In this layout, the objective lens is mounted upon a translation stage with a portion of the reference arm. An axial scan is performed in the same manner as a conventional TD-OCT system by translating this stage to shift the coherence gate. Since the objective lens is mounted upon the same stage as the reference mirror, the confocal gate is shifted in synchronism with the coherence gate. The effect is that an axial scan is produced wherein all points in depth are in focus when they are acquired. This is an improvement over conventional TD-OCT systems with a static focal point. Dynamic focus is not possible in spectral-domain OCT in this way, since all points are acquired simultaneously in SD-OCT.

3.3.0.2 Limitations

Shifting the coherence gate by actuating a mechanical translation stage proves problematic when acquiring cross-sections with TD-OCT. To acquire a complete A-scan, the translation stage must move smoothly from one limit to another, which can be slow.

After a single scan is acquired, the translation stage may be moved to acquire another *en-face* image at a different depth. This can be repeated until a full 3D image volume is acquired. With a 500 Hz line scan and 2 Hz frame scan, for a volume of 500 *en-face* images the acquisition time would be 15.5 s.

3.4 Spectral-Domain Optical Coherence Tomography (SD-OCT)

The chief limitation of TD-OCT is the slow axial scan rate due to signal acquisition occurring at a single point in depth at any given time. Spectral domain OCT (SD-OCT) is a method devised to address the problem of slow A-scans. From Eq. 3.18 it can be seen that varying the OPD (Δl) allows for selection of reflectors in depth, however there is also a relationship with the wavenumber. Fourier analysis of the wavenumber-dependent detector current allows for a reconstruction of a reflectivity profile of the object in depth.

SD-OCT systems are constructed similarly to TD-OCT; an interferometer is used to split light from a broadband optical source into the object and reference arms, though in this case the reference mirror is fixed. The interference of the beams from the object and reference arms will cause a spectral modulation as a function of the optical frequency. The periodicity of the modulation is related to OPD - larger OPD causes an increase in the encoded frequency. Due to the modulation, this is commonly referred to as a channelled spectrum (a series of peaks and troughs). A spectrometer is used to interrogate the spectrum produced at the interferometer output.

A spectrometer usually consists of a prism or diffraction grating to create a chromatic fan of light, which is then projected onto a linear photo-detector array. This photo-detector array is usually a charged couple device (CCD), such as a 1 dimensional camera, or a complementary metal oxide semiconductor (CMOS) camera. Each pixel on the camera interrogates a fraction of the overall optical bandwidth returned to the spectrometer. This output is rescaled from wavelength to frequency and then Fourier transforming the interference signal.

3.4.1 Advantages of SD-OCT over TD-OCT

In TD-OCT, the coherence gate is shifted along the OPD axis by translating the reference mirror to select reflectors in depth. In SD-OCT, the information from all reflectors in depth are acquired simultaneously. Consequently, SD-OCT is much faster (∼50 to 100 times) than TD-OCT when acquiring A-scans [87][88]. This drastically reduces the total acquisition time for a 3D volume when compared with TD-OCT. The high speed of this modality allows for more A-scans to be acquired in a short time, improving the pixel count and consequently the visualisation of the image.

SD-OCT features an improvement in sensitivity over TD-OCT [89]. This allows for a slightly increased range in imaging depth, when compared with TD-OCT. The gain in sensitivity over time domain techniques allows for detection of deeper, weakly reflecting structures in the object. This combination of higher axial scan rate and deeper image penetration due to increased sensitivity makes SD-OCT the preferred method for cross-sectional imaging.

3.4.2 Limitations

There are some limitations to SD-OCT to consider, described in the sections below.

3.4.2.1 *En-face* imaging

TD-OCT remains the preferred modality when acquiring *en-face* OCT images. For *en-face* imaging, all points of interest are at the same depth so there is no need to move the reference mirror during acquisition. This eliminates the problem of slow A-scan acquisition for TD-OCT (as there is only 1 point per A-scan for an *en-face* image), and is actually faster than spectral techniques for this regime [90]. With SD-OCT, a full 3D volume must be acquired before an *en-face* image can be generated, though it will offer an *en-face* slice at all depths. There is a great amount of research conducted into making *en-face* SD-OCT faster [91][92][93].

3.4.2.2 Hardware limitations

To measure the spectral frequencies of the detected wavetrain, the CCD array must have double the sampling frequency δ_s to have sufficient spectral resolution. With spectral sampling interval of $\delta_s k$, the interferogram is split into M spectral channels linearly spaced in k. The total wavenumber range Δk is calculated using Eq. 3.23.

$$\Delta k = M \delta_s k \tag{3.23}$$

which gives the sampling interval in the z-domain:

$$\delta_s z = \frac{2\pi}{2\Delta k} \tag{3.24}$$

Conversion from wavenumber units to wavelength units is given by:

$$k = \frac{2\pi}{\lambda} \tag{3.25}$$

The depth range is given by the Nyquist criterion as shown in Eq. 3.26.

$$\pm\, z_{max} = \pm\frac{\pi}{2 \cdot \delta_s k} = \pm\frac{\lambda_0^2}{4 \cdot \delta_s \lambda} \tag{3.26}$$

The finite length of the CCD pixel array causes a second limitation with regards to sensitivity as spectral resolution $\delta_r k$ (where δ_r denotes the FWHM spectral resolution)is restricted. There is an exponential sensitivity roll-off with depth (as higher fringe frequencies caused by larger OPD become less visible due to the limitation of δ_s) and is characterised by the OPD at which sensitivity is reduced by half (6 dB in optical SNR units) [94]:

$$z_{1/2} = \frac{2ln(2)}{\delta_r k} = \frac{ln(2)}{\pi}\frac{\lambda_0^2}{\delta_r \lambda} \tag{3.27}$$

3.4.2.3 Mirror terms

When a Fourier transform is performed, two peaks will appear for each reflector in depth, centred around zero OPD. The modulation of the spectrum is the same for positive and negative frequencies, which means the FT is unable to determine which arm of the interferometer is longer and this creates some ambiguity in the image. This effect is called mirror terms, and causes an inverted duplicate image to appear around zero OPD. If the position of the reference stage is adjusted such that zero OPD is inside the object, a mirror image will overlap the real image. Several techniques have been reported to eliminate these mirror terms such as using configurations that can generate Talbot bands [95][96].

3.5 Swept-Source Optical Coherence Tomography (SS-OCT)

Swept source (SS) OCT also operates in the spectral domain, however there are some key differences. A SS is a narrow band source that is tunable at high speeds (in excess of 100 kHz) [97][98]. In SD-OCT, a spectrometer analyses the modulation encoded into the detected wavetrains returning from the object. Rather than interrogating the whole spectrum, the SS-OCT system measures each wavelength separately by sweeping the

narrow band emission across the total achievable bandwidth of the source, and then measuring the response using a detector. A single sweep will generate a spectrum with modulation caused by interference, similarly to SD-OCT, with the acquisition occurring sequentially over time (10 microseconds for a 100 kHz SS) rather than simultaneously, as with spectrometer-based OCT.

The processing of the image occurs similarly to SD-OCT. The data from the detector is sent to a digitiser and is then linearised using the frequency output from the SS (k clock). The result is Fourier transformed, producing a relationship of frequency modulation to OPD, which gives information about reflectivity in depth. Galvoscanners are used to raster the beam across the object to build a cross-section image. SS-OCT shares the advantages and disadvantages of SD-OCT. Both techniques operate at high speeds, and technologies are being researched to increase the sweep rate of SS and the line read-rate of cameras for SD-OCT.

3.6 Summary of modalities

Tab. 3.1 shows a summary of the properties of the various OCT modalities discussed in this chapter [99].

Selection of imaging domain and modality is largely contingent on the nature of the desired image. For *en-face* imaging, TD-OCT still provides the fastest, simplest solution. Cross-sectional imaging is performed faster in the spectral domain, though the implementation of spectrometer-based OCT or SS-OCT is largely currently dependent on the cost and availability of resources as both methods produce similar results.

3.7 Noise

The quality of OCT systems are determined as a measurement of several factors, with noise being a key indicator of performance. Sensitivity is often measured as a function of the ratio of the true detected signal over the noise floor, called the signal to noise ratio (SNR). Structures within an object (particularly at larger depths) may have low reflectivity, so a high sensitivity is required to resolve these reflectors. Since it may be difficult to increase the incident power of the signal, particularly in cases when imaging tissues *in-vivo*, an effort should be made to identify the highest contributions of noise to the system and compensate for them [100].

In a dispersion-less OCT system, the photocurrent at a detector is given by

	***En-face* TD-OCT**	**Longitudinal TD-OCT**	**SD-OCT**	**SS-OCT**
Depth resolution determined by	Optical source bandwidth	Optical source bandwidth	Optical source bandwidth	Tuning bandwidth
Axial scan range is	Unlimited	Unlimited	Limited by the spectrometer	Limited by the optical source linewidth
Sensitivity vs. OPD is	Constant	Constant	Maximum in OPD zero	Maximum in OPD zero
Mirror terms	None	None	Manifest if OPD zero is crossed	Manifest if OPD zero is crossed
Line rate determined by	Transversal scanner	Axial scanner	Camera integration time	Sweep rate
Maximum achievable line rate	16 kHz	100 kHz	300 kHz	5 MHz
Time to create *en-face* image (500 x 500)	Given by the time to produce a C-scan frame, 31 ms	Given by the time to acquire a volume, 2.5 s	Given by the time to acquire a volume, 0.83 s	Given by the time to acquire a volume, 50 ms
Time to acquire a volume (500 x 500 x 500	15.5 s	2.5 s	0.83 s	50 ms

TABLE 3.1: Table summarising the differences between the OCT modalities.

$$I_d = p[P_o + P_r + P_x + 2\sqrt{P_o P_r} cos(k_0 \Delta l)] \tag{3.28}$$

where p is the detector response, P_o is the detected optical power backscattered from the object that is coherent with the reference signal, P_r is the detected reference arm power, P_x is the optical power from the object arm that is incoherent with the reference signal, k_0 is the centre wavenumber of the source and Δl is the OPD. The photocurrent from the ac interference signal is given by the term

$$I_s = 2p\sqrt{P_o P_r} cos(k_0 \Delta l) \tag{3.29}$$

Noise is expressed as photonic variance σ_i^2, the main contributors are shot noise σ_{shot}^2, excess photon noise (EPN) σ_{EPN}^2 and thermal noise σ_{th}^2.

with SNR defined as

$$SNR = \frac{\langle I_s^2 \rangle}{\sigma_i^2} \tag{3.30}$$

the mean-squared photocurrent for a single detector can be defined as

$$\langle I_s^2 \rangle = 2p^2 P_o P_r \tag{3.31}$$

and as

$$\langle I_s^2 \rangle = 8p^2 P_o P_r \tag{3.32}$$

for the case of a balanced detector, where the total photocurrent is the sum of the signal photocurrent across both detectors. For an OCT system with Michelson interferometer, the SNR for an unbalanced detection system can be written in terms of P_o, P_r and P_x:

$$P_o = \frac{PR_o}{4} \tag{3.33}$$

$$P_r = \frac{PR_r}{4} \tag{3.34}$$

$$P_x = \frac{PR_x}{4} \tag{3.35}$$

where R_o, R_r and R_x represent the power reflectivity of the coherent backscattered light from the object, the reference optical delay line and the incoherent backscattered light from the object, respectively. P is the power output of the optical source.

In the case of a balanced detector, these terms change to

$$P_o = \frac{PR_o T_c^2}{4} \tag{3.36}$$

$$P_r = \frac{PR_r T_c^2}{4} \tag{3.37}$$

$$P_x = \frac{PR_x T_c^2}{4} \tag{3.38}$$

where T_c is the transmission through the circulator (for typical 0.7 dB insertion loss, $T_c \cong 0.85$) [100].

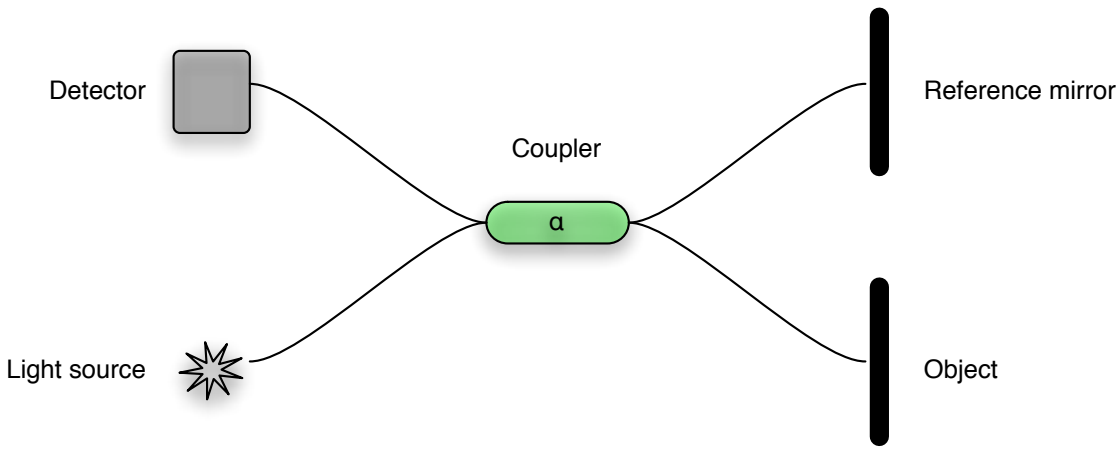

FIGURE 3.10: Diagram showing a non-balanced detection system, where α denotes the splitting ratio of the coupler.

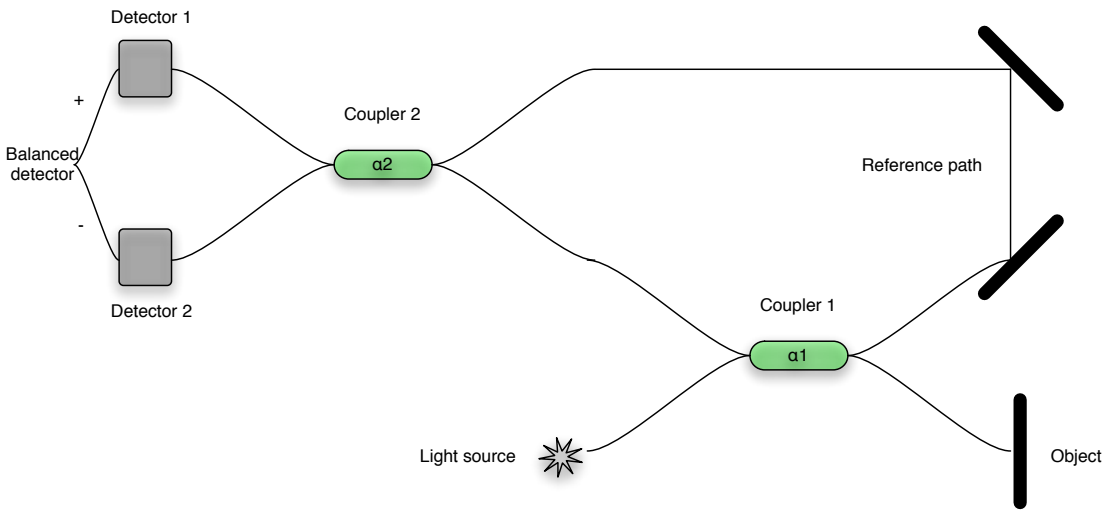

FIGURE 3.11: Diagram showing a balanced detection system, where $\alpha 1$ and $\alpha 2$ denote the splitting ratio of the two couplers.

The following sections discuss these types of noise in detail. Expressions may be presented for the cases of non-balanced detection and balanced detection systems, represented graphically in Fig. 3.10 and Fig. 3.11 respectively.

3.7.1 Shot noise

Eq. 3.39 shows the expression for calculating shot noise

$$\sigma^2_{shot} = 2eB\langle I_s \rangle \tag{3.39}$$

where e is the electron charge, B is the bandwidth of the detector and $\langle I_s \rangle$ is the time averaged photocurrent. When reflectivity from the object is weak, it can be assumed that all the optical noise originates from the reference arm contribution in an unbalanced detection system. The shot noise for this scenario is given by Eq. 3.40:

$$\sigma^2_{ushot} = 2peBPP_r\alpha(1-\alpha) \tag{3.40}$$

where α is the splitting ratio of the coupler. For a balanced detector, the shot noise from both detectors is cumulative, giving the shot noise as

$$\sigma^2_{bshot} = 2peBPP_r\alpha \tag{3.41}$$

which is larger than the unbalanced configuration. Using Eq. 3.30, the SNR for an unbalanced detector may be expressed as

$$SNR_{ushot} = \frac{pPP_o\alpha(1-\alpha)}{eB} \tag{3.42}$$

and for the case of balanced detection it is

$$SNR_{ushot} = \frac{4pPP_o\alpha_1(1-\alpha_1)\alpha_2(1-\alpha_2)}{eB} \tag{3.43}$$

where α_1 and α_2 are the splitting ratios of two couplers.

3.7.2 Excess photon noise

The mean-square photocurrent fluctuations due to excess photon noise only is expressed as

$$\sigma^2_{EPN} = \frac{(BI_s^2)}{\Delta\nu} \tag{3.44}$$

where B is the bandwidth of the detector, Δv is the effective linewidth, with σ^2_{EPN} being the time averaged photocurrent on the detector. If a Gaussian power spectral density is assumed, Δv is given by the expression

$$\Delta\nu = \frac{\nu_0^2}{\Delta\nu_{FWHM}}\sqrt{\frac{\pi}{2ln2}} \tag{3.45}$$

where $\Delta\nu_{FWHM}$ is the FWHM of the wavelength bandwidth of the source.

In effect, σ^2_{EPN} is the EPN for a thermal source. When the light is linearly polarised, this equation becomes

$$\sigma^2_{EPN} = \frac{(1+\Pi^2)}{\Delta\nu} B\langle I_s^2\rangle \tag{3.46}$$

where Π is the degree of polarisation.

For a case of unbalanced detection where contribution from the object arm is significantly lower than the reference arm, EPN is given by

$$\sigma^2_{uEPN} = \frac{(1+\Pi^2)}{\Delta\nu} p^2 B P^2 P_r^2 \alpha^2 (1-\alpha)^2 \tag{3.47}$$

and in the balanced case, EPN is given by

$$\sigma^2_{bEPN} = \frac{(1+\Pi^2)}{\Delta\nu} p^2 B P^2 P_r^2 \alpha_1^2 (1-2\alpha_2)^2 \tag{3.48}$$

When balanced detection is used, the noise contribution of EPN is mostly eliminated. The signal received from the object arm that is incoherent with the reference arm P_x remains, contributing some EPN. This is called beat noise and is characterised by

$$\sigma^2_{beat} = 2 I_x B I_r \frac{(1+\Pi^2)}{\Delta v} \tag{3.49}$$

where $I_x = pP_x$ and $I_r = pP_r$. When the balancing is good, i.e. α_2 is near 0.5, this term replaces the EPN term.

3.7.3 SNR

The total noise in an unbalanced OCT detection system is characterised by

$$\sigma^2_{iu} = \sigma^2_{ushot} + \sigma^2_{uEPN} + \sigma^2_{re} \tag{3.50}$$

and

$$\sigma^2_{ib} = 2(\sigma^2_{ushot} + \sigma^2_{uEPN} + \sigma^2_{re}) \tag{3.51}$$

for a balanced detection configuration, where σ_{re} is the receiver noise of the detector. This receiver noise is inherent in the function of the detector and is invariable with differing power levels. The total contribution of receiver noise is low, and only significantly affects SNR when the signal is weak. Total noise in an unbalanced OCT system is given by

$$\sigma_{iu}^2 = \left(2peBPP_r\alpha(1-\alpha)\right) + \left(\frac{(1+\Pi^2)}{\Delta\nu}p^2BP^2P_r^2\alpha^2(1-\alpha)^2\right) + \left(B\langle\Delta I_p^2\rangle\right) \quad (3.52)$$

and in the balanced case given by

$$\sigma_{ib}^2 = \left(2peBPP_r\alpha\right) + \left(\frac{(1+\Pi^2)}{\Delta\nu}p^2BP^2P_r^2\alpha_1^2(1-2\alpha_2)^2\right) + \left(B\langle\Delta I_p^2\rangle\right) \quad (3.53)$$

The SNR for the unbalanced detection system can be expressed as

$$SNR_u = \frac{2p^2P_oP_r}{\left(2peBPP_r\alpha(1-\alpha)\right) + \left(\frac{(1+\Pi^2)}{\Delta\nu}p^2BP^2P_r^2\alpha^2(1-\alpha)^2\right) + \left(B\langle\Delta I_p^2\rangle\right)} \quad (3.54)$$

and

$$SNR_b = \frac{2p^2P_oP_r}{\left(2peBPP_r\alpha\right) + \left(\frac{(1+\Pi^2)}{\Delta\nu}p^2BP^2P_r^2\alpha_1^2(1-2\alpha_2)^2\right) + \left(B\langle\Delta I_p^2\rangle\right)} \quad (3.55)$$

for the balanced configuration.

SNR presents complicated design decisions for optical imaging systems. An improvement of SNR can be seen at the cost of imaging speed, though this is highly application dependent. For camera-based SD-OCT, the camera must be sufficiently fast to avoid wash out of the fringes. SNR may be sacrificed if speed is more important. A high temporal resolution and stability is necessary for phase measurements, so a system may afford a lower SNR to achieve the speed required [101].

Chapter 4

Adaptive optics

4.1 Introduction

Imperfections in the interface optics of an imaging system will result in a loss of resolution [102]. Resolution is defined as the capacity to distinguish two distinct features in close proximity. With sufficient resolution, a system is capable of detailing two adjacent individual structures, however if the resolution is insufficient then these structures will appear partially or completely merged. Imaging resolution is determined by the value of the point spread function (PSF) as discussed in chapter 2. If the optical components are imperfect or misaligned, or the imaging medium is inhomogeneous, the wavefront becomes aberrated and the PSF is broader as a result [103][104]. This effect is evident by attempting to observe stars at night. The stars will appear to change in intensity as they are observed, creating the known 'twinkling' effect. Atmospheric pressure changes cause temperature variation, resulting in distortion of the light travelling from the star. As the light propagates through the atmosphere it travels through multiple regions of varying refractive index caused by these temperature differences [105][106][107].

Astronomers have long suffered from these effects distorting their observations of space through Earth's atmosphere. The Hubble Space Telescope was a solution born from the idea of removing the atmosphere entirely from the observation process by placing the telescope in space [108][109]. With no atmosphere or other aberration-inducing elements distorting the wavefront, very clear images could be acquired of celestial entities. Of course, this is not an accessible or economical solution to the problem of imaging objects far away. A better solution is to measure the wavefront of the light and rectify the aberrations to flatten the wavefront, thus restoring the PSF. It is through this line of astronomical research that adaptive optics (AO) was conceived.

This task could be broken into two separate paths of research: wavefront measurement and wavefront correction. It was proposed in the 1950s that a reflector could be constructed and shaped to compensate for aberrations in the wavefront [110]. Light would be directed to the surface of this mirror, and then its shape could be changed to alter the wavefront of the reflected light such that it is flattened.

4.2 Wavefront measurement

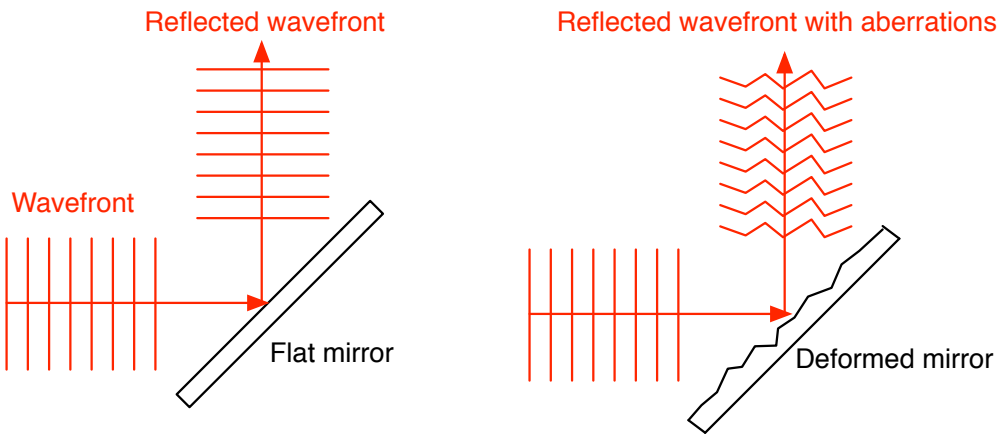

FIGURE 4.1: Diagram demonstrating the effect of irregular optical interfaces on the quality (flatness) of the wavefront.

Accurate wavefront measurement and analysis are crucial to an adaptive optics configuration. A wavefront is defined as a continuous surface of connected points that share the same phase [111]. A collimated plane wave with no aberrations will present a completely flat wavefront when observed perpendicular to the propagation plane. In this case, the rays are parallel to each other. Variations in phase between the points that comprise the wavefront will reduce the flatness, thus adding aberrations. Wavefront measurement of a beam of light can be represented by considering each point on the wavefront as an individual point source. By measuring variation between the phase of these point sources, the total wavefront aberration may be calculated. This is the principle behind the Shack-Hartmann wavefront sensor [112].

The concept of the Shack-Hartmann wavefront sensor (WFS) was to decompose a beam into an array of point sources, as described above, to measure the aberrations [113]. This is achieved by using an array of lenses, each being a fraction of the diameter of the beam, to focus the light onto a detector [114]. Modern Shack-Hartmann sensors consist of a CCD camera with a microlenslet array mounted on the aperture such that the surface of the camera is in the focal plane of the lenses. Due to the commonality

of these components, a Shack-Hartmann wavefront sensor is a relatively low cost device that can be used for measuring wavefront aberrations. In operation, the lenslet array fills the aperture of the camera so that the incident beam is spatially divided into many smaller beams that are focussed onto the camera.

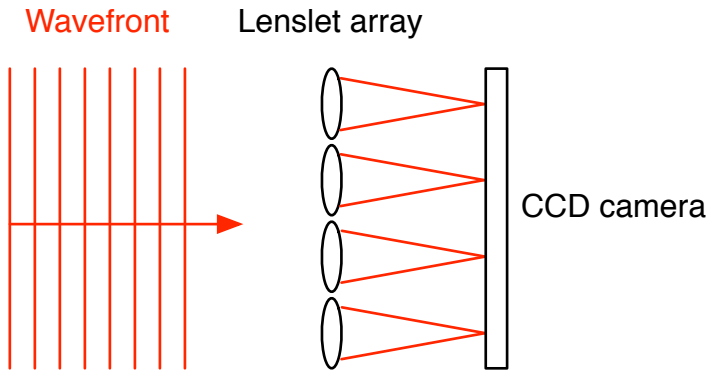

FIGURE 4.2: Diagram representing a Shack-Hartmann wavefront sensor. An unaberrated beam of light presents a flat wavefront. The beam is decomposed by the lenslet array into a spot pattern on the CCD camera.

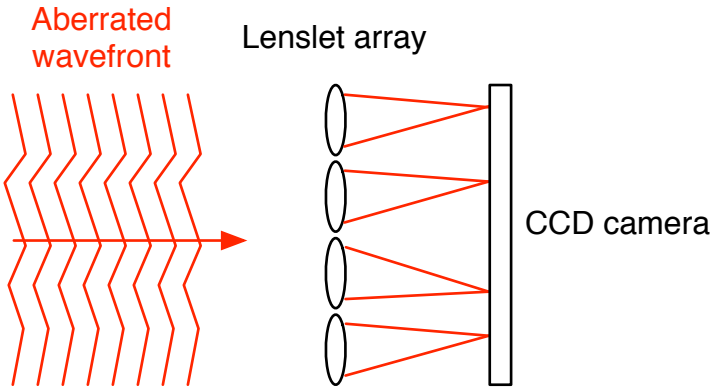

FIGURE 4.3: Diagram representing a Shack-Hartmann wavefront sensor. In this case, the wavefront has aberrations and causes displacement of the spots on the CCD camera

The spot pattern image of the wavefront acquired by the camera may then be analysed to determine the wavefront error [115][116]. If the beam is aberrated, the spots on the camera will appear to be displaced laterally; the magnitude this displacement is proportional to the slope of the wavefront. Repeated measurement of the displacement of these spots from one another provides a dynamic representation of the slope map of the wavefront. To provide a more accurate measurement, increasing the number of lenses that comprise the lenslet array will lead to a more densely populated spot pattern [117]. Though this provides a higher sampling rate of the wavefront, it also reduces the optical power for each spot as detected by the camera. This may be partially compensated by

increasing the integration time of the camera to allow more light per spot, however this will also increase the noise level. Conversely, should the camera receive too much light per pixel and become saturated then each spot will appear larger, reducing the accuracy of the slope measurement as the centroid of the spots become less clear.

From the spot pattern, the wavefront may be reconstructed using a mathematical model. Zernike circle polynomials are the most commonly used method for representing the wavefront state [118] due to the radial representation and close correlation of polynomials with common optical aberrations. Zernike polynomials are used to mathematically describe 3D wavefront deviation from a plane from its zero mean.

Each polynomial describes one specific form of deviation and the summation of a series of these polynomials can produce more complex surface shapes. These polynomials are can be used to describe the aberrations imposed upon a wavefront by imperfect optics. Any wavefront deformation can be described by using a sufficient number of Zernike polynomials.

Zernike polynomials are an orthogonal set defined in polar coordinates (ρ, θ), where ρ is the radial coordinate and θ is the angular coordinate.

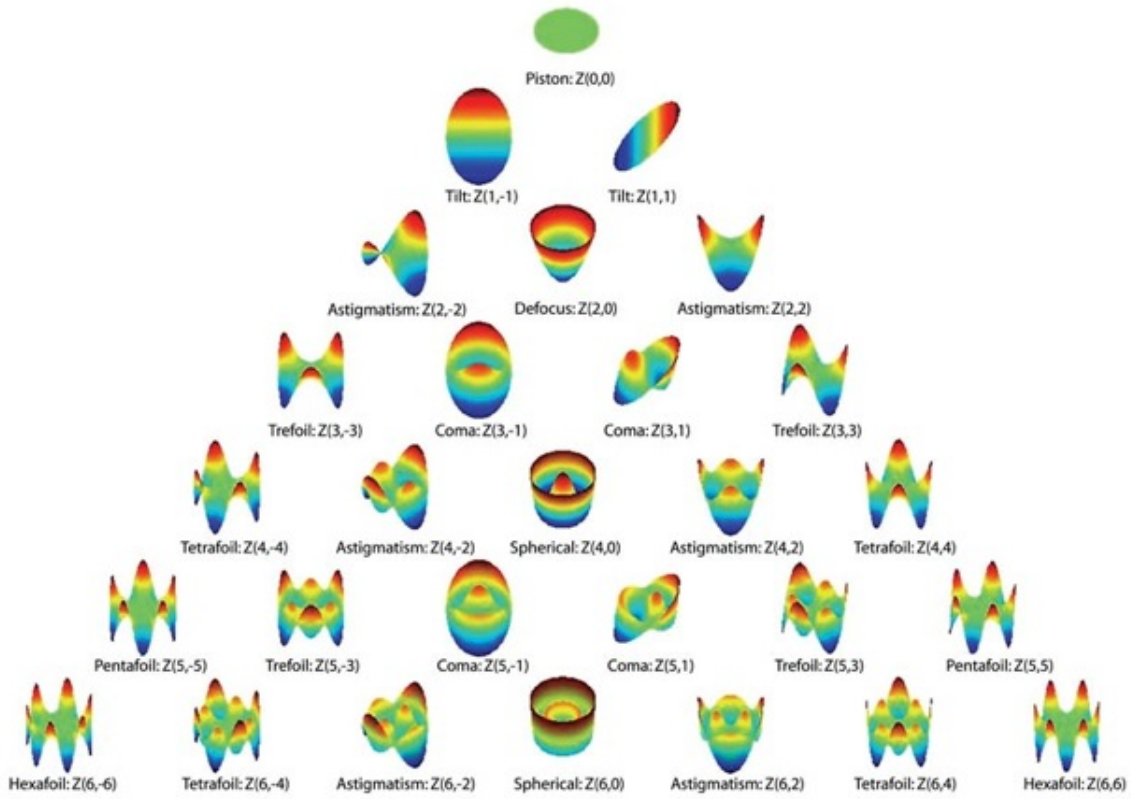

FIGURE 4.4: Image showing Zernike polynomials up to the 6th order. Higher order abberations are towards the base of the pyramid and low order aberrations are at the tip of the pyramid. (http://bme240.eng.uci.edu/students/ 08s/ticenogl/ Wavefront-Guided%20LASIK/Wavefront.html)

Zernikes can be defined as even

$$Z_n^m(\rho, \phi) = R_n^m(\rho) cos(m\theta) \tag{4.1}$$

and as odd

$$Z_n^m(\rho, \phi) = R_n^m(\rho) sin(m\theta) \tag{4.2}$$

where m and n are non-negative integers, ρ is the normalised radial distance, θ is the azimuthal angle in radians and the radial function $R_n^m(\rho)$ is defined as

$$R_n^m(\rho) = \left\{ \sum_{k=0}^{(n-m)/2} \frac{(-1)^k (n-k)!}{k!((n+m)/2-k)!((n-m)/2-k)!} \rho^{n-2k} \right. \tag{4.3}$$

Fig. 4.4 shows the first 6 orders of Zernike polynomials. It can be seen from this diagram that the Zernike mathematical model is well suited to the description of optical wavefronts, especially considering the close relation with aberrations induced by optical components. Featured in the higher orders are tilt (Z_1^{-1} , Z_1^1), defocus (Z_2^0), astigmatism (Z_2^{-2} , Z_2^2) and spherical Z_4^0, all of which are major contributors to wavefront error by optical components used in an imaging system. Further, these may also be attributed to errors induced by biological lenses such as in the eye.

The Shack-Hartmann WFS provides the means to decompose a beam into many constituent parts, providing a means to analyse the wavefront slopes and represent them using the Zernike modes [119]. Using this model, it is possible to calculate the adjustments needed to reverse the aberrations and flatten the wavefront [120]. A wavefront corrector, when placed in the conjugate plane of the WFS, may use this information to impose a phase change on the wavefront as calculated by the Zernike model to flatten the wavefront. To produce a flat wavefront, the corrector needs to apply an inverse function of the calculated phase error. Experiments have been performed using a spatial light modulator as a wavefront corrector [121][122][123][124][125]. The most common type of wavefront corrector is a deformable mirror (DM), described in the following section [126][127][128].

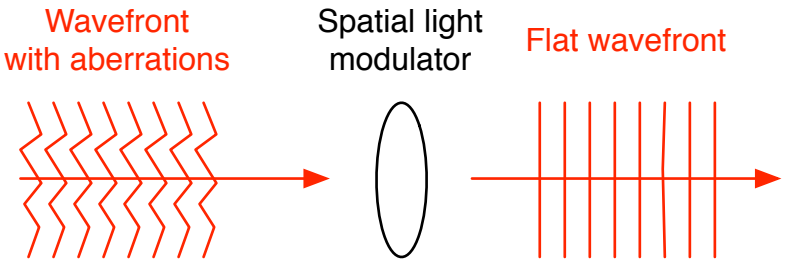

FIGURE 4.5: A diagrammatic representation of wavefront correction in transmission using a liquid-crystal spatial light modulator (SLM)

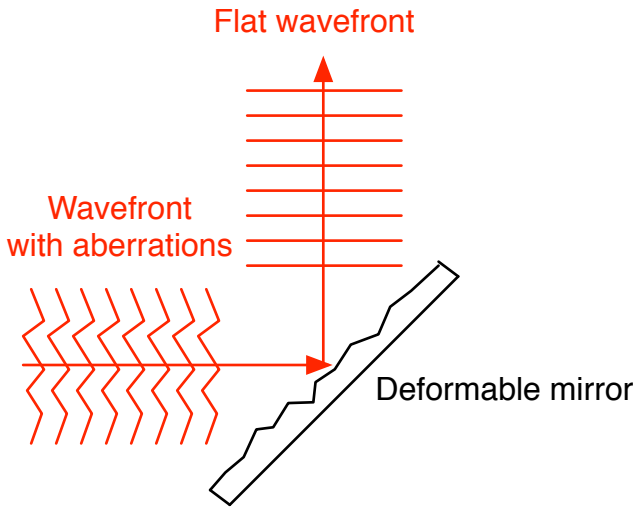

FIGURE 4.6: A deformable mirror is used as a wavefront corrector, applying the inverse function of the combined detected aberrations. The result is a flat wavefront in reflection.

4.3 Wavefront manipulation

A wavefront corrector can be described as a device that may be used to adjust the phase of an aberrated wavefront such that it is brought to a state of correction, i.e. all constituent parts of the detected beam are in phase, presenting a flat wavefront. There are two major types of wavefront correctors, those which are transmissive and those which are reflective.

Transmissive wavefront correctors operate as a light modulator wherein light propagates through a medium wherein it is subjected to a phase change by the corrector. A common example of a transmissive corrector is a modern spatial light modulator (SLM), which

is a liquid crystal device with virtual subsections that may be manipulated to change the shape of the lens [129][130][131]. By varying the voltage applied to each subregions of the lens, the optical path through that particular region is changed. The SLM can be dynamically adjusted to change its refractive index across individual subregions of the aperture, in effect granting modulation of the phase for many parts of an incident beam.

SLMs afford fine control over the phase changes between adjacent subregions, allowing for precise adjustments to the wavefront. In this manner, the inverse of a detected wavefront aberration may be applied to the SLM using the Zernike model. Light propagating through the SLM will be subject to the phase changes induced by the varying refractive indices of the smaller subregions of the lens, causing the wavefront to flatten in transmission.

Since the refractive index is wavelength dependent, this makes SLMs unsuited to the use of broadband optical sources such as those used with OCT. There is also the additional concern that, since the corrector is transmissive, dispersion may be introduced as the light propagates through the SLM [132].

Reflective wavefront correctors operate on a similar principle as SLMs. These devices have a highly reflective metallic surface that is able to be modified to adjust the phase of the reflected wavefront. These devices, commonly called deformable mirrors (DM), do not suffer from the disadvantages of SLMs as the light propagates in reflection, meaning no dispersion is introduced and broadband sources may be used.

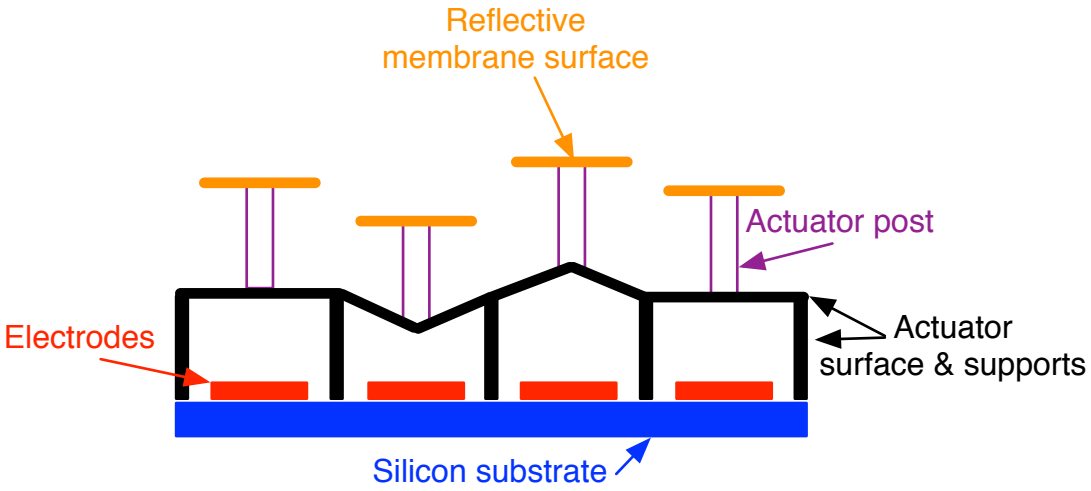

FIGURE 4.7: Diagram presenting the structure of a deformable mirror with a segmented surface.

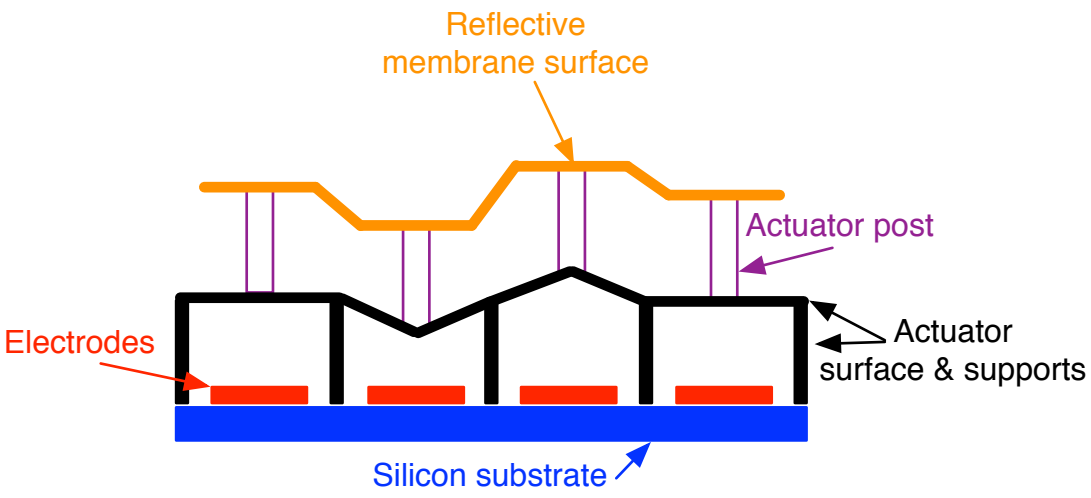

FIGURE 4.8: Diagram presenting the structure of a deformable mirror with a continuous surface.

DMs can either have a continuous or segmented reflective surface. A segmented DM, such as that shown in Fig. 4.7, consists of an array of reflective plates that may be moved individually [133][134]. Each plate is actuated independently of each other, so it is possible to adjust not only their axial position, but also tip and tilt. This affords a huge degree of freedom when manipulating the surface of the mirror, and allows for the DM to assume complex shapes. The key advantage of a segmented mirror is that large local aberrations may be compensated due to the large degree of freedom between adjacent subregions (as in the SLM). The biggest disadvantage is that the interfaces between the reflective plates may not be perfectly flush, causing an amount of scattering around the boundaries of each individual plate.

Fig. 4.8 shows a DM with a continuous surface has a single sheet of reflective material stretched across its aperture, which is conjoined to some control system to deform its shape [135]. The control mechanism may either be piezoelectric or micro-electro-mechanical system (MEMS). A MEMS DM operates by having the reflective membrane positioned above an array of actuators. When a voltage is applied to an actuator, it shifts its axial position and moves a local region of the membrane, causing a deformation in the entire reflective surface of the DM, centred around that actuator. A MEMS DM may be packed with a high number of this actuators, allowing for fine control over the shape of the mirror. This is helpful when correcting for high order aberrations especially, where degree of freedom is important [136][137]. The actuators in a MEMS DM have a limited displacement distance (stroke), though DMs with larger stroke have been

developed recently [138]. A disadvantage of a MEMS DM is that the position of the actuators around the periphery of the reflective aperture are limited.

Additionally, a third type of DM exists called a magnetic membrane mirror. This device is similar to the MEMS DM in that a reflective membrane is deformed using a control mechanism. Instead of mechanical actuators, there is an array of magnetic coils placed behind the membrane that attract or repel a local region of the membrane as the voltage to the coil is adjusted [139][140].

4.4 Open and closed loop correction

There are two main tasks for an adaptive optics system. First, the AO is responsible for the detection and correction of static aberrations. These aberrations are inherent within the optical setup itself, and may be introduced due to misaligned or imperfect optics. Closed loop is the name given to the procedure whereby the AO components operate in a constant feedback loop independent of user input. In this mode, there is a continuous cycle of wavefront detection, aberration calculation and wavefront correction [141]. This cyclical process is necessary since modulating the wavefront corrector will change the parameters of the optical system, and the WFS may determine if further manipulation of the wavefront phase is required. Given a non-moving scattering object and a perfect objective lens, the information seen by the WFS can be assumed to be the cumulative total wavefront error of the system itself. Once the system has been brought to a state of correction, the DM should have minimal work in maintaining this state as the parameters of the optics will not vary significantly. In this case, the closed loop will be seen to make minimal changes to the wavefront unless there is a significant change, such as adjustment of the object in relation to the objective lens.

For static objects, once correction is achieved, the AO may be switched over to open loop. This mode maintains the state of the mirror as dictated by the closed loop, however user input is now enabled. Continuous measurement of the wavefront still occurs in open loop, though the AO will not actuate the DM. Open loop is useful for analysing deviations in the corrected wavefront over time, or allowing the user to manually adjust the shape of the DM to produce various aberrations. Since aberrations are detected and represented by Zernike modes, it is possible for the user to induce a specific aberration using the AO control system. Given a perfect correction - that is, a completely flat wavefront - a user may add and observe any individual aberration using the open loop mode. This is useful in many ways, one example being the adjustment of focus for a corrected wavefront. It is easy to observe this effect by modifying the Zernike polynomial corresponding to focus Z_2^0 such that the DM shape is altered accordingly, and then moving the axial position of

the object relative to the objective lens so it is in focus again. This allows for dynamic adjustment of focus without any additional optical elements. A project based upon this principle is described later in chapter 6.

For moving objects, such as the eye, it is necessary to maintain closed loop corrections at a fast rate to compensate for rapidly fluctuating aberrations (in excess of 30 Hz). A wavefront is described as a sum of Zernike terms. Representation of the performance of the AO is done using a root mean squared (RMS) calculation of the Zernike coefficients.

$$RMS^2 = \sum_{n,m} c_n^{m^2} \tag{4.4}$$

where c is the Zernike coefficient describing the magnitude of each polynomial in the series.

Chapter 5

AO-SLO/OCT for eye imaging and high resolution microscopy

5.1 Introduction

The objective of the work conducted in this chapter is to construct a scanning laser ophthalmoscope (SLO) with sufficient resolution to image photoreceptors in the human eye *in-vivo*. Cone cells have a diameter ranging from approximately 0.5 to 4 μm at the base, which determines the minimum resolution the system must achieve to image them. The smallest cells are located at the centre of the eye near the fovea, and are much more densely packed than at the peripheries. As described in previous chapters, confocal microscope systems may be combined with adaptive optics to achieve the resolution required to image these cells.

It would be preferable when designing such a system to minimise the overall component cost, considering that AO/SLO systems are of interest to medical clinicians with limited funds. A standard design includes the use of a Shack-Hartmann wavefront sensor used in combination with a single MEMS deformable mirror. This is the approach taken with this project, though research has shown the benefits of utilising an additional deformable mirror in a woofer/tweeter configuration [142][143][144].

This chapter describes two system designs that were used through this project. The original system was inherited from a previous PhD candidate, Alexander Meadway. This AO-SLO/OCT system was used to achieve high-resolution simultaneous confocal and OCT *en-face* images. There were limitations in the performance of this system, particularly when used to image the eye *in-vivo*. The overall design and limitations of this system will be explored in a later section of this introduction (section 5.1.1).

The new system was conceived two years into this project, based upon more recent designs reported in the literature [145]. Given the limitations of the legacy system, it was advantageous to refresh ageing components whilst revamping the overall design to be simpler, compacted and more stable. Given the progress of research in the field of AO, the new design benefits from modern approaches. Section 5.2 fully details the new design and the results are presented in section 5.3.

5.1.1 Legacy AO-SLO/OCT

Prior to this project, similar work was conducted on an AO-SLO/OCT system by students Simon Tuohy [146] and Alexander Meadway [147]. The system operated at 830 nm using a Superlum SLD, performing closed loop aberration correction using an Imagine Eyes DM and WFS pair. Software was provided by OTI to produce live simultaneous SLO and TD-OCT images.

5.1.1.1 Design

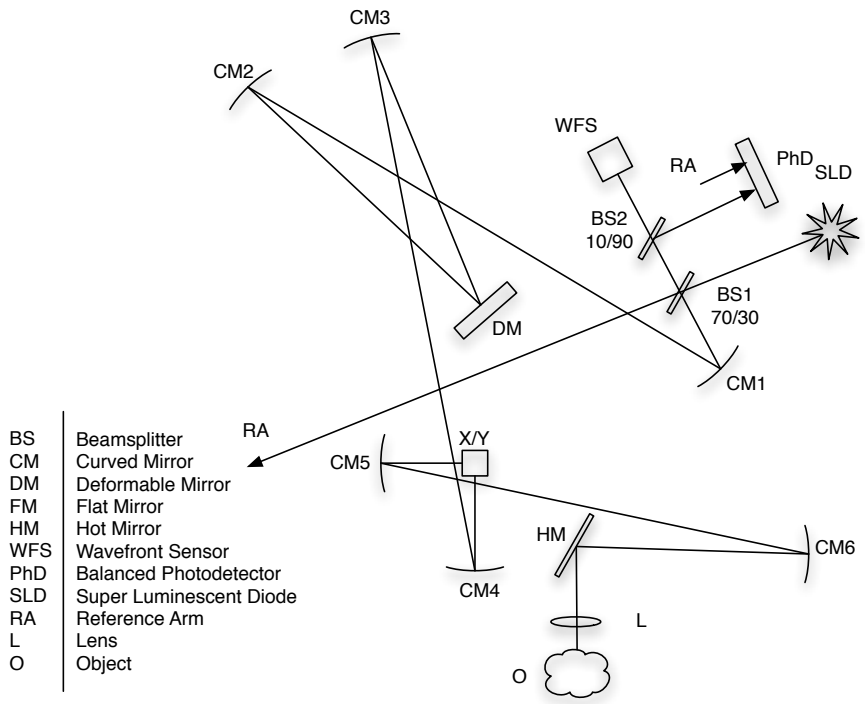

FIGURE 5.1: Diagram showing the legacy AO-SLO/OCT system.

The system presented in Fig. 5.1 uses an SLD (Superlum) broadband optical source emitting light with a central wavelength of 830 nm with a bandwidth of 17 nm. Light

is launched from fibre and collimated to a diameter of 3 mm by a x10 microscope objective. A 1" plate beamsplitter (BS1) is used to split the light into the object and reference paths. 70% of the light is transmitted through the beamsplitter and proceeds into the reference arm, consisting of a series of 1" silver plane mirrors and a linear motorised translation stage. The reference arm is terminated with another x10 microscope objective and the light is coupled into a single-mode fibre.

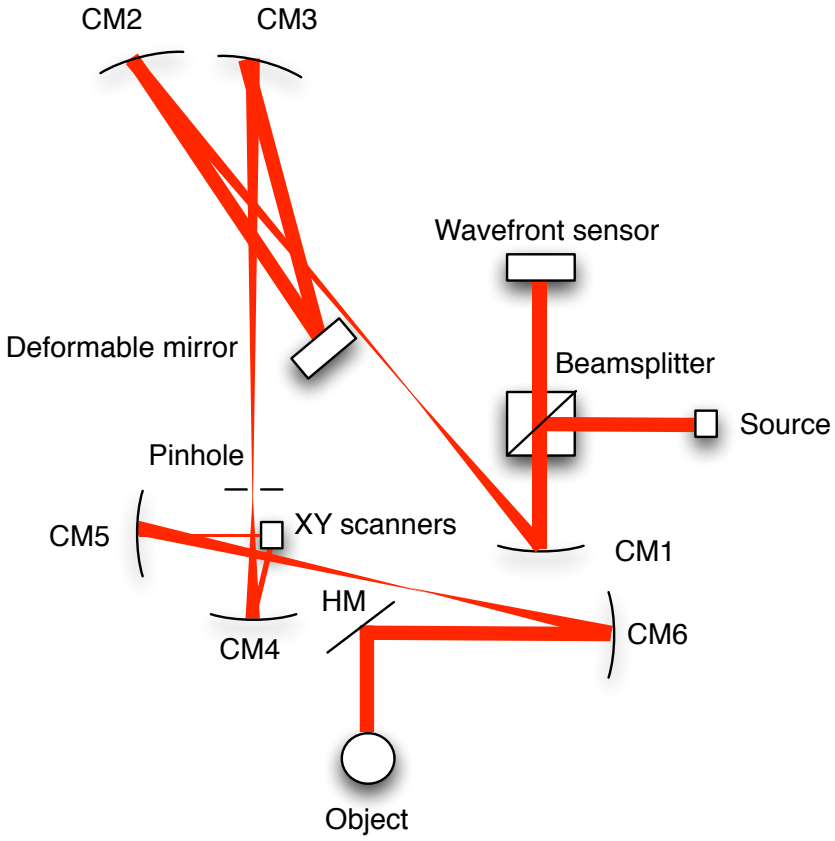

FIGURE 5.2: Diagram showing the resizing of imaging beam in an AO-SLO system.

The remaining 30% of emitted light from the SLD is reflected onto the surface of the first 2" gold-plated curved mirror (CM1) with a focal length of 20 cm. The light reflected from CM1 comes to a focus and expands before reaching the second curved mirror (CM2) with a focal length of 101.6 cm. CM1 and CM2 form the first telescope in the setup, used to magnify the diameter of the 3 mm launched beam by a factor of five such that it fills the 15 mm aperture of the DM. The beam is collimated in reflection from CM2 and travels to CM3 after a reflection from the DM.

CM3 and CM4 have focal lengths of 76 cm and 10 cm respectively, reducing the size of the beam to approximately 2 mm so it may fit on the 3 mm XY galvonometric scanners. Finally, the beam enters the third telescope formed by CM5 (f = 20 cm) and CM6 (f =

60 cm), collimating and magnifying the beam to 6 mm diameter as it enters the eye. A hot mirror (HM) is optionally placed between CM6 and the eye so a fixation target may be used to aid in the stabilisation of the eye when imaging. Fig. 5.2 shows the optical setup as described in Fig. 5.1, with the additional information of beam size evolution as the light propagates through the system.

Backscattered light propagates back through the system to BS1 where 70% is transmitted to BS2 and 30% is reflected back to the SLD. It is known that SLDs are prone to noise under the feedback signal, therefore for highly reflective targets it is expected that extra noise is generated because of the SLD. When the system is employed to image the retina there is no such problem. The 70% of the light that is returned from the object is split again by BS2, a 10:90 beamsplitter. 90% of the remaining light is reflected and focussed into fibre by a x10 objective. This light is joined with the light transmitted through the reference arm using a 50:50 coupler and used to create an OCT image using a Nirvana balanced detector (Newport). A glass slide (GS) is placed between BS1 and CM1 to reflect a small portion of light returned from the object into a multi-mode fibre connected to an avalanche photodetector, which creates the SLO image.

The remaining 10% (of the 70% light returned from the object) is transmitted through BS2 and into the wavefront sensor. The light is decomposed by a 32 x 32 microlenslet array into a spot pattern focussed on the surface of the CCD camera. This information is used by the AO software CASAO (Imagine Eyes) to perform closed loop correction on the detected wavefront.

Simultaneous SLO and OCT images are acquired using software supplied by OTI using National Instruments hardware interfaces.

5.1.1.2 Achievements

The designer claimed the system was capable of achieving roughly 4 μm resolution in air with OCT, and less with SLO due to the multi-mode fibre. The software provided by OTI displayed live *en-face* and B-scan OCT images in addition to the SLO guide channel (only available in the *en-face* regime), with lateral pixel to pixel correspondence. The software generated analogue waveforms to drive the scanners and used this as an internal trigger to synchronise lines and frames. For cross-sectional imaging, a TTL signal was sent to the linear motorised translation stage to trigger the start of the OCT B-scan sweeps. Signal received from the detectors was processed by this software, performing bandpass filtering and BCG (brightness, contrast, gamma) modifications.

5.1.1.3 Limitations

There were limitations with the design of the legacy system that prevented the AO from reaching its maximum potential. These issues are discussed separately below.

Efficiency

It was identified that there was a large power reduction as light propagated through the system. With emission power in excess of 2.5 mW in the object arm alone, only 410 μW reached the eye. This value is only 55% of the maximum permissible power deemed to be safe for the eye (750 μw for a scanning beam at 830 nm). With losses in both directions, the overall efficiency of the system was lower than the potential maximum. A multi-mode fibre was used to collect light for SLO imaging, to maximise light sent to the detector. This has a negative impact on the resolution.

During closed loop correction, the DM is affecting the flatness of the wavefront but this also can cause a repositioning effect. As the corrector brings the wavefront to a corrected state, it may in fact move the beam slightly such that it no longer has good coupling into fibre. In this case, in spite of the increased resolution gained through AO correction, there is a drop in signal to the photodetector. The receiving fibre must be adjusted manually such that optimal injection is achieved, however this position is completely dependent upon the state of the DM. Considering the solution for a corrected wavefront varies between objects (or over time with the same object), the receiving fibre must constantly be adjusted to maximise light sent to the detector.

Stability

Given the long 12 m path length, the optical components tended to misalign frequently and the system required constant maintenance. In addition, it was shown that operating the DM in closed loop caused imaging artefacts through harmonic vibration. These deviations were caused by the actuators within the DM requiring a settling time after receiving a command before remaining stable [148].

Resolution

In air the resolution of the system was measured to be larger than 4 μm, as determined by imaging a USAF resolution target placed within the OCT arm. SLO resolution was reported as worse than this, due to the use of a multi-mode fibre to couple light to the APD.

5.1.2 Objectives

Given the limitations of the previous design and the advances made in AO/SLO systems reported in literature, it is important to outline some objectives before creating a new system. The goal of this project is to produce high resolution images of the retina *in-vivo* in real time. The main criteria for achieving this goal are listed below.

High lateral resolution

The ability to resolve photoreceptors in the living human eye is a critical benchmark for the performance of this AO-SLO system. To achieve this resolution it is vital to reduce optical aberrations as much as possible. As described in chapter 2, imaging resolution is determined by the size of the airy disc. There are many factors which influence this spot size, which all must be considered when attempting to achieve resolution near the diffraction limit. AO is central to the task of achieving this resolution, therefore extensive analysis of its performance must be conducted before eye imaging can be performed.

Fast imaging speed

To produce live images from a rapid-moving target such as the eye *in-vivo* it is vital that the signal received from the photodetector is processed in real-time. National Instruments (NI) provide hardware and software suites specifically designed for high-speed data processing. LabVIEW is a software package that communicates with proprietary NI I/O boards and performs with speeds sufficient for real-time imaging. Custom software is created within the LabVIEW environment to perform all the tasks necessary for imaging. These are described in the methodology section.

Efficiency

To achieve the maximum potential for the SLO system, a power of 750 μW must be measured immediately prior to the pupil of the eye. Further, it is important to minimise losses induced as the light propagates through the system. Even with 750 μW measured at the eye, if the losses are substantial through the system then only a fraction of the useful backscattered light from the eye will reach the detector and WFS. An effort should be made to minimise lossy optical elements and overall launching and receiving efficiency should be measured.

Stability

In-vivo eye imaging is fraught with fixation problems due to the rapid voluntary and involuntary movement of the eye in addition to the instability caused by variability of orientation and position of the patient's head. A fixation image may be projected into the eye to act as a guide for orientation and focus.

During live imaging the DM should be maintaining a state of correction without creating artefacts in the image due to harmonic vibration. Minimising the number of optical elements in the system will also reduce the time maintenance cost of keeping the system correctly aligned.

Versatility and expandability

SLO imaging and wavefront sensing/correction at 830 nm is the central goal for this project, however it is desirable to design the system such that implementing OCT imaging is possible without significant modifications. The system will be designed with a mind for adding a reference arm for OCT imaging at a later date, possibly at different wavelengths.

5.2 Methodology

This section details the initial and final implementations for an AO-SLO/OCT system that fulfills the objectives listed above. First is a presentation on an experiment using a fibre array, followed by a discussion of its flaws and then a detailed description of the final design.

5.2.1 Fibre array

A slight redesign of the original system was trialled where the environment around the source fibre from the SLD was altered. A key limitation of the original design was the relationship between signal received by the photodetector and the side-effects of the wavefront correction process. As the DM brings the wavefront to a corrected state, it often results in a lateral shift of the beam away from the tip of the receiving fibre, causing a drop in photocurrent from the detector and reduced image intensity.

Conceptually, a fibre coupler array could be used to launch light from the SLD and receive backscattered light from the object into the same fibre. Light travelling to and

from the object are completely common-path in this scenario. The array would also allow for OCT imaging by using the second input/output fibres for the reference arm.

5.2.1.1 Design

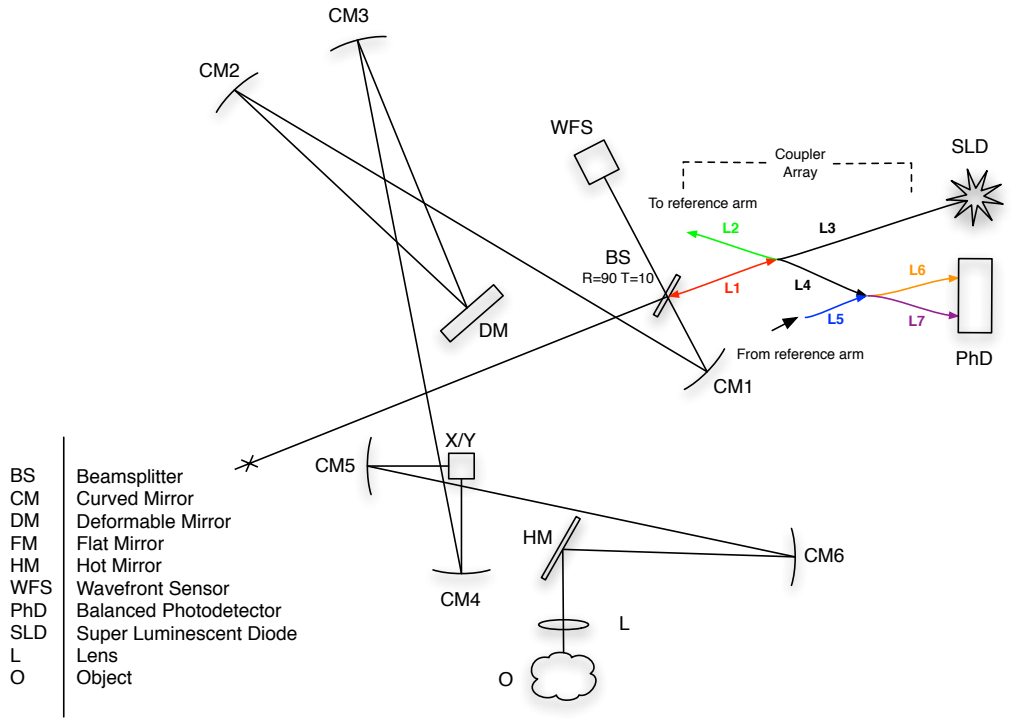

FIGURE 5.3: Diagram showing an AO-SLO/OCT system using a fibre array.

Fig. 5.3 shows a modified version of the system presented in Fig. 5.1 with the addition of a fibre coupler array and the removal of a beamsplitter and glass slide. Light launched from the 830 nm SLD (Superlum) enters the input fibre of the array (L3) and is split 70:30 into the two output fibres L1 and L2 respectively. Light from both of these fibres are collimated using x10 objective lenses. 10% of the light transmitted from L1 into the object arm and through the beamsplitter is wasted, and 90% is reflected to the first curved mirror CM1.

Light propagates through the object arm identically to the legacy system in section 5.1.1 until it returns to the beamsplitter. 10% of the light returned from the object is transmitted to the WFS while the remaining 90% is reflected back into the fibre coupler array through L1. 30% of this light is sent back to the SLD (L3) and the remaining

70% travels to the second coupler (L4). Light launched from L2 into the reference arm propagates through a series of silver planar mirrors and is coupled into fibre L5. Since the reference arm is static there is no issue having the light injected into a separate fibre.

Light returned from the object (L1 to L4) and the reference arm (L5) is then recombined in a 50:50 coupler and sent to a Nirvana balanced photodetector (Newport). If the reference arm is blocked, one of these fibres may be removed and connected to an APD to provide better quality SLO images, due to the single mode structure of the fibre used in the fibre array.

5.2.1.2 Achievements

This design achieved a remarkable increase in efficiency over the previous design. Though 10% of transmitted light was wasted through the beamsplitter, and a further 30% of light returned from the object was wasted on return, there was a significantly higher measured efficiency increase. Considering a 100% reflectance from the object, the total power returned to the detector from the object arm in the legacy system is 18.9% of the emitted power from the SLD, which increases to 39.69% for the new arrangement. Since losses through the reference arm were negligible, it was not harmful to reduce the overall power being transmitted. This increased the power output into the confocal (object) arm. Further, there is now 90% reflectivity of light from the source fibre into the system via the lone beamsplitter.

On return from the object, 90% of the light is injected into fibre. This is a substantial relative increase over the legacy system which used a glass slide to siphon light to the SLO, then 30% was sent back to the source and then 90% of the remaining light was sent to the detector. For SLO imaging, only one of the two output fibres of the 50:50 coupler (L6, L7) could be used. Though a 50% loss in signal is significant, due to the high gain values of the SLD there was still more than sufficient signal to produce quality images. It was also found that, unlike the previous system, running closed loop correction with the AO had negligible effect upon the signal received by the photodetector. It is assumed then that if the DM caused the beam to be shifted, the effect upon detected signal was less than previously reported. In addition, due to the use of a single-mode fibre in the SLO channel rather than a multi-mode fibre, the resolution loss due to coupling was avoided.

5.2.1.3 Limitations

There were several advantages to using the fibre coupler array with the AO-SLO/OCT system, however experimentally there was a significant disadvantage. Since both couplers are joined in an array, there is significant transmission of light in both directions. Imaging with SLO required that the reference arm be blocked to avoid contribution of light entering L5 saturating the APD. Though it was possible to do this, it was discovered that overall SNR was negatively impacted due to fibre-end reflections produced by the reference arm output fibre L2. The fibre tip itself must be cleaned periodically otherwise the reflections return enough light to the detector to saturate before the contribution of light returned from the confocal arm.

Even with a clean fibre tip there was some small contribution of light from L2 to the confocal image, causing a loss of SNR for the SLO image. The other obvious disadvantage of this implementation is that OCT and SLO imaging can no longer be performed simultaneously without an additional beamsplitter, since the SLO channel takes one of the two fibres used for balanced detection.

5.2.2 Improved design with non-planar mirror arrangement

AO introduces additional layers of complexity to the design of the optical imaging system. Compromises must be made between cost, image quality and versatility. The key component in this AO-SLO design is the MEMS deformable mirror from Imagine Optics, which has a reflective membrane of 15 mm diameter (the same device used in the legacy system). The mirror has been designed such that the outer ring of actuators is positioned on the periphery of the visible area of the membrane. The reasoning behind this design decision is that the mirror can impact the full visible area of the reflective surface with no 'dead zones', i.e. regions in which the reflective surface cannot be fully actuated. It is for this reason that AO imaging systems have been designed to resize the imaging beam so it fully illuminates the visible area of the deformable mirror to maximise the effect of the MEMS device on the wavefront.

Given the 15 mm diameter of the visible portion of the deformable mirror and the small size of the other optical elements, telescopes must be employed to resize the beam as it propagates through the system so that the beam is not clipped. Lenses cannot be utilised to resize the beam as they cause back reflections to be directed back through the system to the wavefront sensor. This has a negative impact upon the accuracy of the wavefront measurement and subsequent closed loop correction. Gold-coated curved mirrors of differing focal lengths are used to reflect and refocus the beam, changing the beam diameter, as demonstrated by the legacy system in Fig. 5.2.

Unfortunately, curved mirrors induce aberrations in reflectance, the magnitude of which increases as the angle of off-axis incidence increases. These aberrations will contribute to the overall degradation of the wavefront in the object arm, reducing resolution on the target. This effect was observed with the previous configuration (see section 5.1.1.3). Given the purpose of the AO project to keep optical aberrations to a minimum, efforts must be made to reduce the aberration-inducing effect of the optical elements that comprise the system. Typically this entails careful positioning of the mirrors to minimise the off-axis beam propagation, thus reducing the astigmatism and coma aberrations induced.

More sophisticated techniques have been reported which implement a non-planar reflective telescope design that has the beam propagate in a single dimension per reflection. In addition, each reflectance from a curved surface in one dimension is countered later with a negative equivalent movement. For example, a beam incident upon a curved mirror may be reflected 0 degrees horizontally and 5 degrees vertically. To compensate for the aberrations induced in this movement, a later telescope will apply an inverse reflectance of 0 degrees horizontally and -5 degrees vertically. In essence, the beam is subjected to an inverse set of aberrations of the same magnitude, which should eliminate system-induced astigmatism aberration.

The use of curved mirrors will introduce spherical aberration as the beam is reflected. Spherical aberration is a consequence of reflections from a spherical surface wherein rays that hit the outer edge of a curved optic will focus at different points to the paraxial(central) rays. With multiple focus points the subsequent image may appear blurry. Theoretically, one might combat spherical aberrations with the placement of pinholes at the foci of each telescope to block all but the paraxial rays. This is not always possible with AO systems, particularly those that include large-stroke deformable mirrors as the closed loop corrections may alter the wavefront so much as to deviate the beam slightly, causing a lateral shift that might result in a clipped beam if using fixed pinholes.

5.2.3 Considerations

Translation of theory into a practical imaging system requires careful selection of optical elements and consideration with their arrangement. Given the information discussed above, the following key areas must be considered when designing the AO-SLO system.

5.2.3.1 Beam size

Beam size is a critical consideration when designing any optical system. With AO-enabled designs it is important to resize the beam for maximum effect upon each component involved in the sensing/correcting loop. The following elements in the system have specific requirements for beam size:

- The reflective surface of the Miraro 52-E deformable mirror has a diameter of 15 mm
- Galvoscanners are 5 mm wide
- The HASO wavefront sensor has an aperture size of 5 mm diameter
- The human eye pupil has a diameter ranging 2 to 8 mm (AO systems target pupil diameter greater than 4 mm)

In each case it is beneficial to resize the beam to the maximum diameter allowed by the optical aperture. The DM is afforded greater control over the wavefront if the entire surface is illuminated.

For accurate measurement of the wavefront it is desirable to illuminate as much of the wavefront sensor as possible without clipping the beam. The beam returned from the sample to the WFS is decomposed by the lenslet array into a spot pattern on the CCD (refer to Fig. 4.2). Larger spot patterns provide more detailed information on the distribution of power and the shape of the wavefront. When modulating the stroke of actuators on the DM, the effect of a single movement is more precisely measured with higher numbers of spots on the WFS. This allows for more precise determination of the effect that each single actuator has on the wavefront.

The lens in the human eye is treated as any objective lens in a conventional microscope system. SLO techniques are constrained by the limitations of the eye; the pupil cannot exceed more than ∼8 mm diameter, and even then specialist drugs are required to dilate the pupil to this extent. Designing the system for a best case scenario of a pupil size of approximately 8 mm should help the AO achieve maximum potential by increasing the NA, bringing maximum achievable resolution closer to the diffraction limit. The approximate equation for the diffraction limit of a microscope is given by

$$d = \frac{\lambda}{2n \sin\theta} \tag{5.1}$$

where d is the resolvable feature size, λ is the wavelength, n is the index of refraction and θ is the half-angle of collection of the objective. The drawback of this design would be if the AO fails to provide a correction, since the larger pupil will induce spherical aberration. The larger diameter lens and beam size means that rays passing through the lens near the edge have a different focal point than those near the centre. This error increases with the diameter of the lens, so if not properly compensated this creates problematic 'ghost' images at different axial distances.

5.2.3.2 System induced aberrations

The new design should reduce the system-induced optical aberrations that proved problematic for the legacy system. Attempts should be made to reduce the number of optical elements - particularly the aberration-inducing curved mirrors - to a bare minimum. As with the legacy system, the X and Y scanners should be positioned in close proximity to avoid the lengthening of the optical path. Curved mirrors with large focal lengths are preferred to reduce the negative impact they have on the wavefront, particularly with off-axis reflections. An issue with this implementation is that the optical path becomes long, as evident in the legacy system.

5.2.3.3 Conjugate planes

Adaptive optics using a DM and WFS requires precise positioning of optical components such that the DM, WFS and pupil plane are conjugated. A single point of light in the pupil plane must also be a single point on the surface of the DM and WFS. When using scanning elements, the galvoscanners must also be placed in the conjugate plane. To achieve conjugation, the image from the pupil must be re-imaged on the surfaces of the scanners, DM and WFS. Fortunately telescopes are already in use to resize the beam. There is a slight issue when using integrated XY galvoscanners since only one of the scanning mirrors may be placed in the conjugate plane. A solution would be to separate these scanners and place an additional telescope between, however this will lengthen the optical path further and raise the potential for system induced aberrations. It is for this reason that the concentrated XY scanners are retained.

5.2.3.4 Removal of lenses due to back reflections

A Shack-Hartmann wavefront sensor is used for determining optical aberrations present in the system. This technique requires that all backscattered light is returned from the sample to the WFS, however this may not be true. A problem when using lenses to

propagate light is that they cause back reflections, which distort the readings on the WFS. For the closed loop AO to work correctly, only reflective mirrors may be used in the object arm to resize the beam, to prevent back scattered light from compromising the wavefront measurement. In the previous configuration, 2 inch gold-plated curved mirrors were used, which have a reflectivity of more than 92%.

5.2.4 Optical design

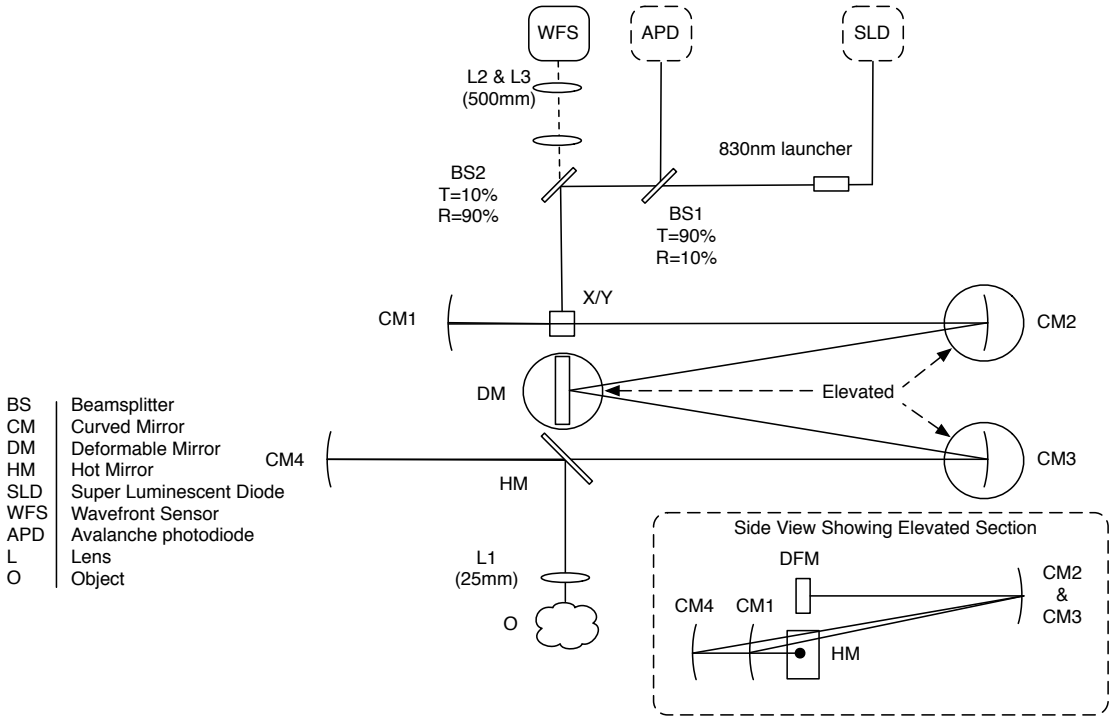

FIGURE 5.4: Schematic of wavefront sensing system. The lens L1 is representative of the eye lens, with the object O representing the retina.

Fig. 5.4 shows the new design for a AO-SLO system. The SLD emits a 830 nm collimated beam of 3 mm diameter that is split by a 90/10 plate beamsplitter (BS2), wherein 90% light is reflected to the object arm and 10% is wasted. In this design, the galvoscanners are swapped with the DM, bringing them closer to the launcher. Larger galvoscanners were selected; the 3 mm mirrors were replaced with 5 mm mirrors, to reduce potential power loss from beam clipping. Bringing the galvoscanners closer to the launcher allows for the elimination of a telescope (two curved mirrors) since the launching beam of 3 mm diameter need not be resized to fit the 5 mm galvoscanner mirrors.

The beam is directed at 90 degrees from the integrated XY galvoscanners. The first telescope is comprised of CM1 with f = 200 mm and CM2 with f = 1000 MM. CM1 and CM2 are positioned opposite each other, with CM2 being elevated. After passing through

this telescope, the collimated beam is enlarged to 15 mm diameter and is reflected from the surface of the DM to the second telescope. CM3 with f = 1000 mm and CM4 with f = 500 mm reduce the beam diameter by half to 7.5 mm. This telescope reverses the height propagation of the first telescope formed by CM1 and CM2.

In reflection from CM4 the collimated beam of 7.5 mm diameter travels to the objective via a hot mirror (HM). The HM is transparent for visible light and reflects light of wavelength larger than 700 nm; it is used in place of a regular plane mirror so that fixation can be implemented for eye imaging. Light returns from the object through the system and is again split by the 90/10 beamsplitter BS2, where 90% returns in reflection to the avalanche photodetector. The remaining 10% transmits through the beamsplitter and reflects 90 degrees off a silver plane mirror. The beam is re-imaged on the WFS using a telescope comprised of two f = 500 mm lenses (L2, L3) before entering the aperture of the Shack-Hartmann WFS. The 90% light reflected from BS2 is again split by BS1, where 90% goes to the APD.

5.2.5 Wavefront optimisation

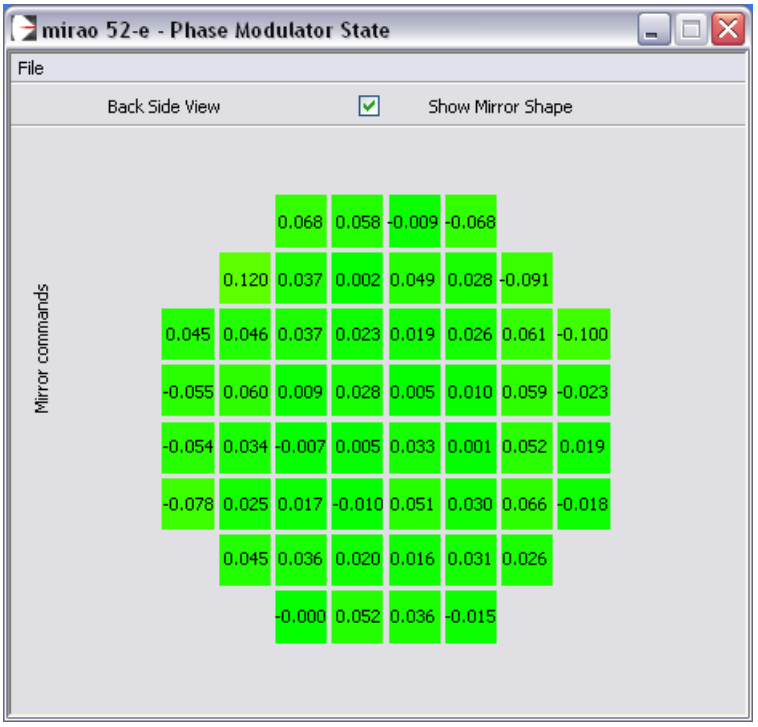

FIGURE 5.5: Layout of 52 actuators with voltages shown.

The critical component in this AO system is the MEMS deformable mirror, which serves as a means to modify the wavefront. Specifically, the device used is a MIRAO 52-E, supplied by Imagine Optics and controlled using specialised software called CASAO.

The deformable mirror is used in combination with a Shack-Hartmann wavefront sensor, which provides accurate measurement of the wavefront. The wavefront sensor consists of a CCD camera with a mounted 32x32 micro-lenslet array that focuses an incoming beam to a spot pattern upon the surface of the camera.

Supplied software called HASO is used to evaluate the spot pattern to provide a detailed measurement of the wavefront. This is accomplished by analysing the shape, size, contrast and placement of the spots in the pattern to determine information on the wavefront. By analysing the spot distribution, the software can generate a set of slopes. These slopes provide vital information on the state of the wavefront, such as tilt, defocus, astigmatism and various other aberrations. Once the incoming beam has been decomposed to a set of Zernike coefficients, the deformable mirror may be modified to apply an inverse of these aberrations, effectively flattening the wavefront.

The Mirao 52-E MEMS device has several possible states. When the driver is powered off, the actuators may be positioned arbitrarily, causing the reflective surface of the mirror to become irregular. A beam reflecting from the surface of the mirror in this state is subjected to severe aberrations. When powered on, the actuators of the mirror assume a 'zero' state; this means that there is a practical application of 0 V to each actuator. In practice this does not mean that the surface is totally flat. Fig. 5.5 shows an example of random voltages applied to each of the 52 actuators in the DM.

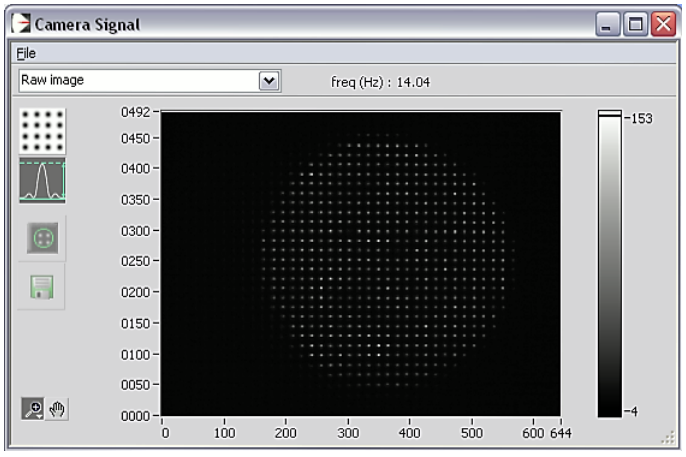

FIGURE 5.6: Spot pattern of uncorrected wavefront.

Fig. 5.6 shows the visualisation of the spot pattern as seen by the WFS. Note the non-uniform intensity distribution of the spots. The shape, size and distribution of these spots can be used to generate wavefront information, aiding in the representation of the wavefront as shown in Fig. 5.7. This figure shows a total wavefront error of 0.638 μm RMS excluding tilts and focus. The image shows that the wavefront has astigmatism aberration.

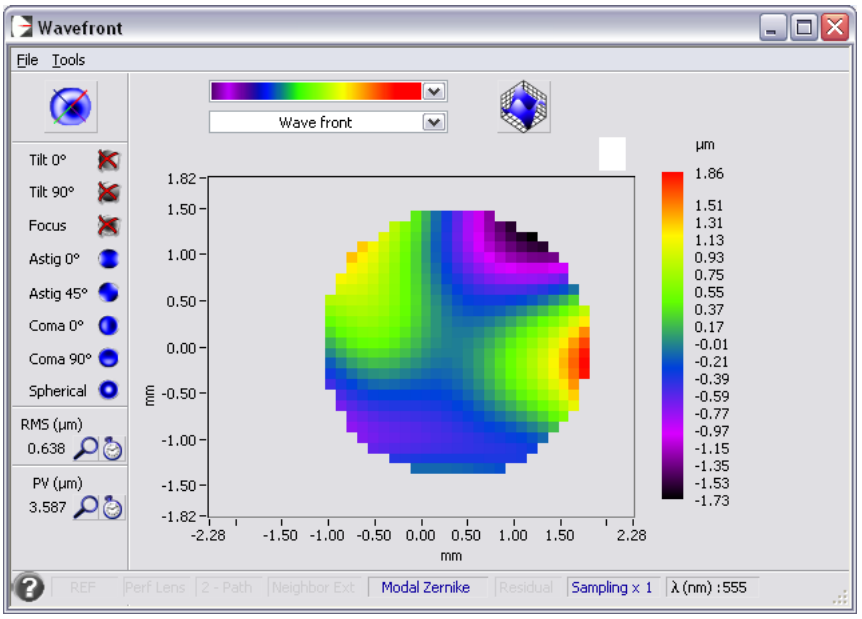

FIGURE 5.7: Uncorrected wavefront measurement.

Active wavefront correction is achieved in two stages: initial computation of the wavefront error and closed loop correction algorithm.

5.2.5.1 Initialisation of adaptive optics

The process of correcting the wavefront requires that there be an object to use as a reference. A scattering target is selected to perform the wavefront measurement on; specular targets saturate the WFS and provide inaccurate measurements due to the sensitivity to tilt. Typically a sheet of white paper is used as a target when determining the nature and magnitude of optical aberrations induced by the components of the imaging system. With a forward current of 100 mA from the SLD controller, the light measured at the pupil is 220 μW. It is important to supply enough light for sufficient readings on the WFS without saturating the CCD camera.

With the galvoscanners stationary and zeroed in a central position, the object is moved into focus. The light returning from the paper is decomposed by the WFS into a spot pattern, which is analysed by the supplied CASAO software. Wavefront measurement is achieved through analysis of this spot pattern to form a 3D profile. By inspecting the intensity, size and arrangement of individual spots, the software forms a series of slopes. For this process we ensure the room is as dark as possible to prevent ambient light from interfering with the calculations.

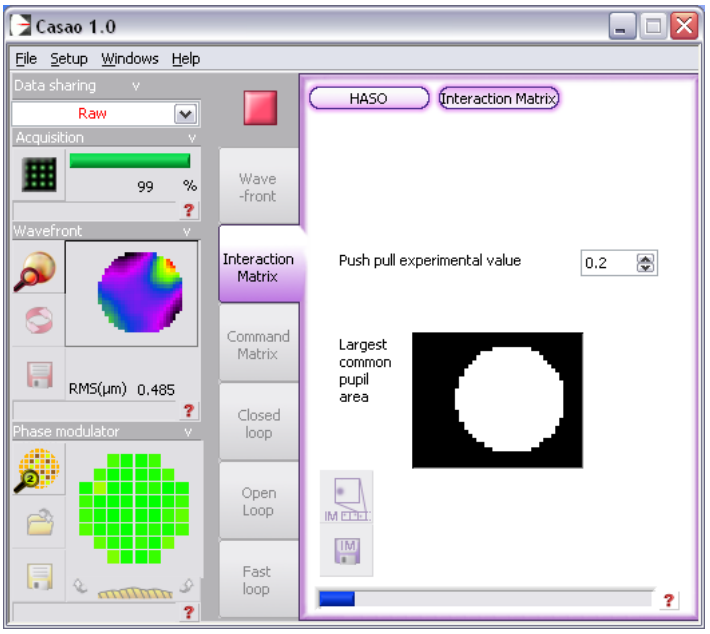

FIGURE 5.8: Building interaction matrix with common pupil shown.

Once a measurement is acquired, the next stage is to modulate the actuators on the DM and determine the effect on the wavefront. The MIRAO 52-E has actuators that may be modulated with a positive or negative voltage. Before closed loop corrections can be made, an **interaction matrix (IM)** must first be constructed. The IM is essentially a set of slopes that are taken as voltage is individually applied to each of the 52 actuators sequentially. Limits for modulation are determined by the user, in this case ± 0.2 V is used. With 2 states for each actuator and another 'neutral' state where no additional voltage is applied, a total of 105 measurements are taken.

Fig. 5.8 shows Casao during IM acquisition. In the bottom left corner is a display of the 52 actuators, with one currently highlighted. This shows which actuator is currently being modified. The main panel has a control that allows for adjustment of the push/pull value. This is the value by which each actuator will be adjusted during the IM acquisition cycle.

The white circle in the main panel is the largest common pupil. The common pupil demonstrates the area of the spot pattern from which measurements can be taken from all permutations of actuator modification. Areas outside of the common pupil are deemed to contain insufficient information on the wavefront, and any weak signal from these areas is ignored. If adjusting an actuator causes part of the spot pattern to become too weak (intensity below threshold required) then the common pupil may begin to shrink.

The effect of a small common pupil is that the outer ring of actuators on the DM may not be used when running closed loop corrections. A large common pupil is desired for best correction, however this is limited by the objective lens diameter. Since an 8 mm objective lens is used for determining the IM, the common pupil is not reduced during phase manipulation. Fig. 5.9 shows the influence of four actuators on the wavefront as determined by the interaction matrix.

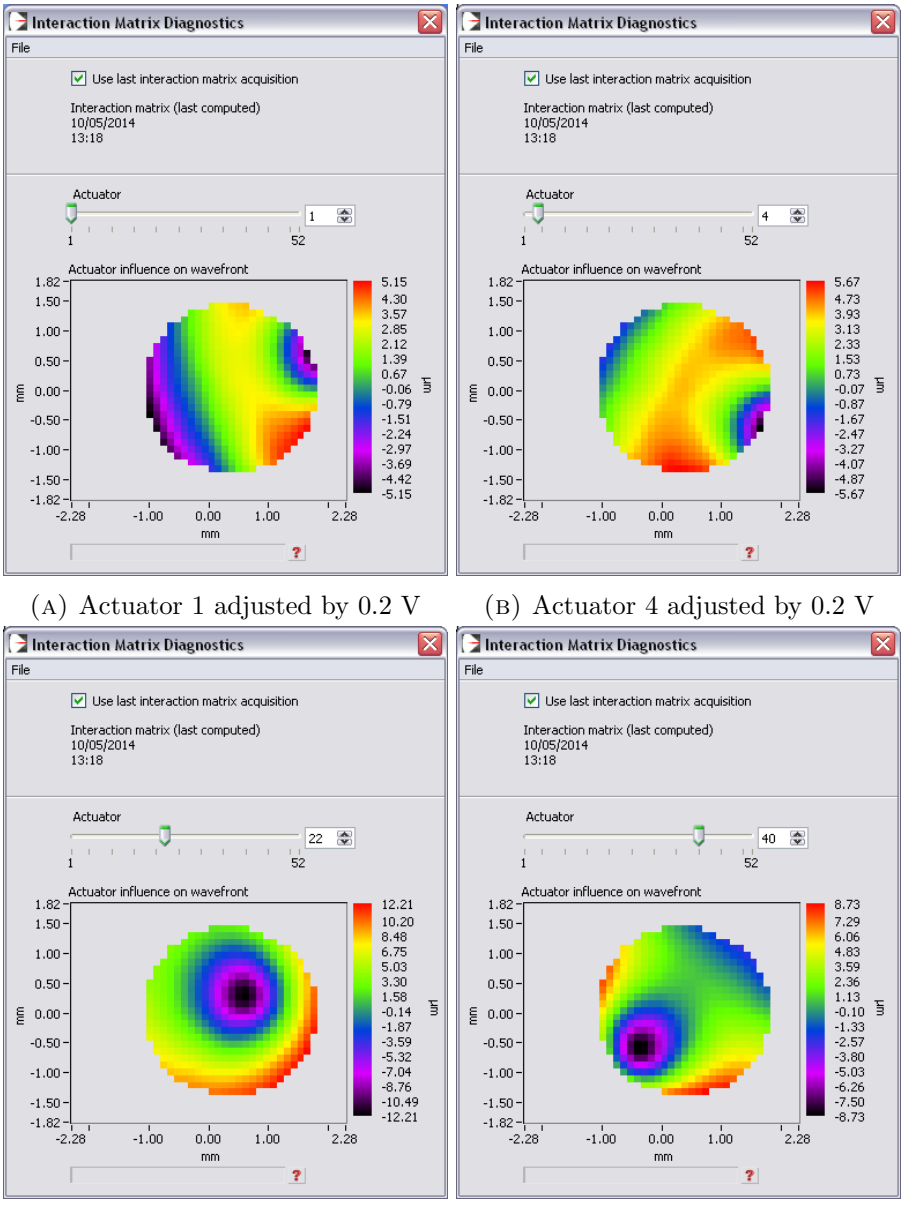

(A) Actuator 1 adjusted by 0.2 V (B) Actuator 4 adjusted by 0.2 V

(C) Actuator 22 adjusted by 0.2 V (D) Actuator 40 adjusted by 0.2 V

FIGURE 5.9: Images of wavefront during 4 of the 105 stages of IM acquisition.

From the IM, a **command matrix (CM)** is created. The CM is a simulated response of the overall wavefront as voltages are applied to the actuators. An accurate CM is essential for the success of the closed loop as it provides information on the effect each actuator has upon the wavefront when modulated. A CM is calculated using a

configurable number of Eigenmodes. Raising the number of modes provides more details on higher order Eigenmodes, though this may come at the cost of an effective correction. For this experiment, 48 modes are calculated.

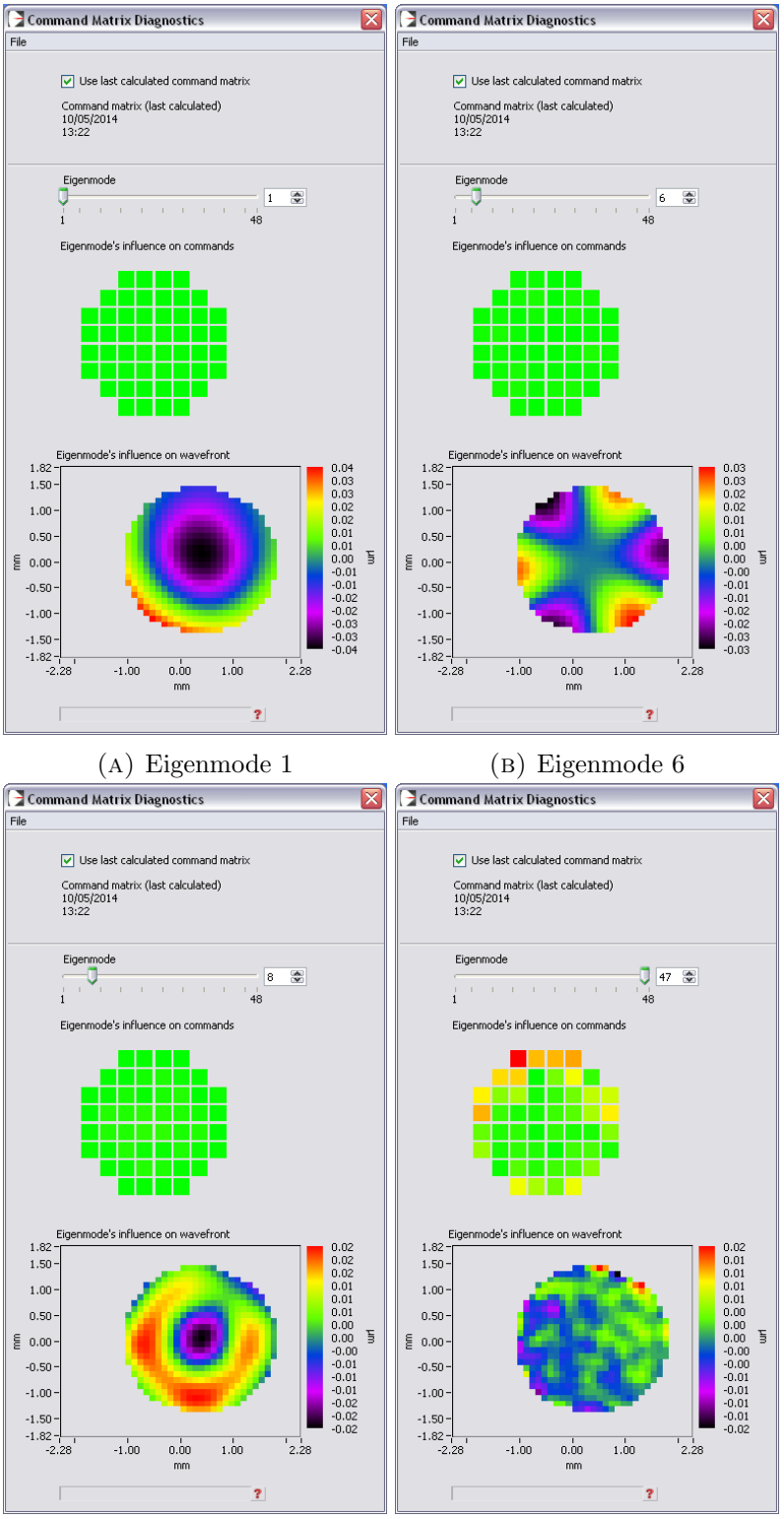

(A) Eigenmode 1 (B) Eigenmode 6

(C) Eigenmode 8 (D) Eigenmode 47

FIGURE 5.10: Calculated Eigenmode influence on wavefront.

Fig. 5.10 shows the calculated influence of 4 of the 48 Eigenmodes on the wavefront. Also displayed is a diagram that describes the commands necessary to minimise the effect of this type of aberration on the wavefront. Low order Eigenmodes (Fig 5.10a, 5.10b, 5.10c) require minor movements of the actuators, typically under 0.5 V. Fig. 5.10d shows that an extensive adjustment of the actuator phase is required to compensate for larger numbers of Eigenmodes.

5.2.5.2 Closed loop correction

The objective of closed loop correction is to flatten the wavefront as much as possible. After the generation of the CM and the determination of the wavefront error is made, the CASAO software is committed to apply an inverse of the detected error. Limits are imposed upon this operation to ensure a solution is reached quickly and efficiently.

Gain is an important contributing factor to maintaining a stable closed correction loop. The closed loop will attempt to incrementally manipulate the actuators every iteration of the loop, and then measure the effect upon the wavefront. A high gain will cause the loop to converge quickly upon a solution, however this may cause the undesirable effect of 'overshooting' the target wavefront. In the case that the gain is too high, the closed loop will continuously overshoot its target, producing an inaccurate and unstable solution.

Low gain values will ensure that the actuators are manipulated in smaller, more precise steps each iteration. This usually raises the accuracy and stability of the closed loop correction at the cost of speed. Reducing the gain too much will cause the corrections to lag behind the detected wavefront error, since the steps are not large enough to correct for variance between each iteration. For this experiment a gain of 0.2 V was found to be a good compromise between speed and stability. With a rate of 20 Hz, it typically takes little more than 2 seconds to achieve optimal correction.

5.2.6 Image acquisition and processing

An avalanche photodiode detector (Hammamatsu) was selected, with peak sensitivity at the operating wavelength of 830 nm. This photodetector has the capability to provide high gain to the received photocurrent; this is vital for the purposes of *in-vivo* eye imaging due to the weak light returned from the patient's eye to the detector. For standard microscopy of scattering and specular targets, we may reduce the gain by reducing the voltage applied to the APD, allowed by a potentiometer on the driving board supplied by Hammamatsu.

5.2.6.1 Synchronised analogue input/output

The imaging software is required to output two signals, one for each of the two galvoscanners responsible for rastering the beam in two dimensions across the sample. A module for LabVIEW named DAQmx provides a means to create connections to an I/O board so it may exchange data through hardware. To control the XY scanners it is required that two waveforms be created before they are digitised and communicated to the scanner driver.

A triangular waveform is generated for the fast line (X) scanner, with a frequency of 500 Hz and a maximum amplitude of 1.5 Vpp. A second, sawtooth, waveform is generated for the slow frame (Y) scanner, with a frequency of 2 Hz and maximum amplitude of 1.5 Vpp. This secures an overall video rate of 2 frames per second (FPS). 1.5 Vpp was determined experimentally to be the maximum voltage that may be applied without scanning the beam off the edges of the other optics. Two DAQmx tasks are created in the LabVIEW software to create analogue output channels to carry voltage to the driver box. Both of these tasks must have a synchronised start to avoid the image 'drifting' out of phase during imaging. This initial synchronisation is used also to determine the splicing of incoming data from the photodetector into usable frames.

5.2.6.2 Image reconstruction

A third DAQmx task is created to retrieve analogue input voltages from the photodetector via the breakout box. This task is also triggered in synchronism with the tasks controlling the galvoscanners. Data acquired from the photodetector is received as a continuous stream and must be digitally spliced into lines, which form frames.

This task will continuously pull a 1 dimensional array of numerical (floating-point) data from the photodetector. Within the software, the image is constructed by restructuring the data as it is received. We construct each complete image with 125,000 sequential samples read from the photodetector. Considering that that horizontal X scanner runs at 500 Hz, our array of 1D data must be re-sampled such that each sample is representative of a single pixel on the object as seen by the imaging beam.

The 125,000 samples are spliced into blocks of 500, where each block is now a separate line in a 2D array. This is performed 250 times until all 125,000 samples have been spliced into lines in a 2D array. The result is a 500 x 250 2D array of floating-point numbers from which an image is constructed. Following the re-sampling process, the data is then subjected to BCG (brightness, contrast, gamma) modifications to create a meaningful image that is displayed live on the screen.

In actuality, the software pulls 250,000 samples per second from the photodetector. With the frame Y scanner running at 2 Hz, this whole process is completed twice per second giving an imaging rate of 2 FPS. Integrated into the software is the capability to acquire snapshots (saving a single image) or indefinite sequential recording of images in real-time.

5.3 Results

The results are presented in multiple sections. To determine if the system is successful in achieving its objectives, characterisation of its performance must be conducted. Section 5.3.1 provides a comprehensive analysis of the system performance with relation to wavefront measurement and correction.

Section 5.3.2 provides results taken from practical experimentation upon a USAF resolution target. This is an important step to characterise the imaging properties of the setup. Section 5.3.3 demonstrates results taken from imaging skin with the confocal setup. Finally the system is used to image the living human eye and the results are shown in section 5.3.4.

5.3.1 Wavefront characterisation

To determine the effectiveness of the wavefront correction, it is necessary to compare measurements of the wavefront pre- and post-correction. Fig. 5.11a displays the spot pattern as detected by the WFS in comparison to a corrected version in figure 5.11b. It is not immediately clear that the corrected version is less aberrated than the pattern detected prior to closed loop. Both spot patterns display spots with irregular brightness levels, so careful analysis is required to differentiate the two. It is worth noting that the scale for intensity in Fig. 5.11a ranges between 4 and 153 while the corrected spot pattern in 5.11b ranges between 0 and 238. This demonstrates that the corrected spot pattern has higher contrast than the uncorrected pattern, and greater overall intensity.

From the spot patterns the slopes are calculated, then an overall wavefront measurement can be represented. Fig. 5.12 displays the calculated wavefront error prior to correction (5.12a) and after correction (5.12b). Focus and tilt are not considered when determining the wavefront error since these may easily be introduced through the placement of the imaging object or the WFS.

Fig. 5.12a shows an overall wavefront error of 0.638 μm RMS. It is clear from the diagram that the wavefront suffers strong astigmatism in addition to other aberrations.

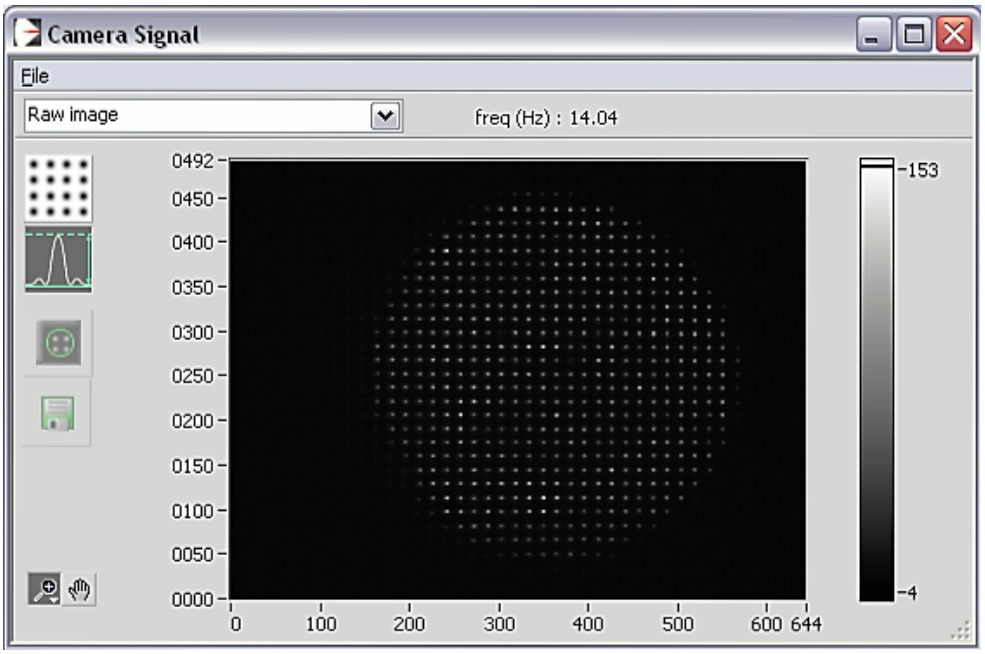

(A) Prior to correction.

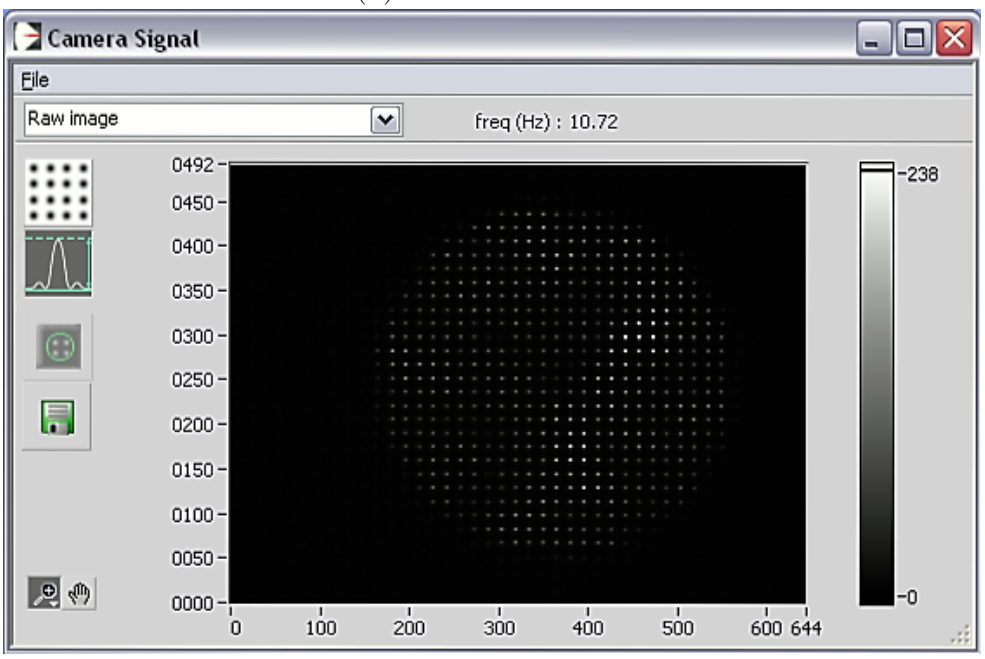

(B) After correction.

FIGURE 5.11: Spot patterns detected by WFS before and after closed loop correction

Post correction, a wavefront error of 0.020 μm RMS is calculated, and visually a much more uniform wavefront can be seen. In this case, a value of 0.090 μm PV is calculated, proving a much flatter surface.

In Fig. 5.13 two 3D representations of the wavefronts can be seen. In 5.13a we see the uncorrected wavefront assumes an irregular 'saddle' shape, with limits between 1.86 μm

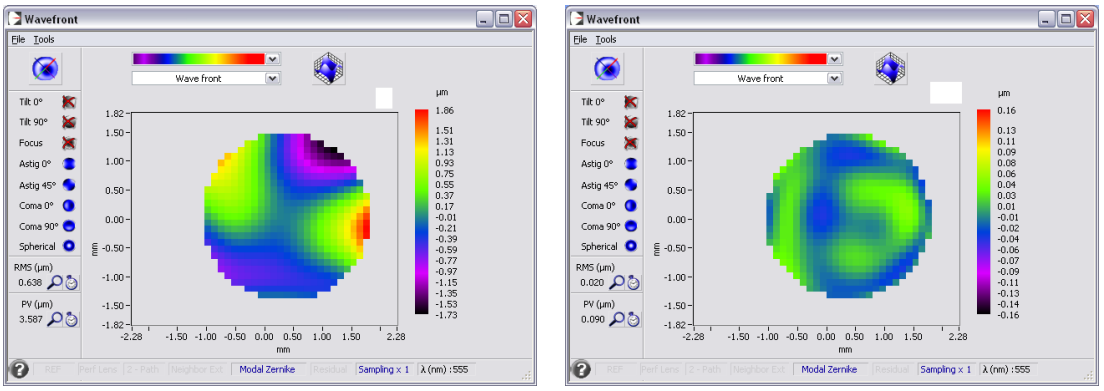

(A) Prior to correction. (B) After correction.

FIGURE 5.12: Wavefront error calculated from spot pattern pre- and post-correction.

and -1.73 μm. The corrected wavefront displays a much flatter surface in figure 5.13b, with the lower limits of ± 0.016 μm.

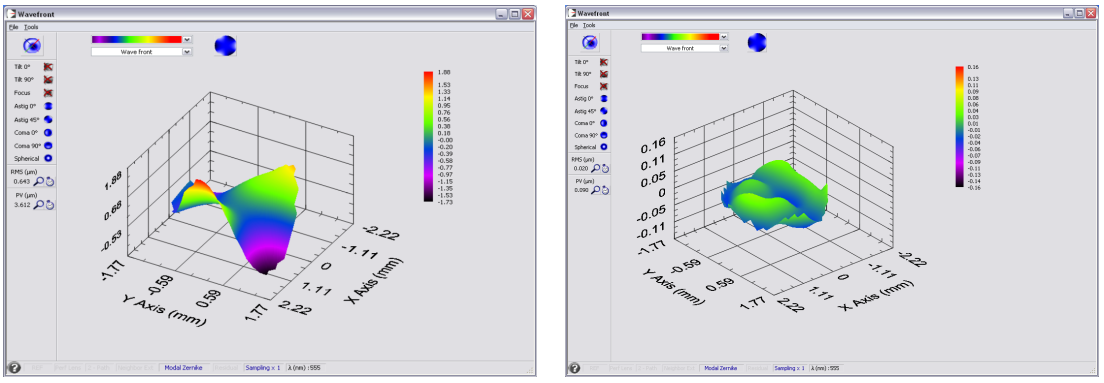

(A) Prior to correction. (B) After correction.

FIGURE 5.13: 3D Wavefront error calculated from spot pattern pre- and post-correction.

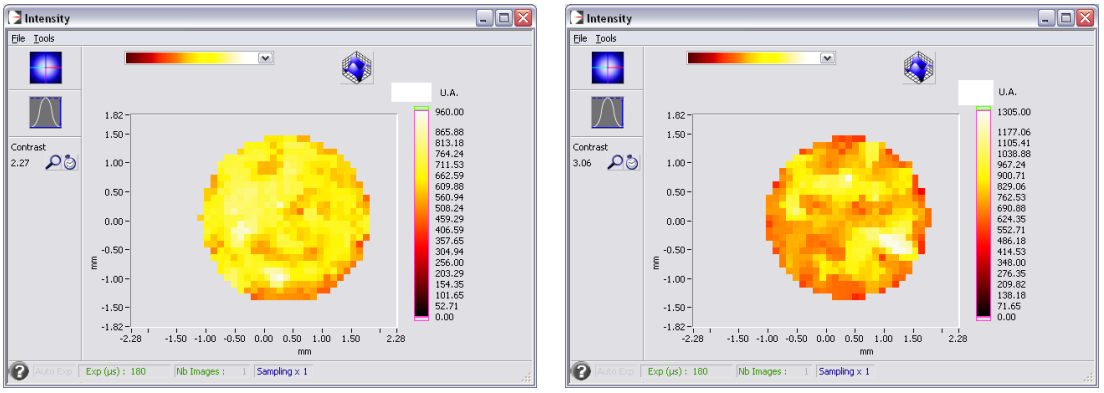

(A) Prior to correction. (B) After correction.

FIGURE 5.14: Pixel intensity distribution pre- and post-correction.

From the spot pattern comparison in Fig. 5.11 a variance in intensity can be noted between the pre- and post-correction states. Further analysis quantifies this difference,

as displayed in figure 5.14. It can be seen that the maximum pixel intensity on the WFS has increased to 1305 AU (arbitrary units) (Fig. 5.14b) from 960 AU (Fig. 5.14a), an increase of 36%. It is also shown how the contrast (as a determination of spot intensity versus background noise) has increased from 2.27 to 3.06 after correction. Worth noting are the regions of low power (coloured deep red) that are predominantly on the edges of the spot, with the yellow and white ('hot') regions of high intensity centralised post-correction. This indicates that the AO loop performs some beam shaping that affects the intensity distribution.

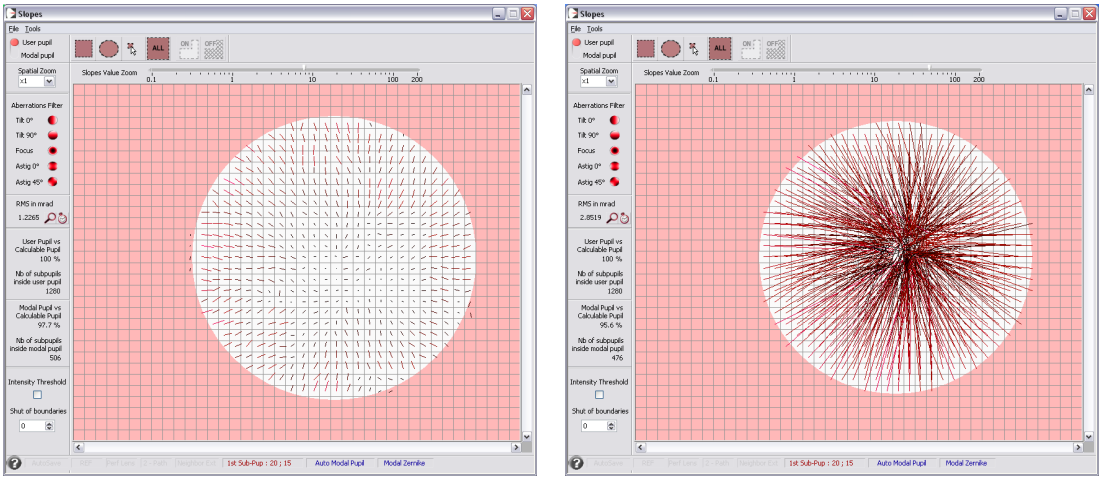

(A) Prior to correction. (B) After correction.

FIGURE 5.15: Calculated slopes post-correction. Image 5.15b shows the slopes extended to emphasize the shape of the wavefront.

Fig. 5.15a shows the slopes (visualised as short lines in the pupil) after closed loop correction. Fig. 5.15b shows the same slopes, with the lines extended for clearer visualisation. It can be seen that the focus is mostly centralised after correction.

	Uncorrected	Corrected
Chief ray		
X tilt (mrad)	0.283	0.244
Y tilt (mrad)	-0.010	0.305
Curvature (m^{-1})	-0.140	-2.777
Focal point position		
Radius (m)	-7.156	-0.360
X position (mm)	0.1539	0.4662
Y position (mm)	0.3036	0.1693
Astigmatism		
Astigmatism angle (°)	61.5	64.0
Sagittal focal length (mm)	1186.096	-364.099
Tangential focal length (mm)	-890.806	-356.197

TABLE 5.1: Beam parameters for the chief ray pre- and post-correction as measured by the WFS.

5.3.2 Experimental analysis of transversal resolution

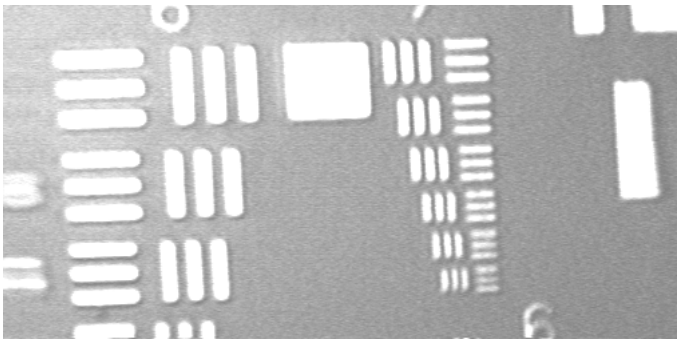

FIGURE 5.16: Confocal image of USAF target displaying the smallest bars 2 μm apart.

To determine practical lateral imaging resolution a USAF target is placed as an object. The target is a glass slide with a number of reflective bars of varying sizes, organised into groups. The smallest set of bars are placed 2 μm apart. As the gap between the bars in Fig. 5.16 is clearly distinguishable, we can assume that the transversal resolution is approximately 2 μm in air.

5.3.3 Microscopy of thumb and skin *in-vivo*

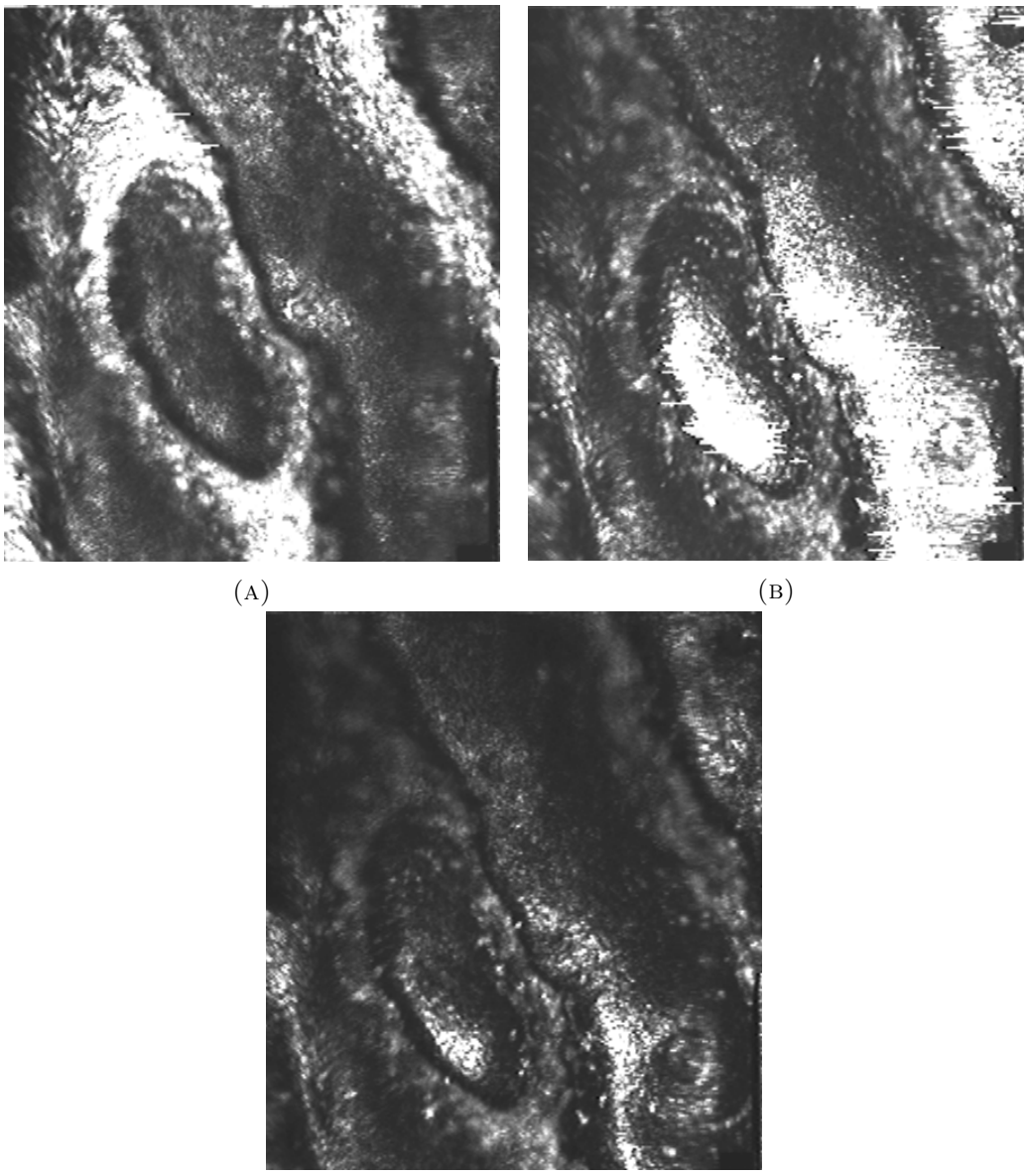

(A) (B)

(C)

FIGURE 5.17: Images of the thumb acquired using a 25 mm lens as the objective. The DM was used to shift the focus to three different depths during imaging. Image size is 1 mm by 1 mm.

Fig. 5.17 shows three *en-face* images acquired from the flesh of the thumb *in-vivo*. Clearly seen in each image are the striations of the surface of the skin. During live imaging, the DM was manipulated to shift the focus to different depths, over a total range of approximately 0.5 mm. This can be observed in the figure as the region of highest intensity changes with depth.

Fig. 5.18 shows a similar confocal image acquired from the skin on the arm. The structure of the skin can be seen in the image, in addition to two hairs.

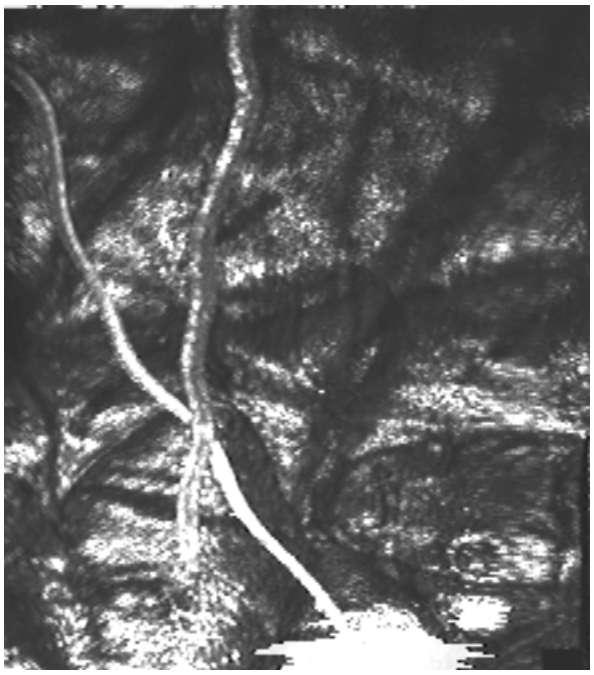

FIGURE 5.18: Image of the skin showing the stratum corneum and hair. Image size is 1 mm by 1 mm.

5.3.4 *In-vivo* human eye imaging

Images acquired from a volunteer's eye are shown in this section. Ethical approval for imaging was acquired from the Faculty Support Office ethics committee for the period 01/06/2013 to 31/05/2015. For a scanning beam, total permissible power to the eye at 830 nm wavelength is less than 700 μW.

Presented are images of the areas of the retina of the right eye proximal to the fovea, exhibiting a high density of photoreceptors. Results are grouped according to practical image size. Fig. 5.19 shows images taken with the widest field of view allowed by the setup, with 1.5V applied to scanners. Figures 5.20, 5.22 and 5.24 show images taken with progressively smaller fields of view: 1.0V, 0.5V and 0.25V respectively. An additional group of images acquired at 1.0V is shown in figure 5.21, displaying areas of the retina with lower photoreceptor density.

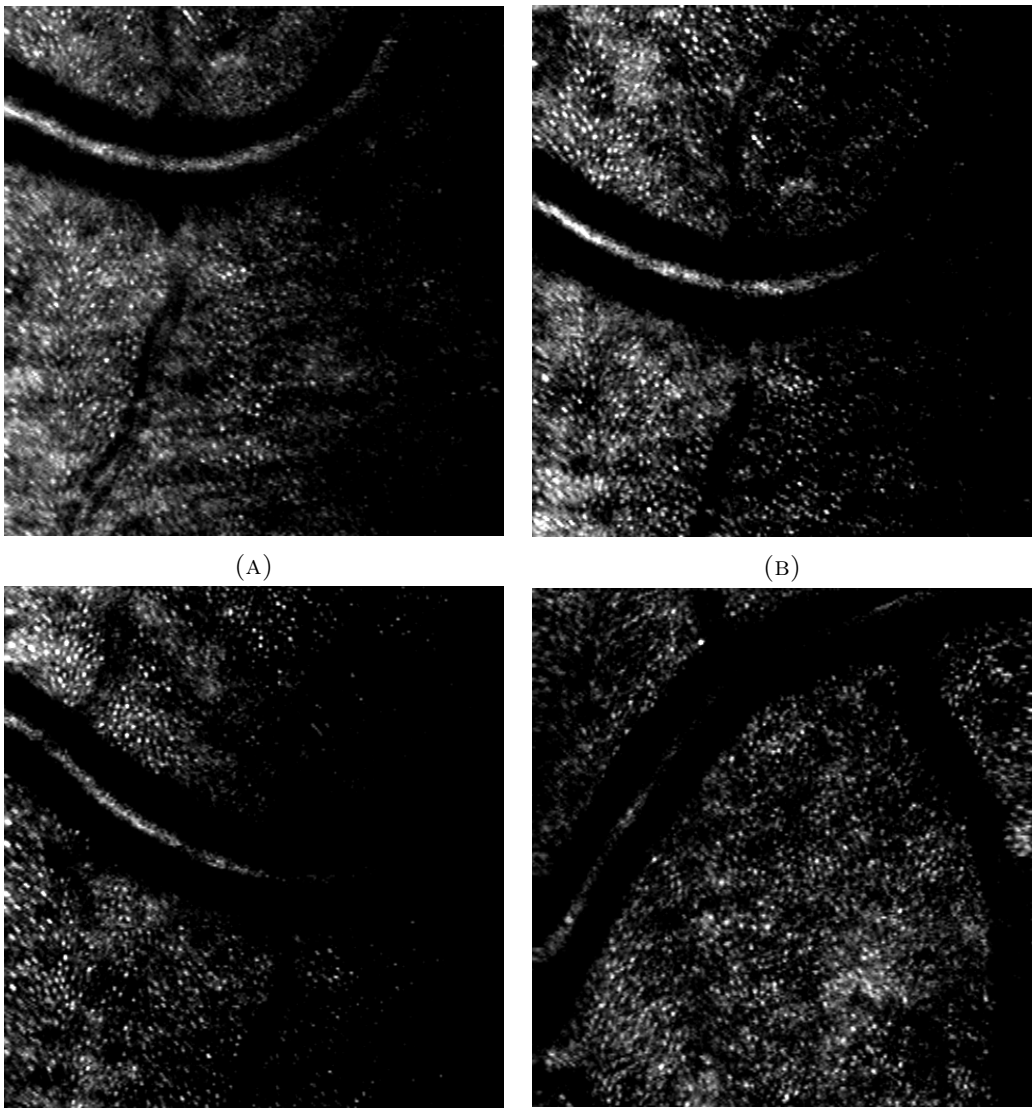

(A) (B) (C) (D)

FIGURE 5.19: Images of retina acquired from human eye *in-vivo* with 1.5 V to scanners. Image size is 1 mm by 1 mm.

The images shown in this first group have been acquired at the widest field of view of 1.5 V to scanners (larger voltage is prevented by clipping of the beam by different mounts in the interface optics). In practice, this is an area of approximately 1 mm x 1 mm. Each image shows a high density of photoreceptors, identified by the distinctive round shape and brightness in contrast with surrounding retinal tissues.

Images 5.19a to 5.19c are taken of the same area, slightly translated vertically. Easily identifiable is a large blood vessel running horizontally across the image, here shown as a thick black band. In the centre of the band is the flowing blood, shown by the thin white stripe. Figure 5.19b shows the large blood vessel with two other smaller vessels intersecting it vertically in the centre.

Note that the first three images show a drop in image intensity in the right side. This is presumed to be a result of increased wavefront aberration causing noise in the image, lowering the contrast. Aberrations may have been due to the curvature of the retina at this point, or some other factor with the eye. The final image in this group (fig 5.19d) shows practically uniform intensity across the frame.

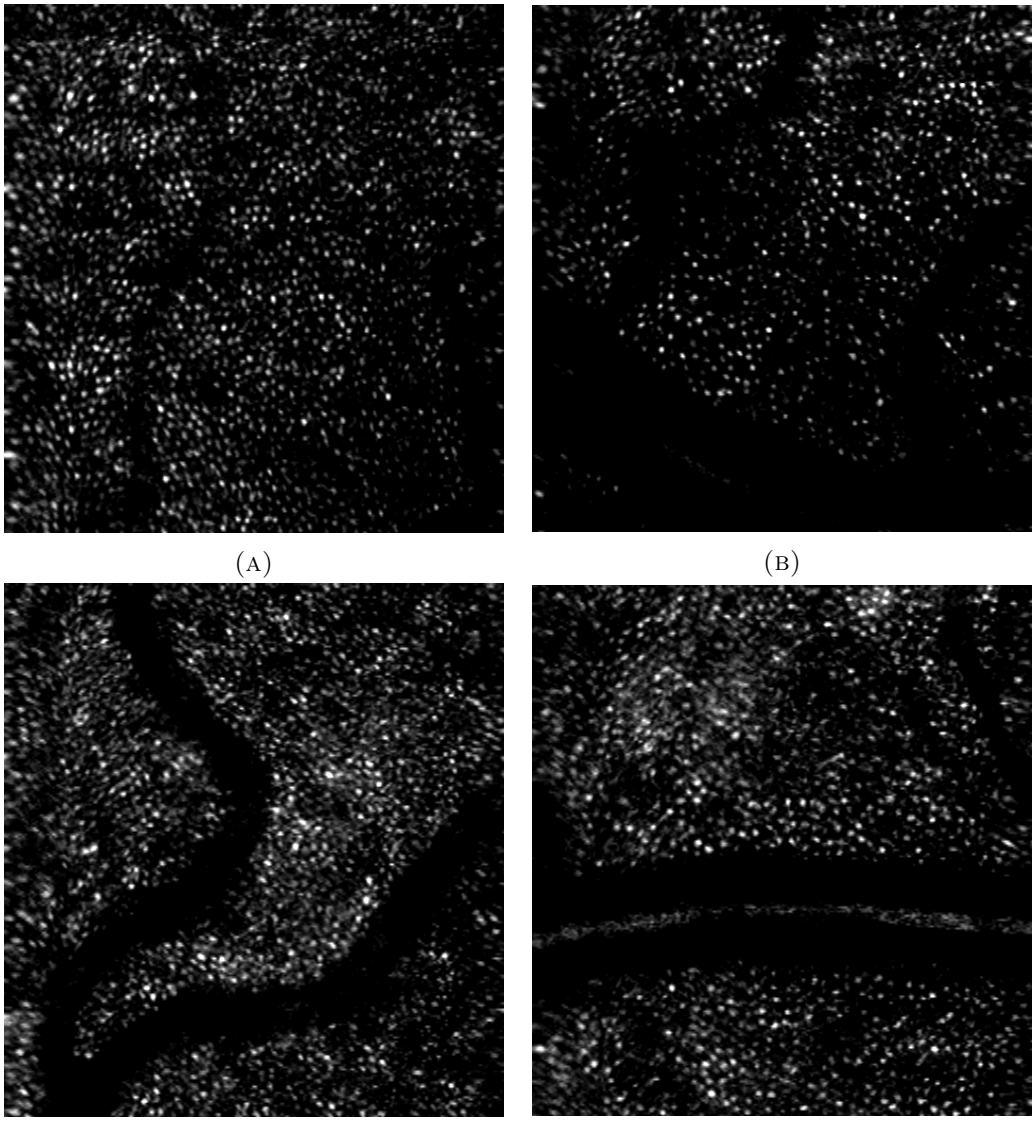

(A) (B) (C) (D)

FIGURE 5.20: Images of retina acquired from human eye *in-vivo* with 1.0 V to scanners. Image size is 700 μm by 700 μm.

The second group of images are zoomed in, 1.0 V applied to both scanners producing a practical image size of 700 μm x 700 μm. Fig. 5.20a shows a regular array of photoreceptors on the retina, with a small blood vessel running vertically. Fig. 5.20b shows a dense set of photoreceptors on the periphery of a large blood vessel in the bottom left corner, and 5.20c displays an 'island' of photoreceptors bordered by a forked vessel. The

final image (Fig. 5.20d) is a closer look at the area surrounding the thick horizontal blood vessel shown in 5.19.

Whilst maintaining the same 700 μm x 700 μm image size as 5.21, the volunteer was asked to tilt the eye such that the imaging beam falls upon an area of the retina less populated by photoreceptors. Figures 5.21a and 5.21b show a dense population of photoreceptors. Less are seen in 5.21c and 5.21d as the the eye is tilted temporarily. Once the beam is positioned near the optic nerve, few photoreceptors can be seen (fig 5.21e, with large blood vessels dominating the image (Fig. 5.21f).

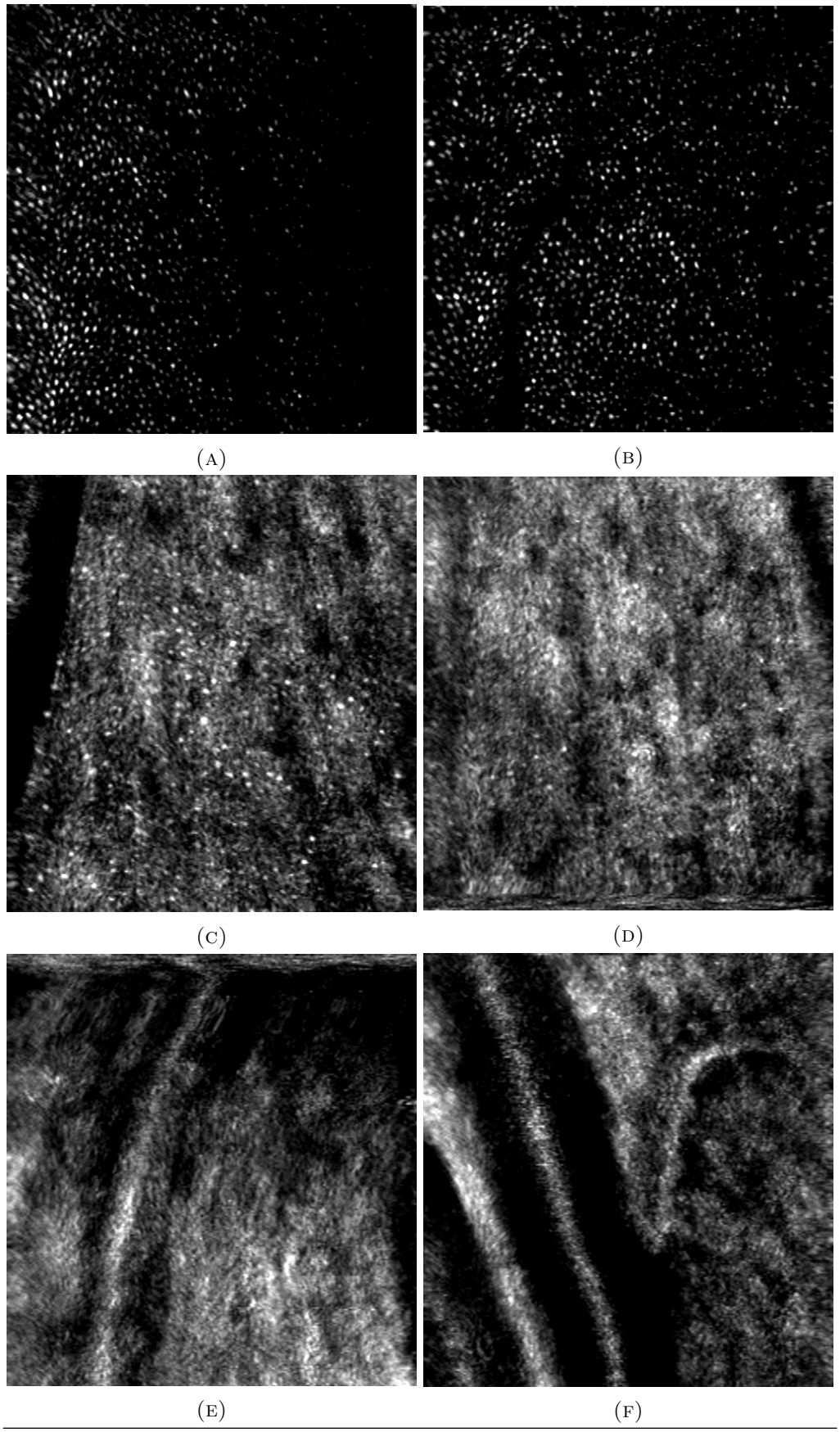

FIGURE 5.21: Images of retina acquired from human eye *in-vivo* with 1.0 V to scanners. Image size is 700 μm by 700 μm.

Images in Fig. 5.22 are taken with 0.5 V applied to scanners, covering an area of 350 μm x 350 μm. Figures 5.22a to 5.22d show zoomed images of photoreceptors in densely populated areas. The final two images (fig 5.22e and 5.22f) show the reduction in photoreceptor count as the eye is turned.

Fig. 5.23 shows an intensity profile taken from a vertical line running down the centre of Fig. 5.22a. This figure shows the regularity and intensity of points in the image that are recognised to be photoreceptors. The sharp contrast and high intensity of each peak clearly identifies these spots as image features and not random noise. In addition, comparing these images to those found in literature can further improve confidence that these are indeed photoreceptors [149].

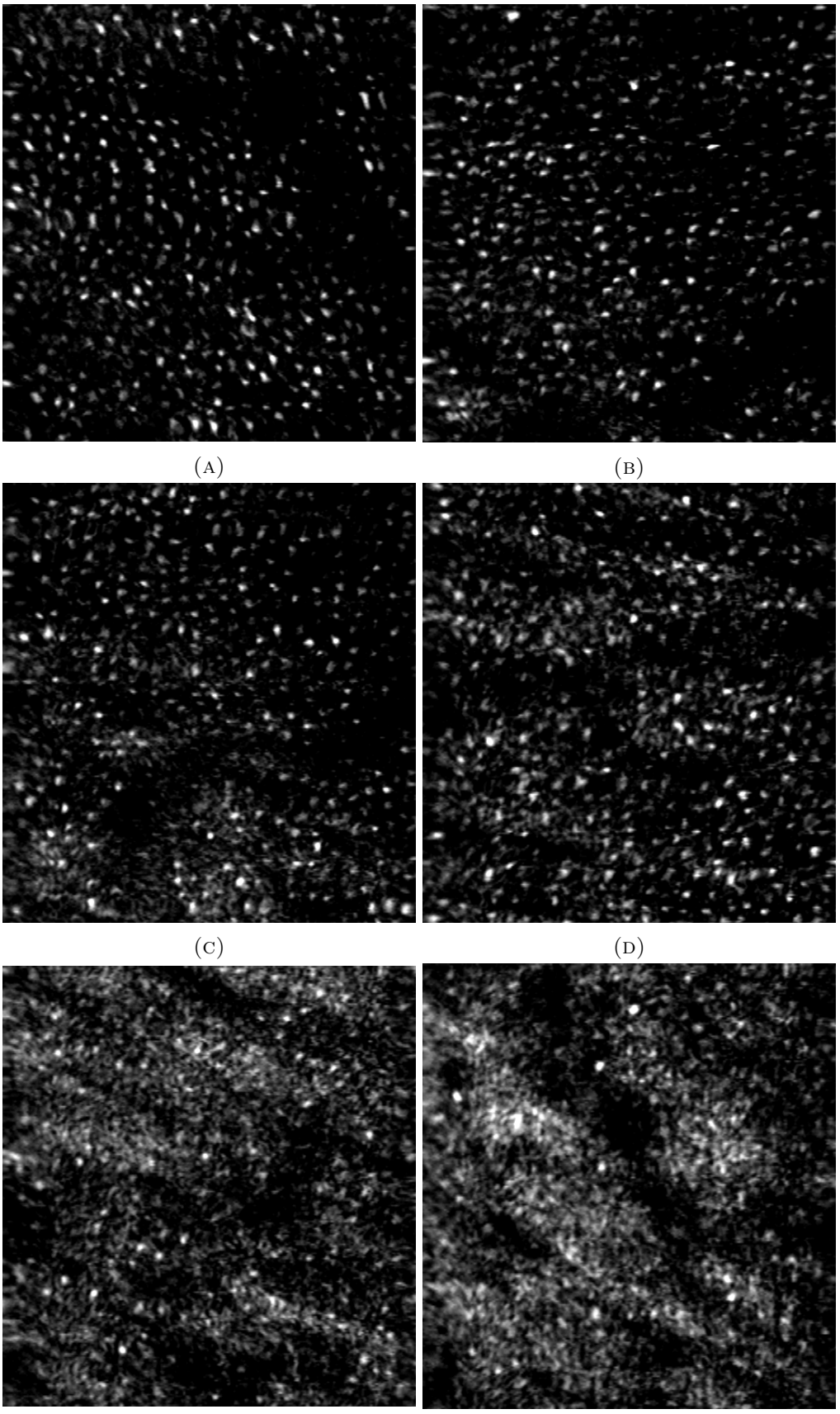

FIGURE 5.22: Images of retina acquired from human eye *in-vivo* with 0.5 V to scanners. Image size is 350 μm by 350 μm.

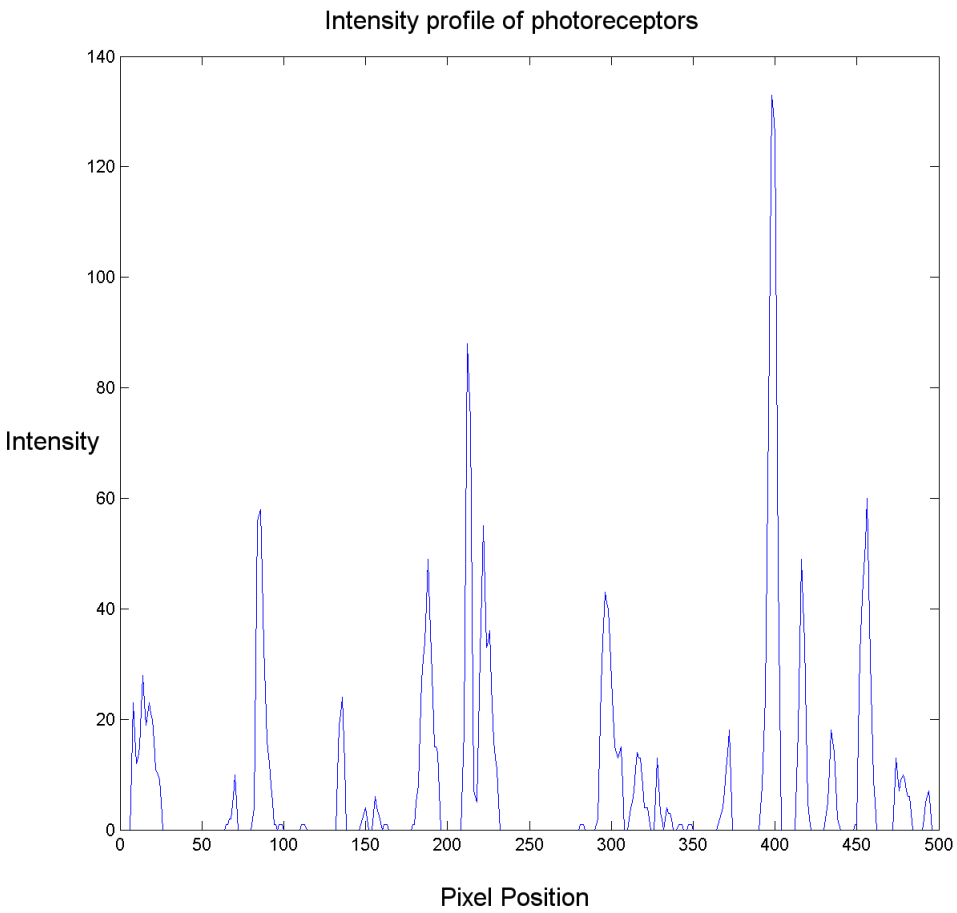

FIGURE 5.23: Image showing intensity profile taken from Fig. 5.22a running vertically down the centre of the image.

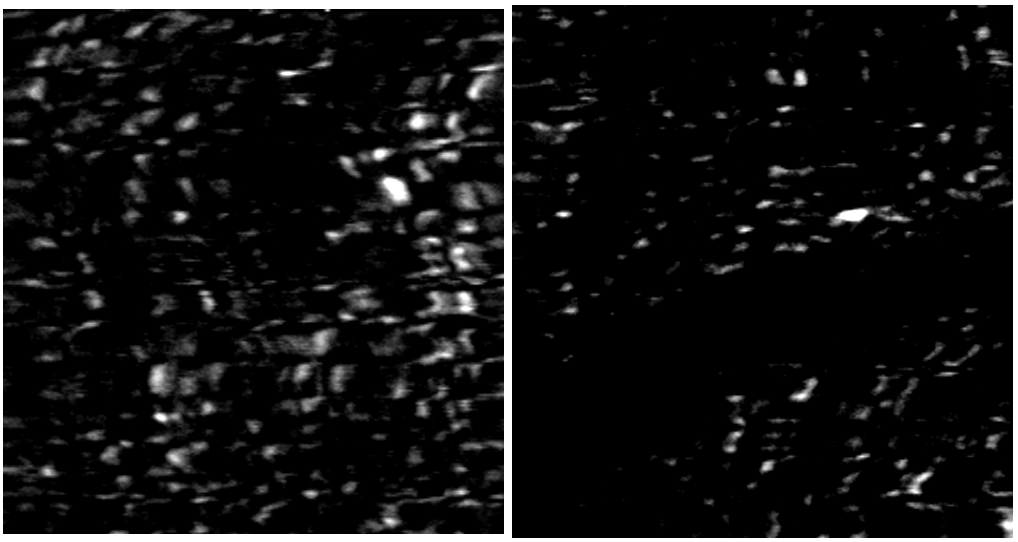

(A) (B)

FIGURE 5.24: Images of retina acquired from human eye *in-vivo* with 0.25 V to scanners. Image size is 175 μm by 175 μm.

The final set of images are acquired with 0.25 V to scanners, with a practical area of 175 μm x 175 μm. Though the photoreceptors can still be seen, they are heavily distorted due to the motion artefacts that are much more pronounced with such a small image size. With the addition of a tracker and some processing, it might be possible to reduce the distortion.

5.4 Conclusions

The primary goal of this project was to produce an imaging system capable of high lateral resolution and real-time imaging of biological tissues. Research proved how intelligent optical design may reduce system-induced aberrations through careful selection and arrangement of each individual element, with a consideration for reversing off-axis reflections.

It is made clear through the implementation of the final system that the organisation of telescopes into non-planar configuration provides a substantial benefit in keeping aberrations low when compared with the legacy design. Simplification of the interface optics is key, as each additional element may introduce a larger margin for error.

Though not a primary concern for this project, it is worth mentioning that the loss of power to the object in transmission has been significantly reduced in the new configuration. The efficiency of power transmission has more than doubled (increase from 18.9% to 39.69% round trip) due to the reduction in optical elements (beamsplitters, curved

mirrors) and thanks in no small part to the larger galvoscanners. Transmission of light in one direction is relatively simple, however the return of heavily aberrated light from the object to the detector may prove problematic. The new configuration certainly increased the tolerance for this aberration, allowing for more light to be captured returning from the object.

Sufficient resolution was achieved to make possible the imaging of photoreceptors in the living non-dilated human eye (transversal resolution of 2 μm established using a USAF target). The FWHM of the confocal profile was measured to be 40 μm, using a mirror as an object. Guidance of the volunteer's eye was achieved through an audio feedback system whereby the signal from the detector was rendered into sound and played through a loudspeaker. It was found that this feedback was greatly beneficial during live imaging as it offered the volunteer feedback as to the effective orientation of their eye to the imaging beam.

Though the system was configured to work with an objective lens up to 7.5 mm in diameter, in actuality it was much lower; without a dilating agent the images in 5.3.4 were acquired with a pupil size between 2 mm and 4 mm. Additionally, there was no fixation or tracker device implemented in the design to assist with the movement of the eye. The capability of the system to acquire clear images of photoreceptors and other features despite these drawbacks represents a significant achievement of the AO.

5.5 Evaluation

Experimentation with the AO system yielded positive results, but also exhibited limitations. A major issue with AO is the long optical path lengths that are a consequence of the telescopes used to resize the beam. Though it is possible to select more powerful mirrors with short focal lengths, this can have a dramatic detrimental effect upon the wavefront due to the off-axis reflections.

In the new system, the object path measured approximately 13.5 metres in length (from launcher to object and back to detector). This length can be problematic as it has a serious effect on system stability. The mounts used in the experimental system often required daily attention as the screws loosen, with even the slightest movement causing a dramatic loss of signal to the detector. Every day the system required a small amount of calibration to ensure the components are adjusted correctly for maximum performance.

Long path lengths can cause engineering problems when attempting to design a system for clinical use. Construction of a commercial AO eye-imaging machine would be a difficult exercise in attempting to reduce its overall footprint. Furthermore, the clinicians

should not be expected to perform manual calibration of components within the device. This could potentially raise the cost of these devices to medical clinics if a maintenance contract is required.

As mentioned in the conclusions, there are several additions that could greatly benefit the performance of the system. Possibly the single greatest improvement in image quality could be achieved through chemical dilation of the human eye to reach a higher NA. Images were acquired with an estimated pupil diameter of 3 mm, though the system performs optimally with a lens diameter of 7.5 mm. Due to time constraints, it was not possible to acquire ethical approval for the use of Tropicamide to dilate the volunteer's eye. This procedure is common clinically, and as mentioned in 5.4 would provide a noticeable increase in image quality.

Though a chin rest was used during experimentation, it was found that there was still a great degree of movement for the volunteer's head during eye imaging. A more restrictive chin rest/bite bar would be desirable, with controls for fine adjustment of the head.

When acquiring images from the human eye, the volunteer was asked to fixate on certain positions in the room or on an illuminated fixation target. This procedure somewhat reduced the tendency for the eye to drift laterally during imaging, but can be further improved. The main problem was the eye's inclination to focus on the fixation itself, causing the imaging beam to be defocussed upon the retina, resulting in lowered signal intensity. The fixation, as implemented, was still insufficient to stabilise the eye for imaging at the smallest size 170 μm^2.

Modern eye imaging systems are equipped with a tracking system that identifies structures or patterns in the object, and works to stabilise them in the image. With the previously mentioned improvements a volunteer should be able to reduce the major motions of the head and eye that cause image distortion. The tracker would then be able to handle the finer motions of the eye (microsaccade) by fixating upon a feature on the retina and using galvoscanners to make a series of fast, small adjustments to the imaging beam to compensate for movement. There has been some research in the field to perform this action as post-acquisition image processing, which may further reduce the motion artefacts [44].

Chapter 6

Swept source optical coherence tomography Gabor fusion splicing technique for microscopy of thick samples using a deformable mirror

6.1 Preface

This chapter has been adapted from a publication to Journal of Biomedical Optics [150]. In this chapter, we present a swept source optical coherence tomography (OCT) system at 1060 nm equipped with a wavefront sensor at 830 nm and a deformable mirror in a closed loop adaptive optics (AO) system. Due to the AO correction, the confocal profile of the interface optics becomes narrower than the OCT axial range, restricting the part of the B-scan (cross-section) with good contrast. By actuating on the deformable mirror, the depth of the focus is axially scanned and the system is used to demonstrate Gabor filtering in order to produce B-scan OCT images with enhanced sensitivity throughout the axial range from a *Drosophila* larvae. The focus adjustment is achieved by manipulating the curvature of the deformable mirror between two user-defined limits. Particularities of controlling the focus for Gabor filtering using the deformable mirror are presented.

6.2 Introduction

Adaptive optics (AO) [151] have been used to great effect in astronomy, eye imaging [149] and confocal microscopy (CM) systems by exploiting the capability to reduce system- and sample-induced optical aberrations to enhance resolution [152]. Adding AO to an OCT set-up enables further reduction of the voxel size of the imaging system, producing a much smaller 3D volume per voxel due to enhanced transversal resolution, in addition to axial [153, 154]. Additionally, swept source OCT (SS-OCT) can provide exceptional imaging speeds due to the rate at which the wavelength can be tuned [54, 155]. The combination of these technologies have produced fast imaging systems capable of high resolution, ideally suited for traditionally difficult clinical applications such as ophthalmology [156].

6.2.1 Problems presented with AO/SS-OCT

There is a trend in developing long coherence length swept sources that can determine an axial range extending over 1 cm and more [157]. On the other hand, an AO enhanced confocal microscope system can shrink the confocal profile width to values of tens of micrometers or even smaller. As the SS-OCT method presents the disadvantage that the reflectance of all points along the axial range are measured under a fixed focus, maximum sensitivity within the cross-sectional (B-scan) OCT image is achieved in the focus only. If the full width half maximum (FWHM) of the confocal profile, acting as a confocal gate (CG) is smaller than the OCT axial range (AR), then the OCT image presents high contrast and good transversal resolution within a spatially restricted stripe determined by the CG only.

6.2.2 Possible solution

The problem presented is that the region of highest quality (as determined by contrast and resolution) is limited by the width and position of the CG. Efforts have been made to extend the depth of focus (DOF) whilst maintaining high lateral resolution. One approach uses an axicon lens to produce a Bessel beam, extending the DOF when compared with a Gaussian beam. The DOF is enlarged at the expense of lowered sensitivity, making the method less suitable for imaging samples of low reflectance [158, 159] although progress has been made to improve its efficiency[160].

A solution was developed based on Gabor filtering [161] that shifts the CG incrementally through the sample; an OCT cross-sectional image was acquired at 5 different focus

positions (R) as manipulated by an electrical lens. From each of the 5 images, the in-focus region was extracted and then spliced together to form a single image wherein all regions are in focus.

It was determined that 5 repetitions of data acquisition with shifted focus were sufficient as the CG profile was approximately 1/5th of the AR. Due to the enhanced coherence length of swept sources, the ratio R = AR / CG may be much larger than 5, in which case the Gabor procedure may slow the acquisition considerably. This presents a problem as the process is largely manual, with a margin for error increasing as there may be variations in the imaging parameters over time, especially with living samples. The next logical step would be the design of a system that simplifies and expedites this procedure.

6.3 Methodology

As detailed in Fig. 6.1, an AO configuration is presented where a deformable mirror (DM), normally employed by the AO closed loop to correct the wavefront, is also used to shift the focus for Gabor filtering. A DM was already reported as the element for focus control in a time domain OCT (TD-OCT) system [162]. The focus was moved in synchronism with the coherence gate, achieving what is known as dynamic focus [163]. This procedure is not applicable in spectral domain OCT. In addition, in a closed loop AO configuration, attempts of focus control have to be disconnected from the feedback loop operation, which actively works to reduce aberrations (including defocus). In a related report [164], an AO system using a DM combined with spectrometer based OCT was used to control the focus position and shape of the confocal gate by actuating on the spherical aberration introduced by the DM itself. Here we actuate on a different aberration component, defocus, and use such control to implement Gabor filtering as detailed below.

6.3.1 Concept

Given the speed of SS-OCT imaging, which allows frame rates as high as 100 Hz, there is room for sufficient high values of R to still secure video rate, which is important in live imaging systems [165]. R B-scans are acquired where the region of maximum intensity as determined by the CG profile is shifted deeper within the object along the z coordinate. After acquisition, each image obtained in this way may then be cropped to isolate the in-focus regions in depth. The cropped images are subsequently assembled together across R into a single synthesized image of uniform intensity.

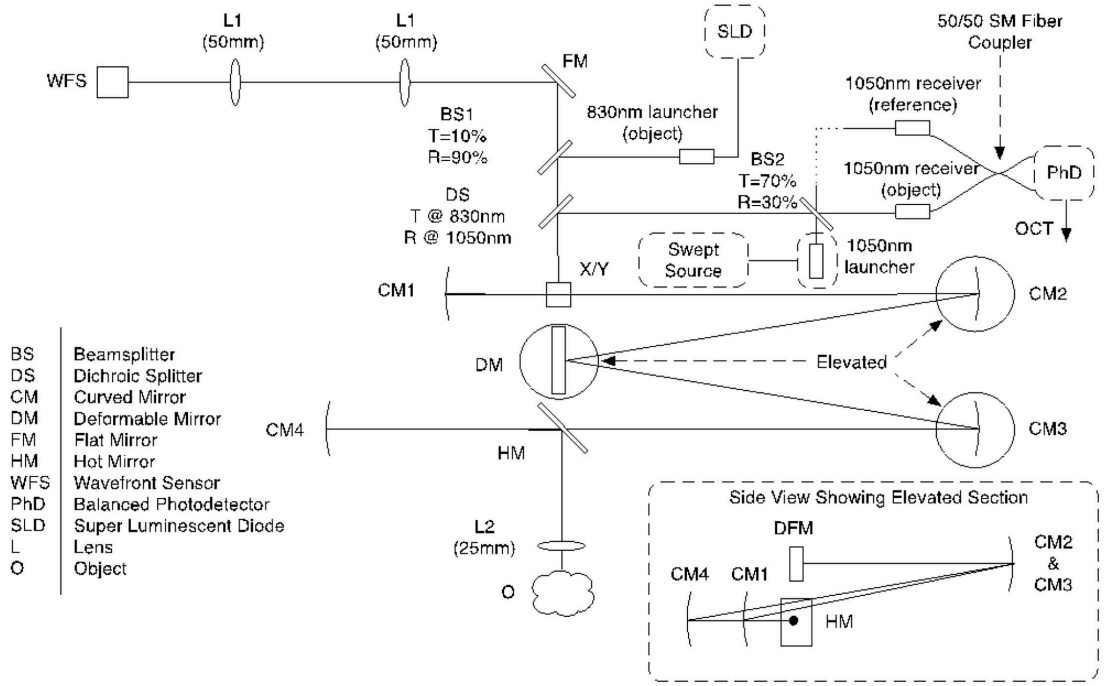

FIGURE 6.1: Schematic of the AO/SS-OCT system with imaging at 1060 nm and wavefront sensing plus confocal microscopy at 830 nm.

The focus control using a DM is achieved by generating a set of corrections by controlling the magnitude of the Zernike polynomial responsible for that of defocus only. Closed loop correction will be conducted to optimize the wavefront, providing a base configuration for the DM. The focus will then be shifted and the closed loop executed again to achieve optimization at the new position. This will provide two states (base state and modified state) from which intermediate positions may be interpolated. In essence, we would have a set of states where the corrections have been optimized for imaging at different axial positions in the sample.

6.3.2 Optical design for minimizing system-induced aberrations

This implementation of DM control utilizes a system of passive and active aberration correction to improve image quality. Passive correction is achieved through an optimized system wherein the number of optical elements (specifically the curved mirrors required to resize the beam, known for inducing aberrations) has been minimized. Collimators (Schafter & Kirchhoff: FC-F-4-M15-37) launch beams of 3 mm diameter.

By using the two galvoscanners, X and Y (5 mm), close to each other, the number of curved mirrors is reduced. Two telescopes (pairs of curved mirrors with different focal lengths) are placed in the setup to increase the beam diameter to 15 mm to fully cover

the reflective surface of a DM (Imagine Optics: Mirao-52e), then to reduce the beam down to 7.5 mm on the final lens (L2) of 25 mm focal length.

Furthermore, these telescopes are arranged in a non-planar configuration with the beam propagating in a single plane, either horizontal or vertical. This is seen in Fig. 6.1 where the beam travels between curved mirrors CM1 and CM2 in the plane Y, with no deviation in X. The beam is then propagated horizontally across the surface of the DM and then vertically to CM4, at the same elevation with CM1. This technique has been shown to compensate for astigmatism aberrations induced by reflections from curved mirrors [145]. We measured sensitivity of the OCT setup to be 100 dB using previously reported techniques [166]. For imaging we use a 100 kHz Axsun swept source with a central wavelength at 1060 nm.

We determine the field of view experimentally by blocking the reference arm (using the confocal signal only) to image a large bar on the USAF resolution target. For this measurement, the DC output of one photodetector from the balanced detector was used. The target is mounted on an XYZ translation stage, allowing movement of the bar to the limits of the displayed image and measurement of the displacement using the micrometer screws. As demonstrated in chapter 5, we determine that for an amplitude of 1 V of driving signals applied to both scanners we achieve a 700 x 700 μm^2 raster size, and with 0.1 V the area is 70 x 70 μm^2.

6.3.3 Active aberration compensation using deformable mirror

Active wavefront correction is achieved using the same 52-actuator MEMS DM (Mirao 52-E, Imagine Optics) described in chapter 5 and appendix A, in conjunction with a Shack-Hartmann sensor (HASO-32, Imagine Optics). Wavefront sensing is performed using light from a 830 nm broadband super luminescent diode (SLD), whose beam path is almost completely shared with the 1060 nm imaging arm. Prior to imaging, using a scattering target such as paper, correction is achieved that brings the DM into an optimal starting configuration where any residual aberrations induced by the optical elements in the system itself are reduced.

With the inclusion of tilts and focus in the wavefront error calculations, we are able to achieve a wavefront RMS value better than 0.02 μm. After a stable correction is achieved, the voltage values applied to the DM are saved into an XML file. This file contains a 1D array of 52 numerical values, each corresponding to a single actuator on the DM. The values of this array represent the voltage settings of the 52 actuators on the DM that achieves the best wavefront correction. This set is considered a base state, i.e. the midpoint of the axial imaging range to be used next.

6.3.4 Shifting the confocal gate

The next stage is to modify the amplitude of a single Zernike polynomial, in this case that of defocus is selected, to a different value. This causes the mirror to adjust its shape to add defocus aberration in addition to its corrected state. With defocus added, the closed loop is executed again to compensate for the possible increase in other aberrations caused by manipulation of the focus. No other types of aberrations are directly added in this way, so it can be assumed that the difference between the original base state and the modified state is the addition of defocus only. Again, the modified state file is a 1D array of 52 values, this time representing the position of every actuator on the DM to form a state with modified focus. This modified state file is also saved alongside the original base state file.

Given that the linearity of the DM is greater than 95% [148], the difference between the base state and the modified state is a linear increase in defocus aberration. Custom software programmed in LabVIEW dynamically interpolates a 2D array of intermediate voltage values for every actuator using these two 1D arrays. The size of the 2D array is R by 52, where R is the number of steps required. Each successive column in this 2D array contains a complete set of 52 actuator voltage values, representing an incremental shift in focus.

This 2D array can be expanded to any size and any range of focus, limited only by the speed and stroke of the DM, respectively. A larger array may impact the rate at which the DM actuates the commands. Increasing the size of the array (number of columns) will adjust the number of incremental steps (R) between two user-defined limits. Shifting the confocal gate by 40 μm in 50 steps covers a 2 mm range as determined experimentally using a mirror as an object and finding the new focus position for the deformed state of the DM.

Adjusting the limits of the array affects the magnitude of defocus aberration applied to the DM, and in this way the AR can be adjusted dynamically while scanning to suit the sample thickness. To produce a smooth focus sweep at a consistent rate, we typically make these limits symmetrical, i.e. between -1 and 1 mm with the midpoint representing zero defocus added. A visible effect on the image is a sweeping region of high intensity through the depth range of the sample.

6.3.5 Analysis of the confocal profile and signal strength during focus sweep

It is important to determine how the confocal profile is affected as we shift the focus through the sample. To test the imaging performance we set the DM to assume the base state corrected configuration. During the measurement we set the AO to run in open loop, i.e. the corrections are maintained without feedback from the WFS. In this mode we may still directly manipulate the mirror to add defocus.

A mirror is mounted on a XYZ translation stage and placed as the object in the imaging arm. We block the reference arm and use the confocal signal (with weak light emitted from the SLD to avoid saturating the detector) to determine the confocal profile of the system at this default state. The DM is then set to add different values of defocus in increments of 1 μm RMS. For each new focus adjustment, the translation stage with the mirror was moved around the focussed position and the strength of the confocal signal was measured to construct the confocal gate profile.

Confocal profiles for three focus adjustments are shown in Fig. 6.2. From the graphs we can ascertain two critical facts about the focus sweep. Firstly, it is clear that the image intensity drops as the DM introduces more defocus.

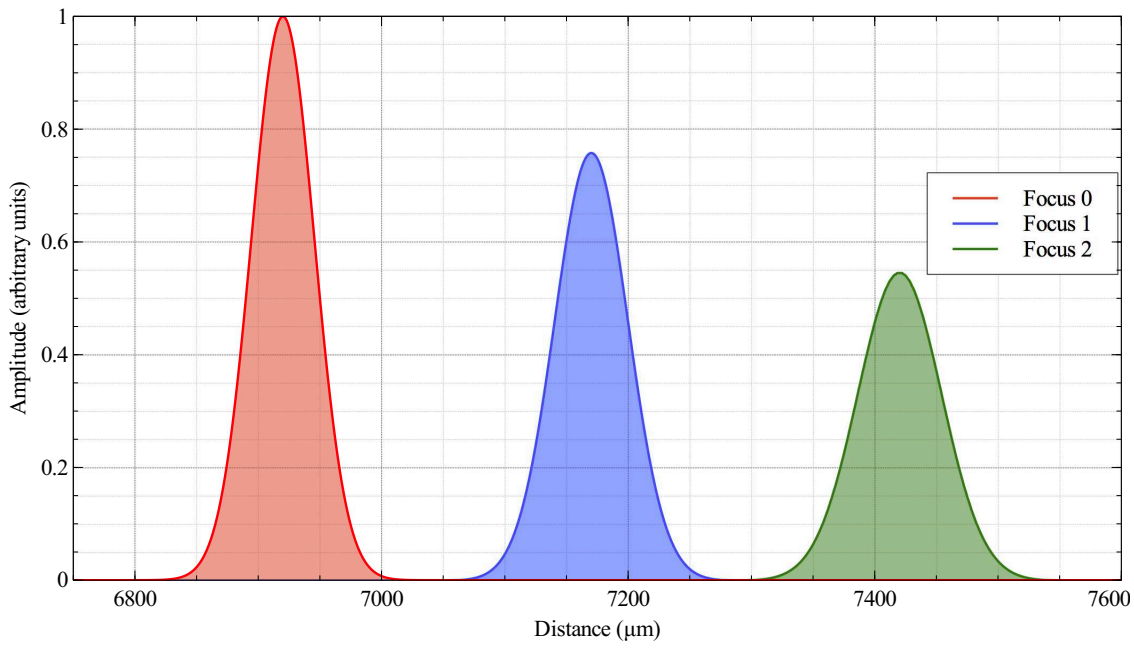

FIGURE 6.2: Chart showing how the confocal profile shifts in depth and changes shape as we add 1 and 2 μm RMS focus.

Secondly, it is important to note that the width of the profile increases with defocus. We start with a FWHM of 60 μm in the base state, which first spreads to a FWHM 70

μm as defocus aberration is increased to 1 μm RMS, then spreads further to FWHM 80 μm with 2 μm RMS defocus. The defocus aberration can also be characterised in terms of W_{20} as a value of 6.08125, 6.25625 and 6.51875 for the first, second and third profiles respectively. The enlargement of the confocal profile and reduction of its maximum with the defocus applied suggests deterioration of the correction. Naturally this would decrease the depth resolution of the confocal microscope (the object arm), though this is not a concern with OCT imaging.

The sensitivity decay with defocus is quantified for larger defocus values in Fig. 6.3. In this case, for each defocus value applied by the DM, the object mirror was moved back into focus using the translation stage and the strength of the confocal signal was measured. There appears to be a sharp drop as the focus first moves from base state, then recorded intensity decreases below 50% for $\pm$ 3 μm RMS defocus, reaching 10% for $\pm$ 8 μm RMS defocus. The power profile is shown as symmetric around base state when adding positive or negative focus.

The chart in Fig. 6.3 can be used to select a useful range to operate the DM where the sensitivity loss can be tolerated for a given imaging object. This sensitivity loss is a limitation of this technique, not observed with other methods of focus control such as using an electrical lens.

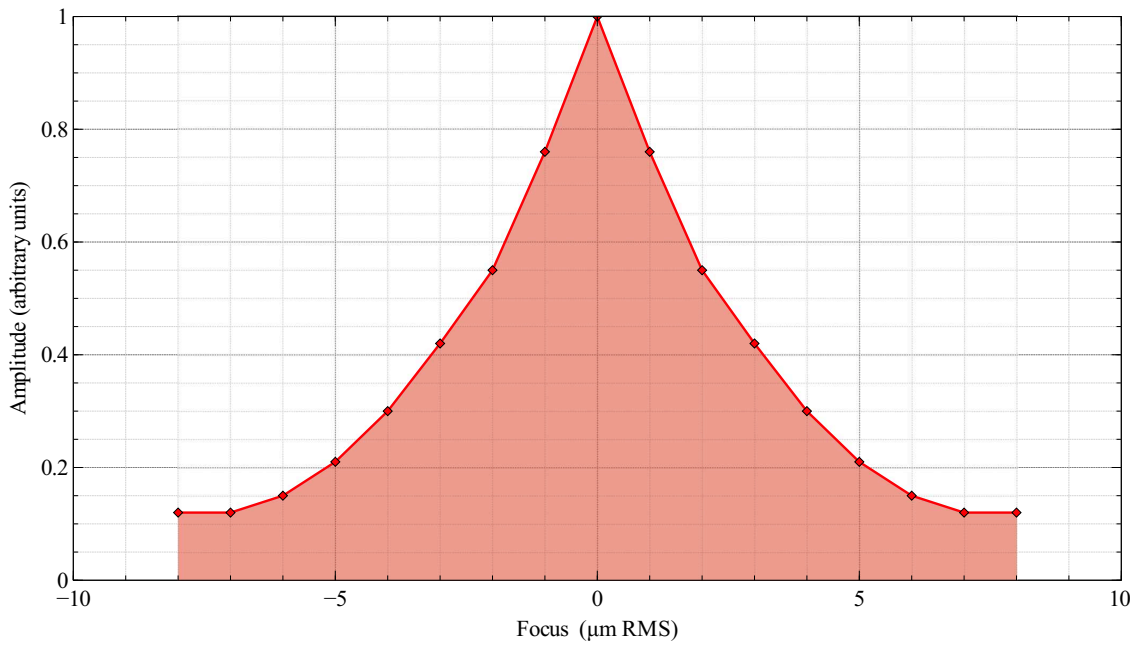

FIGURE 6.3: Chart showing decay in signal intensity with added focus

From the data shown in Fig. 6.2, it is clear that applying 1 μm RMS defocus equates to an axial shift of the focus by 250 μm, therefore a sweep between -2 μm RMS and 2 μm RMS would offer a 1 mm axial imaging range.

6.3.6 Assessment of the transversal resolution

To test practical image resolution, an image is acquired of a USAF 1951 target, as shown in Fig. 6.4. We know from the data shown in section 6.3.2 that for driving signals of 0.1 V amplitude applied to both scanners we achieve a scan area of 70 x 70 μm^2 on the sample. Given an image size of 250 x 250 pixels, it can be deduced that each pixel covers 0.28 μm along horizontal and vertical directions.

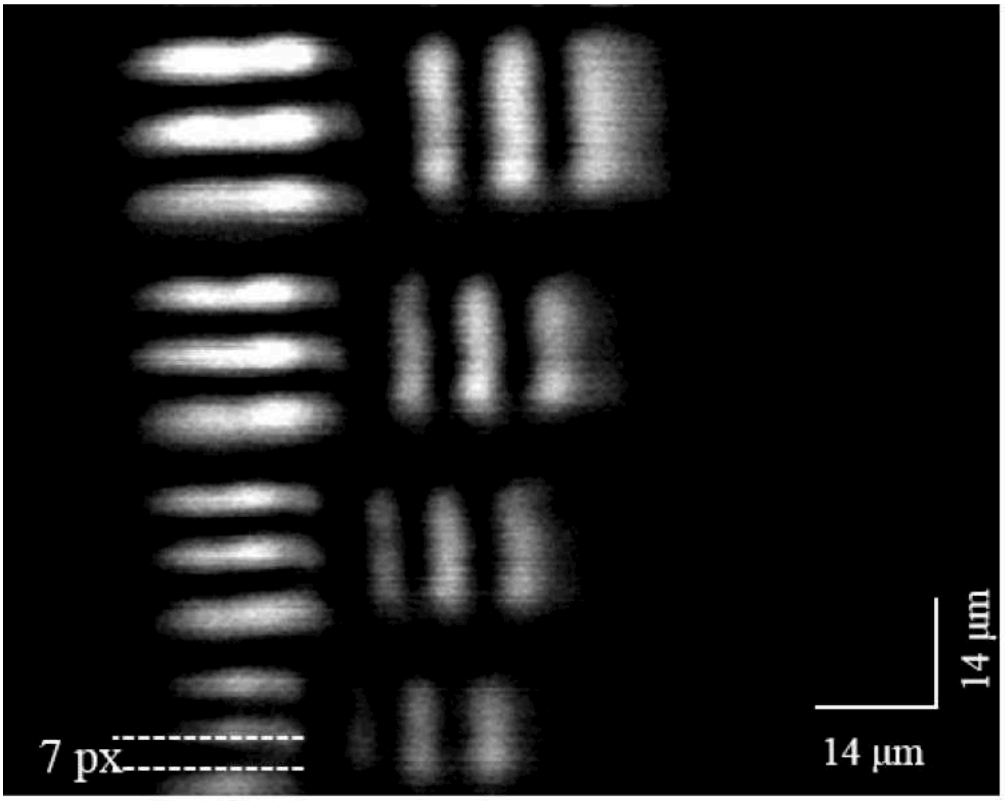

FIGURE 6.4: High contrast confocal image of the USAF target showing the smallest 2 μm bars at the bottom. Two sets of three bars are shown oriented horizontally and vertically. Image size is 250 x 250 pixels covering an actual area of 70 x 70 μm^2 on the target.

Fig. 6.4 shows an image of the USAF target where two sets of three bars (each ~2 μm apart) are shown distributed both vertically and horizontally. Given the parameters described above, we may analyze the distance between the bars in pixels to determine the actual spacing in μm. Both the horizontal and vertical bars are shown to be 7 pixels apart: 7 * 0.32 = 1.96 μm apart. This confirms our reported transversal resolution values.

To determine how lateral resolution is affected when axially shifting the CG, the USAF 1951 resolution target is used as the object and images are acquired for different defocus values. Initially we assume the base state with no defocus, and position the object such

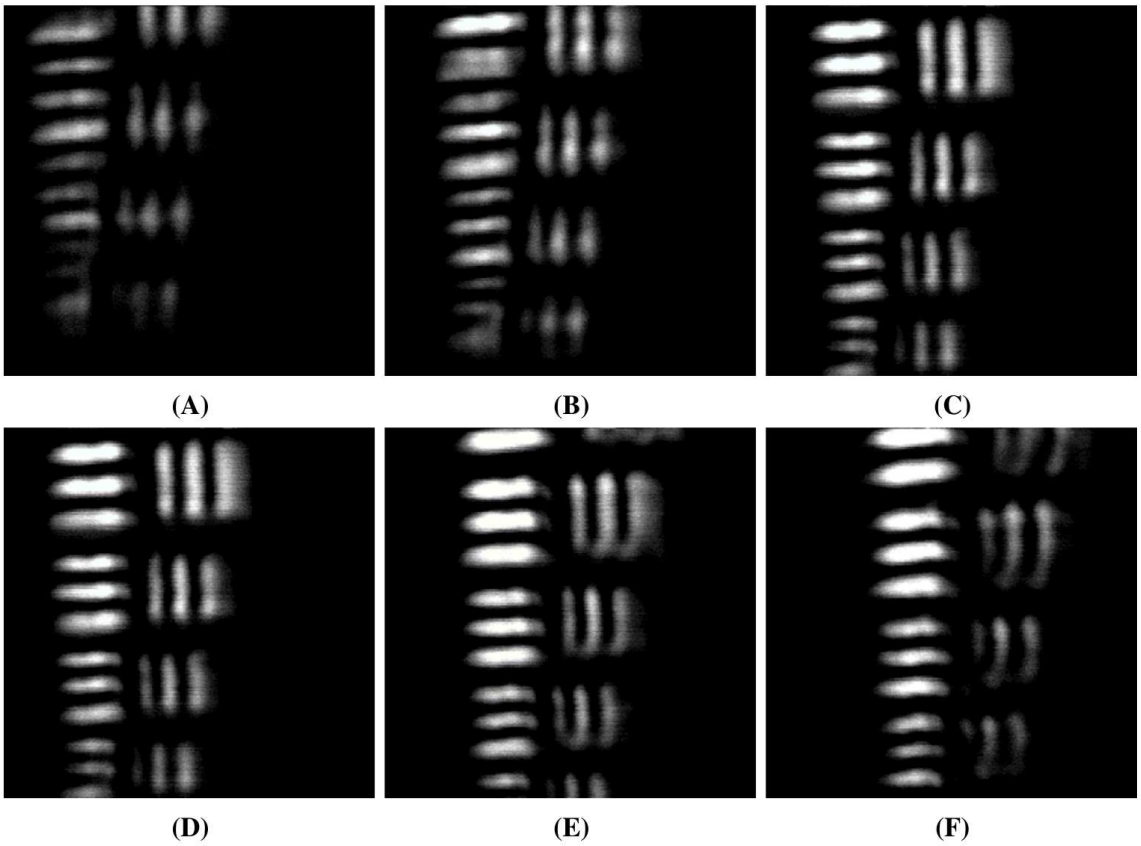

FIGURE 6.5: Effect of defocus on the image acquired from the USAF target, using the same area as in Fig. 4. The original image (C) is repeated in (D) and placed alongside images taken with -2 (A), -1 (B), 1 (E) and 2 (F) μm RMS focus added to the DM.

that the set containing the smallest bars (of 2 μm spacing) are within the centre of the frame. Fig. 6.5 shows four additional images taken of the same region of the target, with different levels of defocus applied to the DM. Each time defocus is applied to the DM, the USAF target is manually moved axially back into focus before acquiring the image. The distance between the bars in the images obtained with focus -1, focus 1 and focus 2 (focus moved at -250 μm, +250 μm and +500 μm respectively) are the same as in the image at focus 0. There appears to be a loss in signal intensity in the image acquired with focus -2 (-500 μm), which is not apparent in the others, but the transversal resolution seems intact.

Some lateral drift is also identified, seen by the bars moving across the image as the focus is changed. From 6.5C to 6.5B, the bars moved up by 7 pixels and from 6.5B to 6.5A by further 7 pixels. The same, from 6.5D to 6.5E, the bars moved down by 7 pixels, and from 6.5E to 6.5F, by further 7 pixels. 7 pixels vertical shift means 2 μm, i.e. comparable and larger than the transversal resolution. In terms of horizontal shift of the image, from 6.5C to 6.5B there is a slight shift of 1 pixel, while from 6.5B to 6.5A

of 7 pixels to the left. From 6.5D to 6.5E, there is a lateral shift to the right of 7 pixels and from 6.5E to 6.5F an additional 7 pixels to the right.

The experiments reported in section 6.3.5 show that the variation of focus imprinted by the DM when obtaining the images in Fig. 6.5 covers a 1 mm axial range. Using the same process described above, the effect of applying larger defocus values to the DM is evaluated by the resolution in the images acquired, shown in Fig. 6.6.

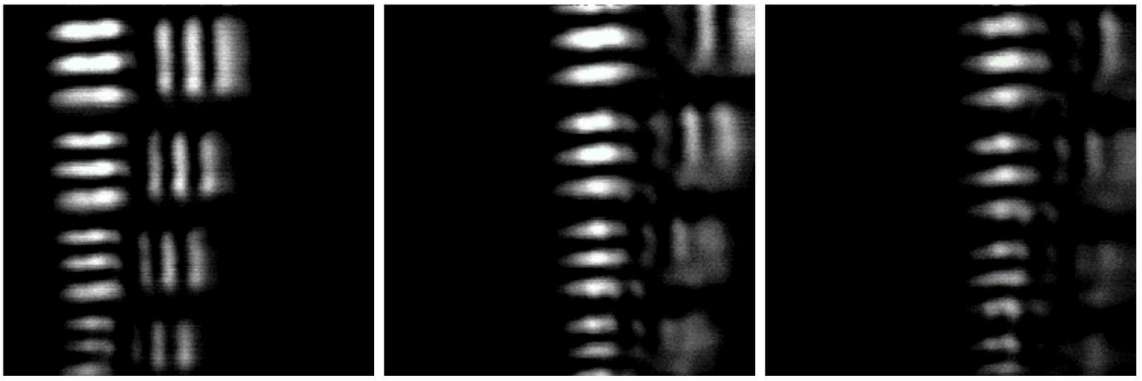

(A) **(B)** **(C)**

FIGURE 6.6: Images of the USAF target obtained using the DM deformed to create 3 μm (B) and 4 μm (C) RMS defocus, with the original 0 μm focus image (A) for comparison.

In the image in Fig. 6.6B, the bars moved to the right by 24 pixels (top of the bar barely visible), i.e. by 6.9 μm. In the image in 6.6C, the bars moved to the right by 28 pixels, i.e. by 8 μm. In terms of vertical shift, the bars moved down in 6.6B by 21 pixels and in 6.6C by 28 pixels. On average, from images in Fig. 6.5 and 6.6, it can be inferred that each 1 μm defocus shifts the image down and to the right by approximately 7 pixels and each -1 μm defocus shifts the image up and to the left by approximately 7 pixels, i.e. 2 μm or a resolution interval.

In conclusion, RMS focus control via the DM in the configuration assembled has a pronounced effect on the lateral drift. It is important to note here that the lateral resolution as determined by the horizontal bars appears to remain unaffected, though the vertical bars have become distorted and blurry. Practically, good signal is obtained from the central part of the image only. We believe this is due to the fact that the correction file was taken with the scanners in a zeroed position, meaning the corrections are less valid for the periphery of the imaged area.

Some lateral shift is expected due to the off axis configuration, typical in AO systems using DMs. This can be further reduced by increasing the focal length of the spherical mirrors CM2 and CM3, with the obvious disadvantage of enlarging the size of the layout and reduction in the axial range of focus change covered. Another factor is the imaging

beam potentially being slightly off-axis to the USAF target. A combination of these two factors may be responsible for the slight horizontal shift between image in Fig. 6.5B and 6.5C. We noticed that by tilting the USAF target, the lateral shifts change. This prevents post processing compensation by software.

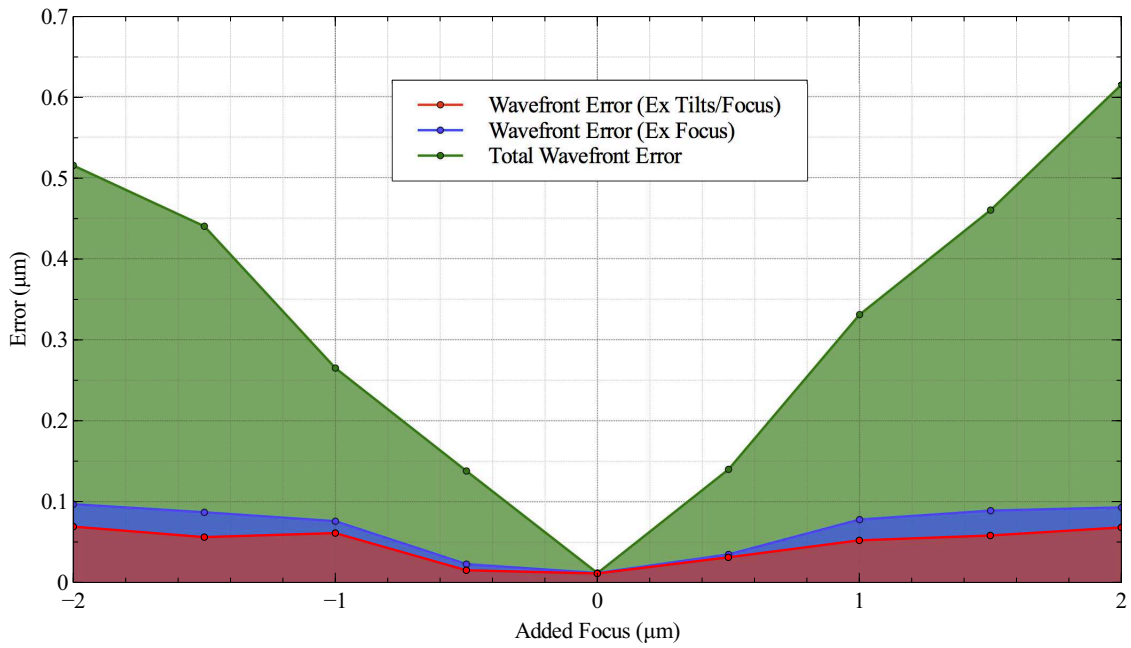

FIGURE 6.7: RMS wavefront error as focus is manipulated. Total error: green region. Error excluding focus: blue region. Error excluding tilts and focus: red region.

6.3.7 Effect upon wavefront when manipulating focus

In-depth analysis of the effect of focus manipulation on other aberrations was conducted. WFS measurements are taken as the DM is set to varying levels of defocus. Fig. 6.7 shows the overall wavefront error as detected by the WFS, with focus varied between -0.5 and 0.5 mm. It can be observed that tilt contributes significantly to the overall wavefront error in comparison to the other aberrations. It can also be inferred from the chart that the total wavefront error excluding defocus is 5 times less than the value with defocus. This demonstrates that the contribution of defocus to wavefront error is much greater than the aberrations that increase as a consequence of focus manipulation.

A breakdown of the first 8 aberrations is shown in Fig. 6.8, where it can be seen that all these aberrations increase as defocus is applied in either direction. Defocus aberration is plotted for reference (green), and appears linear as expected. The red and blue dashed lines represent fluctuating tilt 0 and tilt 90 respectively, and seem to exhibit the highest variance.

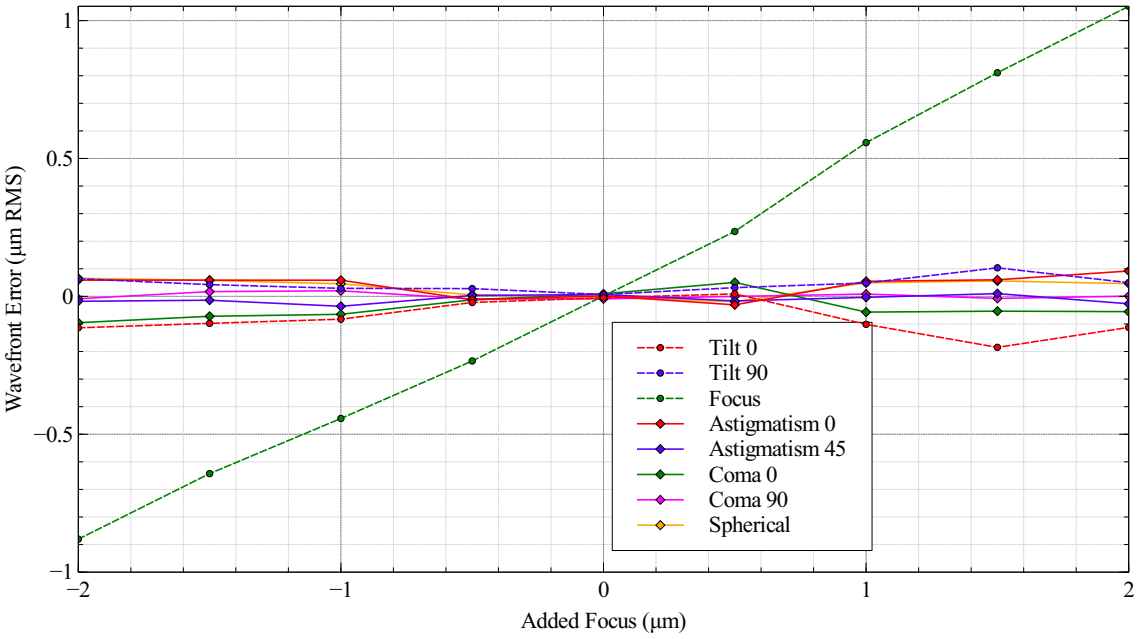

FIGURE 6.8: Effect of focus manipulation on defocus aberration (green) and on seven other high-order aberrations (according to colour in the inset).

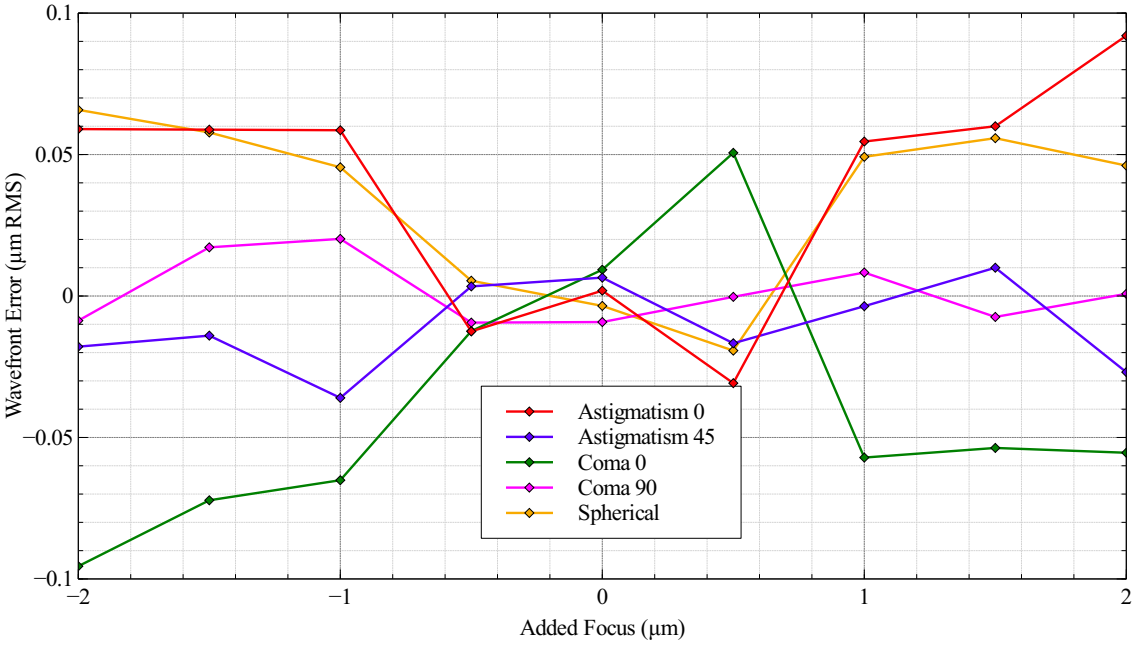

FIGURE 6.9: Magnified view of WFS RMS error showing effect of focus on wavefront excluding tilts and focus aberrations.

Fig. 6.9 displays the RMS error for the data in Fig. 6.8, excluding the tilts and focus aberrations. From this graph, it is seen that the effect of focus manipulation on these aberrations is within a range between -0.1 to 0.07 μm RMS. It is possible that these larger values at the extremities of the range are due to the limited dynamic range of the DM used. If this is the case, these can be made smaller if a second wavefront corrector is employed.

6.3.8 Test procedure

Measurements to test the procedure are conducted on a phantom target constructed using 10 layers of borosilicate glass microscope slide covers, each of thickness between 0.16 to 0.19 mm. Each slide was bound using a single layer of thin clear tape. As the clear tape is extremely thin, distances between the slides are not resolved and so, 11 interfaces should be distinguished only. As seen in Fig. 6.10, even after some tilt, extra layers appear at the bottom and some layers in between the main interfaces, due to multiple reflections between the slide facets. The total thickness of the sample is approximately 2 mm.

During live imaging, a sequence of commands is sent to the DM in rapid succession, with an optional time delay between each command. The magnitude of defocus aberration is swept between the limits of $\pm$ 4 μm RMS using the DM (determining an axial range of 2 mm in depth). The procedure was tested with 50 steps of 40 μm each at a rate of 200 commands sent to the DM per second. Oversampling by using a high number of small steps was found to produce smoother focus transition. Transversal size was maintained at 1 mm and the refresh of the B-scan OCT imaging was 100 Hz.

6.4 Results

Fig. 6.10A and 6.10C show images acquired with the focus position at respective negative (-1 mm) and positive (+1 mm) extremes, while Fig. 6.10B shows an intermediate unmodified state. While images are constantly being acquired we sweep the focus incrementally through 50 steps from one limit to the other, recording a video of the results. The final image in Fig. 6.10D is the Gabor image reconstructed using in-focus regions of all frames acquired during this sweep cycle. Fig. 6.10D has mostly uniform contrast throughout the range.

We can clearly see in Fig. 6.10A, 6.10B and 6.10C a horizontal stripe of high intensity shifting vertically in the image as the commands are applied to the DM. Fig. 6.10A,

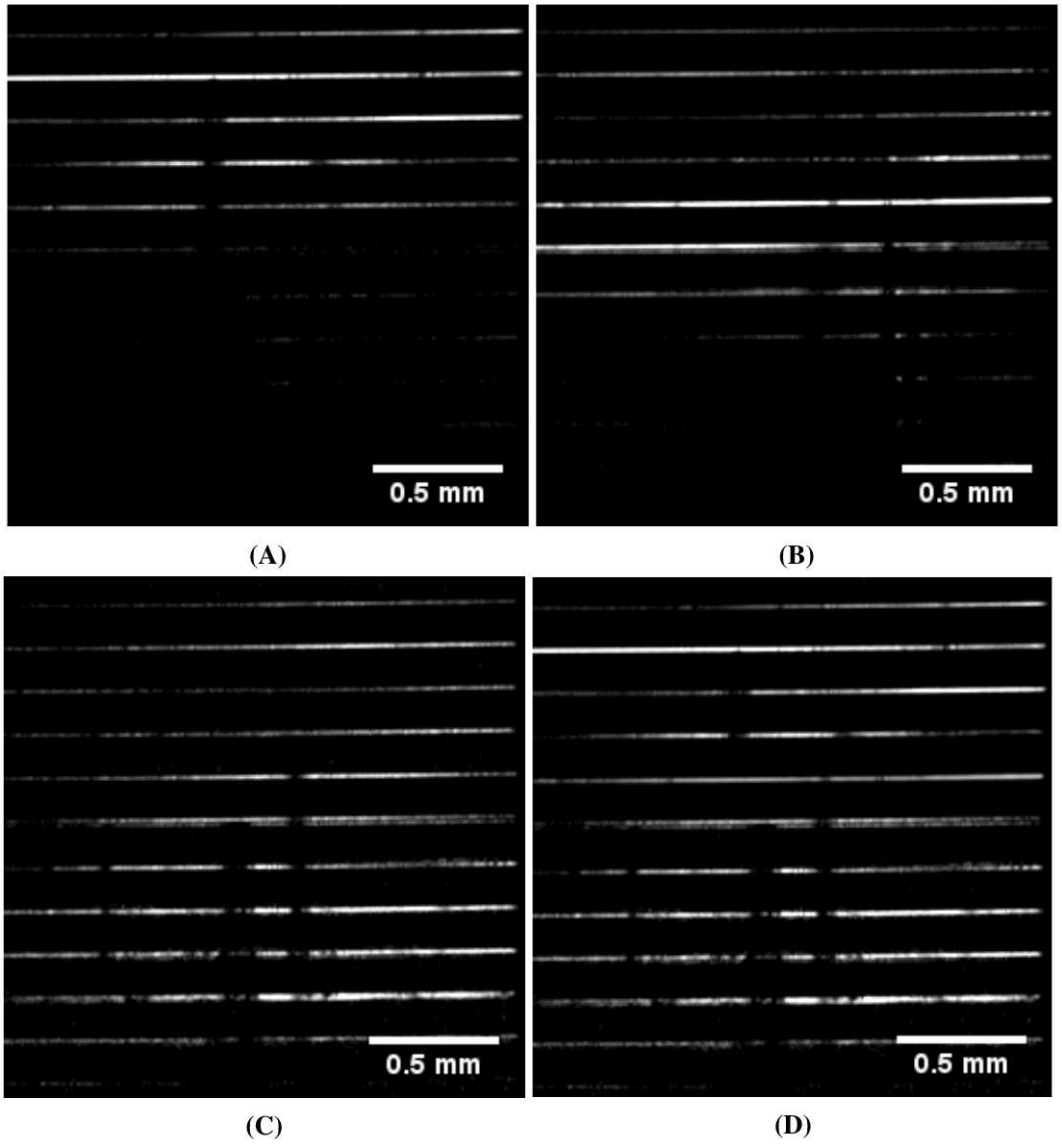

FIGURE 6.10: Images acquired of a phantom constructed from ten 0.17 mm thick glass slides (bound top and bottom with sellotape of similar thickness) with focus set to -4 (A), 0 (B) and 4 (C) covering a total range of 2 mm. Final image (D) is synthesized through extraction of in-focus regions from a stack of images acquired with focus shifted incrementally.

6.10B and 6.10C allow an approximate visual evaluation of the CG profile under AO correction. The profile width in 6.10A looks similar to that in 6.10B, where according to Fig. 6.2 the CG should exhibit a FWHM of 60 μm. The profile in 6.10C displays a much wider width. This suggests that other aberrations are added by the intervening layers, affecting the CG profile at + 4 μm RMS more than at - 4 μm RMS.

Considering the FWHM of the CG given by the minimum width of 60 μm and given the axial range of 2 mm, a minimum value of 33 is obtained for the ratio R. We used an experimental value of $R_{max} = 50$ for oversampling.

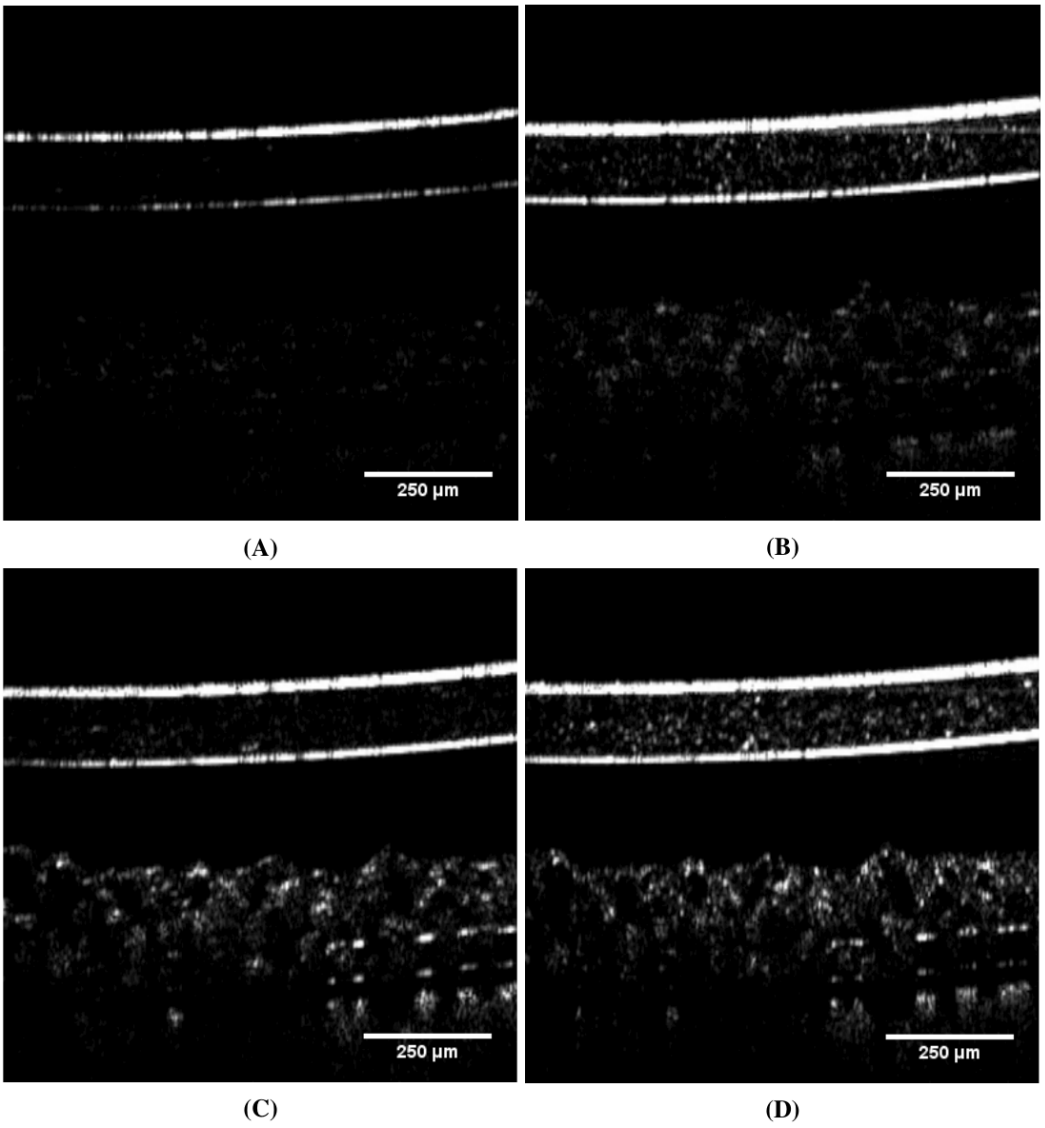

FIGURE 6.11: OCT B-scan images of an infra-red card, with focus set to -1.5 (A), 0 (B), and 1.5 (C) covering a range of 0.75 mm. The final image (D) is the composite Gabor image.

The procedure was repeated using an infra-red card as the object, with the DM configured to sweep ± 375 μm (total axial range of 0.75 mm). Fig. 6.11D is assembled by stitching the in-focus regions of images acquired during the focus sweep (Fig. 6.11A through 6.11C). It can be observed that the Gabor image in 6.11D exhibits the details in both the superficial layers (shown in Fig. 6.11A), intermediate layers (Fig. 6.11B) and deeper layers (Fig. 6.11C).

To verify that this procedure is suitable for *in-vivo* imaging of live samples we performed the same experiment on a wild-type *Drosophila* larvae. Several larvae were chosen at varying stages of development and secured using strong double-sided tape. All larvae are highly active and move constantly, potentially compromising the integrity of acquired

images. This time we reduce the focus sweep to ± 500 μm, covering a total axial range of 1 mm. Total power to the sample was measured to be 2.3 mW, which is well within safety range for a scanning beam at 1060 nm.

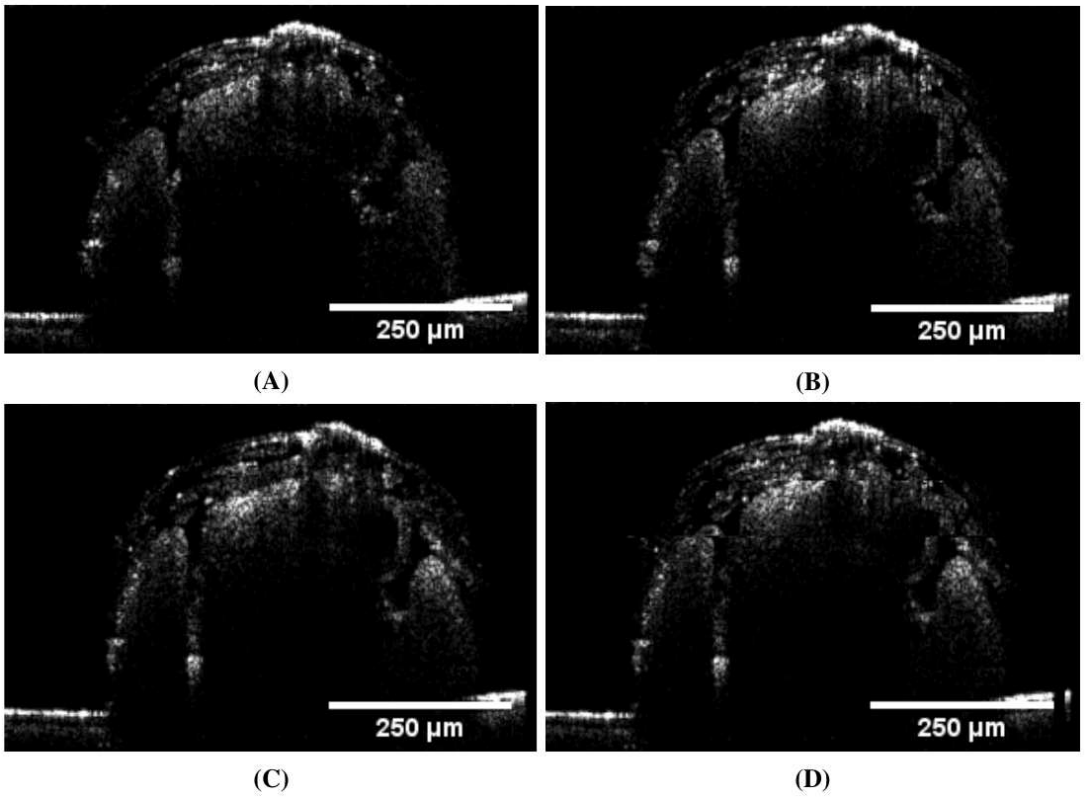

FIGURE 6.12: B-scan-OCT images of *in-vivo Drosophila* with focus at -1 (A), 0 (B), and 1 (C) covering a total range of 1 mm axial range measured in air. Final image (D) is synthesized through extraction of in-focus regions from a stack of images acquired with focus shifted incrementally.

Raw images from a *Drosophila* larvae taken with the focus shifted at - 0.5 mm, 0 and 0.5 mm in air are presented in Fig. 6.12A, 6.12B and 6.12C respectively. Fig. 6.12D shows the final Gabor filtered synthesized image, produced by compounding the regions of maximum intensity in each image from a stack of images recorded during a full sweep cycle.

Finally, the procedure was tested upon the thumb of a volunteer using an axial sweep range of 1 mm. Fig. 6.13A shows an image taken with static focus in the base state. The surface of the thumb is highly visible, as is the general position and structure of two sweat ducts. The distinctive spiral structure of the sweat duct is well documented in literature [167]. Fig. 6.13B shows the thumb with focus swept deeper into tissue; not only have the sweat ducts become more clearly defined, but also the deeper structures of the epidermis.

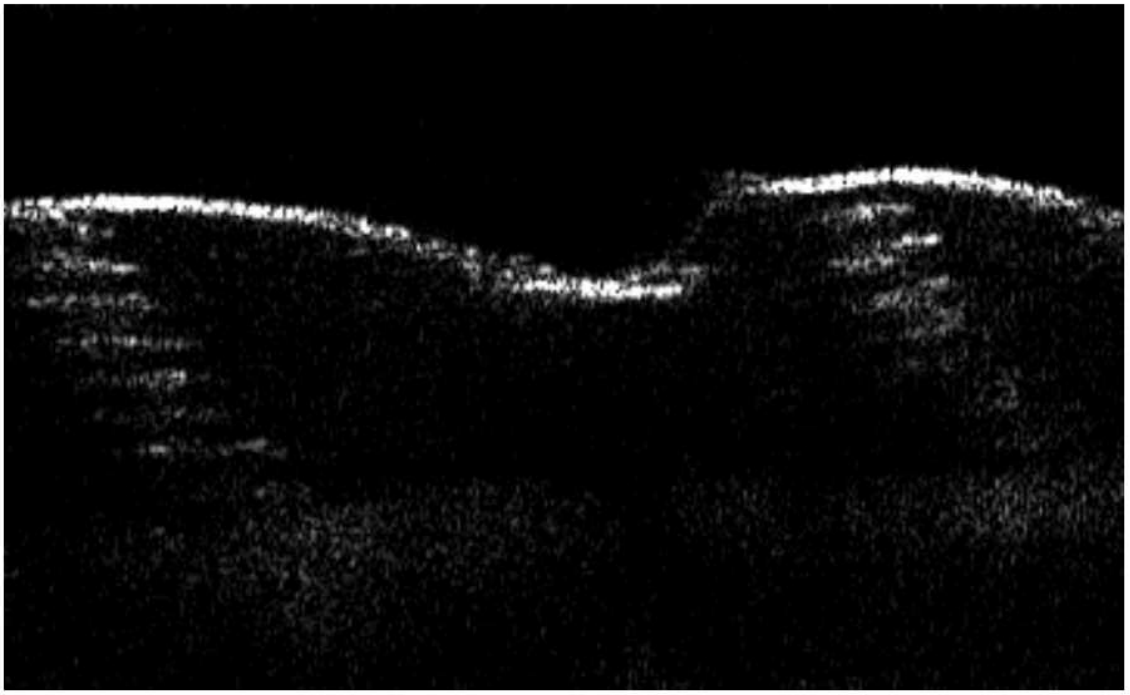

(A)

(B)

FIGURE 6.13: *In-vivo* OCT B-scan images acquired of thumb with fixed focus (A) at the surface and after Gabor splicing (B). Visible are the distinctive spiral structures of the sweat ducts, and the deeper tissues are enhanced in (B) due to focus sweep. Image size is 1 mm (horizontal) by 2 mm (vertical) measured in air.

To produce the synthesized images in Fig. 6.10D, 6.11D, 6.12D and in Fig. 6.13B, ImageJ was used post-acquisition. Given the speed of the image acquisition and DM

command rate it would be a simple evolutionary step to perform the splicing of cropped images live.

Artifacts may form in the synthesized image should the sample move during acquisition, which is a common problem in live imaging. One avenue of compensation is to increase the rate at which commands are sent to the DM, either by adjusting the delay between each command or simply reducing the number of incremental focus shifts to the minimum required for sufficient sampling as determined by R.

6.5 Conclusions

The study demonstrates that fine control over the curvature of a DM can be employed to perform Gabor splicing and yield better uniformity in terms of signal intensity throughout depth in a SS-OCT configuration.

This technique presents a clear advantage over possible implementations of focus control using a liquid crystal lens added to an AO configuration, as there exists potential to perform the focus shift whilst maintaining closed loop corrections using the DM. Even without updating the correction, the loss of signal up to half of its maximum can be tolerated within a significant axial scanning range of more than 2 mm. In addition, we would emphasize the benefit and sophistication of the DM as we are able to make several hundreds of incremental high-precision focus adjustments every second.

6.6 Evaluation

However, a number of shortcomings should be considered in practice. In addition to variation in sensitivity with defocus as shown in Fig. 6.3, there is a marked lateral shift of the image, in both vertical and horizontal direction. This was quantified here using confocal images of a USAF target, observing a lateral shift of approximately 2 μm per each 1 μm defocus applied to the DM. Large images were used here, where such lateral shifts could be ignored. Small size images however would require correction for the lateral shifts.

The lateral shifts induced by deforming the DM were stable in time, however the dependence of such shift to the object tilt prevents a universal compensation algorithm. An individual case solution can be implemented by first tracking the lateral shift for a given orientation and then correcting for the lateral shift by applying corresponding bias values to the two transversal scanners. Knowing that 100 mV determines an image size

of 70 μm, a 2 μm correction would require approximately 3 mV bias to each driver signal applied to the two transversal scanners. This would have some limited applicability, as individual layers with different inclinations inside the tissue will register different lateral shifts.

In the case presented here, a single DM is used to compensate for all aberrations and then used to manipulate defocus. Advanced designs may use multiple DMs to great effect, for example one DM may exclusively control tilts to compensate lateral shift. Alternatively, one DM could be set to continuously run closed loop correction (excluding focus control) whilst the second DM shifts the focus. This would eliminate the procedure of pre-processing the files for focus manipulation. Utilization of two deformable mirrors may improve the correction of the wavefront when limited by the dynamic range of a single corrector.

It can also be noticed by inspecting Fig. 6.10D, 6.11D, 6.12D and in Fig. 6.13B that the CG stripe can be seen moving axially with defocus aberration in Fig. 6.10D, but less in Fig. 6.11D and much less in Fig. 6.12D and Fig. 6.13B . This is a clear indication of enlargement of the CG profile due to aberrations created by the intermediate interfaces up to the depth of interest. Also, the variation of brightness amongst the sequence of images versus focus is not as sharp as illustrated by the profile in Fig. 6.3. This is another consequence of extra aberrations than those measured in Fig. 6.8 and 6.9; scattering caused by intermediate micro interfaces and scattering centres in the *Drosophila* and the thumb alter the shape and peak of the CG profile. This also shows that the correction determined by the WFS based on the dominant signal collected from the surface of a scattering sample is not so useful for imaging inside the volume of the sample.

6.7 Acknowledgments

C. Costa, A. Bradu and A. Podoleanu acknowledge the support of the European Research Council (http://erc.europa.eu), grant 249889. A. Podoleanu also acknowledges support from the Biomedical Research Centre at Moorfields Eye Hospital NHS Foundation Trust and UCL Institute of Ophthalmology.

Chapter 7

AO/SS-OCT Master/Slave interferometry for simultaneous live *en-face* imaging at different depths

7.1 Introduction

The previous work presented in chapter 6 demonstrated the capability of generating cross-sectional images *in-vivo* using AO-SSOCT. Acquisition and processing of frames occurs in real time, generating one B-scan in 100 ms. Traditionally, during SS-OCT imaging a B-scan is constructed by performing a fast Fourier transform (FFT) for each channelled spectrum as the beam is scanned across the object. For increased image quality, several steps prior to the FFT must be performed, such as zero padding, spectral shaping and re-sampling. With modern hardware, computers may perform each of these functions quickly, however the limitation is that they must be performed sequentially. Therefore, for every given B-scan, the total acquisition and processing time can increase with additional operations. Swept sources often have an integrated clock, allowing for re-sampling of the spectral data. This process requires additional hardware in the form of a specialised digitiser, which is costly and may not provide perfect re-sampling.

This execution time is compounded when attempting construction of an *en-face* image. To produce an *en-face* C-scan, a full 3D volume of data must be acquired and sliced orthogonal to the imaging plane in post-processing. Given the large number of intensive computational operations required to generate each image, the frame rate rarely

approaches the acquisition rate of the optics. Any additional processing to enhance the image quality will only exacerbate the problem, further reducing imaging frame rate. Most algorithmic operations such as image segmentation, phase correction and dispersion compensation must be post-processed.

It is beneficial for clinical use to retain the capability to produce live *en-face* images [168]. Research has been conducted at the University of Kent to produce multiple *en-face* images in real time using a graphics processing unit (GPU) to perform parallel computations at a far greater rate than a central processing unit (CPU) is able. A technique called Master-Slave interferometry (MSI) replaces the FFT with cross-correlation, removing the requirement for some preparatory steps such as re-sampling and dispersion compensation [169][170][171].

In traditional Fourier domain OCT, B-scans are produced by sweeping the probing beam across the same and acquiring a set of sequential longitudinal A-scans. Before the cross-section may be reconstructed, an FFT must be performed on each channelled spectrum acquired at different transversal positions of the probing beam. A single B-scan may therefore be expressed as a set of A-scans

$$B_{FD} = \begin{bmatrix} A_1 \\ A_2 \\ \vdots \\ A_n \end{bmatrix} = \begin{bmatrix} |FFT(s_1)| \\ |FFT(s_2)| \\ \vdots \\ |FFT(s_n)| \end{bmatrix} \tag{7.1}$$

where B_{FD} is the cross-section produced in FD-OCT, A_n is a longitudinal reflectivity profile at position n, and s_n is the raw channelled spectrum acquired at transversal position n. For each A-scan, all components q (points in depth) are obtained simultaneously in the FFT operation. Though $A_n(A_{n1}, A_{n2}, \ldots, A_{nq})$ is half the length of the sampled spectrum s_n, in reality q is often increased using zero padding [172]. Given a set of channelled spectra, it is theoretically possible to perform the FFT of s_1 to s_n for an image of size n x q in parallel, generating the B-scan in the time taken to complete a single FFT.

An *en-face* image may be considered as a collection of points from the same axial position

$$C_{FD} = \begin{bmatrix} B_{1q} \\ B_{2q} \\ \vdots \\ B_{nq} \end{bmatrix} \tag{7.2}$$

where B_{nq} is a cross-section at transversal position n, and q denotes the axial position. For each longitudinal scan, the modulation seen in the spectrum at each axial position is the same. A transversal reflectivity profile (T-scan) may be assembled by reading along the axial coordinate.

A new design utilising a master interferometer (MI) and slave interferometer (SI) operates similarly to a TD-OCT system whereby signal is only recorded from a single depth. The imaging signal is acquired by the SI, which operates as a normal SS-OCT system. The MI is responsible for providing the OPD information.

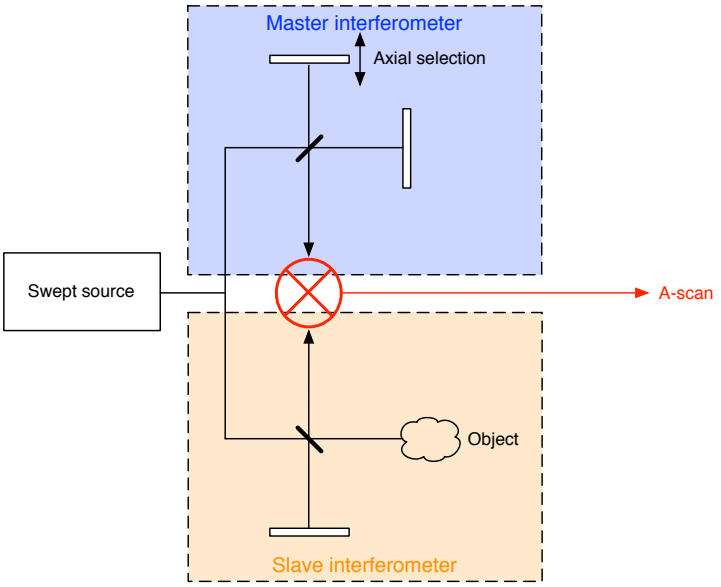

FIGURE 7.1: Diagram showing master-slave interferometry configuration. Both interferometers operate in Fourier domain, however the master interferometer acts as a reference for axial selection as in TD-OCT. The electrical signal proportional to the shape of the channelled spectrum from the slave interferometer is cross-correlated with the electrical signal proportional to the shape of the channelled spectrum from the master.

Fig 7.1 shows a system design for an MSI implementation. The MI in this case is a simple Michaelson interferometer where both arms are terminated with mirrors. The SI is typical of a Fourier domain imaging interferometer, with an object arm and a reference arm. The channelled spectra output from each interferometer are cross-correlated. When the two channelled spectra are perfectly matched, the amplitude of this cross-correlation reaches its maximum. The translation stage in the MI may be shifted to change the interrogation depth in the object, as in TD-OCT.

An alternative approach would be to use a single interferometer as both the MI and the SI as shown in Fig 7.2. By replacing the object with a mirror, the SI may act as the MI. A set of channelled spectra, called masks, may be recorded at a range of OPD

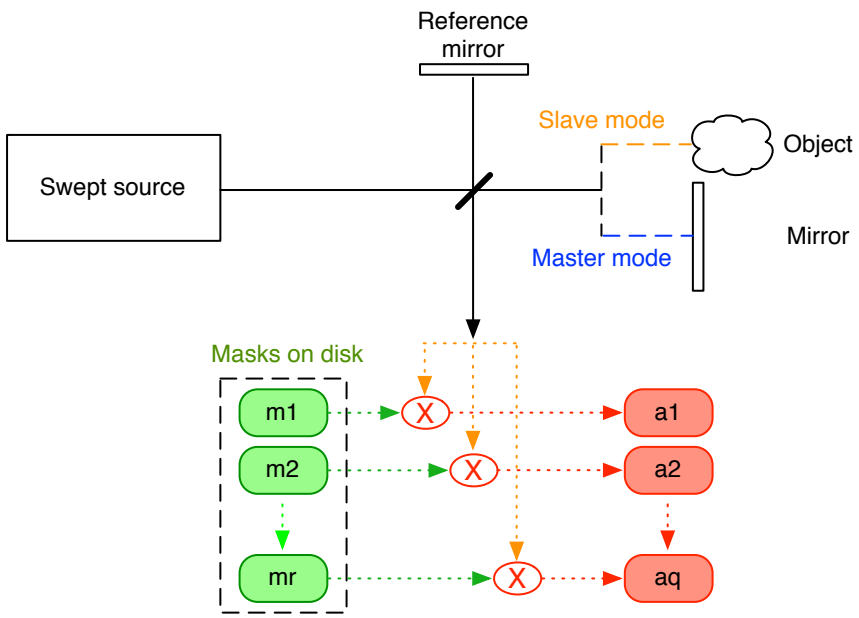

FIGURE 7.2: Diagram showing alternate MSI configuration where a single interferometer is used. The object can be replaced with a mirror to switch the system to master mode for mask acquisition.

values and saved. The mirror may then be replaced with another object and the system can operate as the SI. In this case, the channelled spectra output of the SI (acquired live) may then be compared with the entire set of masks (pre-acquisition channelled spectra). Again, the greater the similarity between the SI output and a given mask, the greater the amplitude of the correlation result. Poor correlation will produce weak signal. Since all masks are acquired pre-acquisition, given sufficient computational resources it is possible to form an image at all depths (where each masks corresponds to a different depth) simultaneously in one parallel process:

$$A_n(OPD) = \sum_{-k=(w-1)}^{k=(w-1)} \left| s_n \otimes m_n \right| \tag{7.3}$$

where m denotes the mask. These masks should be recorded for OPD values denser than half the coherence length of the optical source. For comparison with the B-scan produced by FD-OCT shown in Eq. 7.1, the MSI image can be expressed as:

$$B_{MSI} = \begin{bmatrix} A_1 \\ A_2 \\ \vdots \\ A_n \end{bmatrix} = \begin{bmatrix} s_1 \otimes m_1 & s_1 \otimes m_2 & \dots & s_1 \otimes m_p \\ s_2 \otimes m_1 & s_2 \otimes m_2 & \dots & s_2 \otimes m_p \\ \vdots & \vdots & \ddots & \vdots \\ s_n \otimes m_1 & s_n \otimes m_2 & \dots & s_n \otimes m_p \end{bmatrix} \tag{7.4}$$

where p denotes the number of recorded masks. It can be seen from Eq. 7.4 that the MSI method produces a 3D volumetric image, where each row represents a A-scan and each column is a T-scan. The speed of the MSI method comes from the capability to compute any value in this matrix independently. Given the capability to perform all these operations in parallel, it is theoretically possible to generate the whole volume in the time it takes to perform a single cross-correlation. In addition to the potential speed increase for imaging at multiple depths simultaneously, this implementation of MSI has also been shown to completely negate system-induced dispersion since this information is present in both the mask and the channelled spectrum [173].

Presented in this chapter is the usage of the MSI method towards high-resolution *en-face* eye imaging and multiple depths simultaneously.

7.2 Methodology

For experimentation, the implementation of MSI using a single system as both the master and the slave was chosen. The reason for this decision was to lower the cost of the system by eliminating the separate master interferometer, and also to exploit the immunity to system-induced dispersion.

7.2.1 System design

The optical system design is the same as that seen in chapter 6. Fig. 7.3 shows a detailed schematic of the optical system. There are two light sources used for this arrangement, a 830 nm SLD for wavefront sensing and a 1060 nm SS for imaging. The SLD light is launched into the system using a collimator and the beam propagates through the interface optics to the object and is back reflected. Upon returning to BS1, 10% of the light is diverted through a telescope formed of two identical lenses to be re-imaged on the WFS. The remaining 90% of the light is returned to an APD, though this device is not used in this experiment.

The imaging beam is split by BS2 into two arms, with 70% of light sent in transmission through the reference arm to be coupled back to a 50/50 coupler. The remaining 30% of light is reflected to the object arm, propagating through the same optics as the wavefront sensing arm and being back scattered by the object for collection into the second branch of the same 50/50 coupler. The outputs of the coupler are then connected to a balanced photodetector, which outputs an RF signal to a digitiser board on the PC.

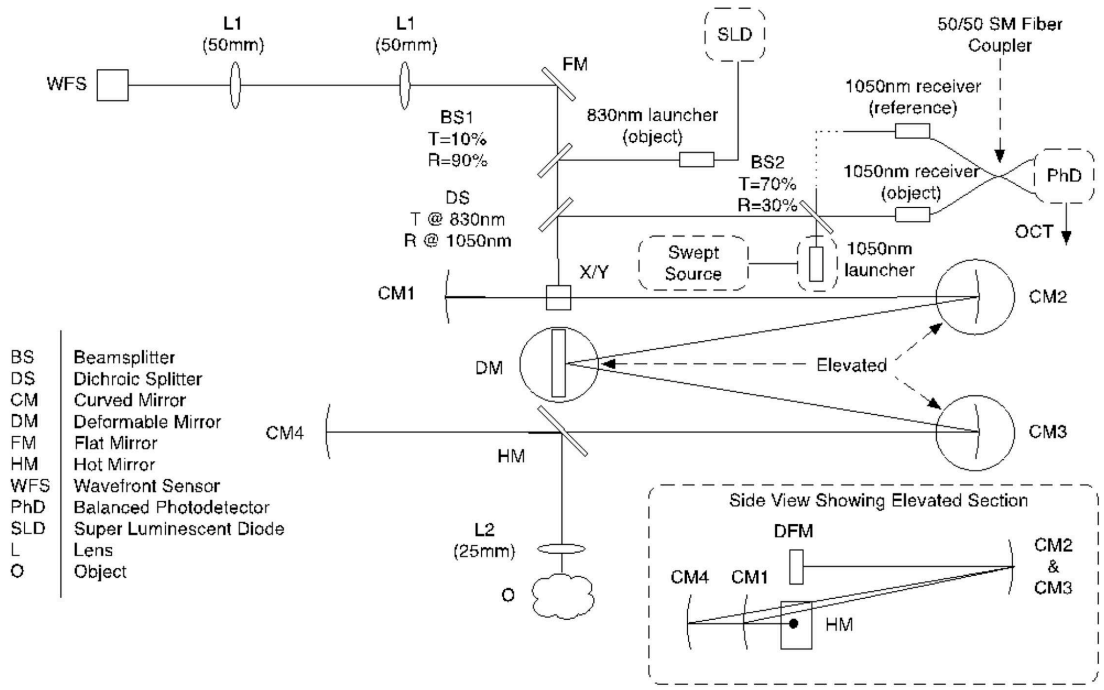

FIGURE 7.3: Schematic of the AO/MSI-OCT system with imaging at 1060 nm and wavefront sensing at 830 nm.

Prior to imaging, white paper was placed as the object in the focal plane of the objective lens L2. The scanners remain stationary for the wavefront optimisation step. With the 830 nm SLD source illuminating the object, the WFS is able to determine the total wavefront error. The CASAO software interprets this data and operates a closed feedback loop between the WFS and the DM until the wavefront is brought to a corrected state. At this point, the SLD is switched off and the swept source is switched on.

Once the AO has been completed and the swept source has been switched on, a mirror is placed as the object and the system operates as the MI. Custom software written in LabVIEW is used to send a series of small movement commands to a motorised translation stage (VPX-25) via RS232 link to a Newport stage controller. At each position of the stage p, the software saves a mask to disk. The scanners are kept stationary during this process, at a zeroed position. Once all masks have been acquired, the stage is shifted back to its original position and the mirror in the object arm is replaced with the sample to be imaged. The scanners may now be activated to raster the imaging beam across the object.

For experimentation, the translation stage was moved a total of 100 times over a distance of approximately 4 mm in the reference arm. Since the reference arm is in transmission, the actual axial scan range in the object is 2 mm.

7.2.2 Signal acquisition and processing

A different LabVIEW package is responsible for providing the triangular waveforms that drive the scanners using a National Instruments data acquisition board (NI-DAQ model 6110). The output of the photodetector is read by a fast digitiser (Alazartech model ATS9350) and linearised using the clock output from the swept source. The software communicates with a dedicated graphics card using a dynamic link library (DLL) by NVidia. The data acquired from the digitiser is stored as a buffered stream of information, which is piped to the graphics processing unit (GPU) of the card. The GPU is capable of running many threads in parallel, allowing in this case for the live simultaneous generation of 12 *en-face* images at different depths.

To form an image, a number of A-scans are acquired for different transversal positions n of the imaging beam, in this case a value of $n = 500$ is used to build a B-scan. Each longitudinal A-scan consists of 1472 points q. With a sweep rate of 10 μs, a B-scan may be acquired in 5 ms. Time to transfer the data to the shared memory accessible by both the CPU and the GPU must be considered. The LabVIEW and CUDA code were written by other researchers in the AOG at Kent [174]. This is the first report of MS applied to an AO-OCT system.

7.3 Results

In this section, results from several experiments are presented with a detailed description.

7.3.1 Elimination of fringes in images of specular targets

When imaging highly reflective specular targets, fringes may be observed. These fringes appear as large black bars as shown in Fig. 7.4. Sub figures 7.4a, 7.4b and 7.4c show *en-face* images of a USAF resolution target at three values of p corresponding to different masks (OPD).

Fig. 7.5 shows that by averaging several consecutive images together, the fringes can be eliminated. Since the target is specular, it can be assumed that the useful information is at the same depth, on the surface of the USAF slide. By creating multiple *en-face* images at varying OPD and averaging them, the image is made clearer through elimination of the fringes.

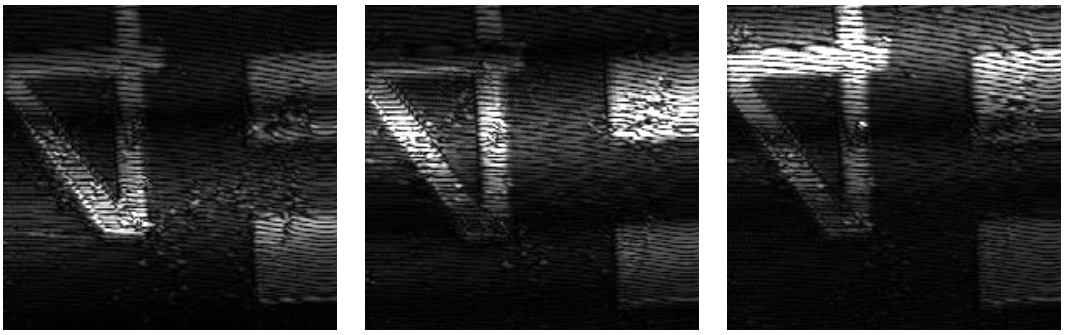

(A) $p = 1$ (B) $p = 10$ (C) $p = 20$

FIGURE 7.4: Images of USAF target at three values of p.

FIGURE 7.5: Averaged image over $p = 1$ to $p = 20$. Large horizontal black bars indicating fringes have been eliminated.

7.3.2 Imaging the thumb at different depths simultaneously

The imaging modality was tested on a live biological tissue by imaging the thumb of a volunteer. Presented in Fig. 7.6 are six *en-face* images of the thumb. Visible are the grooves of the skin running predominantly vertically across the image. Fig. 7.6a is an image acquired with $p = 1$ and shows the most superficial features of the thumb. Fig. 7.6b through 7.6f are images acquired from deeper layers in the thumb.

Visible from Fig. 7.6d to 7.6f are three circular structures running parallel with the grooves of the thumb. These are sweat ducts, characterised by their distance spiral structure in depth. These images are all generated simultaneously in real time, allowing for instant sectioning of biological tissues *in-vivo* using MSI methods without any post-processing.

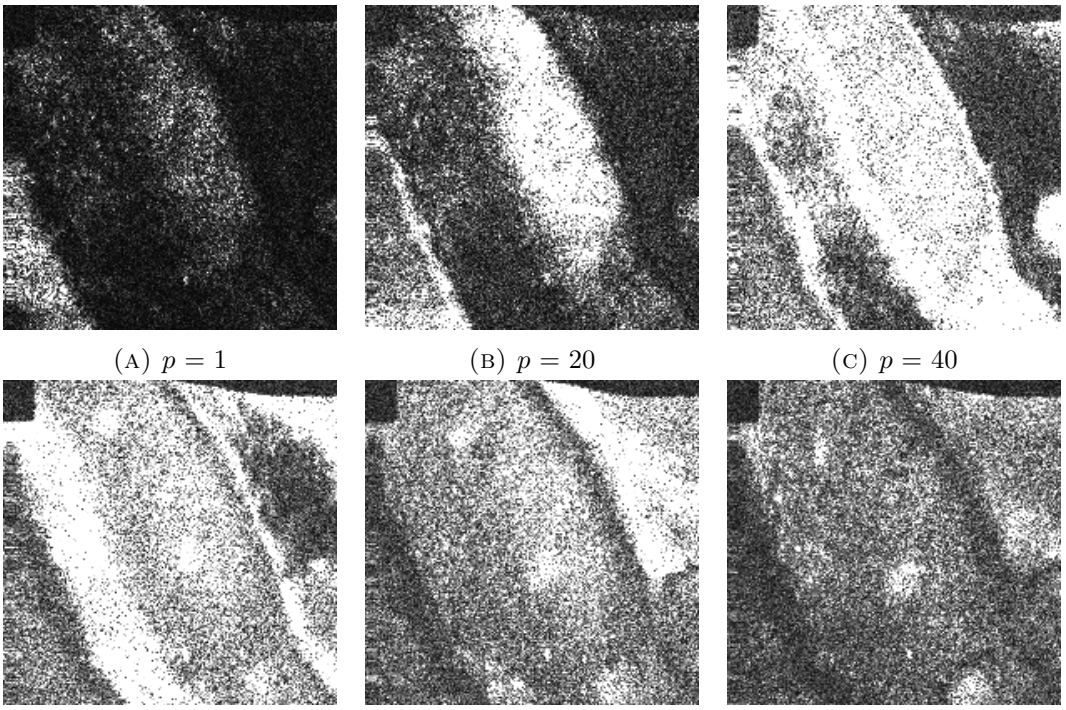

(A) $p = 1$ (B) $p = 20$ (C) $p = 40$

(D) $p = 60$ (E) $p = 80$ (F) $p = 100$

FIGURE 7.6: Images of the thumb acquired simultaneously using MSI with $p = 1$ to $p = 100$.

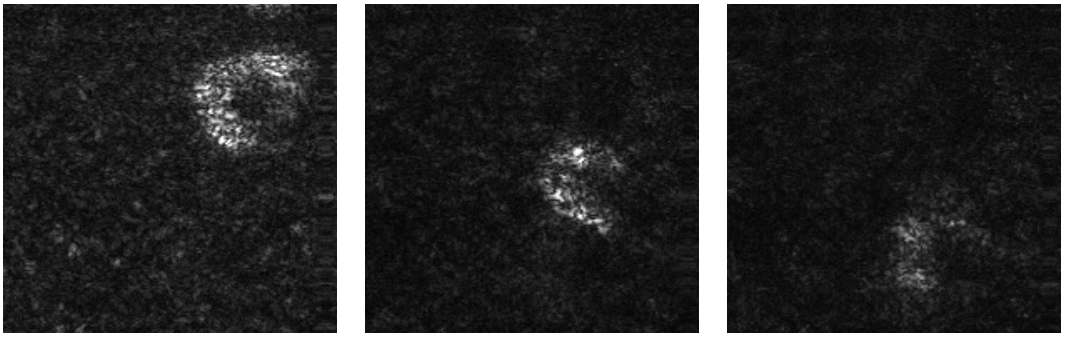

(A) $p = 25$ (B) $p = 32$ (C) $p = 45$

FIGURE 7.7: Images of a sweat duct in the thumb at three values of p.

7.3.3 Sectioning of sweat duct in thumb

Having identified the spiral structures as sweat ducts, it is possible to scan the beam over a smaller transversal range to isolate a single duct in the image. The amplitude to the scanners is reduced until visualisation of the sweat duct is clear and centred in the image.

Fig. 7.7 shows three *en-face* images selected from the acquired volume, demonstrating axial sectioning of a single sweat duct. Fig. 7.7a shows an image of the region of the

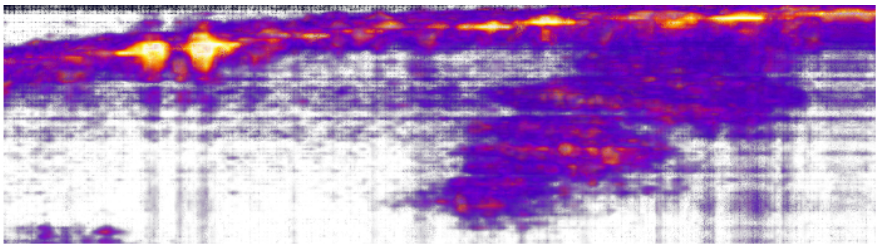

(A) Side view with fire LUT applied

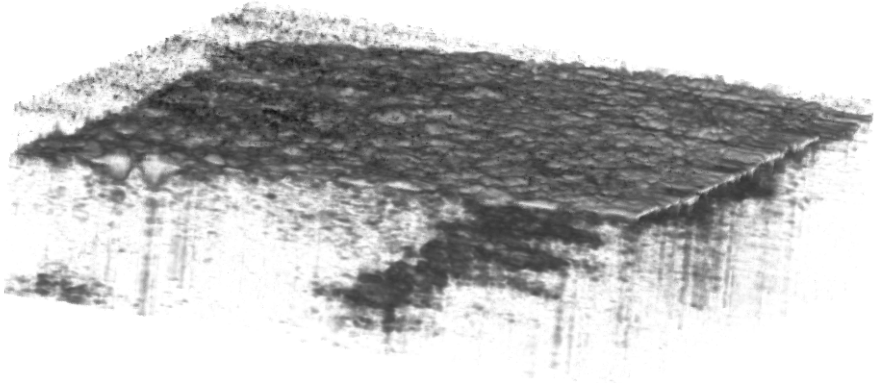

(B) Tilted view in grey scale

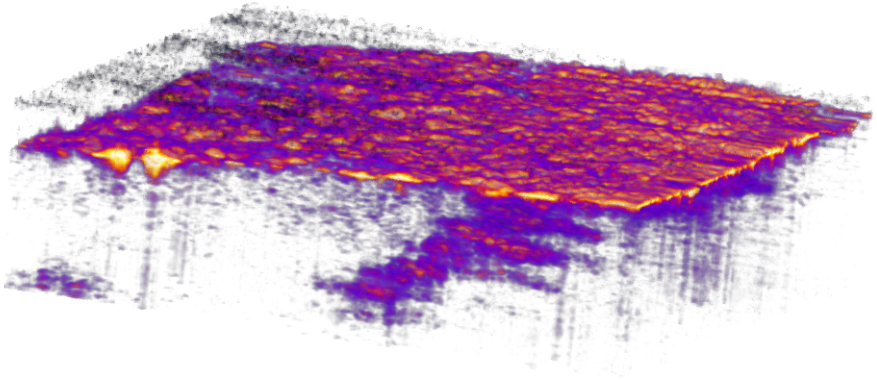

(C) Tilted view with fire LUT applied

FIGURE 7.8: 3D volume images of the sweat duct in thumb at two orientations.

sweat duct closest to the surface of the thumb, and the spiral can be observed in the images that section deeper into tissue (7.7b, 7.7c).

The view can be expanded slightly to encompass a larger transversal region, whilst maintaining isolation of a single sweat duct. A volume may be saved and post-processed to generate a 3D image. Fig. 7.8 shows three images acquired by reorienting the data in the volume.

Fig. 7.8a shows a side-view of the 3D volume acquired around a sweat duct. A fire lookup table (LUT) has been applied to increase visibility of the features. Running horizontally across the top of the image is the surface of the thumb. The spiralling

structure of the sweat duct can be seen descending from the surface of the thumb to the centre-left of the image.

Fig. 7.8b shows a tilted view of the same volume. In this grey scale image, the surface of the thumb can be clearly seen with the sweat duct descending from it. Again, for clarity, this image is represented again in Fig. 7.8c using a fire LUT.

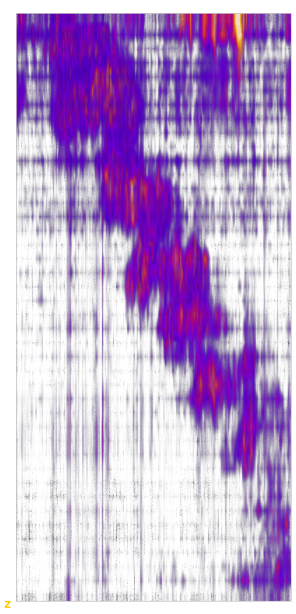

FIGURE 7.9: Cross-sectional image of the sweat duct in the thumb extracted from a volume produced by MSI method. Fire LUT has been applied to increase clarity of the image.

As in Fig. 7.7a to 7.7c, the view can be compressed close to the transversal limits of the sweat duct. Using the same method as in Fig. 7.8, a volume can be created and reoriented to show a cross-section. Fig. 7.9 is the result of this process, showing a close view of the spiralling structure of the sweat duct.

7.3.4 Imaging the retina and photorecptors *in-vivo*

Finally, images were acquired of a volunteer's retina *in-vivo* using the MSI method. A chin bar was used to stabilise the head and the patient was asked to focus at infinity. Tropicamine was administered to dilate the eye prior to imaging. Fig. 7.10 shows a collection of three *en-face* images acquired from the retina in three different experiments.

Fig. 7.10a shows a close view of the area near the fovea. Running vertically down the centre of the image is a blood vessel, though poorly defined. It is possible to determine the general shape and distribution of photoreceptors in this image, though they appear large due to defocus, and distorted due to motion.

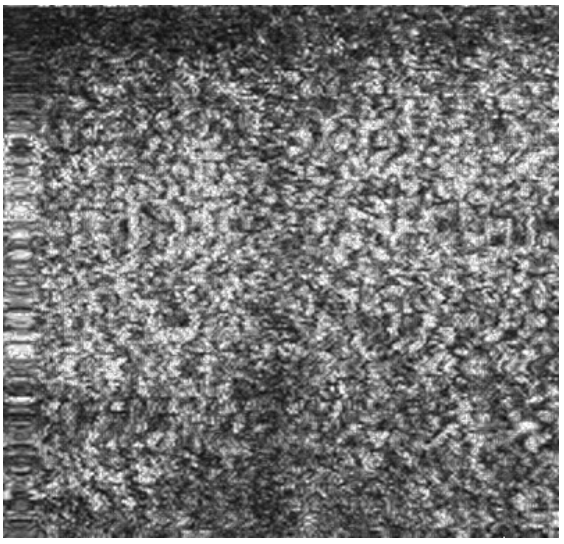

(A) Image showing zoomed-in view on photorecptors

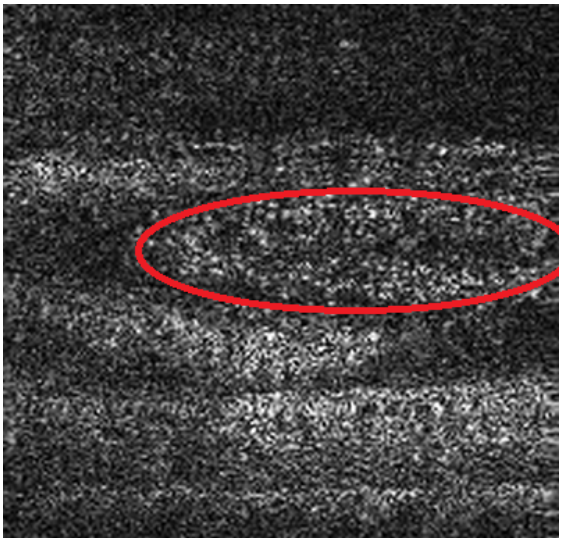

(B) Image showing broad view with photorecptors highlighted

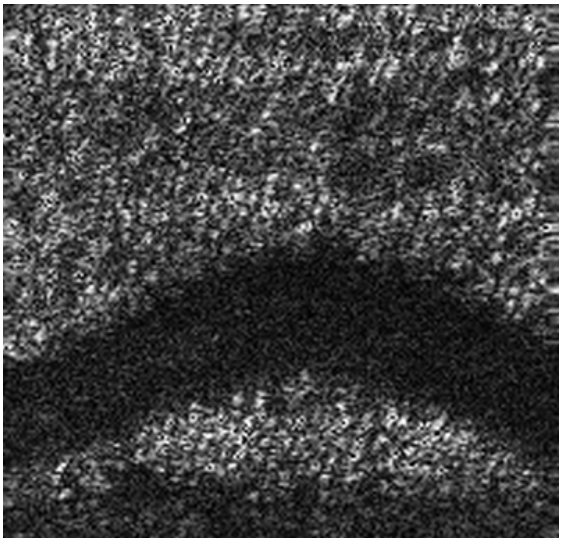

(C) Image showing large blood vessel with photoreceptors visible

FIGURE 7.10: Images acquired from the retina *in-vivo* using MSI.

Fig. 7.10b is a broader view of the retina. The motion artefacts are evident in this image, identifiable by the wave-like regions of high and low intensity. This indicates axial motion during the acquisition of the image. Circled in this image is a small region that is in-focus, presenting a regular distribution of photoreceptors.

The final image is taken near a blood vessel. Fig. 7.10c presents a dark region indicating a blood vessel interrupting the dense pattern of bright blobs. These blobs are photoreceptors, which can be generally resolved in most regions of the image.

7.4 Conclusions

The method of MSI for live simultaneous imaging of stationary targets, including highly reflective specular surfaces, is promising as presented by these results. The clarity of images are improved through the averaging of several adjacent axial scans spaced a few microns apart. This is a simple process and can be performed live without significant computational cost. Given a stage and controller that can translate in small enough increments, masks at sufficiently proximal axial increments (smaller than the axial resolution) can be acquired. By using such masks, a novel despeckle method is demonstrated here.

MSI is also a useful tool for depth sectioning of objects, such as the biological tissues presented here. Live sectioning of organic samples could prove highly beneficial to clinicians as they perform live optical biopsies of tissue *in-vivo*.

The marriage of MSI with AO/SS-OCT provides images with high transversal and axial resolution. Further, the DM used for AO may be exploited to shift the focus within the object during live imaging, similarly to the method presented in chapter 6. In this case, a clinician would be able to use MSI to view *en-face* images acquired at multiple depths simultaneously, and then use the DM to shift the focus to an axial region of interest.

Using a sufficiently powerful GPU, MSI is proven to be suitable for parallel programming. Each mask may be correlated with the channelled spectrum to produce a T-scan in parallel, rather than in sequence as in conventional OCT. This advantage increases with the number of post-processing operations performed on each B-scan before the final volume is assembled.

7.5 Evaluation

The results show that the current implementation of the MSI method for eye imaging is less convincing. Several problems were presented during this experimental work, culminating in low-quality images. A key problem was the time required to assemble and re-slice the volume for cross-sections. Conventional SS-OCT may provide B-scans at greater than 50 Hz, however for MSI the B-scan must be extracted from a 3D data set. This data set is only produced after the beam has been scanned transversally across the object in two dimensions. This is a problem similar to TD-OCT whereby the axial probing position may only be shifted after the scanners have completed their movement to acquire a 2D *en-face* image. With MSI, though the depth information is coded instantly in the modulation of the channelled spectra, a B-scan may only be generated after the slow frame scanner completes its scan across the object. This may be alleviated slightly by generating a B-scan from the first line scan only, though is a strict limitation.

The overall effect of having a slow B-scan image display is the loss of guidance. The clinician relies upon the information presented in the B-scan to guide the patient in positioning and orienting their eye relative to the probing beam. In addition, the software produces an audio signal from this B-scan that lowers in frequency as the eye reaches zero OPD, indicating good positioning for imaging. This signal, used by the patient to guide themselves, is subject to the same delay as the B-scan and can therefore be misleading. Images of the photoreceptors appear out of focus and jagged due to the difficulty in positioning and orienting the eye.

This effect compounds the problems present in *in-vivo* eye imaging with regards to motion artefacts. Side views of retinal images show a wavy pattern, indicating varying axial positioning of the eye even in the few milliseconds of acquisition time per frame. Despite using a chin rest, the variance in movement was significant, resulting in a drastic loss of image quality when compared with the detailed images acquired from the thumb.

This is a problem that may be resolved with a more sophisticated head-cage stabilisation system, and an illuminated fixation target for the patient to focus upon. In addition, generating a faster B-scan may make guidance easier, allowing for better positioning of the eye. A fixation target, an OLED display with a remotely controllable illuminated crosshair, was eventually used to aid this process. This provided great benefit in guiding the volunteer to the correct position, however stabilisation was still an issue. Even with fixation, the *en-face* images acquired were prone to 'tearing' artefacts, caused by movement of the eye during a volume acquisition.

It must be noted here that the transversal resolution of this system is high (approximately 2 μm), and the field of view is low (maximum of 1 mm^2). Much larger images of the retina may be acquired with MSI using different interface optics that grant a wider field of view. The motion artefacts in this case would have a far lesser negative effect on the image quality as presented here. MSI has been used to effectively image the optic nerve *in-vivo* without presentation of the issues described here [166].

Chapter 8

Genetic programming technique for sensor-less wavefront optimisation

8.1 Introduction

Genetic and biological algorithms are a product of research into biologically-inspired computation. This field of research is dedicated to computationally solving complex problems with specifically tailored approaches [175][176][177]. In nature there are many examples of biological organisms that have evolved, genetically or behaviourally, to increase their chances of survival. Behavioural developments may cause individuals within a larger system to function, either consciously or instinctively, in a way that is most beneficial for the system as a collective [178]. From a set of individuals behaving in a specific way, a greater behavioural system emerges [179][180].

The aim of this project is to perform optimisation of an optical system using a wavefront corrector and a search algorithm. Optimisation is a complex process involving intelligent design and fine control to minimise aberrations induced by optical components in the system. Adaptive optics (AO) systems typically employ a wavefront sensor (WFS) to detect aberrations, and a deformable mirror (DM) or other wavefront corrector to compensate.

AO systems are complex to design. As detailed in Chapter 4, there are many factors to consider when placing components in the system. The WFS must be placed in the conjugate plane of the object, the DM and any galvoscanners. This requires that many telescopes are used to resize and re-image the beam at these points. Since lenses may

produce back reflections that confuse the measurement on the WFS, curved mirrors must be employed in off-axis configurations, leading to increased aberrations.

Additionally, the nature of some objects may not allow for accurate wavefront measurement and subsequent correction. Highly reflective objects such as mirrors may saturate the WFS and destroy the measurement process.

This project is an attempt to simplify the optimisation process by eliminating the requirement of the WFS and relaxing the rules governing the positioning of the DM. The assumption is made that enough information is returned from the object to the photodetector to perform optimisation without a comprehensive measurement and analysis of the wavefront. Without a real AO closed loop, the DM is treated simply as a dynamically variable optical interface that affords some control over the wavefront. An important advantage of a sensor-less method is that correction driven by sharpness should reach a better correction, as this process does not depend on the balance of common and uncommon paths in the interface optics.

All previous configurations suffered due to the aberration of uncommon paths (such as the path from DS to BS2 and the PhD in Fig. 7.3), which is not corrected by the closed loop. Additionally, this approach will enable wavefront correction using the imaging beam itself as the sensing beam. This eliminates the possibility of disparity between these beams if they are separate, as described in chapter 7.

The premise is made that if there exists a configuration of the DM that reduces aberrations to a minimum, then that state could be found experimentally using a search algorithm. There are two suitable methods discussed below.

8.1.1 Particle Swarm Optimisation (PSO)

Particle Swarm Optimisation (PSO) is a method inspired by the movement of individuals in bird flocks and fish schools [181][182]. Birds are known to adopt flying formations that benefit the flock as a whole, with individuals periodically shifting positions to even the strains of flying between them. Similarly, penguins huddle for warmth, and take turns to face the freezing temperatures on the periphery of the group. Through the simplistic actions of these individuals, the group gains benefits and a complex system is developed.

It is upon these principles that PSO techniques are used to find solutions. Each individual 'particle' represents a potential solution for a given problem. The particles are placed within a defined mathematical search-space, and the particles are free to move around. A particle has two main properties, its position and velocity. Positions are

randomised upon initialisation of the PSO algorithm. Each particle is assessed at every iteration of the algorithm for their suitability. Each particle will remember its best known position within the search space; that is, the value at which it best meets the search criteria. Particles are also able to determine the best position achieved overall by a particle within the swarm.

Once the assessment has been completed, particles are free to move a certain distance in the next iteration. The movement of each particle is influenced by their individual best-known position, and also by the best positions discovered by the swarm as a whole. Every iteration, each particle updates its target position as the swarm discovers more of the search-space. Particles that make minor changes in vector will move a greater distance each iteration. Conversely, particles that are constantly changing direction will move by smaller distances. An emergent effect is that particles accelerate towards better positions, then slow down as they start to converge on the optimal positions.

8.1.2 Genetic Algorithm (GA)

Genetic algorithms are learning systems that attempt to 'brute force' a solution by exploring a search space. The general theory of survival of the fittest is what drives this optimisation process. Solutions in the search space are rated based on their suitability to solving a given task, and over time the best solutions 'breed' to produce more possibilities while the weaker solutions die out.

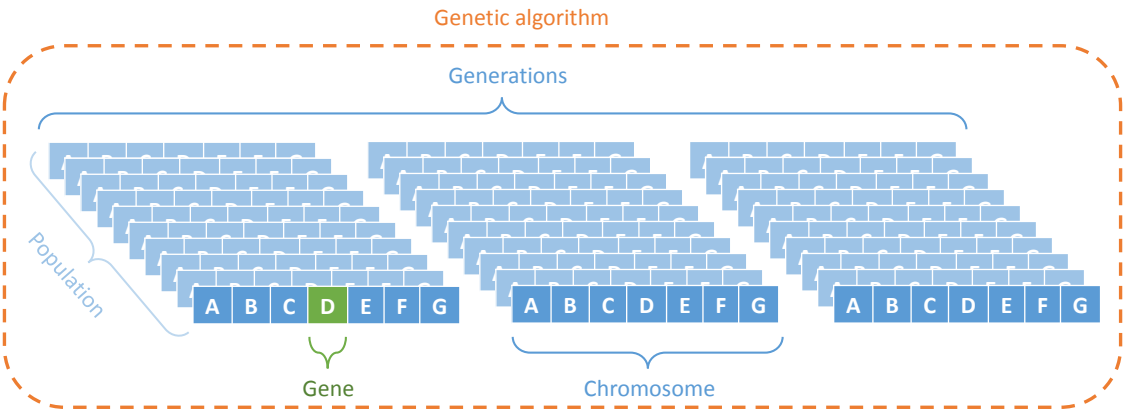

FIGURE 8.1: Diagram showing structure of a GA, with generations progressing from left to right.

8.1.2.1 Genes and the gene pool

Within the context of genetic programming, a gene is the simplest and smallest element in the structure. Each individual gene represents a piece of data or an instruction; its complexity can vary from numerical values, to basic logic (AND, OR, NOT) even blocks of high-level code. Genes are not intelligent, they are not able to make decisions or interact with other genes directly [183].

The design of a gene within a genetic algorithm is highly dependant on the desired effect of the overall system. A basic system may only require that genes store a piece of data, such as a letter or number. More complex systems may wish to construct evolving procedures, wherein each gene contains an instruction that modifies input data to produce an output. These instructional genes act as black boxes - once data goes into the gene, it cannot be affected by the parent systems until the gene produces an output.

A collective of genotypes is donated as the gene pool, and represents the resources available to the genetic algorithm. Genotypes are templates for created genes, and multiple genes may be created of the same genotype. As an analogy, for basic systems it is helpful to consider each genotype as a letter, and the gene pool as an alphabet. When running the genetic algorithm, the procedures are restricted to using genes from this pool of genotypes only. Taking the English alphabet as an example gene pool, a genetic algorithm will only be able to produce strings with letters A to Z.

More complex genetic algorithms contain genotypes that are best analogised to tools. Each tool (genotype) performs a specific function, and acts individually without being influenced by other tools. The gene pool in this case could be described as a toolbox, wherein each tool inside is different. Tools may be taken out, used and then replaced.

8.1.2.2 Chromosome

Next up the hierarchy of a genetic algorithm is a chromosome, which is best described as a *sequence* of genes. Simple chromosomes act as an ordered set of data; a word is a precession of letters as a chromosome is a precession of genes. Chromosomes made from complex instructional genes act more like a pipeline of instructions, with an input and an output. When data is passed into the pipeline the algorithm loses control of the intermediary steps until an output is produced.

Chromosomes are no more intelligent than the individual genes from which they are comprised. Each chromosome is a series of data or instructions, and once created the algorithm loses control and vision of its inner workings. Chromosomes are generated by

creating genes at random (restricted by the genotypes available in the gene pool) and linking them together in sequence.

Size of the chromosome is specified by the parameters of the algorithm, dictating how many genes are required to construct a chromosome. Most commonly the genetic algorithm will ensure that all chromosomes are created with equal size. It is possible to code the algorithm to construct chromosomes of varying length, between two limits, however this may dramatically impact the performance of the algorithm (for better or worse) due to much larger chromosome diversity.

8.1.2.3 Individuals, populations and generations

An individual is a self-contained, complex, intelligent system that is comprised of one or more chromosomes (depending on the design of the genetic algorithm). Individuals have their own motives, priorities and environmental pressures as dictated by the parameters of the genetic algorithm. The goal of the algorithm will determine the complexity of an individual; often it is sufficient that an individual be comprised of just one chromosome. In this case, the algorithm has been tightly defined: '*how well can we solve this specific problem?*'. Individuals comprised of multiple chromosomes are more suited to issues of larger scope: '*how can we navigate this maze?*'.

Regardless of the complexity, each individual represents a potential solution to a particular problem. Individuals are fully autonomous systems; they have a problem set by the algorithm and are able to test their performance in attempting to solve this problem. Individuals contain the functionality to assess themselves and breed with other individuals, should they survive. The assessment procedure gives the individual a 'fitness' value; this value determines how well they are able to solve the given problem.

A collection of individuals is called a population. As with the chromosome size, the size of the population is usually kept static to offer greater control over the algorithm. Increasing the size of a population will expand the pool of potential solutions, producing a two-fold effect. A larger population may produce more 'rolls of the dice' when generating individuals, potentially increasing the number (not the chance) of quality individuals. This will, of course, also increase the number of poor solutions, however the algorithm is designed to select only the strongest for reproduction. The problem with a large population is the greatly increased time it takes to assess every individual, slowing down the whole algorithm. A smaller population will take much less time to assess, however progress will be made in smaller steps. A compromise must be made between size and speed for the best performance.

Consider that a population is a collection of individuals at a given time, called a generation. The first generation will contain individuals all created at the same time. When they are assessed by the algorithm, individuals are given a fitness rating that determines if they survived long enough to reproduce. The offspring, along with some of the fittest individuals, will be brought forward into the next generation. Only individuals that comprise the new generation will be assessed for fitness in the next iteration of the algorithm. This evolution procedure continues so that the fittest individuals survive and reproduce, while the weaker individuals do not.

8.1.2.4 Fitness

At every iteration of the algorithm, the whole population of individuals are assessed for their ability to perform a task and are then given a fitness value. This value is not a simple binary decision, i.e. *'was the individual successful?'*. It is more like an examination - there is a perfect score (100%), and a scale of success (0% to 100%). This system allows the algorithm to compare the individuals with each other, sorting them by ability. The determination of this fitness value is achieved through a fitness function, and is the most critical part of the genetic algorithm.

Though the GA is often simply designed and will search for solutions autonomously, it is not a trivial or lazy approach to programming. The successful operation of the GA hinges completely on the quality of the fitness function. The programmer must have intimate knowledge of the nature of the task being addressed. Fitness functions can range from a simple measurement to a biased compound formula wherein all individual elements are weighted differently by their importance to the overall result.

Gold standard

The fitness function provides an objective assessment of the performance level of an individual. With the analogy of the examination, the fitness function is the process of checking an individual's responses to questions against an answer sheet. The answer sheet in this case contains all the right information to obtain a perfect score. This is what is known as a 'gold standard'. Gold standards are not a good way to form a fitness function for a GA, as the solution must first be discovered through some other means and then fed into the algorithm.

Using the previous analogy, this is equivalent to handing the student the answer sheet during the examination. This may prove that the student has the capability to correct their answers for a perfect score, however it does not allow the student to achieve the

result on their own merit. It is, however, a good way to test that the GA functions correctly if it can generate the same result.

The simplest fitness functions are those of basic measurement: '*How much power do I have?*'. In these cases the GA may be designed to obtain as high power as possible, or perhaps a power within two user-defined limits.

Though most GAs operate autonomously without any user input, this may not be possible with complex or subjective tasks: '*Have I perfectly segmented tissue from bone in this CT image?*'. In these cases it may be beneficial if the algorithm is configured to allow user input after every n number of generations. The algorithm could present the results of the fittest solutions and an expert user could select the most accurate. This could potentially override the decision of the fitness function, and guide the evolution through expert user evaluation.

8.1.2.5 Creating a new generation

Once every individual in the population has been tested for fitness, the algorithm begins creating individuals for the new generation. The new generation is populated in three ways:

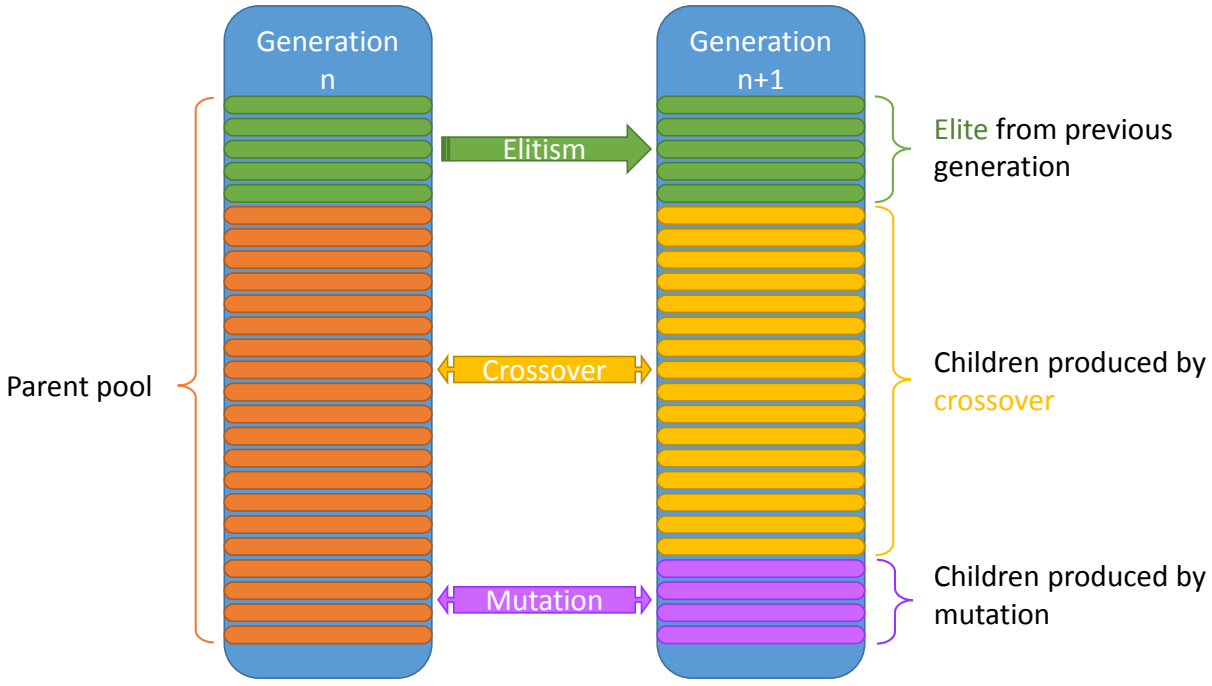

FIGURE 8.2: Diagram showing the composition of a generation. A portion of a created generation will be the best performing individuals from the previous generation, with the remaining slots filled by children produced during the reproduction cycle.

Elitism

The best individuals of the current generation are transferred directly to the next generation without change. This is done to ensure preservation of the fittest individuals between generations. Only a few elite individuals should be selected, usually making up 5% of the new population

Once the elite individuals have been transferred over, the remainder of the new generation is populated by offspring of the current generation. Both methods involve the selection of one or more parents, covered in section 8.1.2.6. When child is being produced, there is a chance it is created using either the *crossover* or *mutation* methods:

Crossover

It is most likely that a child is created using crossover. Crossover is the act of selecting two or more parents and combining them to produce a child. Given a good genetic diversity, crossover reproduction should develop varied offspring that combine elements of their parents. Crossover breeding typically encourages a steady increase in average fitness over the course of the GA

Mutation

There is a small chance that a child is created using the mutation method instead of crossover. Mutation involves the selection of a single parent and then making a small adjustment to its genetic composition. Mutation often changes the individual in a radical way, causing a large change in fitness when compared with the original version.

Mutation can be responsible for sharp increases of the maximum and minimum fitness values in a generation. Since weak individuals will have a low chance of breeding, there is an overall positive effect of strong mutants encouraging the GA to expand the search space away from local maxima

8.1.2.6 Parent selection

Once the elite individuals of the current generation have been transferred to the new generation, the remaining slots must be populated with individuals. All these individuals are offspring of the current generation. The algorithm iteratively creates a child for every remaining slot of the new population, until reaching the maximum specified population size. Each time a child is created, a decision is made on the method of reproduction as outlined in section 8.1.2.5. The reproduction method determines the number of parents the child will have, and then the algorithm must select each parent.

The purpose of this phase is to evaluate which individuals in the current generation are fitter than others and have them breed to produce a new, stronger generation. Weaker individuals will be prohibited from breeding, or given a low chance to breed. In cases of multiple parents, one individual cannot be selected twice (i.e. to breed with itself), however this does not prohibit a single individual from being selected again during the production of another child.

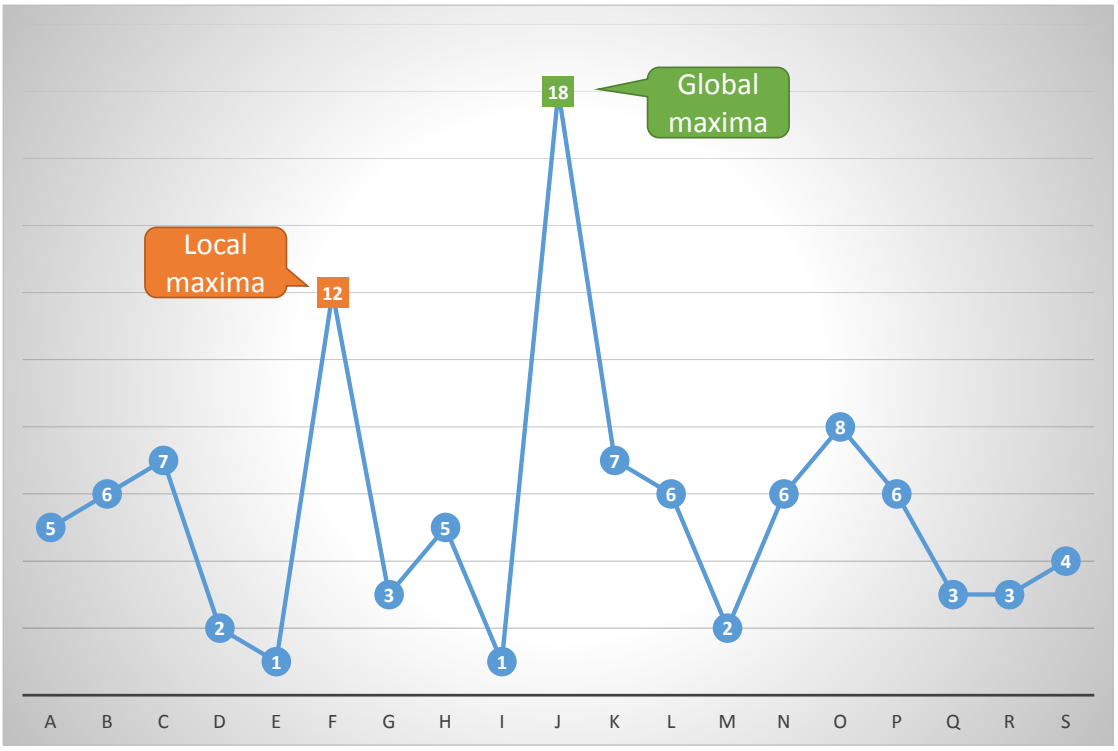

FIGURE 8.3: Diagram demonstrating local and global maxima in the search space for a GA.

There are several ways of selecting parents for reproduction; it is not as straightforward as choosing only the few strongest individuals. It is desirable to breed from a genetically diverse set of parents, as the offspring of a strong and comparatively weak individual may be stronger than the offspring of two similarly strong parents. If the parent diversity is too small then the GA may get stuck on local maxima. Several techniques for parent selection are described below.

Random selection

Selecting individuals completely at random without regard to their fitness is a chaotic method that certainly encourages genetic diversity. Without any bias in the decision making process, weak and strong individuals are equally likely to be selected as eligible

for breeding. This is not usually an attractive choice for parent selection, however due to its unbiased selection it can be beneficial as a secondary selection method. The GA could be configured to use a more structured selection method for the majority of the parent pool, and then fill the remaining slots at random to add some diversity, a 'wild card' element.

Random selection is the method used to create the first generation of individuals when a GA is executed. It can also be used to save a GA from stagnation during execution. If little progress is being made with regards to average population fitness, the GA can be configured to produce lower than the normal amount of children during the next reproduction phase. The remainder of the available positions for the new generation are filled with randomly generated individuals, much like the initial starting population. These individuals are injected into the GA to provide genetic diversity in an attempt to guide the GA away from local maxima.

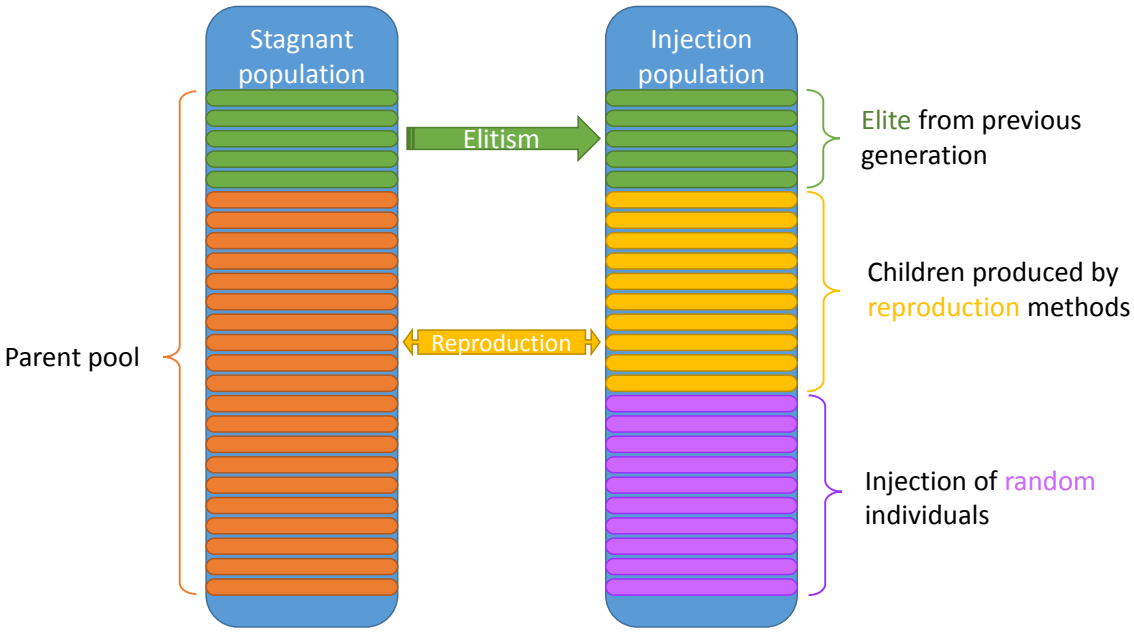

FIGURE 8.4: Diagram depicting the injection of random individuals into the next generation to revitalise a stagnant GA.

Truncation selection

Truncation selection is almost as simple as random selection. Given a population of individuals sorted in descending order by fitness, the truncation method simply pulls a parent from a subset of the fittest individuals. The size of the subset can range from

80% of the population down to 20%. Although breeding from the top 20% individuals may seem like a good idea, it can rapidly reduce the genetic diversity of the population.

Roulette wheel selection

$$p_i = \frac{f_i}{\sum_{i=1}^{N} f_i} \tag{8.1}$$

Also called the *fitness proportionate selection* method, roulette wheel is also a method of selecting parents based upon fitness. This is a more sophisticated method than truncation; the core idea is that every individual is eligible for breeding, though individuals with higher fitness are more likely to be selected. Roulette wheel is a formulaic representation of *survival of the fittest*, wherein the probability of survival (and reproduction) increases with fitness.

All individuals are first sorted by their fitness, and then a sum of all these fitness values is made. Selection chance for an individual is calculated through a fraction of individual fitness over total population fitness. Equation 8.1 depicts the probability p of individual i being selected for reproduction based upon its fitness f_i as a fraction of sum population fitness $\sum_{i=1}^{N} f_i$.

This selection method can be represented visually with a pie chart, with a segment for every individual in the population. The size of the segment is directly related to the fitness of the individual in relation to the sum fitness of all individuals in the population. There may be a case where only one individual has high fitness in the population. In this instance, the selection chance of this individual will be very high, potentially producing many children.

Rank selection

Rank selection is a variant of the roulette wheel selection described above. The chief problem with roulette wheel is the case described where only a small number of individuals in the population have a very high fitness. The effect would be a very high selection chance for these few individuals, vastly limiting the genetic diversity of the individuals in the next generation.

$$rsum_i = \sum_{i=1}^{N} r_i \tag{8.2}$$

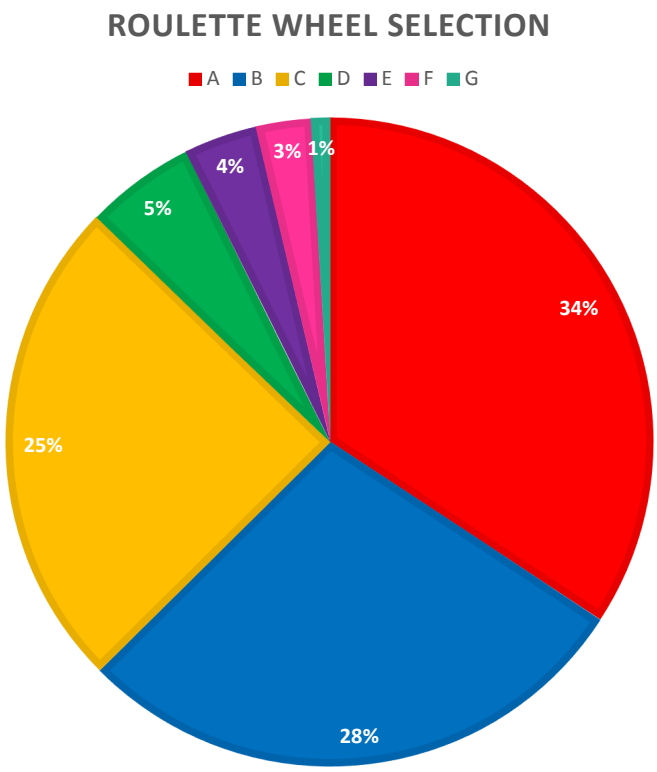

FIGURE 8.5: Diagram representing roulette wheel selection. Each individual has a percentage chance to be selected for reproduction derived from its fitness as a fraction of the average fitness of the generation.

This method is designed to counter this problem, whilst still giving increased selection chance to fitter individuals. The first step remains the same: the population is sorted by fitness. Once individuals are sorted by fitness, the algorithm assigns a sequentially decreasing numerical rank to every individual in the sorted population. For a population of 100 individuals, the fittest individual will be assigned a rank of 100 and the weakest will be assigned 1. Equation 8.2 shows the calculation for the rank sum $rsum_i$ of all individual ranks r_i.

$$rank_i = \frac{r_i}{rsum_i} \tag{8.3}$$

The roulette wheel is now created again, using the rank value instead of fitness. This time, the segment for each individual is only slightly smaller than its fitter neighbour, preserving the bias for fitter individuals without them dominating the selection wheel. Equation 8.3 shows the calculation of an individual's rank $rank_i$ as a simple fraction of its rank r_i over the sum of all ranks $rsum_i$. For the example population of 100, a range of the fittest to weakest individuals will have the following selection chance:

Rank	Selection Chance
100	1.98 %
75	1.48 %
50	0.99 %
25	0.49 %
1	0.0198 %

TABLE 8.1: Sample selection chances for rank based selection.

In this case, the weakest solution is 100 times less likely to be selected than the strongest individual, even though their actual fitness difference could be several orders of magnitude more.

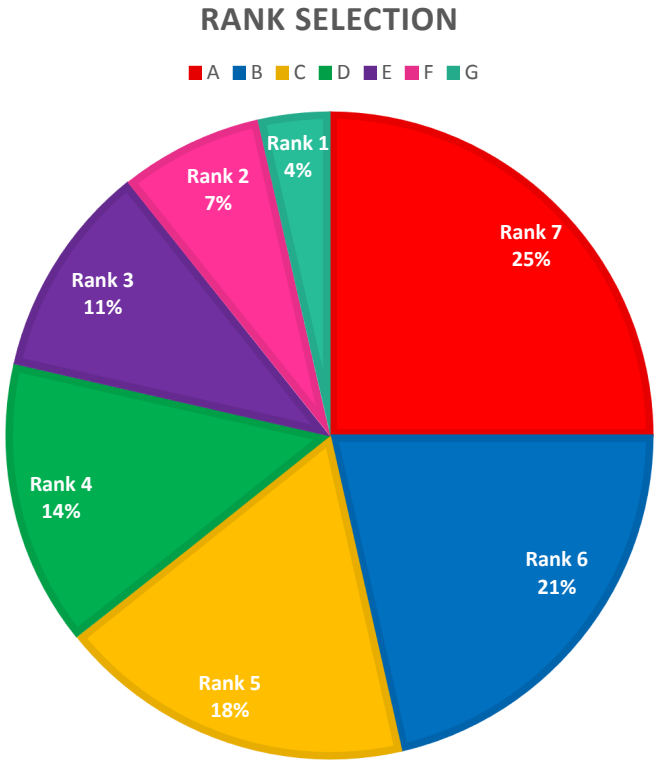

FIGURE 8.6: Diagram demonstrating rank based selection. Similar to roulette wheel selection, though selection chance is based upon individuals fitness rank in their generation rather than their actual fitness value.

Tournament selection

A different approach to the ranking methods is a combination of random selection and elitism. Tournament selection involves the random selection of individuals from a population and selection of the fittest. Binary tournament selection is the process of picking two random individuals from the population and choosing the fittest. Both large and

binary tournament selection can be repeated as necessary for each parent until the mating pool is filled. Increasing the size of the tournament will increase selection pressure; individuals with lower fitness will have a smaller chance of being selected in larger tournaments.

8.1.2.7 Reproduction

As described in section 8.1.2.5 there are two ways of producing a new individual for the next generation. Crossover has the highest chance of occurring and will involve the selection of two or more parents for reproduction. Mutation is the alternative and involves taking a single parent and modifying it in some small way to produce offspring. This section explains both methods and their variants in detail.

Crossover (1-point)

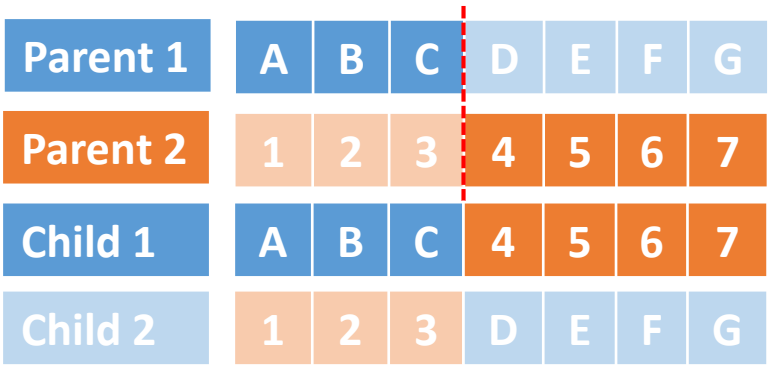

FIGURE 8.7: Diagram showing two parents undergoing crossover reproduction. The red dashed line indicates a mutually shared crossover point. Genetic material up to this point is extracted from parent 1 and added to the child. The genetic data after the crossover point is extracted from parent 2 and added to the child. The result is a child with shared genetic data from both parents; all chromosomes maintain the same length. Child 2 is optionally used by some GAs, formed from the remaining segments.

Crossover is the process of taking chromosomes from both parents and combining them to create new chromosomes. Depending on the complexity of the algorithm, individuals may be constructed of multiple chromosomes or, more often, just a single chromosome. In the case of multiple chromosomes, only equivalent chromosomes will crossover.

Recall from section 8.1.2.2 that a chromosome is a sequence of genes of (usually) fixed length. Crossover involves random selection of a crossover point and cutting the chromosome into two parts. Fig 8.7 represents crossover production of a child from two parents, where the chromosome length is constant. This method can be used to produce

a single child if the remaining segments are discarded, or a second child can be formed using these segments.

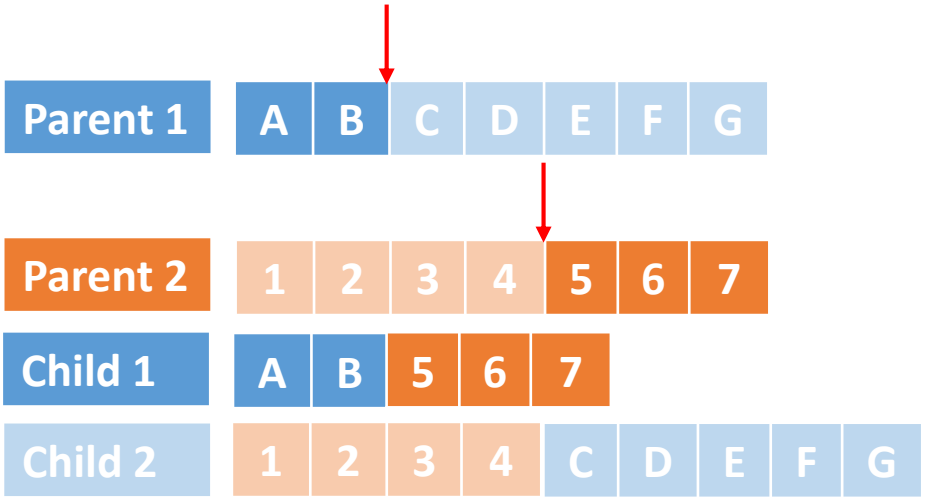

FIGURE 8.8: Diagram showing two parents undergoing crossover reproduction. The red arrows show randomly determined crossover points for both parents. Genetic material up to this point is extracted from parent 1 and added to the child. The genetic data after the crossover point is extracted from parent 2 and added to the child. The result is a child with shared genetic data from both parents; in this case both children have variable length chromosomes.

If the algorithm is not concerned with preserving chromosome length, the crossover procedure can be modified slightly. Fig 8.8 shows two parents each having a randomly determined crossoverpoint. Both chromosomes are cut at the crossover points and a child is assembled. In this case, the child chromosome is over 5 genes long compared with the parents chromosome of 7 genes. Again, a second child can optionally be constructed from the remaining segments, in this case child 2's chromosome is 9 genes long.

Crossover (Multi-point)

A different approach is to perform crossover reproduction with multiple points of crossover. In this case each chromosome is cut multiple times and the child assembled from a combination of cut segments.

2-point crossover reproduction is shown in Fig 8.9 with constant chromosome length, and in Fig 8.10 with variable chromosome length. In both cases, the second child can be optionally used each time to add a second individual to the next population. For ease of use it is more common to discard the second child so that the parent selection procedure is performed more often to fill the new generation.

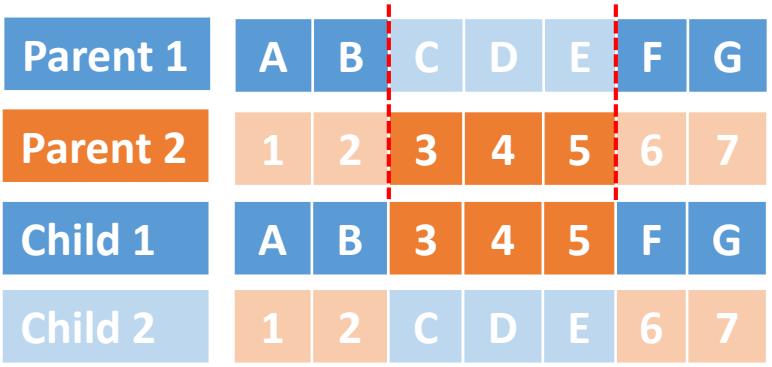

FIGURE 8.9: Diagram showing two parents undergoing crossover reproduction. The red dashed lines indicate mutually shared crossover points. Genetic material up to the first crossover point is extracted from parent 1 and added to the child. The genetic data after the first crossover point is extracted from parent 2 and added to the child. Finally, the data after the second crossover point is taken from parent 1 to add to the child. Chromosome length here is preserved. Child 2 is optionally used.

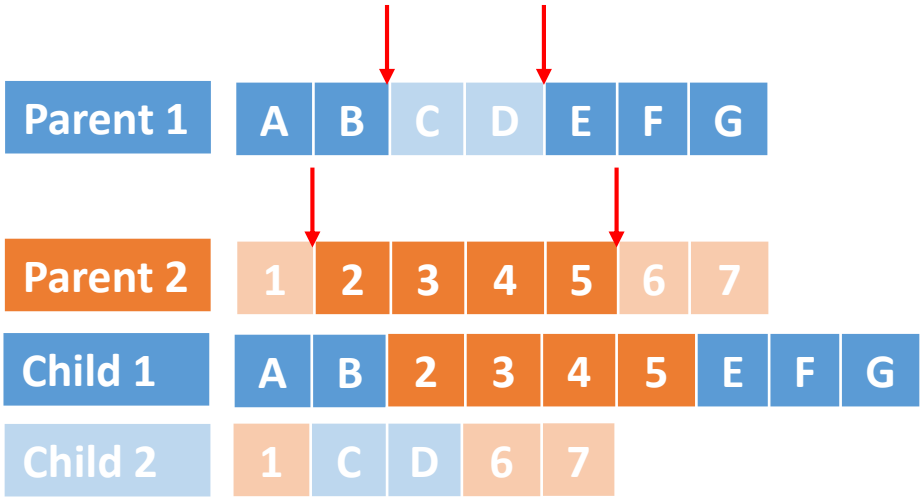

FIGURE 8.10: Diagram showing two parents undergoing crossover reproduction. The red arrows indicate random crossover points. Chromosome length here is variable. Child 2 is optionally used.

Crossover (Uniform)

An alternative crossover method is presented in Fig 8.11. Instead of cutting parent chromosomes at randomly determined positions, the child is instead formed by determining crossover points for every gene. For a $p = 0.5$ uniform crossover, every gene in the child has a 50% chance to be taken from either parent at the same point in the sequence. This method achieves almost equal contribution of genetic material from both parents to the children.

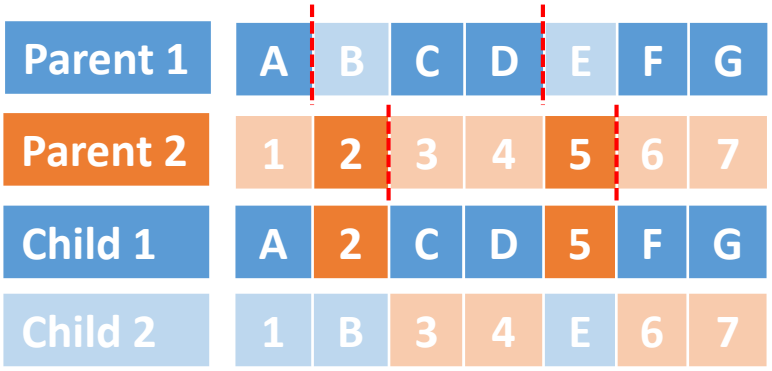

FIGURE 8.11: Diagram showing uniform crossover with $p = 0.5$. Each gene has a 50% chance of being taken from either parent. Child 2 is optionally used.

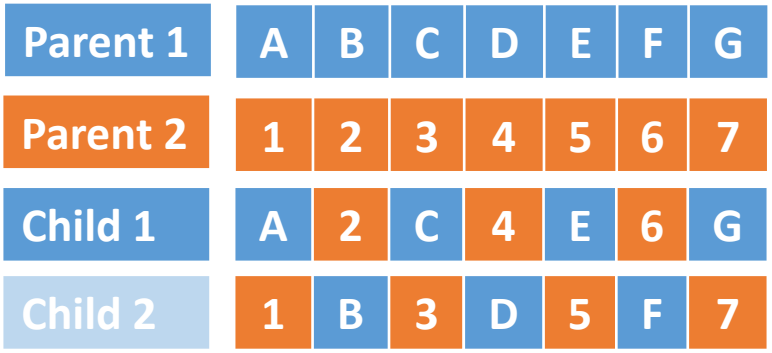

FIGURE 8.12: Diagram showing uniform crossover with $p = 1$. This guarantees that crossover occurs after every gene, ensuring an equal contribute to the child by both parents. Child is formed by taking every second gene from both parents and interweaving them together. Child 2 is optionally used.

The method can be forced to generate a child by interweaving genetic material from both parents by setting $p = 1$ as in Fig 8.12, guaranteeing alternating gene selection. This is slightly limited as it introduces too much selection bias, but it can have uses for certain algorithms.

Mutation (change)

If the algorithm determines that the child is not to be produced by crossover, it is produced by mutation instead. Mutation involves copying the chromosome(s) from a parent and making a slight modification. 1-point mutation involves making a single gene modification to the parent chromosome(s) to produce a child. Multi-point mutation may involve several of these modifications. There are three methods of mutation, the most

common being *change*. This involves randomly selecting a gene in the chromosome and swapping it with another from the gene pool, as seen in Fig 8.13.

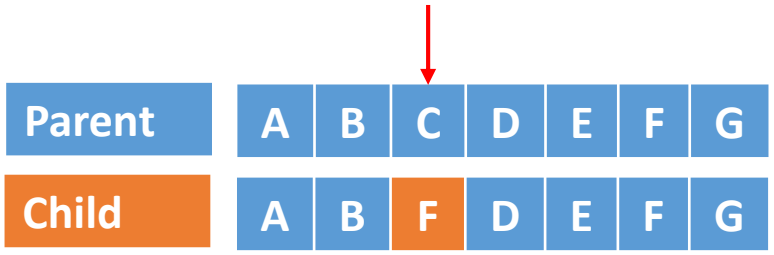

FIGURE 8.13: Diagram showing 1-point mutation, resulting in a single gene being swapped for another in the gene pool. Chromosome length is preserved.

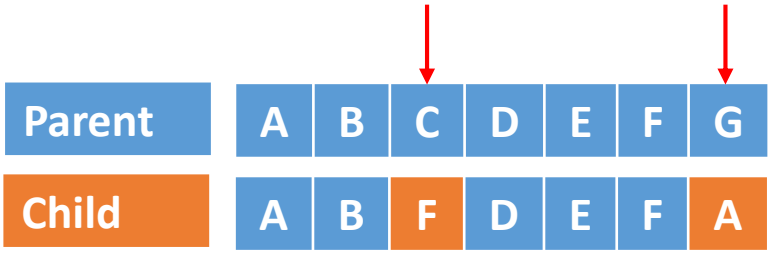

FIGURE 8.14: Diagram showing 1-point mutation, resulting in two genes being swapped for another in the gene pool. Chromosome length is preserved.

Fig 8.14 shows mutation occurring at 2 randomly selected gene positions in the chromosome.

Mutation (destroy)

Mutation can also cause the destruction of a gene in the parent chromosome to produce a new, shorter child chromosome. This method should not be used as the main form of mutation (if at all), as it may adversely affect the individual's capability to solve the problem. Destroy can be useful if implemented properly, particularly in the case where genes are functions. An example would be a chromosome designed to perform image processing, comprised of genes that modify the image in some way. Destroying one or more genes in the sequence would reduce the number of operations that modify the image. In some cases the reduction of operations can prevent corruption of the input image, improving the output quality of the chromosome.

Since this form of mutation removes genes from the chromosome, it is generally unsuitable for algorithms that handle data. Many data-driven GAs require that the output

data length matches that of the input data, in which case this method is not suitable and *change* may be better utilised.

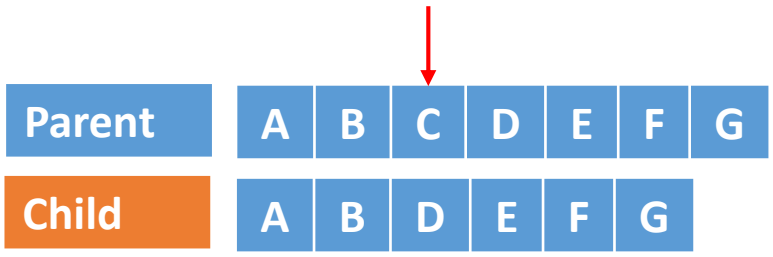

FIGURE 8.15: Diagram showing 1-point mutation, resulting in a single gene being destroyed. Chromosome length is shortened.

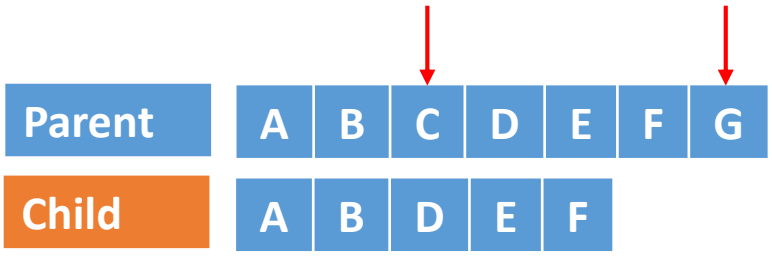

FIGURE 8.16: Diagram showing 2-point mutation, resulting in two genes being destroyed. Chromosome length is shortened.

Examples of 1-point (Fig 8.15) and 2-point (Fig 8.16)destructive mutations are shown. The child chromosome length is always less than that of the parents. When implementing an algorithm with the potential for destructive mutation, there exists a chance that some chromosomes become very short. This can severely limit the potential of the chromosome, often resulting in its removal from the population during the reproduction phase. This can be moderated with the *create* mutation method.

Mutation (create)

In addition to destroying genes, mutation can cause the insertion of new genes into the chromosome. In this case, an insertion point is randomly determined for each mutation and then a gene is selected randomly from the gene pool and placed at this point in the chromosome.

Fig 8.17 shows a single gene being inserted into the child chromosome, lengthening it. An example of multi-point creation is also shown in Fig 8.18. Predictably, the effect of

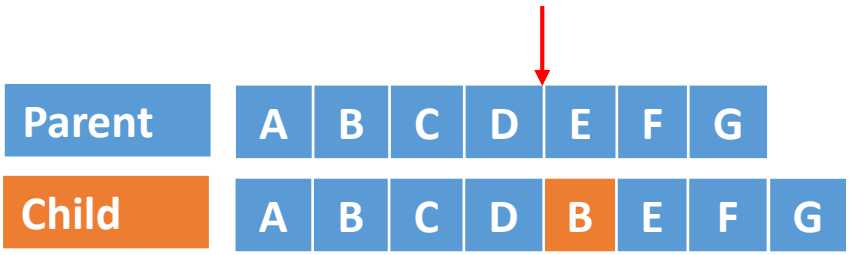

FIGURE 8.17: Diagram showing 1-point mutation, resulting in a single gene B being created and placed between D and E. Chromosome is lengthened.

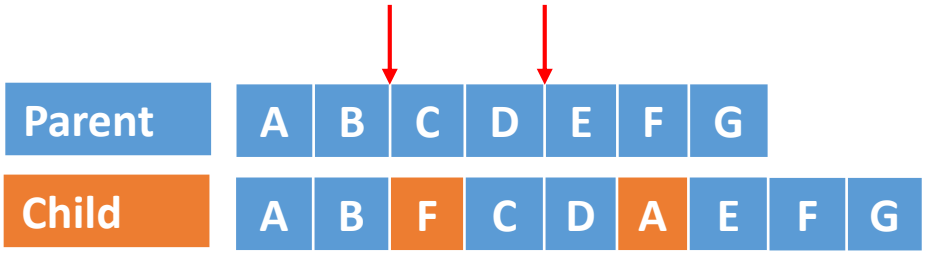

FIGURE 8.18: Diagram showing 2-point mutation, resulting in two genes F and A being created. Chromosome is lengthened.

this method is the opposite of destructive mutation. The child chromosome is lengthened and becomes more complex.

A combination of destructive and creative mutation can be used as a variation of the standard *change* mutation. The benefit of using this combination is that the GA may preserve chromosome length, and it also performs some gene 'shuffling', modifying the sequence slightly.

8.1.2.8 Iteration and evolution

At the end of a generation the GA completes the reproduction phase and creates a new population that forms the next generation of individuals to be tested. The new generation is fed into the start of the GA and the whole process is performed again. At each iteration of the GA, a new population is created during the reproduction phase and used as a starting point for the next generation of testing.

The general processes of a GA are summarised in Fig 8.19. Fig 8.20 shows pseudocode for a basic genetic algorithm. What follows is a basic description of the steps involved in programming a GA, with reference to lines in the pseudocode.

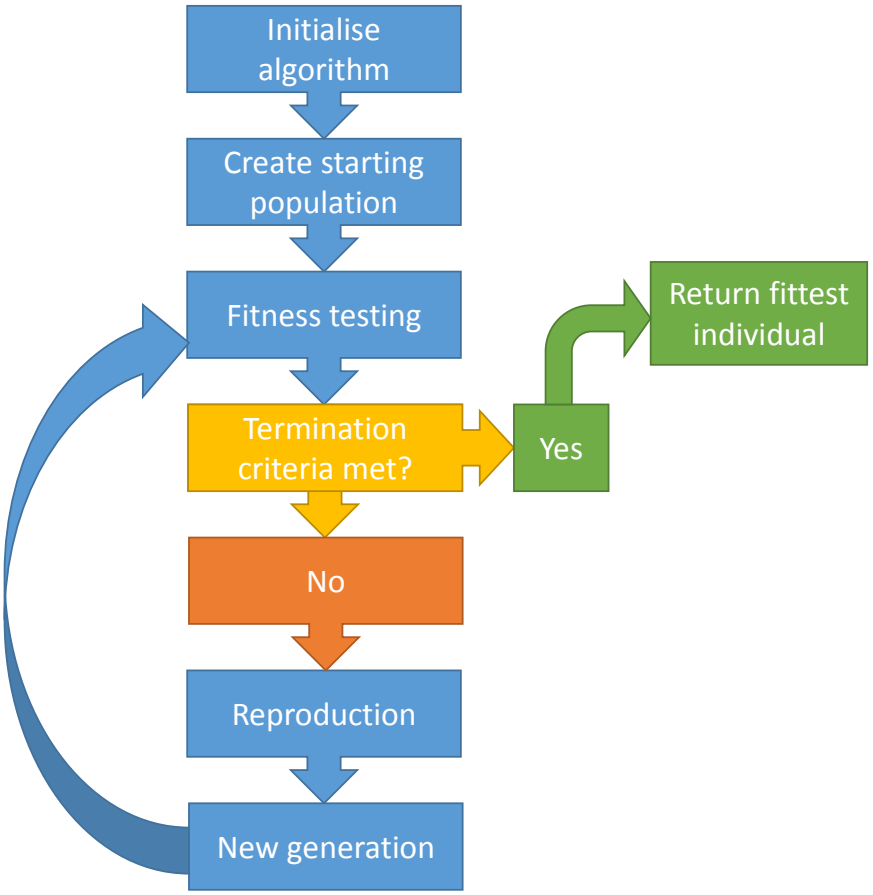

FIGURE 8.19: Diagram summarising the processes of a GA.

Starting parameters (lines 5 to 9)

- *popSize* determines the maximum number of individuals that may be created per generation. In this case, popSize is kept constant throughout the runtime of the GA
- *maxGens* is a user defined cap on the number of iterations that the GA will run for. The GA will run a number of iterations equal to this value and then terminate, if no other termination criteria are met before this time
- *mutationChance* is a percentage chance of a child being created through mutation rather than crossover. In this case, the mutation chance has been set low at 5%
- *numElite* specifies the number of fittest individuals to be preserved into the next generation at the end of every iteration. In this case, once the population has been sorted by fitness, the top 10 individuals will be placed directly into the new population without modification

```
Step 1: Initialisation
==========================================================================
Algorithm parameters
--------------------------
popSize = 1000;
maxGens = 50;
mutationChance = 5;
numElite = 10;
cLength = 10;
--------------------------
Placeholders
--------------------------
pop = zeros(cLength, popSize);
newPop = zeros(cLength, popSize);
popFitness = zeros(1, popSize);
individual = zeros(cLength, 1);
--------------------------
Generate starting population
--------------------------
for i = 1 : popSize
  for j = 1 : cLength
    individual(j) = randomGene();
  end
end
==========================================================================
Step 2: Evolution
==========================================================================
for generation = 1 : maxGens
  --------------------------
  Check termination criteria
  --------------------------
  if generation == maxGens
    break;
  end
  --------------------------
  Test population fitness
  --------------------------
  for i = 1 : popSize
    individual = pop(:, i);
    fitness = testFitness(individual);
    popFitness(:, i) = fitness;
  end
  --------------------------
  Sort population by fitness
  --------------------------
  [sortedFitness, indexes] = sort(popFitness, 2);
  sortedPop = pop(:, indexes);
  --------------------------
  Select elite individuals and promote to next generation
  --------------------------
  for i = 1 : numElite
    newPop(:, i) = sortedPop(:, i);
  end
  --------------------------
  Generate children and place in next generation
  --------------------------
  for i = 1 : (popSize - numElite)
    parent1 = randomParent();
    if randi(100, 1) <= mutationChance
      mutatePoint = randi (cLength);
      child = mutate(parent1);
    else
      parent2 = randomParent();
      crossOverPoint = randi(cLength);
      child = [parent1(1 : crossOverPoint);
               parent2(crossOverPoint + 1 : cLength)];
    end
    newPop(:, i + numElite) = child;
  end

  pop = newPop;
end
```

FIGURE 8.20: Pseudocode for genetic algorithm

- *cLength* determines the chromosome length. For this algorithm, every chromosome will be created with 10 genes

Placeholders (lines 13 to 16)

- *pop, newPop* are both initialised here as 2D arrays of dimension (10, 1000). *pop* will store the current population from which each iteration of the GA starts. *newPop* will be filled with both elite and child individuals during the reproduction phase
- *popFitness* is a 1D array that will contain a single fitness value for every individual in the population. During the fitness testing phase, this indexed array will be filled with the fitness value of the individual at the corresponding index in the *pop* array
- *individual* is also a 1D array, and will be used to contain an individual (consisting of cLength number of genes)

Generation of starting population (lines 20 to 24)

There are two loops in this section of code. The outer loop runs from 1 to *popSize* (1000) and is responsible for creating an individual for each cell in the *pop* array. The inner loop runs from 1 to *cLength* (10) and, for each new individual in *pop*, will create a sequence of *cLength* genes using the *randomGene* function

Evolution loop (lines 26 to 72)

This is the main loop of the GA, and runs from 1 to *maxGens* (50) unless otherwise interrupted by the termination criteria. Details of the contents of the loop follow.

Termination criteria check (lines 32 to 34)

There is only one termination criteria for this GA. When the current *generation* is equal to *maxGens*, the loop ends and the GA is complete. Usually there are several termination criteria, such as a time limit or when sufficient fitness has been reached

Fitness testing phase (lines 38 to 47)

This loop iterates over the entire population. For each i an *individual* is selected from the *pop* array and the *testFitness* function determines the individual's fitness. This value is then stored at position i in the *popFitness* array. The *popFitness* array is used to reorder data in the *pop* array using matching index (i) values. This has the effect of sorting individuals in *pop* by fitness value

Reproduction phase (lines 51 to 71)

- **Elite promotion**
  Before reproduction commences, the top *numElite* fittest individuals are placed directly into *newPop*.
- **Parent1 selection**
  Reproduction is performed by creating a single new individual for each remaining slot (*popSize* - *numElite*) in *newPop*. Regardless of the method of reproduction, at least one parent is needed. *parent1* is selected by the function *randomParent*. The selection method itself is not described here, however it may take the form of roulette wheel or rank selection as described in section 8.1.2.6
- **Determination of reproduction method**
  A random integer between 1 and 100 is generated by the algorithm. If this number is less than or equal to *mutationChance* then the child will be produced by mutation. With *parent1* already selected, another random number between 1 and *cLength* is selected to determine the *mutatePoint*. With the gene selected, the child is created by copying *parent1* and mutating the gene at *mutatePoint* using the *mutate* function (not shown)

  If the criteria fails the mutation check then the child will be produced via crossover. A second parent, *parent2*, is selected using the *randomParent* function. As above, a number between 1 and *cLength* is generated to determine the *crossOverPoint*. The child is then created using 1-point crossover at this point

  Once created, either by mutation or crossover, the child is placed into *newPop* and the loop continues

Iteration (line 71)

This final line replaces *pop* with *newPop*, effectively discarding the old population for the new generation of individuals to be tested by the next iteration of the GA. It may be beneficial instead to store *pop* in a matrix (ordered by generation) to preserve the history of the GA

8.1.2.9 Termination of the GA

GAs need to eventually terminate and present a final 'fittest' solution. The termination of a GA is a delicate balancing act and is usually governed by several parameters. The GA could terminate if one of the following criteria are achieved:

- The algorithm has reached the maximum number of generations as specified by the GA parameters
- The algorithm has found a perfect solution as determined by the fitness function
- The evolution has stagnated: average fitness of individuals in the population has not increased for the threshold number of generations specified in the GA parameters.
- The running time of the algorithm has exceeded the limit specified in the GA parameters

The procedure of the GA searching for a result is called *convergence*. The most desirable termination case is when the GA converges on the global maxima of the search space and is unable to find a better result. There are several indications that a GA has performed poorly:

Fast convergence

The GA converges very quickly on a solution and terminates early. It is likely in this case that the GA has reached a local maxima and the configuration of the algorithm prevents searches outside this space. This can happen when the population size is too small or the reproduction parameters are too restrictive

Slow convergence

The opposite scenario of fast convergence is when the GA terminates (due to timeout or by reaching the maximum number of generations) while progress is still being made. If there is still an obvious trend of increasing fitness as the algorithm terminates, either the termination criteria could be adjusted or it could mean the reproduction system is not aggressive enough in weeding out weaker individuals

Fluctuating average and best fitness values

An observant user may watch the GA reports and discover the average and best fitness values for each generation are not trending upwards. Though it is expected that these values may plateau occasionally, they should not ever decrease. If the values dip then this could indicate that there is a problem in the selection or reproduction system. Specifically, the elite individuals are not being preserved perfectly between generations

Stagnation

GAs may experience periods of slow growth where fitter solutions are not being

found for several successive generations. This should not occur too often - if the algorithm is seen to chart average fitness over time as a sequence of plateaus punctuated with sharp increases, this is a problem.

This behaviour would suggest that the starting population was poor, and the algorithm is having difficulties in finding direction through standard reproduction techniques and may be relying heavily (or solely) on mutation to produce children, which would explain the occasional sharp increase in fitness. It would be best to alter the selection and breeding parameters in this case, or cull the population and inject fresh randomised individuals to replace them

After every generation the GA may present a report. The most important factors to the running of a GA are contained within this report. This information is used internally by the algorithm to evaluate the stopping criteria presented in section 8.1.2.9.

- Fitness value of fittest solution
- Fittest solution result (e.g. image, measurement ...)
- Fitness value of weakest solution
- Average fitness of population this generation
- Difference of average fitness from previous generation (value and percent)
- Number of mutations

8.2 Methodology

8.2.1 Overview

For this experiment a DM with 52 actuators is used. The DM will accept a range of decimal voltage values between ± 1 V. A genetic algorithm will be required to send a set of 1D arrays containing 52 values to the DM in sequence. Each cell of the 1D array represents the voltage sent to a single actuator, and will contain a valid value between -1 and 1. The optical configuration itself is the same as that described in section 5.2.2. For this experiment the WFS is not utilised to detect optical aberrations.

8.2.2 Optical system

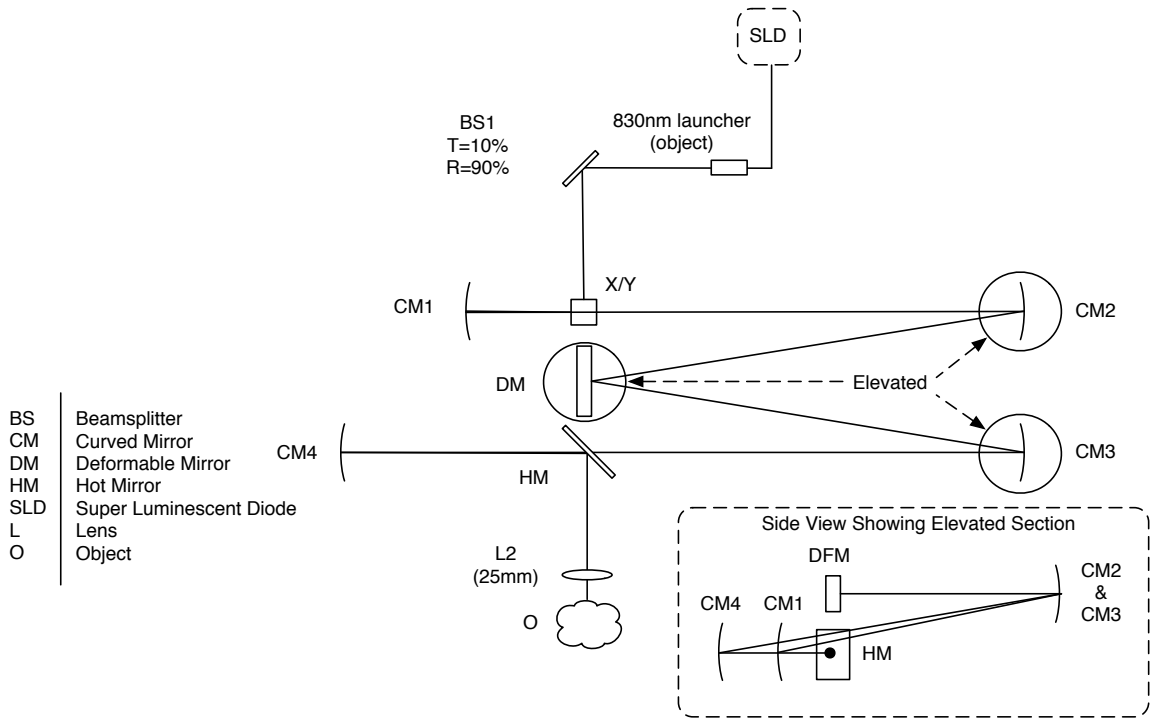

FIGURE 8.21: Diagram showing an AO/SLO system without the WFS.

An AO system equipped with a 840 nm broadband SLD confocal arm is used for this experiment. Fig. 8.21 shows the optical setup used; note the removal of the WFS when compared with Fig. 5.4. During the execution of the GA the XY galvoscanners remain static and in a zeroed position. The object in this case is a mirror for maximum reflectance. Being a specular target, the mirror also proves to be a trickier target than a scattering surface as any slight variation can cause all rays returning from the object to miss the injection fibre. Returned light is measured using an APD with peak sensitivity at 840 nm.

All software is written in LabVIEW to enable real time processing. The software initialises with a population of randomly constructed individuals and then begins the testing sequence.

8.2.3 GA structure

This section will describe the process of fitting DM manipulation and wavefront optimisation to the architecture of a GA. The introductory section on GAs (section 8.1.2) decomposed the premise of a GA into a simple hierarchical structure as shown in Fig.

8.1. What follows is a detailed correlation of the wavefront optimisation method to the basic GA structure.

8.2.3.1 Genes and the gene pool

In the context of wavefront manipulation using a DM, a gene will be the voltage setting for an individual actuator. Logically, the gene pool will therefore be the range of voltage values that are accepted by the DM. The specifications of the DM are described in Appendix A. Tab. A.1 shows that the actuator output voltage is in the range ± 1 V for each of the 52 channels. This range of values will be the effective gene pool for the GA; a gene may only take a value within this range. The GA will operate with genes that are numerical values between -1 and 1, which should limit the complexity of the system.

8.2.3.2 Chromosome

The next step in the hierarchy is the chromosome. Since a gene represents the voltage value of a single actuator, the chromosome therefore exists as a set of voltages. The Mirao-52e DM contains 52 actuators which will determine chromosome length. The DM will accept a 1D array of 52 numerical values provided they are within the acceptable voltage range. Tab. A.3 shows the layout of the actuators in the Mirao-52e, and indicates the positions of the actuators corresponding to indexes in the 1D array of 52 values. The central four actuators are governed by the values at indexes 22, 23, 30 and 31 in the 1D array, for example.

This GA does not require that an individual has more than one chromosome. One individual will contain one chromosome, which is comprised of 52 voltage values to configure the shape of the DM.

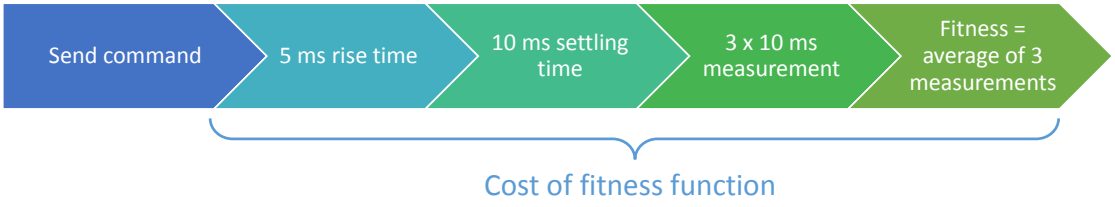

FIGURE 8.22: Diagram showing the workflow of a fitness measurement for a single individual.

8.2.4 Fitness function

The fitness function chosen in this case is of the simplest form: magnitude of power received by the photo-detector. There are many complex ways to judge the suitability of a given DM configuration with regards to wavefront correction, however it can be assumed that better corrections always have the effect of increasing detected signal from the object. The GA itself will be blind to the particulars of the optical system and the state of the wavefront. Instead, a simple metric of output voltage from the photo-detector will be used as a basis for comparison of individuals. The APD chosen for this experiment saturates at a maximum output of -10 V. The output power of the SLD will need to be moderated such that the APD does not reach saturation during the evolution of the GA algorithm.

Tab. A.1 shows that the rise time is $\leq$ 5 ms for a single actuator with a voltage step of 0.3 V. There is also a settling time of approximately 10 ms, though this varies with step voltage magnitude. Measurements of the photo-detector should therefore be taken at no more than intervals of 15 ms. Each individual measurement will acquire voltage from the detector for 10 ms, with the peak value being retained. This will be performed three times per individual and the average of the peak values taken. Given the parameters specified above, it can be calculated that a fitness measurement will take approximately 45 ms. For a population of 100 individuals, fitness testing will take 4.5 seconds. The cost of the fitness function is shown diagrammatically in Fig 8.22.

8.2.5 Reproduction

Rank selection (as described in section 8.1.2.6) is chosen as the parent selection method for reproduction.

Fig 8.23 shows a prediction of the composition of a new population after reproduction. After fitness testing is complete, the top 5% of individuals will be copied without variation into the next generation. The remaining 95% of available slots will be filled with children produced using rank selection. Most children will be produced using 1-point crossover with two parents. Approximately 10% of the new generation are children produced via the 1-point mutation method, whereby a single parent is selected and one gene is changed.

Since chromosome length must be preserved, the only mutation method used will be *change* and crossover will maintain a maximum length of 52. Since there is great variability in the genetic composition of each individual, it is likely that most randomised solutions will be ineffective at configuring the mirror into a shape that returns any light

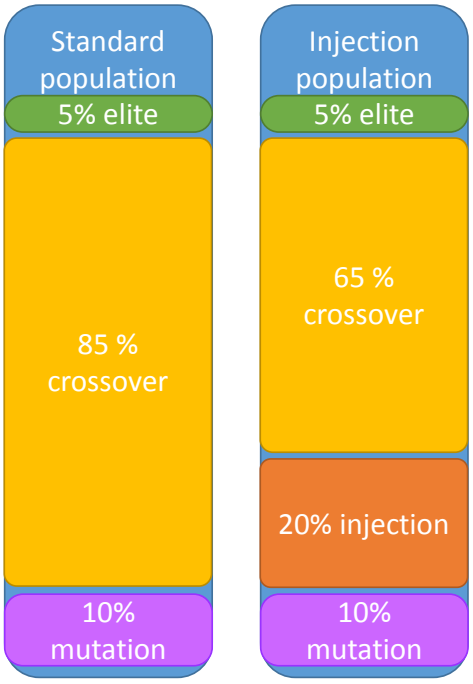

FIGURE 8.23: Diagram showing population composition prediction of new generation after reproduction phase. Presented is the composition of a standard population (left) and a population with injection of random individuals (right).

at all to fibre. Though these solutions will be bred out of the population over time, it is helpful to apply some bias to the selection method for reproduction to aid the starting speed of the GA. The bias will restrict parent selection to the top 80% fittest solutions of the latest generation. Rank based selection will choose individuals from this shortened list of individuals rather than the total population. The desired effect is a great increase in convergence speed without suffering a loss in genetic variation.

8.2.6 Calibration

The effectiveness of the GA can vary drastically with manipulation of the input parameters and the implementation of reproduction. This project will test several configurations of the GA to determine the most effective parameters. Described below are the experiments performed to test the effect of individual parameters on the overall GA performance.

8.2.6.1 Population size

The first test will determine the effect of population size on the overall speed of the GA. Three values will be used for this test: populations consisting of 1000, 500 and 250

individuals. All other values, excepting those that are calculated from population size, will remain the same. The algorithm will run until 10 generations have been created and the total elapsed time will be recorded.

Initialisation	Population size	**50 / 100 / 200 / 250 / 500**
	Chromosome length	52
	Gene pool	-1 to 1
Reproduction	Parent selection	Rank selection
	Crossover method	1-point
	Crossover chance	80%
	Mutation method	1-point
	Elite size	**3 / 5 / 10 / 13 / 25**
Termination	Fitness threshold	10 (saturation)
	Maximum generations	100
	Maximum runtime	NA

TABLE 8.2: Table showing the parameters of the GA while testing the effect of population size on execution speed of the algorithm.

8.2.6.2 Crossover/mutation chance

The effect of varying the percentage chance that a child is produced using the crossover or mutation method is tested next.

Initialisation	Population size	100
	Chromosome length	52
	Gene pool	-1 to 1
Reproduction	Parent selection	Rank selection
	Crossover method	1-point
	Crossover chance	**50 / 60 / 70 / 80 / 90 %**
	Mutation method	1-point
	Elite size	5
Termination	Fitness threshold	10 (saturation)
	Maximum generations	100
	Maximum runtime	NA

TABLE 8.3: Table showing the parameters of the GA while testing the effect of crossover and mutation probability.

8.2.6.3 Injection frequency

For those experiments that use a periodic injection of random individuals, it must be tested whether high frequency of injections are destructive and if low frequency of injections are ineffective. Tab. 8.4 shows a range of frequencies, in generations, that will be tested.

Initialisation	Population size	100
	Chromosome length	52
	Gene pool	-1 to 1
Reproduction	Parent selection	Rank selection
	Crossover method	1-point
	Crossover chance	90 %
	Mutation method	1-point
	Elite size	5
	Injection size	10
	Injection frequency	**5 / 10 / 15 / 20 / 25**
Termination	Fitness threshold	10 (saturation)
	Maximum generations	100
	Maximum runtime	NA

TABLE 8.4: Table showing the parameters of the GA while testing the effect of injection frequency.

8.2.7 Monitoring

Progress of the GA can be monitored through two files that will be created and updated during execution. Data recorded in each of the two logs are presented in the tables below.

Population log	Timestamp	Exact time of occurrence
	Generation	Specifies the generation of the individual
	Individual	Unique identifier for individual in generation
	Actuator 1-52	Voltage values of each actuator
	Fitness	Measured fitness value
	Result	Boolean stating if command was accepted by the DM
Generation log	Generation	Specifies the generation
	Peak fitness	Measured fitness value of fittest individual
	Average fitness	Measured average fitness value of generation

TABLE 8.5: This table describes the content of the two output logs. Population log is a comprehensive report of the creation and testing of every individual throughout the life cycle of the GA. Generation log records a single line for each generation, detailing the fittest individual and average fitness for that generation.

Population log will record every individual generation for every generation, along with their associated fitness value. For ease of reporting, generation log will simply record one entry for every generation containing the fittest individual and the average fitness

of the generation. This data will also be displayed live on the screen as the algorithm is running.

8.3 Results

8.3.1 Calibration

This section details the result of the calibration tests. In these tests, the GA is executed several times with variation of a single parameter such as population size. Monitoring of the fitness progression and total execution time allows for experimental determination of optimal settings for the GA.

8.3.1.1 Population size

These tests determine the optimal population size for effective and efficient running of the algorithm. Five settings were used: 50, 100, 200, 250 and 500 individuals per generation. In each test a limit of 100 generations was set. Termination of the GA in each case is determined by the time stamp of the final generation, achieved either through reaching the limit of 100 or by saturating the detector. Total run time is calculated as the time of termination minus the time of the first command sent to the DM as the GA initialises.

Population size	**Run time**	**Final fitness**	**Fitness gain**	**Fitness/minute**
50	10:08	7.39	5.88	0.58
100	13:33	10	8.49	0.64
200	39:59	9.22	7.71	0.19
250	56:05	9.50	6.75	0.12
500	01:17:47	7.54	4.89	0.06

TABLE 8.6: This table shows the run time for 100 generations with various population sizes. Also displayed is the total gain in fitness from the initial value to the final value, and a measure of fitness gained per minute of running time.

Tab. 8.6 shows the total running time of the five experiments. Fitness gain refers to the fittest value achieved at the termination of the algorithm minus the fitness of the initial command sent to the DM. Predictably, the lowest run time of just over 10 minutes is achieved by the GA running the smallest population size of 50. A respectable fitness value of 7.39 is achieved here, though it is the lowest of the reported final fitness values. The fitness per minute is calculated as 0.58, which is the second highest value.

The GA with a population size of 500 ran for the longest time (1 hour 17 minutes) and was terminated manually at generation 57. It was evident from the data that a

population of this size was a detriment to the overall efficiency of this algorithm, given the fact that the smaller population GAs achieved much higher fitness values in a greatly reduced period of time.

Running a population size of 100 appears to be optimal as it reaches the maximum achievable fitness value in a little over 13 minutes. This iteration has the highest fitness gain and fitness per minute values, meaning it converges on the solution quicker than the other experiments.

These calibration results make it clear that the defining factor for efficiency is the number of reproduction cycles that occur within the shortest period of time, as seen with populations of 50 and 100. For an increase in effectiveness, a larger population is required for more diversity, though this can drastically reduce run time.

Fig. 8.24 shows the rising maximum fitness value per generation for each GA with varying population size. The experiment using a population size of 500 can be seen to terminate early due to its inefficiency. Reaching the maximum fitness value of 10 signifies saturation of the detector, and this is achieved by the GA using a population size of 100 in generation 69 after 13 minutes and 33 seconds. Using the results in Tab. 8.6 and Fig. 8.24, it was decided to proceed with a population size of 100 for future experiments.

8.3.1.2 Crossover/mutation chance

The results of experiments to test the effect of mutation chance on peak fitness over 100 generations are shown in Fig. 8.25. Somewhat surprisingly, the higher mutation chances appear to have a greater beneficial effect on the progression of the GA over time.

8.3.1.3 Injection frequency

Three tests were conducted to assess the effectiveness of population injection after 10, 20 and 30 generations. The experiments ran for 60 generations each and the results are presented in Fig. 8.26. From the chart it is clear that higher frequency injections have a greater positive effect on peak fitness in the short to mid term. After 60 generations, all three experiments terminate with similar peak fitness. The experiment with injections after 30 generations experiences a different growth pattern to the other experiments, though overall progress is very similar.

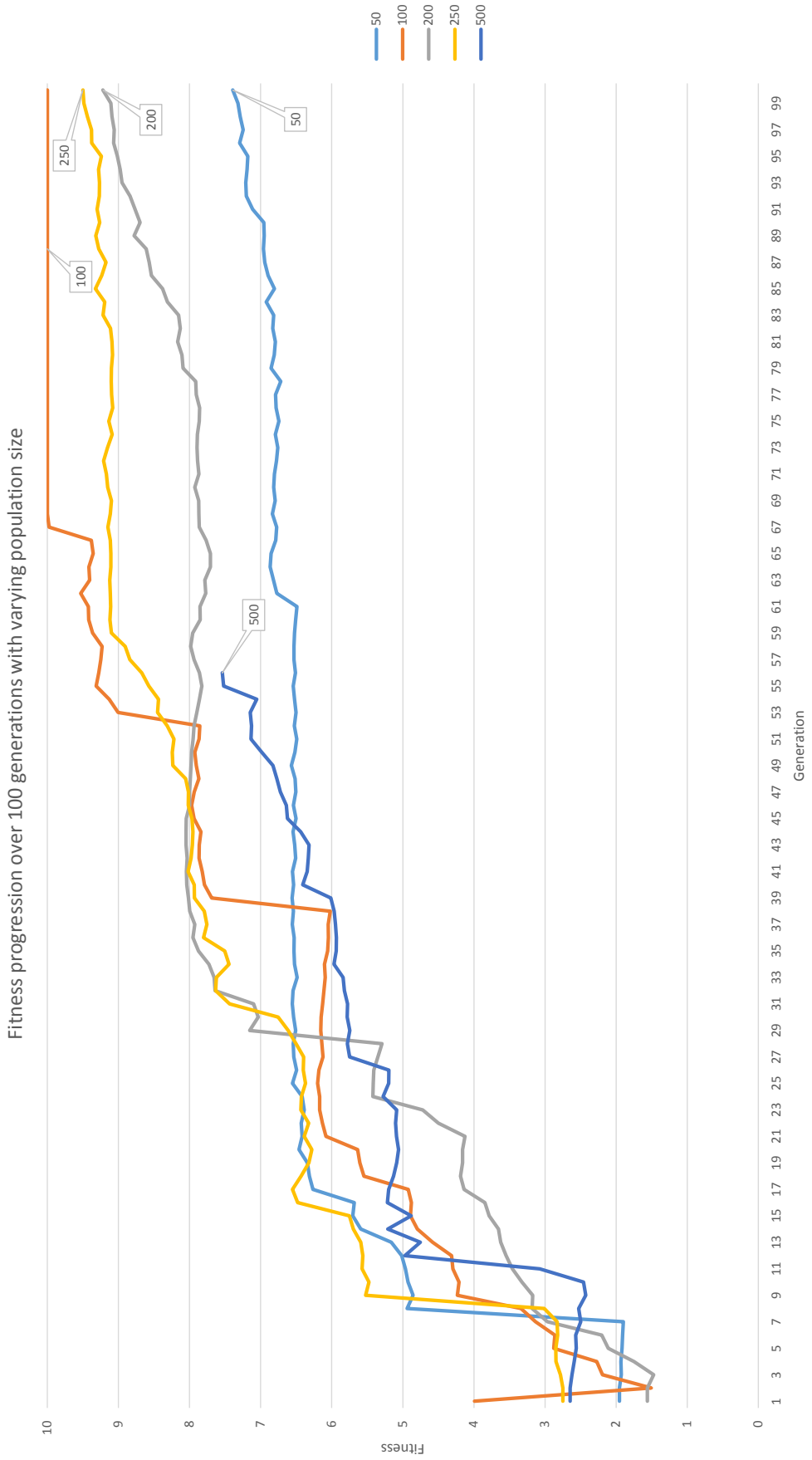

FIGURE 8.24: Graph showing results from calibration test. Presented are the progression of fittest individuals over 100 generations for five population sizes.

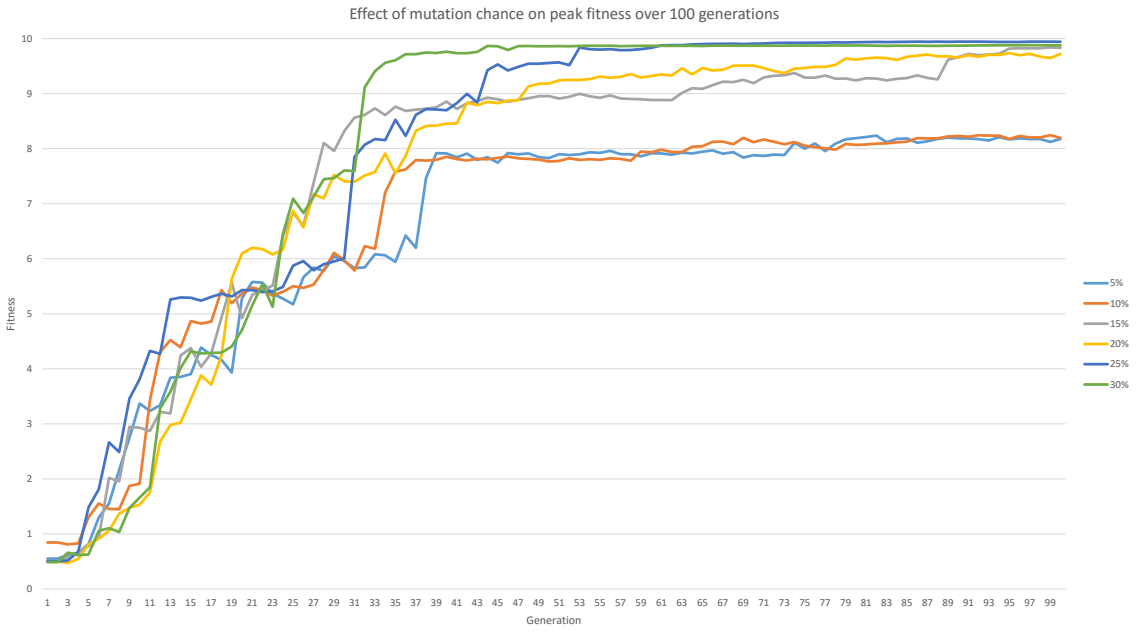

FIGURE 8.25: Graph displaying the effect of mutation chance on peak fitness over 100 generations.

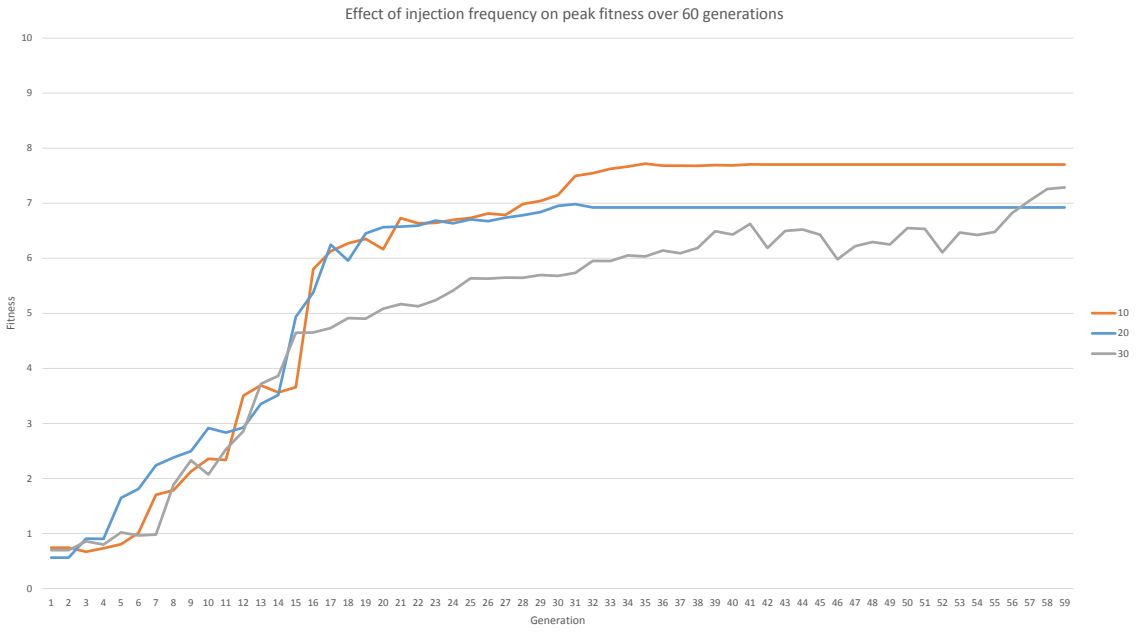

FIGURE 8.26: Graph displaying the effect of modifying the frequency of the injection of random individuals into the population over 100 generations.

These experiments were inconclusive with regards to the effect of injection frequency on peak fitness in the long term. It was decided to progress with injection frequency of 10 for faster growth.

8.3.2 Experiment without injection

After calibration, the parameters were set as shown in Tab. 8.7. The experiment was run 10 times and the results recorded. At the initialisation of every experiment, the same seed command was sent to the DM, which reported the same starting fitness value of 1.11.

Initialisation	Population size	100
	Chromosome length	52
	Gene pool	-1 to 1
Reproduction	Parent selection	Rank selection
	Crossover method	1-point
	Crossover chance	70%
	Mutation method	1-point
	Elite size	5 %
	Injection size	NA
	Generations till injection	NA
Termination	Fitness threshold	10 (saturation)
	Maximum generations	100
	Maximum runtime	NA

TABLE 8.7: Table showing GA parameters for a experimentation with population size of 100. For these experiments, the periodic injection of random individuals has been disabled.

Fig. 8.27 shows the peak fitness per generation for each of the 10 experiments. It can be seen that the maximum fitness value was achieved in 8 out of the 10 experiments, with one experiment reporting an abnormally low maximum fitness of 6.88 and exhibiting slow growth throughout the run time.

Fig. 8.28 shows the fitness over time data plotted on the same graph for comparison. It can be seen clearly here that experiment 9 experiences an abnormally slow growth rate when compared with the others. Also evident from this graph is the experiments reaching maximum peak fitness experience one or more large increases in fitness during the run time. Experiment 7 also shows two sharp increases in peak fitness, though it appears to plateau early at a value of 7.62.

8.3.3 Experiment with injection

A further set of experiments were performed with injections enabled. The configuration was similar to the experiments described in section 8.3.2. Tab. 8.8 describes the parameters used for these experiments. Note that injections occur every 10 generations and comprise 50% of the population created during the reproduction cycle.

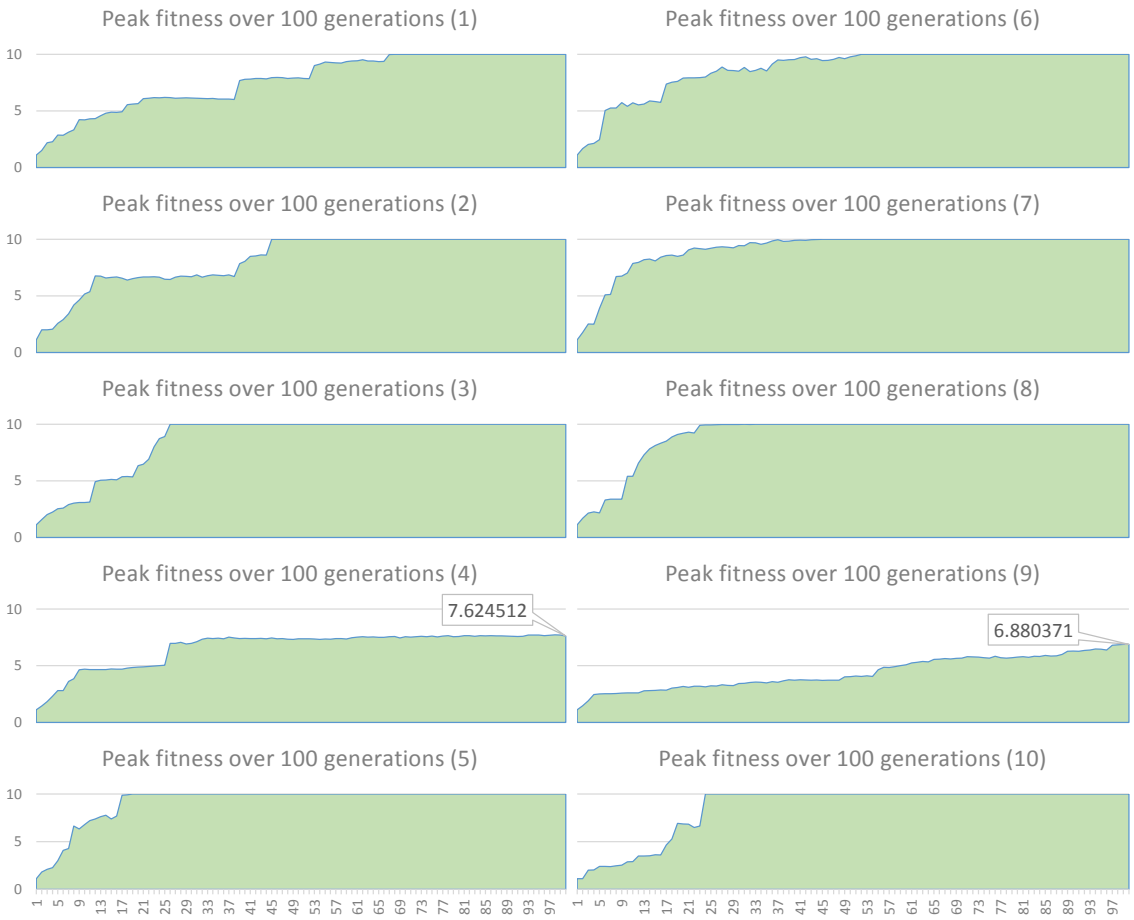

FIGURE 8.27: Graphs showing the results of running the GA with a population size of 100 for a total of 10 times. The GA achieves saturation of the photo-detector 8 times.

Initialisation	Population size	100
	Chromosome length	52
	Gene pool	-1 to 1
Reproduction	Parent selection	Rank selection
	Crossover method	1-point
	Crossover chance	70%
	Mutation method	1-point
	Elite size	5 %
	Injection size	50%
	Generations till injection	10
Termination	Fitness threshold	10 (saturation)
	Maximum generations	100
	Maximum runtime	NA

TABLE 8.8: Table showing GA parameters for a experimentation with population size of 100. Injection of randomised individuals occur every 10 generations and comprise approximately 50% of the total population after reproduction.

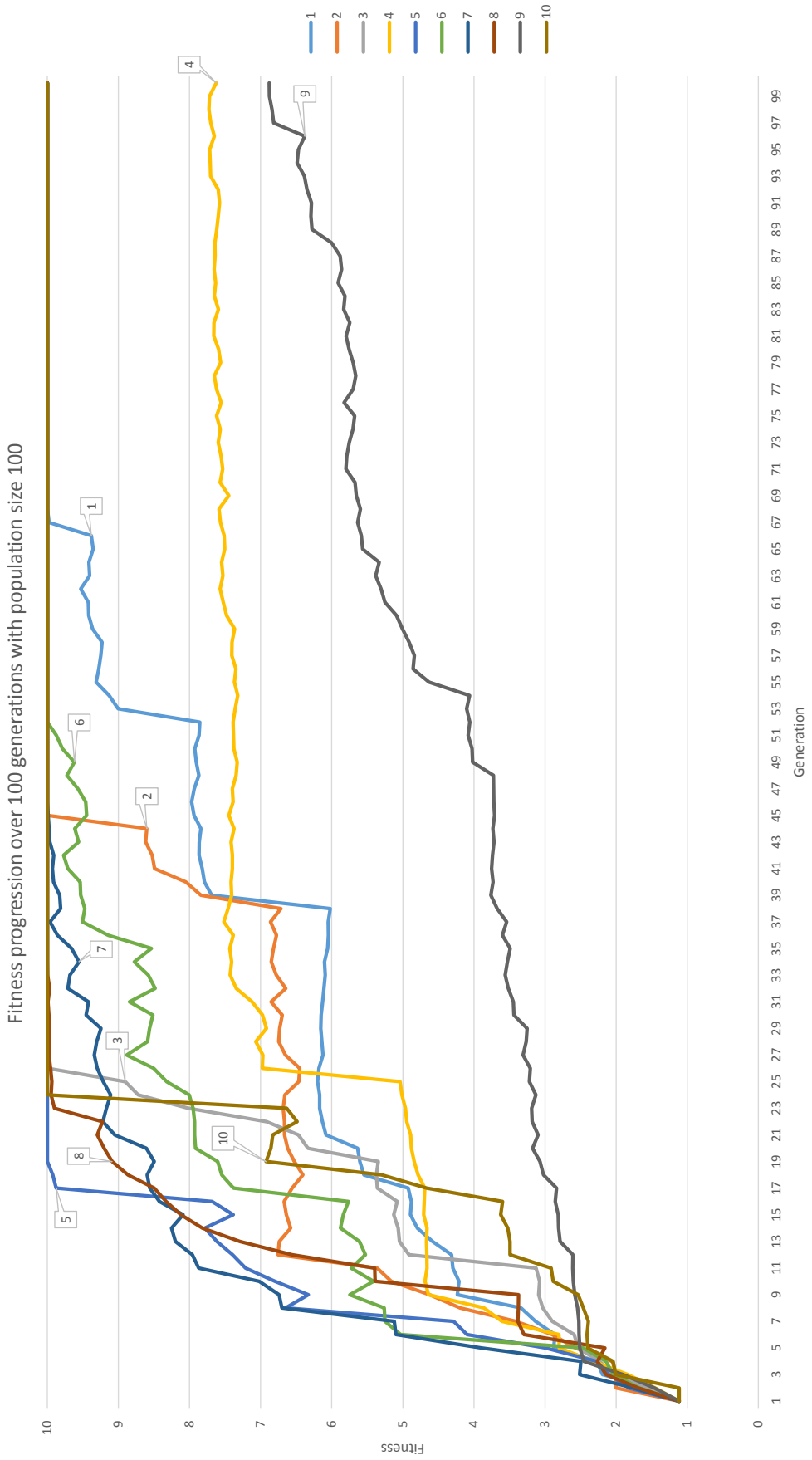

FIGURE 8.28: Graph showing fittest values of each generation for population size of 100. Experiment was run 10 times, each represented by a single line in the chart.

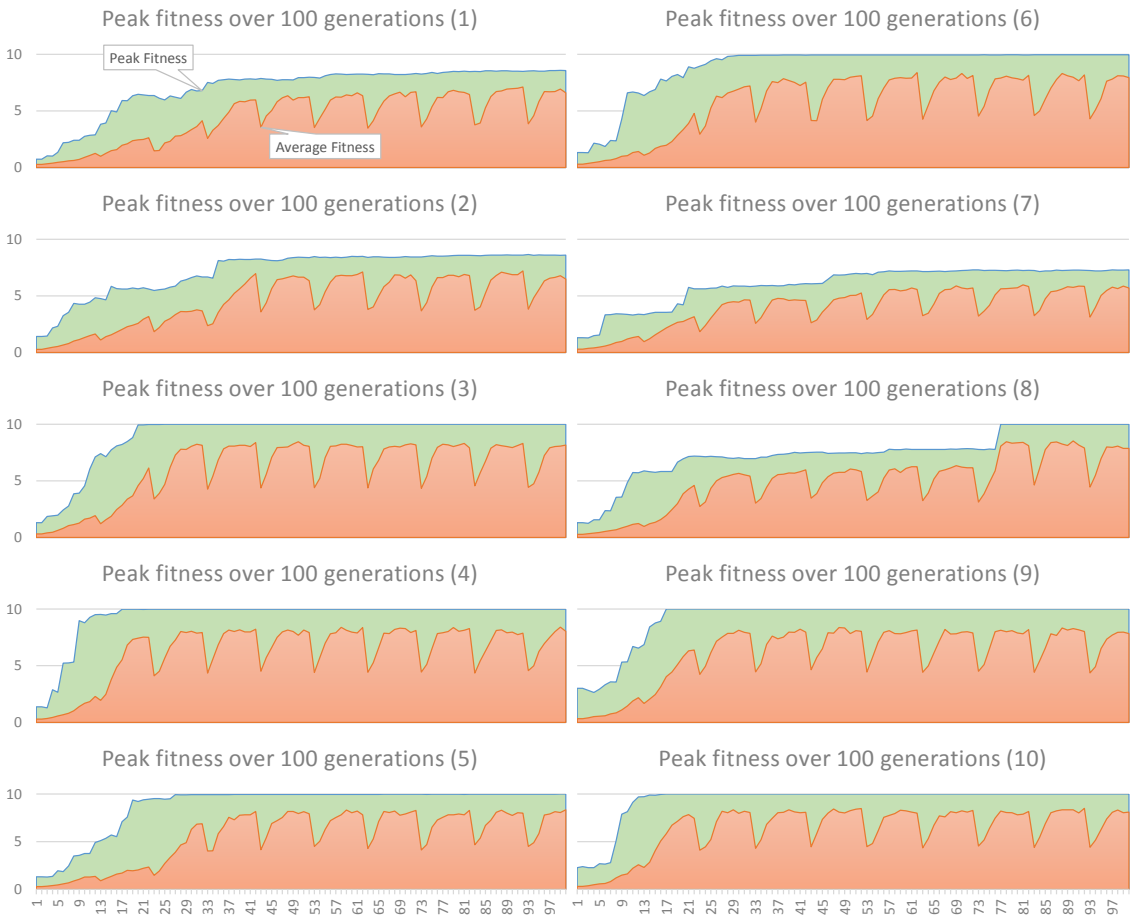

FIGURE 8.29: Graphs showing the results of running the GA with a population size of 100 for a total of 10 times. In these experiments, an injection of random individuals occurs every 10 generations and the average fitness is displayed in red. A sharp drop in average fitness occurs immediately after an injection.

Fig. 8.29 shows the outcome of the 10 experiments with injection enabled. The upper portion of each graph (shaded green) is the value of the fittest individual for each generation. The lower portion (shaded red) is the average fitness of the population.

Note that after every 10 generations there is a sharp drop in average fitness. This is the expected (and desired) effect of injection a group of randomly generated individuals into the population during reproduction. In Fig. 8.29, experiment 8 shows a long period of stagnation wherein the peak fitness has not increased significantly. Eventually, directly after an injection event, there is a sharp increase in peak fitness bringing the GA to an optimal state. This demonstrates the long term value of periodic injections of random individuals when progression stagnates.

Fig. 8.30 shows the increase in peak fitness for all 10 experiments with injection enabled. When compared with the results in Fig. 8.28, there appears to be a much faster conversion on the optimal solution when injection is enabled. There is an outlier case

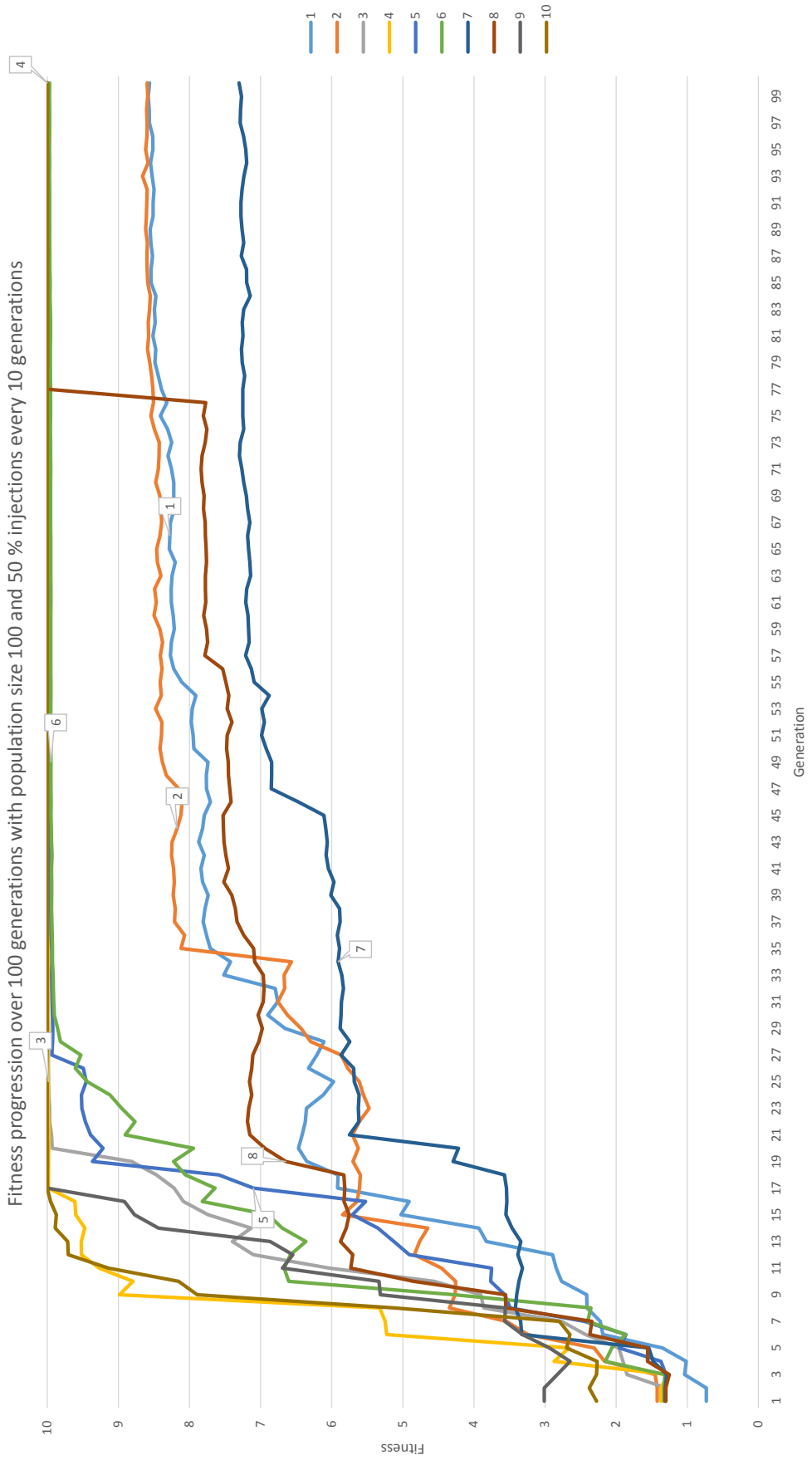

FIGURE 8.30: Graph showing peak fitness of 10 iterations of the GA with population size of 100 with injection enabled.

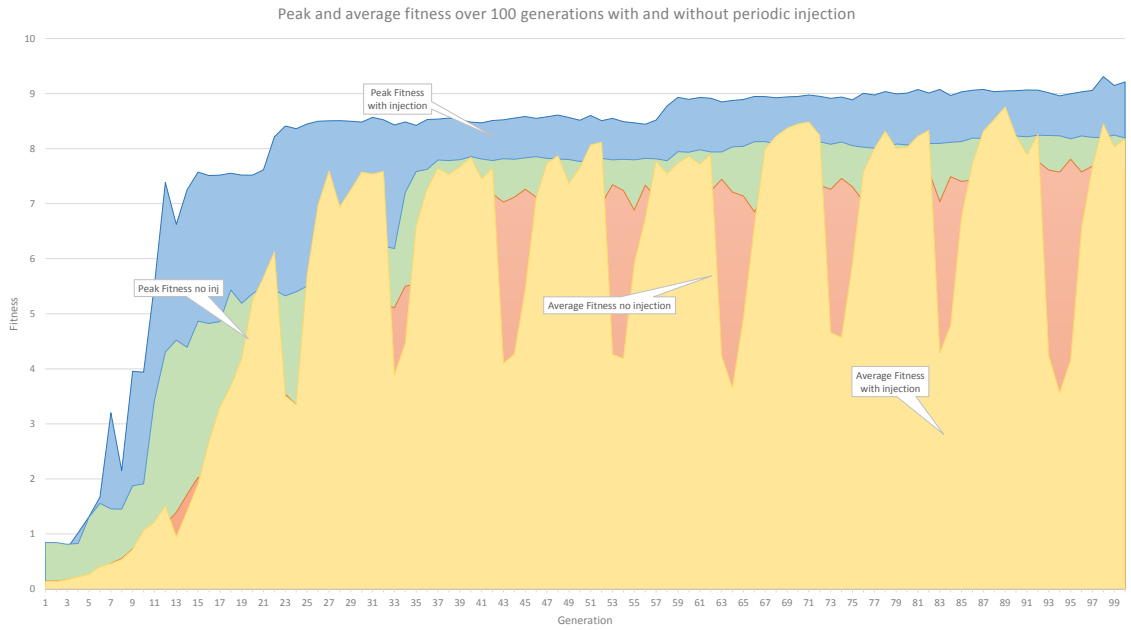

FIGURE 8.31: Graph showing a comparison of GA experiment with and without injection. The blue and yellow regions represent the peak and average fitness of the GA with injection enabled, respectively. The green and red regions represent the peak and average fitness of the GA without injection enabled, respectively.

in each set of experiments where a low peak fitness was achieved: the lowest fitness reached without injection was 6.88 in experiment 9. With injection, the lowest peak fitness achieved was 7.62 in experiment 7.

In the experiments without injection, Fig. 8.28 shows that 4 experiments reached saturated in under 30 generations. With injected enabled, Fig. 8.30 shows that 6 experiments reached saturation in under 30 generations, a notable improvement.

8.3.4 Sensitivity

The sensitivity of the GA was tested by reducing the optical power by half and then half again. These experiments test the performance of the GA in situations where little light is delivered to the photo-detector.

Optical power returned to the photo-detector was first reduced by half. This was done by tuning down the forward current of the SLD controller and observing the response of the photo-detector to back reflected light using an oscilloscope until half power was achieved. SLD forward current was reduced from 110 mA to 75 mA. Experiments were conducted as in section 8.3.3 5 times. Fig. 8.32 shows the results of the 5 experiments with half optical power.

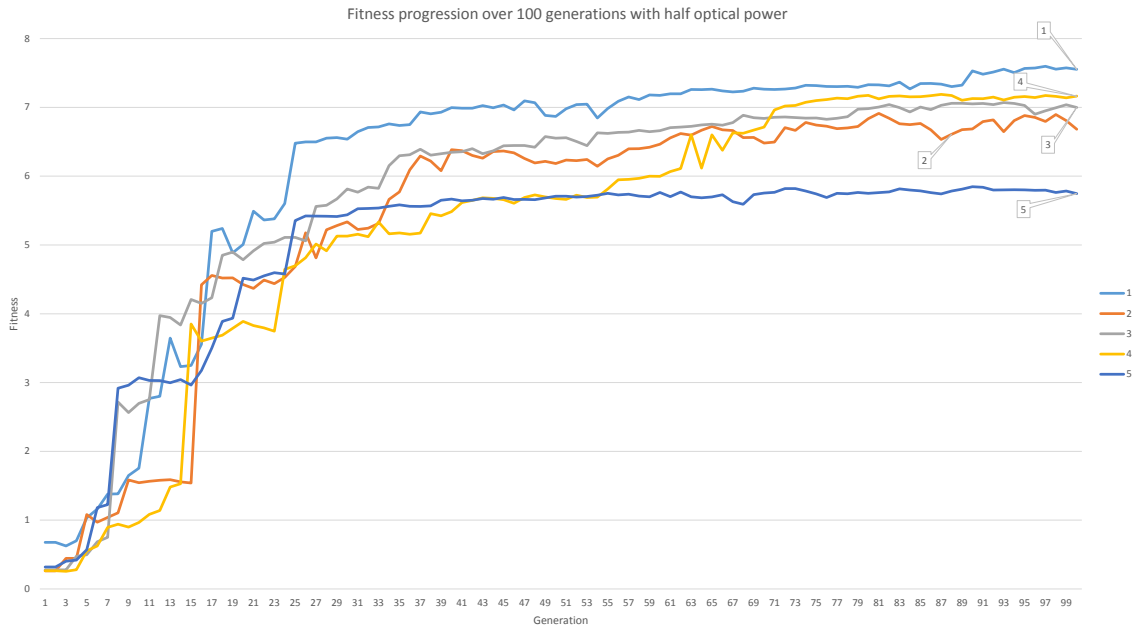

FIGURE 8.32: Graph showing the results of the sensitivity experiment with the SLD power halved.

It can be seen that the GA is unable to saturate the detector, and all experiments produced a fitness result under 8. This loss in photocurrent is to be expected with the reduction of optical power in the system. It is promising that the GA continues to function well with half the optical power returned to the detector.

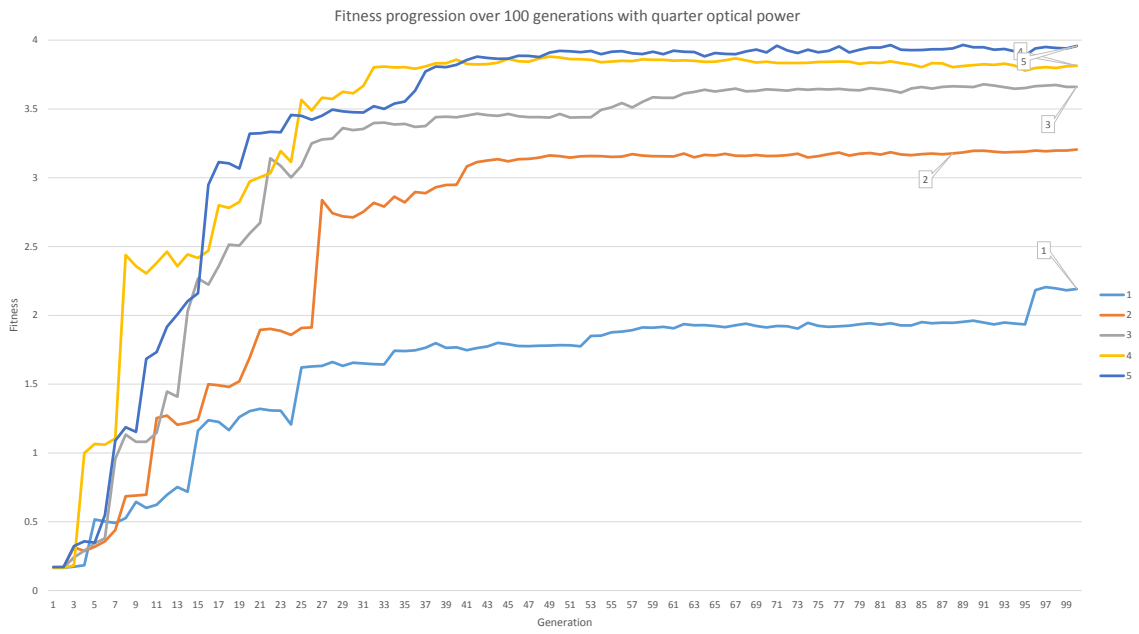

FIGURE 8.33: Graph showing the results of the sensitivity experiment with the SLD power quartered.

In the same manner, the optical power was reduced by half again so that total power returned to the photo-detector is a quarter of that reported in sections 8.3.3 and 8.3.2. Forward current of the SLD was reduced to 64 mA. Fig. 8.33 shows the results of these 5 experiments. The figure clearly shows the fitness is approximately half that shown in Fig. 8.32. Experiment 1 performed poorly, however three experiments achieved over 3.5, with the remaining experiment 3.25.

Experiments were also conducted using the AO closed loop with half and quarter power. In each case, the exposure time of the WFS was increased and the correction achieved was degraded. The closed loop was not able to exceed the performance of the GA in either case, with respect to intensity of detected light.

8.3.5 Robustness

The primary issue with GA is the total execution time, which can cause problems if there is variability in the system within the run time. An example of variability for these experiments is the movement of the object or drifting in the alignment of the optics. The following experiment tests how robust the GA is to change. During execution, when the GA reaches saturation or plateaus, the object is manually shifted out of focus using the micrometer screws. The response of the GA is then observed to determine if recovery is possible.

With the object in focus, the GA may achieve an optimised state. At this point, the object will be moved 250 μm backwards with respect to the objective lens. Once the GA settles on a new state, the object will be moved 500 μm forward. This tests whether the GA can compensate for $\pm$250 μm defocus, and also if it can compensate for the greater movement of 500 μm. One further test will be conducted by moving the object forward by a further 500 μm, for a total of 750 μm defocus. To observe the long term effects of these movements, the generation limit was increased to 200.

Fig. 8.34 shows the result of the robustness experiment. The GA achieves saturation early at generation 12. Just prior to generation 32, the GA was paused and the object moved back by 250 μm and then the GA was resumed. It can be noted that the peak fitness drops sharply from 10 to 5.74, and the average fitness drops from 5.32 to 4.15.

The GA recovers quickly: at generation 42 the detector is saturated again with peak fitness 10 and average fitness 6.91. At generation 48 the GA was paused and the object moved 500 μm forward and the GA was resumed. Peak fitness drops to 3.55 and average fitness drops to 1.61.

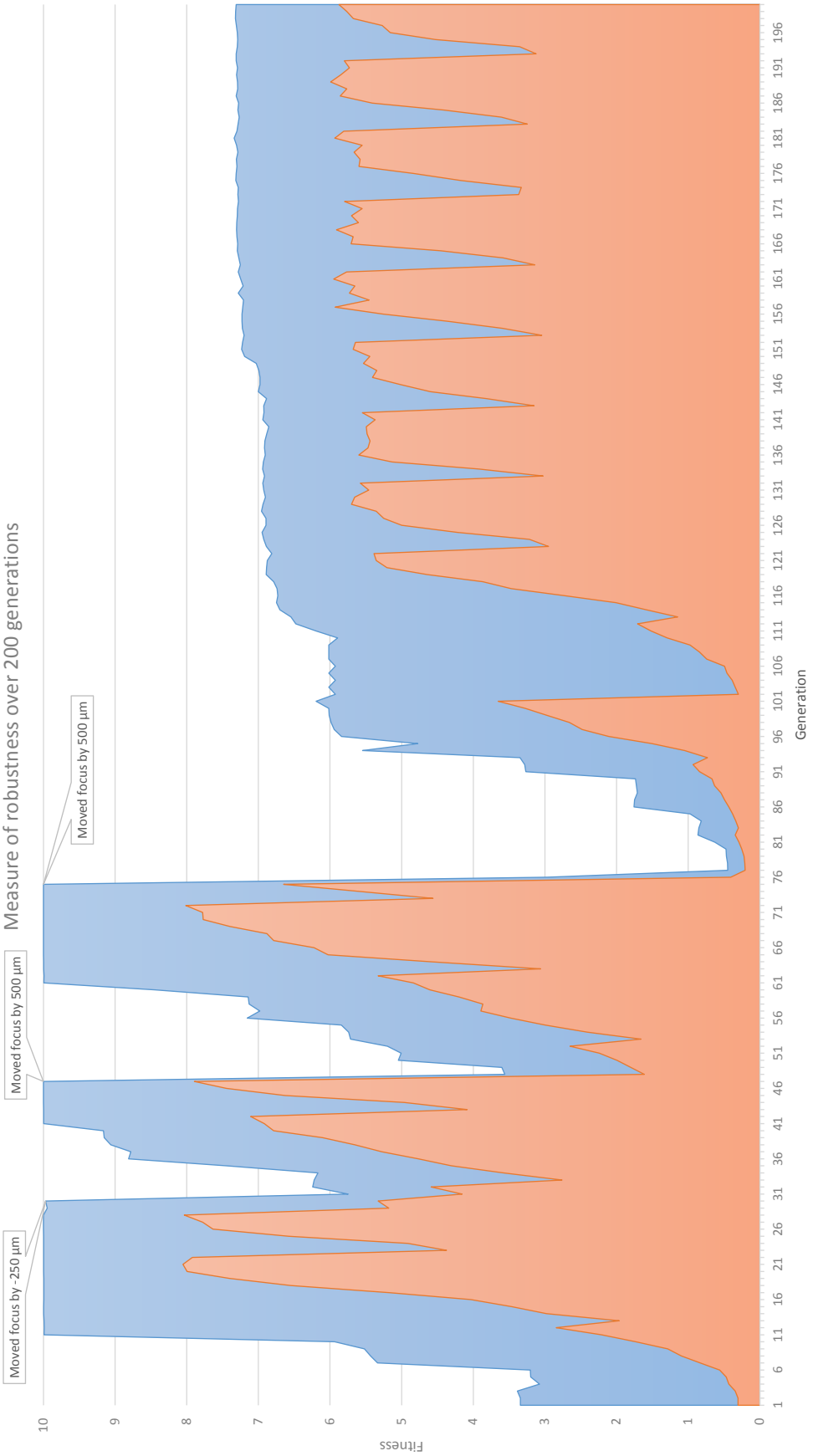

FIGURE 8.34: Graph showing the results of the robustness experiment. At the three points indicated on the graph, the object was physically moved out of focus of the objective lens and the results observed.

By generation 62 the GA has recovered again, reaching peak fitness of 10 with an average fitness of 4.83 (just after an injection). At generation 75 the final movement of 500 μm forward was performed, reducing peak fitness to 0.44 and average fitness to 0.4.

8.3.6 Experiment at 1060 nm

Finally the GA was tested using the swept source centred at 1060 nm. For this experiment, the APD was replaced with the DC monitor output of a balanced photo-detector (ThorLabs) normally used for SSOCT imaging. Since the sensitivity of this detector is much lower than that of the APD, the output is sent via a pre-amplifier (Stanford Research) and a gain of 200 is applied. There are some uncommon elements in the path travelled by the 1060 nm beam when compared with the 830 nm beam. The GA operates as normal with the parameters seen in Tab. 8.8.

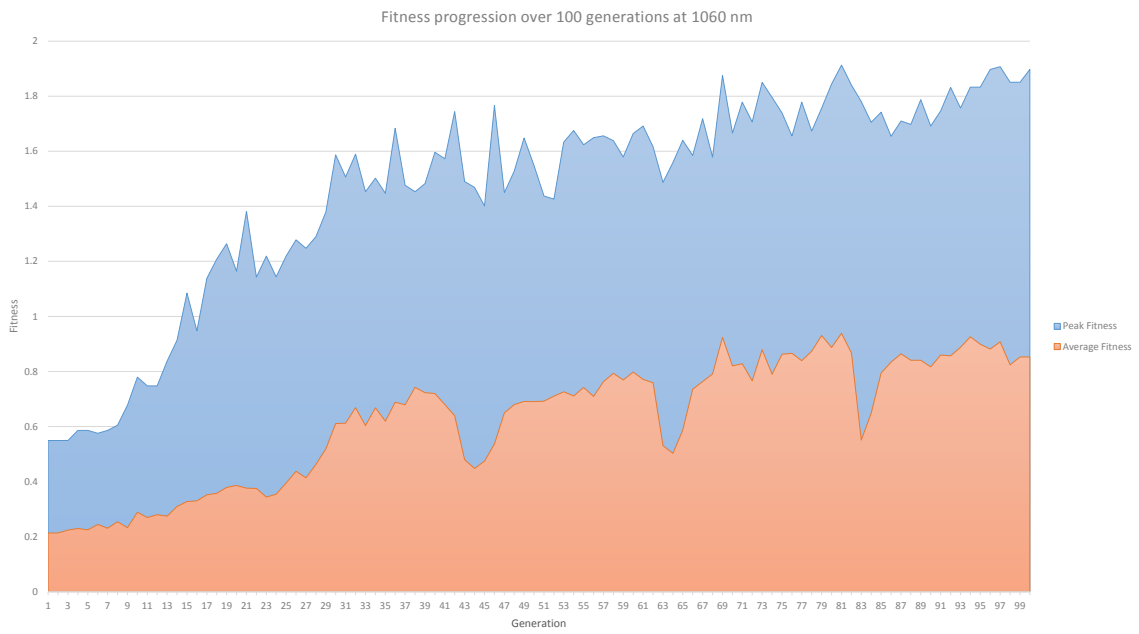

FIGURE 8.35: This diagram displays the results of the genetic algorithm as it achieves optimisation of the wavefront through measurement of 1060 nm light using a low-gain photo-detector. The blue region describes peak fitness levels per generation, and the red region is the average fitness.

Fig. 8.35 shows the results of the GA using the 1060 nm source and low sensitivity photo-detector. Immediately obvious is the low overall fitness levels, indicating much less photocurrent produced by the detector due to the low sensitivity. From an initial fitness value of 0.54, the GA manages to achieve around 1.89 by termination. This is an increase of 3.45 times more power to the detector than was achieved using the closed loop AO with a wavefront sensing wavelength of 830 nm and an imaging wavelength of

1060 nm. The variance of the peak fitness between generations can be attributed to the lower SNR when compared with the experiments using 830 nm SLD and an APD.

8.3.7 Resolution

The final determination for the effectiveness of the GA for wavefront optimisation is the measurement of imaging resolution and quality. A test was conducted using the GA to achieve correction with the 830 nm source as guidance, and then a USAF target was placed as an imaging object. An SLO image was acquired using the 830 nm SLD and compared with an image acquired of the same target after the closed loop correction generated using the commercial software was set.

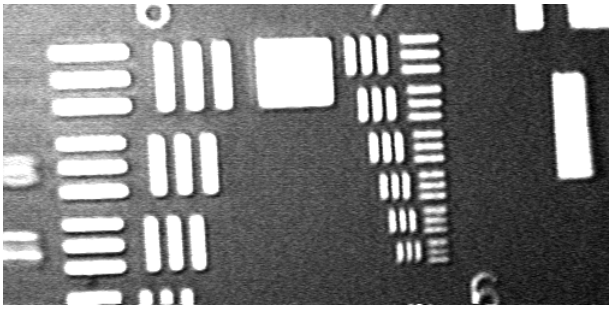

FIGURE 8.36: Image of the USAF resolution target acquired using 830 nm SLO. This image was acquired after bringing the system to a corrected state using CASAO's closed loop.

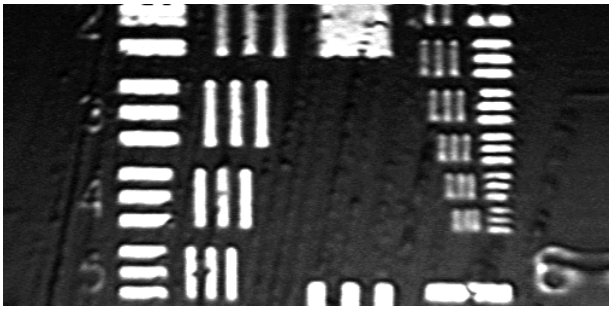

FIGURE 8.37: Image of USAF resolution target acquired using 830 nm SLO. This image was acquired after bringing the system to a corrected state using the GA.

The two images are incredibly similar, though Fig. 8.37 appears to resolve finer detail on the glass slide. It can be seen that transversal resolution was unaffected by the GA optimisation process.

Fig. 8.38 shows the lateral position from both images of the USAF target selected for profiling. Fig. 8.39 shows the intensity profile along groups 1 to 6 on the USAF target. The distance between two bars in group two is measured to be 29 pixels, and 34 pixels

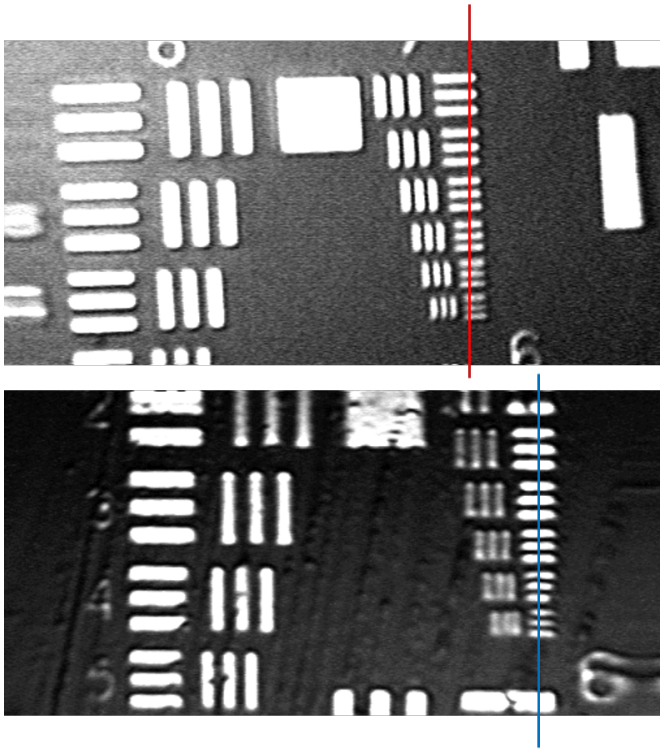

FIGURE 8.38: Figure demonstrating the location of the profiles seen in Fig. 8.39 and 8.40 from the images in Fig. 8.36 and 8.37.

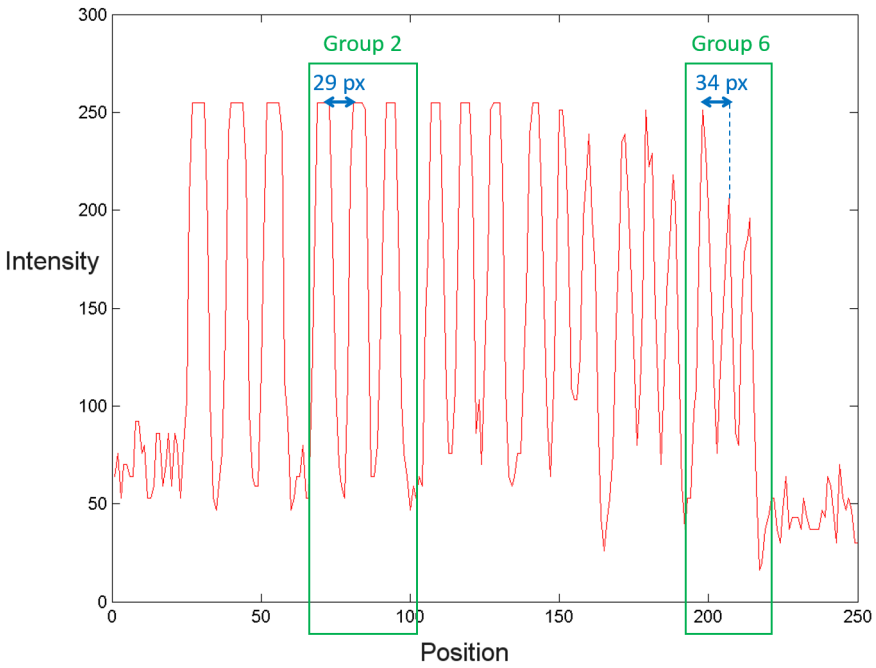

FIGURE 8.39: Intensity profile of the USAF target after normal closed loop acquisition.

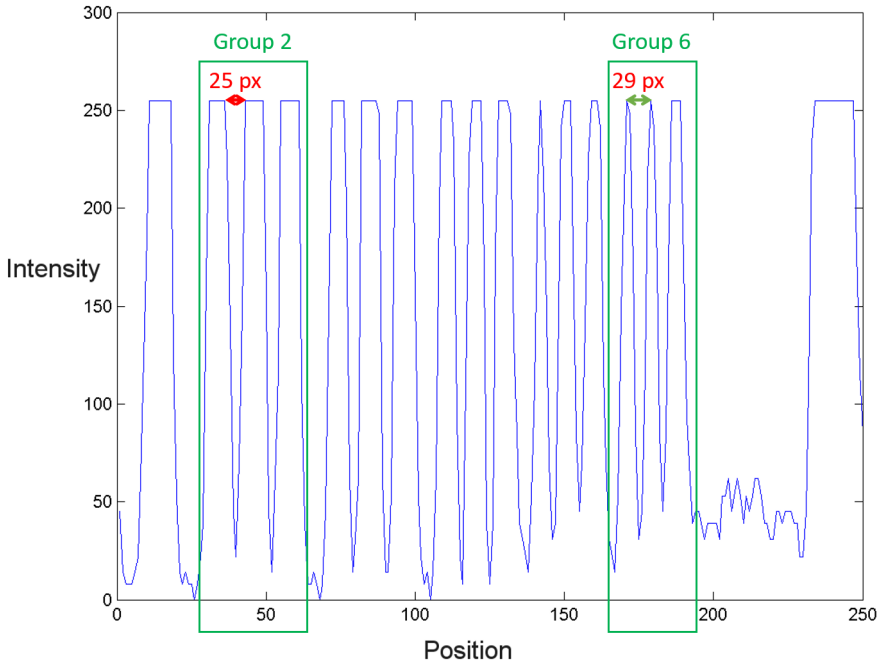

FIGURE 8.40: Intensity profile of the USAF target after GA correction.

between two bars in group six. Fig. 8.40 shows the profile taken from the USAF image after the GA optimisation. Though the image is displaced slightly, groups two to six are still visible. Noteworthy is the uniform intensity across all these groups, unlike the drop in intensity for later groups as seen in Fig. 8.39. Additionally, the bars are closer together indicating better resolution. Group two bars are spaced 25 pixels apart and group six bars are spaced 29 pixels apart.

8.4 Conclusions

The results demonstrate that the GA is effective as a tool for injecting light into fibre through wavefront optimisation without any sensing equipment required. It can be seen that the algorithm is capable of converging upon a solution that matches or exceeds that produced by the closed loop of the commercial software. This determination is made by examining a single, simple variable - the intensity of light backscattered from the object and coupled by fibre to a photo-detector.

The performance of the GA is measured by its efficacy and efficiency. A direct comparison of the solution produced by the GA and that of the closed loop shows that the GA achieves greater return of light to the photo-detector, without compromising the wavefront and therefore the imaging resolution. With favourable input parameters, the GA is able to converge upon an optimal solution very quickly - in some cases under a minute (Fig. 8.29). Though the closed loop itself is very quick - achieving correction in under 10 seconds - it may only be achieved after several time-intensive preparatory steps are performed (section 5.2.5), which may take several minutes.

A key advantage of the GA technique is the use of the imaging beam as the guidance for optimisation. In the case of the AO-SLO/OCT system presented in previous chapters, wavefront sensing was performed at 830 nm and imaging was often performed at 1060 nm. The wavefront sensing and imaging paths had several non-common optical elements, possibly resulting in a loss of correction potential as the WFS would be blind to the uncommon part of the optical path and cannot compensate for these aberrations. Further, the process of optimising the wavefront as detected by the WFS may shift the imaging beam away from the coupling fibre end, resulting in a loss of light on the photo-detector. This may occur if the two beams are not perfectly superposed throughout the common path.

Using the imaging beam as the guidance for correction has a second important benefit. With the redundancy of the wavefront sensing arm of an AO setup, the WFS and other optical components may be removed from the optical configuration. The removal of the WFS, telescope, beamsplitter, SLD and other interface optics will result in a smaller, more compact system that is also cheaper and easier to maintain.

Finally, credit must be given to the GA technique for its robustness and versatility when compared with the closed loop. The commercial software will only operate effectively when the object is a scattering target placed very closed to the focus, using a static beam. The intensity of backscattered light on the WFS is critical to accurate measurement, and a large portion of the pupil must be illuminated. Erroneous contributions to the

wavefront measurement caused by back reflections from optical elements degrade the quality of the measurement, often making correction impossible. For objects that are weakly reflecting, the exposure time of the WFS must be increased, which also brings additional noise. The GA has proven effective in high and low light intensity situations, producing a result with such low detected light that the closed loop failed to achieve a solution. Further, the GA operates even with highly specular objects and with a scanning beam. Finally, Fig. 8.34 shows that the GA is still able to perform even when the object is placed far from the focus. Even if the object is moved out of focus whilst the algorithm is operational, the GA is still able to recover fully for small movements and partially for larger movements (a maximum shift of 750 μm was tested in section 8.3.5). This is impossible for the closed loop software to achieve.

8.5 Evaluation

There are disadvantages inherent with the GA technique. The key disadvantage of any GA is the cost of time, as the algorithm must 'train' for several generations before optimisation progresses. For small systems this may not take long, however GAs will scale poorly with larger systems. The GA presented in this chapter was able to find solutions in a matter of minutes given the parameters provided, however this is still only effective against objects that are largely stationary. Fig. 8.34 shows that the GA is able to react to a moving object, however it is far too slow for the GA to provide accurate live correction from a rapidly moving target such as the human eye.

It is conceivable that a fast, low-population GA could provide some benefit for *in-vivo* eye imaging. Though the eye is moving constantly, given a suitable fixation and fast enough evolution process, the GA may still be able to achieve an improvement in signal. In this case, the relative fitness measurements of individuals in a population may be less accurate due to eye movement, however the overall population should slowly tend towards higher fitness. Future work would involve testing a faster GA on the fixated eye to see if there is some improvement over time.

Aside from DM manipulation, there is the possibility of GA being used for software-based AO correction. Research has been conducted into improving the resolution and image quality post-acquisition through software algorithms [184], and GA could potentially be employed to do the same. The fitness measurement for this GA would be a weighted product of several factors, such as sharpness, contrast and brightness.

Chapter 9

Conclusions

9.1 Summary

The projects presented in this thesis are focussed on the use of AO for the improvement of imaging with confocal microscopy and OCT. Emphasis has been placed on imaging of biological tissues *in-vivo*, with the eye in particular being a subject of great interest. The research has explored multiple modalities and techniques with AO being the core principle that underpins the whole venture.

The first four chapters provide an introduction to the experimental works in this thesis. The theory presented in chapters 2 to 4 provide context to the fields of microscopy, adaptive optics and OCT.

Chapter 5 introduces the experimental work with AO integrated into a confocal microscope system. Particular attention was paid to the capacity of the WFS to determine wavefront aberration, and the capability of the DM to compensate for the detected errors. A brief review of a legacy AO-SLO/OCT system was conducted, identifying the strengths and weaknesses of such a configuration. The concept of non-planar folding of mirrors to reduce astigmatism was discussed, and a new design incorporating this idea was presented. The new system was fully detailed and characterised, and the performance of the AO was evaluated. As a demonstration of the potential of this system, high resolution images were acquired from living tissue. In particular, high quality images of the retina were presented with photoreceptors visible and well defined.

Chapter 6 is a presentation of work published in the Journal of Biomedical Optics. This project was an attempt to simulate the dynamic focussing potential of using a DM to shift the confocal gate whilst imaging in the spectral domain. With the capabilities of the AO to compensate aberrations well documented in chapter 5, the focus of chapter 6

was on exploiting the DM to induce aberrations dynamically whilst imaging. The DM was used to first correct the wavefront, and then to incrementally add defocus aberration such that the confocal gate was shifted deeper into the object. The system was capable of achieving this in real-time during imaging with a swept source at 100 KHz sweeping rate. Many sequential images were acquired as the confocal gate was shifted, and then fused together to create an image wherein all axial regions are in focus. The improvement was evident in the phantoms, though less pronounced with highly scattering thick biological samples such as the *Drosophila*. Regardless, the principle of achieving Gabor filtering in spectral domain using a DM was presented experimentally with good result.

Chapter 7 is an exploration into MSI OCT. The AO in this case took a passive role after the initial correction, as in chapter 5. With the high transversal resolution afforded by AO, and the high axial resolution as determined by the swept source, MSI was used as an optical depth sectioning tool for specular and biological samples *in-vivo*. The capability of the MSI method to produce a set of *en-face* images at multiple depths simultaneously in the spectral domain is a great benefit. Further work in this field was briefly discussed, as the DM could again be used to shift the confocal gate to the desired depth during live depth sectioning using MSI.

Chapter 8 is a slight departure from the principles of OCT and optics itself, and focusses heavily on the capabilities of the DM. The issues of an AO system reliant upon a WFS are discussed, and a solution is presented that eliminates the necessity for a WFS. A GA is presented that automatically determines the optimal configuration of the surface of the DM, as determined by light coupled back to a photodetector. The effectiveness of the GA in accomplishing this task is demonstrated in the results, and the GA is comprehensively characterised.

9.2 Achievements

Across all the works presented in this thesis there have been a number of significant accomplishments. A new AO-SLO/OCT system was constructed based upon modern design philosophies, particularly that of non-planar mirror arrangement [150] for reduction of astigmatism aberration. This configuration was capable of achieving a wavefront error of 0.002 μm RMS, the best possible result achievable by the hardware as shown in Tab. A.1. Transversal resolution of this imaging system was better than 2 μm in air, enabling the accurate imaging of photoreceptors *in-vivo*. The system was designed to be expanded for different purposes - chiefly being the implementation of OCT. Using the same 830 nm broadband SLD light source, a time domain OCT system was integrated into the system.

The versatility of this system was demonstrated in later chapters as additional modalities and technologies were used. A 1050 nm broadband source was used with a custom APD to create confocal images, and the addition of a spectrometer led to Fourier domain OCT imaging. This channel later upgraded to a swept source OCT system at 1060 nm, allowing for much faster imaging rates (in excess of 50 FPS) with higher sensitivity (over 100 dB). The AO was still capable of providing exceptionally high transversal resolution.

Experimentation with the DM yielded results in the form of a Gabor filtering design for SS-OCT imaging. Defocus aberration was modified on-the-fly whilst B-scans were acquired to sweep the confocal gate through the depth of the sample. Further experimentation culminated in an AO system that dropped the requirement for the WFS by using a genetic optimisation algorithm to guide the DM into a good configuration. Through the implementation of the MSI principle, the AO system was employed to acquire multiple live *en-face* images at a range of depths.

The sum total of this research is a highly versatile system capable of exceptional resolution and imaging speeds, with the capacity to self-correct the wavefront without the use of a sensor and the possibility to image at multiple depths simultaneously whilst retaining control of focussing using the DM.

9.3 Evaluation

There were a number of problems that hindered the progress of this research, with the AO being the chief among them. Being a commercial hardware and software suite, the AO operated largely as a closed 'black box' system with the internal functions being obscured from the end user. The entire AO process, starting with the capture and determination of the wavefront and terminating in the manipulation of the DM in a feedback loop, is abstracted. When the AO fails to find a correction, it is a difficult task to diagnose the problem.

The core concept of the Shack-Hartmann is valid, however there are many problems with implementation. Ambient light in the environment, or light backscattered from imperfect or unclean optics, entering the WFS confuses the measurement and the AO often reaches a failure state quickly. In addition, when the WFS detects an error, it is blind to the location of this error. A wavefront detected to have high tilt aberration (for example) may be due to the interface optics, the orientation of the sample to the objective lens, or even the orientation of the WFS to the backscattered light from the object. Tilt in this case could be eliminated by adjusting the tilt of the object or

the WFS, thus satisfying the measurement produced by the WFS but producing an uncertainty in the placement of the optics.

Control over the wavefront was possible using the commercial software provided, however there were limitations that prevented use of CASAO for experimental work with the DM. The research presented in chapter 6 required rapid adjustment of the defocus aberration in synchronism with the imaging software in LabVIEW. This necessitated the development of custom software to rapidly send a series of commands to the DM independently of the CASAO software. The closed loop was also incapable of achieving a good correction if the object was not positioned exactly in the focal plane. The results presented in Fig. 8.34 demonstrate that it is physically possible to manipulate the DM to achieve good correction despite the deviation of the object from the focal plane, however CASAO would fail in this instance due to a blurred wavefront image.

The greatest disappointment of this research was the inability of the AO to consistently provide correction from the eye *in-vivo*. Many attempts were made to run the closed loop correction from the eye, though many resulted in erratic behaviour and a swift convergence to a failure state. Many preparatory steps were taken to maximise the effectiveness of the AO - the eye was dilated, the room was darkened, the eye was stabilised with fixation and the exposure time of the WFS was increased - but nothing resulted in consistent success.

Eventually, the 90/10 beamsplitter was replaced with a 50/50 beamsplitter, increasing light returned to the WFS at the cost of signal received by the APD. The reliability of the AO was greatly increased, and it could more frequently achieve a noticeable improvement. There remained an issue that the AO was not consistent enough in its operation. Though the AO often failed when running closed loop on the eye, good images were still obtained by first running the AO closed loop on paper and freezing the state of the DM for eye imaging.

9.4 Future work

The primary objective for any future work would be to establish the AO operational on the eye. It cannot yet be determined what the cause of the problem is, however several solutions have been considered. Potentially the light returning from the eye to the WFS is too weak, and the increased gain of the WFS results in too much noise. This would cause an inaccurate wavefront measurement and could result in a failure of the AO. In this case, the 90/10 beamsplitter might be replaced with a beamsplitter that has a more generous splitting ratio. Since APDs are very sensitive, the loss of light

returning to the photodetector should be insignificant, especially when compared to the gain in sensitivity achievable by a properly corrected wavefront. It is also true that a more sophisticated method for stabilising the head and fixating the eye could benefit the wavefront measurements.

MSI was used in chapter 7, though there exists much more potential in this method. It could be interesting to manipulate the focus using the DM whilst imaging with the MSI method. In addition, more powerful GPUs or even FPGAs could rapidly expand the potential of this technology in the near future.

Bibliography

[1] Andrew R. Parker. On the origin of optics. *Optics & Laser Technology*, 43(2): 323–329, mar 2011. ISSN 00303992. doi: 10.1016/j.optlastec.2008.12.020. URL http://www.sciencedirect.com/science/article/pii/S0030399208002454.

[2] C A Curcio, K R Sloan, R E Kalina, and A E Hendrickson. Human photoreceptor topography. *The Journal of comparative neurology*, 292(4):497–523, 1990. ISSN 0021-9967. doi: 10.1002/cne.902920402.

[3] T H Goldsmith. Optimization, constraint, and history in the evolution of eyes. *The Quarterly review of biology*, 65(3):281–322, 1990. ISSN 0033-5770. doi: 10.1086/416840.

[4] Susana Martinez-Conde, Stephen L. Macknik, Xoana G. Troncoso, and Thomas A. Dyar. Microsaccades counteract visual fading during fixation. *Neuron*, 49(2):297–305, 2006. ISSN 08966273. doi: 10.1016/j.neuron.2005.11.033.

[5] C J Ellis. The pupillary light reflex in normal subjects. *The British journal of ophthalmology*, 65(11):754–759, 1981. ISSN 0007-1161. doi: 10.1136/bjo.65.11.754.

[6] P. H. Heller, F. Perry, D. L. Jewett, and J. D. Levine. Autonomic components of the human pupillary light reflex. *Investigative Ophthalmology and Visual Science*, 31(1):156–162, 1990. ISSN 01460404.

[7] G WALD and D R GRIFFIN. The change in refractive power of the human eye in dim and bright light. *Journal of the Optical Society of America*, 37(5):321–336, 1947. ISSN 0030-3941. doi: 10.1364/JOSA.37.000321.

[8] Martina Angi, Helen Kalirai, Sarah E. Coupland, Bertil E. Damato, Francesco Semeraro, and Mario R. Romano. Proteomic analyses of the vitreous humour, 2012. ISSN 09629351.

[9] Eugene Hecht. *Optics 4th edition*, volume 1. 2001. ISBN 9780321188786. doi: 10.1119/1.3274347. URL http://adsabs.harvard.edu/abs/2001opt4.book.....H.

[10] D. B. Farber, J. G. Flannery, R. N. Lolley, and D. Bok. Distribution patterns of photoreceptors, protein, and cyclic nucleotides in the human retina. *Investigative Ophthalmology and Visual Science*, 26(11):1558–1568, 1985. ISSN 01460404.

[11] Gurprit S. Lall, Victoria L. Revell, Hiroshi Momiji, Jazi Al Enezi, Cara M. Altimus, Ali D. Güler, Carlos Aguilar, Morven A. Cameron, Susan Allender, Mark W. Hankins, and Robert J. Lucas. Distinct contributions of rod, cone, and melanopsin photoreceptors to encoding irradiance. *Neuron*, 66(3):417–428, 2010. ISSN 08966273. doi: 10.1016/j.neuron.2010.04.037.

[12] Debarshi Mustafi, Andreas H. Engel, and Krzysztof Palczewski. Structure of cone photoreceptors, 2009. ISSN 13509462.

[13] J. L. Schnapf, T. W. Kraft, and D. A. Baylor. Spectral sensitivity of human cone photoreceptors, 1987. ISSN 0028-0836.

[14] H. Strasburger, I. Rentschler, and M. Juttner. Peripheral vision and pattern recognition: A review, 2011. ISSN 1534-7362.

[15] A Pechmann and D Czepita. Epidemiology of myopia. *Klinika oczna*, 102(4): 297–300, 2000. ISSN 0219-0303. doi: 10.1142/S0219030302000149.

[16] W. N. Charman. Aberrations and myopia, 2005. ISSN 02755408.

[17] Jane Gwiazda. Treatment options for myopia. *Optometry and vision science : official publication of the American Academy of Optometry*, 86(6):624–628, 2009. ISSN 1040-5488. doi: 10.1097/OPX.0b013e3181a6a225.

[18] Jeffrey J Caspar. Hyperopia and Presbyopia, 2004. ISSN 0277-3740.

[19] Salomon Esquenazi, Viet Bui, and Olga Bibas. Surgical Correction of Hyperopia. *Survey of Ophthalmology*, 51(4):381–418, 2006. ISSN 00396257. doi: 10.1016/j.survophthal.2006.04.009.

[20] Agnieszka Popiolek-Masajada, Agnieszka Popiolek-Masajada, Henryk Kasprzak, and Henryk Kasprzak. Model of the optical system of the human eye during accomodation. *Opthal. Physiol. Opt.*, 22:201, 2002.

[21] Bin Wang and Kenneth J. Ciuffreda. Depth-of-focus of the human eye: Theory and clinical implications, 2006. ISSN 00396257.

[22] Susan A. Strenk, Lawrence M. Strenk, and Jane F. Koretz. The mechanism of presbyopia, 2005. ISSN 13509462.

[23] D. A. Atchison. Accommodation and presbyopia, 1995. ISSN 02755408.

[24] Antonio Guirao, C González, M Redondo, Edward Geraghty, Sverker Norrby, and Pablo Artal. Average optical performance of the human eye as a function of age in a normal population. *Investigative ophthalmology & visual science*, 40(1):203–13, 1999. ISSN 0146-0404. URL http://www.ncbi.nlm.nih.gov/pubmed/9888445.

[25] Jan van de Kraats and Dirk van Norren. Optical density of the aging human ocular media in the visible and the UV. *Journal of the Optical Society of America. A, Optics, image science, and vision*, 24(7):1842–1857, 2007. ISSN 1084-7529. doi: 10.1364/JOSAA.24.001842.

[26] Richard Dawkins. *The Blind Wathcmaker. Why the Evidence of Evolution Reveals a Universe without Design*. 1986. ISBN 0393315703.

[27] A L Coleman. Glaucoma. *Lancet*, 354(9192):1803–1810, 1999. ISSN 0140-6736. doi: 10.1016/S0140-6736(99)04240-3.

[28] Harry A Quigley. Glaucoma. *Lancet*, 377(9774):1367–1377, 2011. ISSN 1474-547X. doi: 10.1016/S0140-6736(10)61423-7.

[29] Hanna R Coleman, Chi-Chao Chan, Frederick L Ferris, and Emily Y Chew. Age-related macular degeneration. *Lancet*, 372(9652):1835–1845, 2008. ISSN 1474-547X. doi: 10.1016/S0140-6736(08)61759-6.

[30] Laurence S Lim, Paul Mitchell, Johanna M Seddon, Frank G Holz, and Tien Y Wong. Age-related macular degeneration. *Lancet*, 379(9827):1728–38, 2012. ISSN 1474-547X. doi: 10.1016/S0140-6736(12)60282-7. URL http://www.sciencedirect.com/science/article/pii/S0140673612602827.

[31] Paulus T V M de Jong. Age-related macular degeneration. *The New England journal of medicine*, 355(14):1474–1485, 2006. ISSN 1533-4406. doi: 10.1056/NEJMra062326.

[32] David R Matthews, Irene M Stratton, Stephen J Aldington, Rury R Holman, and Eva M Kohner. Risks of progression of retinopathy and vision loss related to tight blood pressure control in type 2 diabetes mellitus: UKPDS 69. Technical Report 11, 2004.

[33] David a Antonetti, Ronald Klein, and Thomas W Gardner. Diabetic Retinopathy. *The New England Journal of Medicine*, 366(13):1227–39, 2012. ISSN 1533-4406. doi: 10.1056/NEJMra1005073. URL http://www.ncbi.nlm.nih.gov/pubmed/22455417.

[34] B R Masters and M Böhnke. Confocal microscopy of the human cornea in vivo. *International ophthalmology*, 23(4-6):199–206, 2001. ISSN 0165-5701.

[35] Barry R. Masters. Correlation of histology and linear and nonlinear microscopy of the living human cornea, 2009. ISSN 1864063X.

[36] Jennifer J. Hunter, Jessica I W Morgan, William H. Merigan, David H. Sliney, Janet R. Sparrow, and David R. Williams. The susceptibility of the retina to photochemical damage from visible light, 2012. ISSN 13509462.

[37] J van Zuylen. The microscopes of Antoni van Leeuwenhoek. *Journal of microscopy*, 121(Pt 3):309–328, 1981. ISSN 1365-2818. doi: 10.1111/j.1365-2818.1981.tb01227.x.

[38] Marvin Minsky. Memoir on Inventing the Confocal Scanning Microscope. *Scanning*, 10:128–138, 1988. ISSN 01610457. doi: 10.1002/sca.4950100403. URL citeulike-article-id:4270177$\delimiter"026E30F$nhttp://web.media.mit.edu/{~}minsky/papers/ConfocalMemoir.html.

[39] P Davidovits and M D Egger. Scanning laser microscope for biological investigations. *Applied optics*, 10(7):1615–1619, 1971. ISSN 0003-6935. doi: 10.1364/AO.10.001615.

[40] C.J.R. Sheppard and A. Choudhury. Image Formation in the Scanning Microscope, 1977. ISSN 0030-3909.

[41] W B Amos, J G White, and M Fordham. Use of confocal imaging in the study of biological structures. *Applied optics*, 26(16):3239–3243, 1987. ISSN 0003-6935. doi: 10.1364/AO.26.003239.

[42] W.B. Amos and J.G. White. How the Confocal Laser Scanning Microscope entered Biological Research. *Biology of the Cell*, 95(6):335–342, 2003. ISSN 02484900. doi: 10.1016/S0248-4900(03)00078-9. URL http://doi.wiley.com/10.1016/S0248-4900{%}2803{%}2900078-9.

[43] R H Webb, G W Hughes, and F C Delori. Confocal scanning laser ophthalmoscope. *Applied optics*, 26(8):1492–1499, 1987. ISSN 0003-6935. doi: 10.1364/AO.26.001492.

[44] Kari V. Vienola, Boy Braaf, Christy K. Sheehy, Qiang Yang, Pavan Tiruveedhula, David W. Arathorn, Johannes F. de Boer, and Austin Roorda. Real-time eye motion compensation for OCT imaging with tracking SLO, 2012. ISSN 2156-7085.

[45] Michael Pircher, Bernhard Baumann, Erich Götzinger, Harald Sattmann, and Christoph K Hitzenberger. Simultaneous SLO/OCT imaging of the human retina with axial eye motion correction. *Optics express*, 15(25):16922–16932, 2007. ISSN 1094-4087. doi: 10.1364/OE.15.016922.

[46] Joseph W Goodman. *Speckle phenomena in optics: theory and applications*. 2007. ISBN 0974707791. doi: 9781936221141. URL http://books.google.com/books?hl=en{&}lr={&}id=TynXEcS0DncC{&}oi=fnd{&}pg=PR9{&}dq=goodman+speckle{&}ots=4WN4XqX0{_}J{&}sig=rMF3sY0dDD7TBfSWqIRA6S8g3CE.

[47] Guy Cox and Colin J R Sheppard. Practical Limits of Resolution in Confocal and Non-Linear Microscopy. *Microscopy Research and Technique*, 63(1):18–22, 2004. ISSN 1059910X. doi: 10.1002/jemt.10423.

[48] T. Wilson. Resolution and optical sectioning in the confocal microscope, 2011. ISSN 00222720.

[49] P Török and T Wilson. Rigorous theory for axial resolution in confocal microscopes, 1997. ISSN 00304018.

[50] A K Ruprecht, T F Wiesendanger, and H J Tiziani. Chromatic confocal microscopy with a finite pinhole size. *Optics letters*, 29(18):2130–2132, 2004. ISSN 0146-9592. doi: 10.1364/OL.29.002130.

[51] Michelle L Gabriele, Gadi Wollstein, Hiroshi Ishikawa, Larry Kagemann, Juan Xu, Lindsey S Folio, and Joel S Schuman. Optical coherence tomography: history, current status, and laboratory work. *Investigative ophthalmology & visual science*, 52(5):2425–2436, 2011. ISSN 1552-5783. doi: 10.1167/iovs.10-6312.

[52] J.M. Schmitt. Optical coherence tomography (OCT): a review. *IEEE Journal of Selected Topics in Quantum Electronics*, 5(4), 1999. ISSN 1077-260X. doi: 10.1109/2944.796348.

[53] Wolfgang Drexler. Ultrahigh-resolution optical coherence tomography, 2004. ISSN 10833668.

[54] Wolfgang Wieser, Benjamin R Biedermann, Thomas Klein, Christoph M Eigenwillig, and Robert Huber. Multi-megahertz OCT: High quality 3D imaging at 20 million A-scans and 4.5 GVoxels per second. *Optics express*, 18(14):14685–704, jul 2010. ISSN 1094-4087. doi: 10.1364/OE.18.014685. URL http://www.opticsexpress.org/abstract.cfm?URI=oe-18-14-14685.

[55] James G Fujimoto. Optical coherence tomography for ultrahigh resolution in vivo imaging. *Nature biotechnology*, 21(11):1361–1367, 2003. ISSN 1087-0156. doi: 10.1038/nbt892.

[56] W Drexler, U Morgner, F X Kärtner, C Pitris, S A Boppart, X D Li, E P Ippen, and J G Fujimoto. In vivo ultrahigh-resolution optical coherence tomography.

Optics letters, 24(17):1221–1223, 1999. ISSN 0146-9592. doi: 10.1364/OL.24.001221.

[57] W Drexler, U Morgner, R K Ghanta, F X Kärtner, J S Schuman, and J G Fujimoto. Ultrahigh-resolution ophthalmic optical coherence tomography. *Nature medicine*, 7(4):502–507, 2001. ISSN 1078-8956. doi: 10.1038/86589.

[58] C L Smithpeter, A K Dunn, A J Welch, and R Richards-Kortum. Penetration depth limits of in vivo confocal reflectance imaging. *Applied optics*, 37(13):2749–2754, 1998. ISSN 0003-6935. doi: 10.1109/CLEO.1997.602210.

[59] M Xu and R R Alfano. Fractal mechanisms of light scattering in biological tissue and cells. *Optics letters*, 30(22):3051–3053, 2005. ISSN 0146-9592. doi: 10.1364/OL.30.003051.

[60] Colin J R Sheppard. Fractal model of light scattering in biological tissue and cells. *Optics letters*, 32(2):142–144, 2007. ISSN 0146-9592. doi: 10.1364/OL.32.000142.

[61] J R Mourant, J P Freyer, A H Hielscher, A A Eick, D Shen, and T M Johnson. Mechanisms of light scattering from biological cells relevant to noninvasive optical-tissue diagnostics. *Applied optics*, 37(16):3586–3593, 1998. ISSN 0003-6935. doi: 10.1364/AO.37.003586.

[62] Alwin Kienle and Raimund Hibst. Light guiding in biological tissue due to scattering. *Physical Review Letters*, 97(1), 2006. ISSN 00319007. doi: 10.1103/PhysRevLett.97.018104.

[63] Janak Ramachandran, Tamara M Powers, Susan Carpenter, Alicia Garcia-Lopez, James P Freyer, and Judith R Mourant. Light scattering and microarchitectural differences between tumorigenic and non-tumorigenic cell models of tissue. *Optics express*, 15(7):4039–4053, 2007. ISSN 1094-4087. doi: 10.1364/OE.15.004039.

[64] Carmel M. Moran, Stephen D. Pye, William Ellis, Anna Janeczko, Keith D. Morris, Alan S. McNeilly, and Hamish M. Fraser. A comparison of the imaging performance of high resolution ultrasound scanners for preclinical imaging. *Ultrasound in Medicine and Biology*, 37(3):493–501, 2011. ISSN 03015629. doi: 10.1016/j.ultrasmedbio.2010.11.010.

[65] F. Stuart Foster, Charles J. Pavlin, Kasia A. Harasiewicz, Donald A. Christopher, and Daniel H. Turnbull. Advances in ultrasound biomicroscopy, 2000. ISSN 03015629.

[66] P N T Wells. Ultrasound imaging. *Physics in medicine and biology*, 51(13):R83–R98, 2006. ISSN 0031-9155. doi: 10.1088/0031-9155/51/13/R06.

[67] Jørgen Arendt Jensen. Medical ultrasound imaging, 2007. ISSN 00796107.

[68] Donald A. Knapik. A 100-200 MHz ultrasound biomicroscope. *IEEE Transactions on Ultrasonics, Ferroelectrics, and Frequency Control*, 47(6):1540–1549, 2000. ISSN 08853010. doi: 10.1109/58.883543.

[69] P.R. Herz, P. Hsiung, S. Bourquin, T.K. Ko, K. Schneider, H. Ishikawa, and J.G. Fujimoto. Micro-motor endoscope with adjustable focus for ultrahigh resolution OCT. *Conference on Lasers and Electro-Optics, 2003. CLEO '03.*, 2003. ISSN 10945695. doi: 10.1109/CLEO.2003.1297822.

[70] Alexandre R Tumlinson, Lida P Hariri, Urs Utzinger, and Jennifer K Barton. Miniature endoscope for simultaneous optical coherence tomography and laser-induced fluorescence measurement. *Applied optics*, 43(1):113–121, 2004. ISSN 0003-6935. doi: 10.1364/AO.43.000113.

[71] Xiumei Liu, Michael J Cobb, Yuchuan Chen, Michael B Kimmey, and Xingde Li. Rapid-scanning forward-imaging miniature endoscope for real-time optical coherence tomography. *Optics letters*, 29(15):1763–1765, 2004. ISSN 0146-9592. doi: 10.1364/OL.29.001763.

[72] Brian J F Wong, Ryan P Jackson, Shuguang Guo, James M Ridgway, Usama Mahmood, Jianping Su, Terry Y Shibuya, Roger L Crumley, Mai Gu, William B Armstrong, and Zhongping Chen. In vivo optical coherence tomography of the human larynx: normative and benign pathology in 82 patients. Technical Report 11, 2005.

[73] James A Burns. Optical coherence tomography: imaging the larynx. *Current opinion in otolaryngology & head and neck surgery*, 20(6):477–81, 2012. ISSN 1531-6998. doi: 10.1097/MOO.0b013e3283582d7d. URL http://www.ncbi.nlm.nih.gov/pubmed/22913932.

[74] Owain R. Hughes, Nicholas Stone, Marcel Kraft, Christoph Arens, and Martin A. Birchall. Optical and molecular techniques to identify tumor margins within the larynx, 2010. ISSN 10433074.

[75] J C Wyant. White light interferometry. *Proceedings of the SPIE - The International Society for Optical Engineering*, 4737(2002):98–107, 2002. ISSN 0277786X. doi: 10.1117/12.474947. URL <GotoISI>://INSPEC:7536620.

[76] Ceyhun Akcay, Pascale Parrein, and Jannick P Rolland. Estimation of longitudinal resolution in optical coherence imaging. *Applied optics*, 41(25):5256–5262, 2002. ISSN 0003-6935. doi: 10.1364/AO.41.005256.

[77] A.S. Gerges, F. Farahi, T.P. Newson, J.D.C. Jones, and D.A. Jackson. Fibre-optic interferometric sensor utilising low coherence length source: resolution enhancement, 1988. ISSN 00135194.

[78] Alfredo Luis. Coherence versus interferometric resolution. *Physical Review A - Atomic, Molecular, and Optical Physics*, 81(6), 2010. ISSN 10502947. doi: 10.1103/PhysRevA.81.065802.

[79] A Unterhuber, B Povazay, K Bizheva, B Hermann, H Sattmann, A Stingl, T Le, M Seefeld, R Menzel, M Preusser, H Budka, Ch Schubert, H Reitsamer, P K Ahnelt, J E Morgan, A Cowey, and W Drexler. Advances in broad bandwidth light sources for ultrahigh resolution optical coherence tomography. *Physics in medicine and biology*, 49(7):1235–1246, 2004. ISSN 0031-9155. doi: PiiS0031-9155(04)74338-9$\backslash$rDoi10.1088/0031-9155/49/7/011.

[80] R. A. Leitgeb, W. Drexler, A. Unterhuber, B. Hermann, T. Bajraszewski, T. Le, A. Stingl, and A. F. Fercher. Ultrahigh resolution Fourier domain optical coherence tomography, 2004. ISSN 1094-4087.

[81] Kaijie Wu. Research on the effect of numerical aperture on probing depth of OCT system with new Monte Carlo simulation model. In *Optics in Health Care and Biomedical Optics: Diagnostics and Treatment II*, volume 5630, pages 703–710, 2005. doi: 10.1117/12.574917. URL http://link.aip.org/link/?PSI/5630/703/1{&}Agg=doi.

[82] J A Izatt, M R Hee, G M Owen, E A Swanson, and J G Fujimoto. Optical coherence microscopy in scattering media. *Optics letters*, 19(8):590–592, 1994. ISSN 0146-9592. doi: 10.1364/OL.19.000590.

[83] E Beaurepaire, A C Boccara, M Lebec, L Blanchot, and H Saint-Jalmes. Full-field optical coherence microscopy. *Optics letters*, 23(4):244–246, 1998. ISSN 0146-9592. doi: 10.1364/OL.23.000244.

[84] R A Leitgeb, M Villiger, A H Bachmann, L Steinmann, and T Lasser. Extended focus depth for Fourier domain optical coherence microscopy. *Optics letters*, 31 (16):2450–2452, 2006. ISSN 0146-9592. doi: 10.1364/OL.31.002450.

[85] F. Lexer, C. K. Hitzenberger, W. Drexler, S. Molebny, H. Sattmann, M. Sticker, and A. F. Fercher. Dynamic coherent focus OCT with depth-independent transversal resolution, 1999. ISSN 0950-0340.

[86] B Bouma and G Tearney. *Handbook of optical coherence tomography*. 2002. ISBN 0824705580. URL http://www.imalux.com/documents/HandbookofOpticalCoherenceTomography.pdf.

[87] Nader Nassif, Barry Cense, B Hyle Park, Seok H Yun, Teresa C Chen, Brett E Bouma, Guillermo J Tearney, and Johannes F de Boer. In vivo human retinal imaging by ultrahigh-speed spectral domain optical coherence tomography. *Optics letters*, 29(5):480–482, 2004. ISSN 0146-9592. doi: 10.1364/OL.29.000480.

[88] S Yun, G Tearney, B Bouma, B Park, and Johannes de Boer. High-speed spectral-domain optical coherence tomography at 1.3 mum wavelength. *Optics express*, 11 (26):3598–3604, 2003. ISSN 1094-4087. doi: 78225[pii].

[89] R Leitgeb, C Hitzenberger, and Adolf Fercher. Performance of fourier domain vs. time domain optical coherence tomography. *Optics express*, 11(8):889–894, 2003. ISSN 1094-4087. doi: 10.1364/OE.11.000889.

[90] Adrian Gh Podoleanu, John A. Rogers, and David A. Jackson. OCT en-face images from the retina with adjustable depth resolution in real time. *IEEE Journal on Selected Topics in Quantum Electronics*, 5(4):1176–1184, 1999. ISSN 1077260X. doi: 10.1109/2944.796344.

[91] Kang Zhang and Jin U Kang. Real-time 4D signal processing and visualization using graphics processing unit on a regular nonlinear-k Fourier-domain OCT system. *Optics express*, 18(11):11772–11784, 2010. ISSN 1094-4087. doi: 10.1364/OE.18.011772.

[92] Vivek J. Srinivasan, Desmond C. Adler, Yueli Chen, Iwona Gorczynska, Robert Huber, Jay S. Duker, Joel S. Schuman, and James G. Fujimoto. Ultrahigh-speed optical coherence tomography for three-dimensional and en face imaging of the retina and optic nerve head. *Investigative Ophthalmology and Visual Science*, 49 (11):5103–5110, 2008. ISSN 01460404. doi: 10.1167/iovs.08-2127.

[93] Benjamin R Biedermann, Wolfgang Wieser, Christoph M Eigenwillig, Gesa Palte, Desmond C Adler, Vivek J Srinivasan, James G Fujimoto, and Robert Huber. Real time en face Fourier-domain optical coherence tomography with direct hardware frequency demodulation. *Optics letters*, 33(21):2556–2558, 2008. ISSN 0146-9592. doi: 10.1364/OL.33.002556.

[94] J A Izatt, M A Choma, and A Dhalla. Theory of Optical Coherence Tomography. In *Optical Coherence Tomography Second Edition*, pages 65–94. Second edition, 2015.

[95] A G Podoleanu, D Woods, and M Hughes. From Talbot Bands to No Mirror Terms in Fourier Domain OCT, a Quest on the Fundamental Origin of the Sensitivity Decay with Depth. *Optical Coherence Tomography and Coherence Domain Optical*

Methods in Biomedicine Xiii, 7168, 2009. ISSN 16057422. doi: Artn71681l$\backslash$rDoi10.1117/12.808327. URL <GotoISI>://000285711500025.

[96] Manuel J. Marques, Adrian Bradu, Carla C. Rosa, and Adrian Podoleanu. Attenuation of mirror terms in Fourier-domain optical coherence tomography using Talbot bands. In *X SEONS 2012*, 2012.

[97] Christoph M Eigenwillig, Benjamin R Biedermann, Wolfgang Wieser, and Robert Huber. Wavelength swept amplified spontaneous emission source. *Optics express*, 17(21):18794–18807, 2009. ISSN 1094-4087. doi: 10.1364/OE.17.018794.

[98] Michael P. Minneman, Jason Ensher, Michael Crawford, and Dennis Derickson. All-semiconductor high-speed akinetic swept-source for OCT. *Proceedings of SPIE*, 8311:831116, 2011. ISSN 21622701. doi: 10.1117/12.912119. URL http://proceedings.spiedigitallibrary.org/proceeding.aspx?doi=10.1117/12.912119.

[99] A. Gh Podoleanu. Optical coherence tomography. *Journal of Microscopy*, 247(3): 209–219, 2012. ISSN 00222720. doi: 10.1111/j.1365-2818.2012.03619.x.

[100] A M Rollins and J A Izatt. Optimal interferometer designs for optical coherence tomography. *Optics letters*, 24(21):1484–1486, 1999. ISSN 0146-9592. doi: 10.1364/OL.24.001484.

[101] Hendrik Spahr, Dierck Hillmann, Carola Hain, Clara Pfäffle, Helge Sudkamp, Gesa Franke, and Gereon Hüttmann. Imaging pulse wave propagation in human retinal vessels using full-field swept-source optical coherence tomography. *Optics Letters*, 40(20):4771, 2015. ISSN 0146-9592. doi: 10.1364/OL.40.004771. URL https://www.osapublishing.org/abstract.cfm?URI=ol-40-20-4771.

[102] L.R. Baker. Aberrations of Optical Systems, 1987. ISSN 0950-0340.

[103] D. L. FRIED. Optical Resolution Through a Randomly Inhomogeneous Medium for Very Long and Very Short Exposures, 1966. ISSN 0030-3941.

[104] PER A. STOKSETH. Properties of a Defocused Optical System, 1969. ISSN 0030-3941.

[105] John W Hardy. *Adaptive optics for astronomical telescopes*, volume 53. 1998. ISBN 0195090195. doi: 10.1063/1.883053. URL http://books.google.com/books?hl=en{&}amp;lr={&}amp;id=-0aAWyckS{_}8C{&}amp;oi=fnd{&}amp;pg=PR10{&}amp;dq=Adaptive+optics+for+astronomical+telescopes{&}amp;ots=k66h8QtWPu{&}amp;sig=PrAK{_}AsHGASO1DR6nTAf2EolWHw.

[106] Richard Davies and Markus Kasper. Adaptive Optics for Astronomy, 2012. ISSN 0066-4146.

[107] R W Wilson and C R Jenkins. Adaptive optics for astronomy: theoretical performance and limitations. *Monthly Notices of the Royal Astronomical Society*, 278: 39–61, 1996. ISSN 00358711.

[108] P C Anderson. Hubble Space Telescope., 1990. ISSN 00266620.

[109] Julianne J Dalcanton. 18 years of science with the Hubble Space Telescope. *Nature*, 457(7225):41–50, 2009. ISSN 0028-0836. doi: 10.1038/nature07621.

[110] H. W. Babcock. The Possibility of Compensating Astronomical Seeing. *Publications of the Astronomical Society of the Pacific*, 65(386):229–236, 1953. ISSN 0004-6280. doi: 10.1086/126606.

[111] H.I. Campbell and A.H. Greenaway. Wavefront Sensing From Historical Roots to the State-of-the-Art, 2006. ISSN 1633-4760.

[112] Jim Schwiegerling and DR Neal. Historical development of the Shack-Hartmann wavefront sensor. *Legends in Applied Optics*, 2005. URL http://lyle.smu.edu/{~}msomayaj/5392-7392/4(d).SHWS.pdf.

[113] Jerome Primot. Theoretical description of Shack-Hartmann wave-front sensor. *Optics Communications*, 222(1-6):81–92, 2003. ISSN 00304018. doi: 10.1016/S0030-4018(03)01565-7.

[114] L. Seifert, H. J. Tiziani, and W. Osten. Wavefront reconstruction with the adaptive Shack-Hartmann sensor. *Optics Communications*, 245(1-6):255–269, 2005. ISSN 00304018. doi: 10.1016/j.optcom.2004.09.074.

[115] R G Lane and M Tallon. Wave-front reconstruction using a Shack-Hartmann sensor. *Applied optics*, 31(32):6902–6908, 1992. ISSN 0003-6935. doi: 10.1364/AO.31.006902.

[116] J Pfund, N Lindlein, and J Schwider. Misalignment effects of the Shack-Hartmann sensor. *Applied optics*, 37(1):22–27, 1998. ISSN 0003-6935. doi: 10.1364/AO.37.000022.

[117] Daniel R. Neal, James Copland, and David A. Neal. Shack-Hartmann wavefront sensor precision and accuracy. In *Proc. SPIE 4779, Advanced Characterization Techniques for Optical, Semiconductor, and Data Storage Components, 148*, volume 4779, pages 148–160, 2002. doi: 10.1117/12.450850. URL http://proceedings.spiedigitallibrary.org/proceeding.aspx?articleid=893787.

[118] J Y Wang and D E Silva. Wave-front interpretation with Zernike polynomials. *Applied optics*, 19(9):1510–1518, 1980. ISSN 0003-6935. doi: 10.1364/AO.19.001510.

[119] Martin J. Booth. Direct measurement of Zernike aberration modes with a modal wavefront sensor. In *Optical Science and Technology, SPIE's 48th Annual Meeting*, pages 79–90, 2003. ISBN 0-8194-5035-9. doi: 10.1117/12.503695. URL http://proceedings.spiedigitallibrary.org/proceeding.aspx?articleid=768595.

[120] Jayoung Nam, Larry N Thibos, and D Robert Iskander. Zernike radial slope polynomials for wavefront reconstruction and refraction. *Journal of the Optical Society of America. A, Optics, image science, and vision*, 26(4):1035–1048, 2009. ISSN 1084-7529. doi: 10.1364/JOSAA.26.001035.

[121] G D Love. Wave-front correction and production of Zernike modes with a liquid-crystal spatial light modulator. *Applied optics*, 36(7):1517–1520, 1997. ISSN 0003-6935. doi: 10.1364/AO.36.001517.

[122] T L Kelly and J Munch. Phase-aberration correction with dual liquid-crystal spatial light modulators. *Applied optics*, 37(22):5184–5189, 1998. ISSN 0003-6935. doi: 10.1364/AO.37.005184.

[123] Lifa Hu, Li Xuan, Yongjun Liu, Zhaogliang Cao, Dayu Li, and Quanquan Mu. Phase-only liquid crystal spatial light modulator for wavefront correction with high precision. *Optics express*, 12(26):6403–6409, 2004. ISSN 1094-4087. doi: 10.1364/OE.12.006403.

[124] F Vargas-Martín, P M Prieto, and P Artal. Correction of the aberrations in the human eye with a liquid-crystal spatial light modulator: limits to performance. *Journal of the Optical Society of America. A, Optics, image science, and vision*, 15(9):2552–2562, 1998. ISSN 1084-7529. doi: 10.1364/JOSAA.15.002552.

[125] P M Birch, J Gourlay, G D Love, and A Purvis. Real-time optical aberration correction with a ferroelectric liquid-crystal spatial light modulator. *Applied optics*, 37(11):2164–2169, 1998. ISSN 0003-6935. doi: 10.1364/AO.37.002164.

[126] Denis Brousseau, Ermanno F Borra, and Simon Thibault. Wavefront correction with a 37-actuator ferrofluid deformable mirror. *Optics express*, 15(26):18190–18199, 2007. ISSN 1094-4087. doi: 10.1364/OE.15.018190.

[127] Amita Gupta, Shailesh Kumar, Ranvir Singh, Monika Chaudhary, A. K. Meena, and V. K. Sarvanan. Deformable membrane mirror for wavefront correction. *Defence Science Journal*, 59(6):590–594, 2009. ISSN 0011748X.

[128] Gleb Vdovin, Oleg Soloviev, Alexander Samokhin, and Mikhail Loktev. Correction of low order aberrations using continuous deformable mirrors. *Optics express*, 16 (5):2859–2866, 2008. ISSN 1094-4087. doi: 10.1364/OE.16.002859.

[129] C Kohler, F Zhang, and Wolfgang Osten. Characterization of a spatial light modulator and its application in phase retrieval. *Applied optics*, 48(20):4003–4008, 2009. ISSN 0003-6935. doi: 10.1364/AO.48.004003.

[130] A Bergeron, J Gauvin, F Gagnon, D Gingras, H H Arsenault, and M Doucet. Phase calibration and applications of a liquid-crystal spatial light modulator. *Applied optics*, 34(23):5133–5139, 1995. ISSN 0003-6935. doi: 10.1364/AO.34.005133.

[131] Vincent Bagnoud and Jonathan D Zuegel. Independent phase and amplitude control of a laser beam by use of a single-phase-only spatial light modulator. *Optics letters*, 29(3):295–297, 2004. ISSN 0146-9592. doi: 10.1364/OL.29.000295.

[132] Dirk-Mathys Spangenberg, Angela Dudley, Pieter H. Neethling, Erich G. Rohwer, and Andrew Forbes. White light wavefront control with a spatial light modulator. *Optics Express*, 22(11):13870, 2014. ISSN 1094-4087. doi: 10.1364/OE.22.013870. URL http://www.opticsinfobase.org/abstract.cfm?URI=oe-22-11-13870.

[133] Adisorn Tuantranont and Victor M. Bright. Segmented silicon-micromachined microelectromechanical deformable mirrors for adaptive optics. *IEEE Journal on Selected Topics in Quantum Electronics*, 8(1):33–45, 2002. ISSN 1077260X. doi: 10.1109/2944.991397.

[134] Y.-A. Peter, E. Carr, and O. Solgaard. Segmented deformable micro-mirror for free-space optical communication. *IEEE/LEOS International Conference on Optical MEMs*, 2002. doi: 10.1109/OMEMS.2002.1031509.

[135] Thomas G. Bifano. Continuous-membrane surface-micromachined silicon deformable mirror, 1997. ISSN 00913286.

[136] Curtis R Vogel and Qiang Yang. Modeling, simulation, and open-loop control of a continuous facesheet MEMS deformable mirror. *Journal of the Optical Society of America. A, Optics, image science, and vision*, 23(5):1074–1081, 2006. ISSN 1084-7529. doi: 10.1364/JOSAA.23.001074.

[137] Brian P Wallace, Peter J Hampton, Colin H Bradley, and Rodolphe Conan. Evaluation of a MEMS deformable mirror for an adaptive optics test bench. *Optics express*, 14(22):10132–10138, 2006. ISSN 1094-4087. doi: 10.1364/OE.14.010132.

[138] Jason B Stewart, Alioune Diouf, Yaopeng Zhou, and Thomas G Bifano. Open-loop control of a MEMS deformable mirror for large-amplitude wavefront control.

Journal of the Optical Society of America. A, Optics, image science, and vision, 24(12):3827–3833, 2007. ISSN 1084-7529. doi: 10.1364/JOSAA.24.003827.

[139] Enrique Fernandez and Pablo Artal. Membrane deformable mirror for adaptive optics: performance limits in visual optics. *Optics express*, 11(9):1056–1069, 2003. ISSN 1094-4087. doi: 10.1364/OE.11.001056.

[140] C Paterson, I Munro, and J Dainty. A low cost adaptive optics system using a membrane mirror. *Optics express*, 6(9):175–185, 2000. ISSN 1094-4087. doi: 10.1364/OE.6.000175.

[141] Enrique J. Fernández, Ignacio Iglesias, and Pablo Artal. Closed-loop adaptive optics in the human eye. *Optics Letters*, 26(10):746, may 2001. ISSN 0146-9592. doi: 10.1364/OL.26.000746. URL http://ol.osa.org/abstract.cfm?URI=ol-26-10-746.

[142] Chaohong Li, Nripun Sredar, Kevin M Ivers, Hope Queener, and Jason Porter. A correction algorithm to simultaneously control dual deformable mirrors in a woofer-tweeter adaptive optics system. *Optics express*, 18(16):16671–16684, 2010. ISSN 1094-4087. doi: 10.1364/OE.18.016671.

[143] Weiyao Zou, Xiaofeng Qi, and Stephen A Burns. Woofer-tweeter adaptive optics scanning laser ophthalmoscopic imaging based on Lagrange-multiplier damped least-squares algorithm. *Biomedical optics express*, 2(7):1986–2004, 2011. ISSN 2156-7085. doi: 10.1364/BOE.2.001986.

[144] Peter J Hampton, Pan Agathoklis, Rodolphe Conan, and Colin Bradley. Closed-loop control of a woofer-tweeter adaptive optics system using wavelet-based phase reconstruction. *Journal of the Optical Society of America. A, Optics, image science, and vision*, 27(11):A145–A156, 2010. ISSN 1084-7529. doi: 10.1364/JOSAA.27.00A145.

[145] Alfredo Dubra and Yusufu Sulai. Reflective afocal broadband adaptive optics scanning ophthalmoscope. *Biomedical optics express*, 2(6):1757–1768, 2011. URL http://www.pubmedcentral.nih.gov/articlerender.fcgi?artid=3114240{&}tool=pmcentrez{&}rendertype=abstract.

[146] Simon Gerard Tuohy. *Progress in adaptive optics for high resolution imaging*. PhD thesis, University of Kent, 2009.

[147] Alexander Meadway. *Combinations of techniques for the advancement of scanning laser opthalmology and optical coherence tomography*. PhD thesis, University of Kent, 2013.

[148] Erika Ödlund, Henri-François Raynaud, Caroline Kulcsár, Fabrice Harms, Xavier Levecq, Franck Martins, Nicolas Chateau, and Adrian Gh. Podoleanu. Control of an electromagnetic deformable mirror using high speed dynamics characterization and identification. *Applied Optics*, 49(31):G120, sep 2010. ISSN 0003-6935. doi: 10.1364/AO.49.00G120. URL http://ao.osa.org/abstract.cfm?URI=ao-49-31-G120.

[149] Alfredo Dubra, Yusufu Sulai, Jennifer L Norris, Robert F Cooper, Adam M Dubis, David R Williams, and Joseph Carroll. Noninvasive imaging of the human rod photoreceptor mosaic using a confocal adaptive optics scanning ophthalmoscope. *Biomedical optics express*, 2(7):1864–1876, 2011. URL http://www.pubmedcentral.nih.gov/articlerender.fcgi?artid=3130574{&}tool=pmcentrez{&}rendertype=abstract.

[150] Christopher Costa, Adrian Bradu, John Rogers, Pauline Phelan, and Adrian Podoleanu. Swept source optical coherence tomography Gabor fusion splicing technique for microscopy of thick samples using a deformable mirror. *Journal of Biomedical Optics*, 20(1):016012, 2015. ISSN 1083-3668. doi: 10.1117/1.JBO.20.1.016012. URL http://biomedicaloptics.spiedigitallibrary.org/article.aspx?doi=10.1117/1.JBO.20.1.016012.

[151] Martin Booth. Adaptive Optics for High-resolution Microscopy. In J. Christou and D. Miller, editors, *Imaging and Applied Optics*, page OM1A.2, Washington, D.C., jun 2013. OSA. ISBN 978-1-55752-975-6. doi: 10.1364/AOPT.2013.OM1A.2. URL http://www.opticsinfobase.org/abstract.cfm?URI=AOPT-2013-OM1A.2.

[152] Enrique J. Fernandez, Laurent Vabre, Boris Hermann, Angelika Unterhuber, Boris Povazay, and Wolfgang Drexler. Adaptive optics with a magnetic deformable mirror: applications in the human eye. *Optics Express*, 14(20):8900, oct 2006. ISSN 1094-4087. doi: 10.1364/OE.14.008900. URL http://www.opticsexpress.org/abstract.cfm?URI=oe-14-20-8900.

[153] Robert J. Zawadzki, Steven M. Jones, Scot S. Olivier, Mingtao Zhao, Bradley A. Bower, Joseph A. Izatt, Stacey Choi, Sophie Laut, and John S. Werner. Adaptive-optics optical coherence tomography for high-resolution and high-speed 3D retinal in vivo imaging. *Optics Express*, 13(21):8532, oct 2005. ISSN 1094-4087. doi: 10.1364/OPEX.13.008532. URL http://www.opticsexpress.org/abstract.cfm?URI=oe-13-21-8532.

[154] Barry Cense, Erik Koperda, Jeffrey M. Brown, Omer P. Kocaoglu, Weihua Gao, Ravi S. Jonnal, and Donald T. Miller. Volumetric retinal imaging with ultrahigh-resolution spectral-domain optical coherence tomography and adaptive optics using two broadband light sources. *Optics Express*, 17(5):4095, mar 2009. ISSN 1094-4087. doi: 10.1364/OE.17.004095. URL http://www.opticsexpress.org/abstract.cfm?URI=oe-17-5-4095.

[155] WooJhon Choi, Benjamin Potsaid, Vijaysekhar Jayaraman, Bernhard Baumann, Ireneusz Grulkowski, Jonathan J Liu, Chen D Lu, Alex E Cable, David Huang, Jay S Duker, and James G Fujimoto. Phase-sensitive swept-source optical coherence tomography imaging of the human retina with a vertical cavity surface-emitting laser light source. *Optics letters*, 38(3):338–40, feb 2013. ISSN 1539-4794. doi: 10.1364/OL.38.000338. URL http://ol.osa.org/abstract.cfm?URI=ol-38-3-338.

[156] Mircea Mujat, R Daniel Ferguson, Ankit H Patel, Nicusor Iftimia, Niyom Lue, and Daniel X Hammer. High resolution multimodal clinical ophthalmic imaging system. *Optics express*, 18(11):11607–21, may 2010. ISSN 1094-4087. doi: 10.1364/OE.18.011607. URL http://www.opticsexpress.org/abstract.cfm?URI=oe-18-11-11607.

[157] Benjamin Potsaid, Bernhard Baumann, David Huang, Scott Barry, Alex E Cable, Joel S Schuman, Jay S Duker, and James G Fujimoto. Ultrahigh speed 1050nm swept source/Fourier domain OCT retinal and anterior segment imaging at 100,000 to 400,000 axial scans per second. *Optics express*, 18(19):20029–48, sep 2010. ISSN 1094-4087. doi: 10.1364/OE.18.020029. URL http://www.opticsexpress.org/abstract.cfm?URI=oe-18-19-20029.

[158] Zhihua Ding, Hongwu Ren, Yonghua Zhao, J. Stuart Nelson, and Zhongping Chen. High-resolution optical coherence tomography over a large depth range with an axicon lens. *Optics Letters*, 27(4):243, feb 2002. ISSN 0146-9592. doi: 10.1364/OL.27.000243. URL http://ol.osa.org/abstract.cfm?URI=ol-27-4-243.

[159] R. A. Leitgeb, M. Villiger, A. H. Bachmann, L. Steinmann, and T. Lasser. Extended focus depth for Fourier domain optical coherence microscopy. *Optics Letters*, 31(16):2450, 2006. ISSN 0146-9592. doi: 10.1364/OL.31.002450. URL http://ol.osa.org/abstract.cfm?URI=ol-31-16-2450.

[160] Dirk Lorenser, C Christian Singe, Andrea Curatolo, and David D Sampson. Energy-efficient low-Fresnel-number Bessel beams and their application in optical coherence tomography. *Optics letters*, 39(3):548–51, feb 2014. ISSN 1539-4794. URL http://www.ncbi.nlm.nih.gov/pubmed/24487862.

[161] Jannick P Rolland, Panomsak Meemon, Supraja Murali, Kevin P Thompson, and Kye-sung Lee. Gabor-based fusion technique for Optical Coherence Microscopy. *Optics Express*, 18(4):3632–3642, 2010. URL http://www.ncbi.nlm.nih.gov/pubmed/20389373.

[162] Bing Qi, A Phillip Himmer, A. Phillip Himmer, L. Maggie Gordon, X.D. Victor Yang, L. David Dickensheets, and I. Alex Vitkin. Dynamic focus control in high-speed optical coherence tomography based on a microelectromechanical mirror. *Optics Communications*, 232(1-6):123–128, mar 2004. ISSN 00304018. doi: 10.1016/j.optcom.2004.01.015. URL http://www.sciencedirect.com/science/article/pii/S0030401804000367.

[163] Michael Hughes and Adrian Gh Podoleanu. A simplified dynamic focus method for time domain OCT. 46(1):1–6, 1991.

[164] Kazuhiro Sasaki, Kazuhiro Kurokawa, Shuichi Makita, and Yoshiaki Yasuno. Extended depth of focus adaptive optics spectral domain optical coherence tomography. *Biomedical optics express*, 3(10): 2353–70, oct 2012. ISSN 2156-7085. doi: 10.1364/BOE.3.002353. URL http://www.pubmedcentral.nih.gov/articlerender.fcgi?artid=3469993{&}tool=pmcentrez{&}rendertype=abstract.

[165] Cristiano Torti, Boris Povazay, Bernd Hofer, Angelika Unterhuber, Joseph Carroll, Peter Kurt Ahnelt, and Wolfgang Drexler. Adaptive optics optical coherence tomography at 120,000 depth scans/s for non-invasive cellular phenotyping of the living human retina. *Optics express*, 17(22):19382–400, oct 2009. ISSN 1094-4087. doi: 10.1364/OE.17.019382. URL http://www.opticsexpress.org/abstract.cfm?URI=oe-17-22-19382.

[166] Adrian Gh Podoleanu and Adrian Bradu. Master-slave interferometry for parallel spectral domain interferometry sensing and versatile 3D optical coherence tomography. *Optics express*, 21(16):19324–38, aug 2013. ISSN 1094-4087. doi: 10.1364/OE.21.019324. URL http://www.opticsexpress.org/abstract.cfm?URI=oe-21-16-19324.

[167] Masato Ohmi, Motomu Tanigawa, Yuki Wada, and Masamitsu Haruna. Dynamic analysis for mental sweating of a group of eccrine sweat glands on a human fingertip by optical coherence tomography. *Skin research and technology : official journal of International Society for Bioengineering and the Skin (ISBS) [and] International Society for Digital Imaging of Skin (ISDIS) [and] International Society for Skin Imaging (ISSI)*, 18(3):378–83, aug 2012. ISSN 1600-0846.

doi: 10.1111/j.1600-0846.2011.00580.x. URL http://www.ncbi.nlm.nih.gov/pubmed/22092881.

[168] Shuliang Jiao, Robert Knighton, Xiangrun Huang, Giovanni Gregori, and Carmen Puliafito. Simultaneous acquisition of sectional and fundus ophthalmic images with spectral-domain optical coherence tomography. *Optics express*, 13(2):444–452, 2005. ISSN 1094-4087. doi: 10.1364/OPEX.13.000444.

[169] Adrian Gh Podoleanu and Adrian Bradu. Master-slave interferometry for parallel spectral domain interferometry sensing and versatile 3D optical coherence tomography. *Optics express*, 21(16):19324–38, 2013. ISSN 1094-4087. doi: 10.1364/OE.21.019324. URL http://www.opticsexpress.org/abstract.cfm?URI=oe-21-16-19324.

[170] Adrian Bradu and Adrian Gh Podoleanu. Imaging the eye fundus with real-time en-face spectral domain optical coherence tomography. *Biomedical optics express*, 5(4):1233–49, 2014. ISSN 2156-7085. doi: 10.1364/BOE.5.001233. URL http://www.pubmedcentral.nih.gov/articlerender.fcgi?artid=3985995{&}tool=pmcentrez{&}rendertype=abstract.

[171] Adrian Bradu and Adrian Gh. Podoleanu. Calibration-free B-scan images produced by master/slave optical coherence tomography. *Optics Letters*, 39(3):450, 2014. ISSN 0146-9592. doi: 10.1364/OL.39.000450. URL http://www.opticsinfobase.org/abstract.cfm?URI=ol-39-3-450.

[172] Yuuki Watanabe, Seiya Maeno, Kenji Aoshima, Haruyuki Hasegawa, and Hitoshi Koseki. Real-time processing for full-range Fourier-domain optical-coherence tomography with zero-filling interpolation using multiple graphic processing units. *Applied optics*, 49(25):4756–4762, 2010. ISSN 0003-6935. doi: 10.1364/AO.49.004756.

[173] Adrian Bradu, Michael Maria, and Adrian Gh. Podoleanu. Demonstration of tolerance to dispersion of master/slave interferometry. *Optics Express*, 23(11):14148, 2015. ISSN 1094-4087. doi: 10.1364/OE.23.014148. URL https://www.osapublishing.org/abstract.cfm?URI=oe-23-11-14148.

[174] Adrian Bradu, Konstantin Kapinchev, Fred Barnes, David F Garway-Heath, Ranjan Rajendram, Pearce Keane, and Adrian G Podoleanu. Real-time calibration-free C-scan images of the eye fundus using Master Slave swept source optical coherence tomography, 2015. URL http://dx.doi.org/10.1117/12.2078956.

[175] RL Haupt and SE Haupt. The continuous genetic algorithm. *Practical Genetic Algorithms, Second ...*, pages 51–66, 2004. doi: 10.1002/0471671746.ch3. URL http://onlinelibrary.wiley.com/doi/10.1002/0471671746.ch3/summary.

[176] Ujjwal Maulik and Sanghamitra Bandyopadhyay. Genetic algorithm-based clustering technique, 2000. ISSN 00313203.

[177] Georges R. Harik, Fernando G. Lobo, and David E. Goldberg. The compact genetic algorithm. *IEEE Transactions on Evolutionary Computation*, 3(4):287–297, 1999. ISSN 1089778X. doi: 10.1109/4235.797971.

[178] Charles Darwin. Origin of Species. *Library*, 475(7357):424, 1859. ISSN 14764687. doi: 10.1038/475424a. URL http://www.pubmedcentral.nih.gov/articlerender.fcgi?artid=3203181{&}tool=pmcentrez{&}rendertype=abstract.

[179] Josiah Poon and M L Maher. Emergent behaviour in co-evolutionary design. In *Artificial Intelligence in Design*, volume 96, pages 703–722, 1996. URL http://scholar.google.com/scholar?hl=en{&}btnG=Search{&}q=intitle:EMERGENT+BEHAVIOUR+IN+CO-EVOLUTIONARY+DESIGN{#}0.

[180] D G Green. Emergent Behaviour in Biological Systems. *Complexity International*, 1:http://www.csu.edu.au/ci/vol1/David.Green/paper.ht, 1993.

[181] Riccardo Poli, James Kennedy, and Tim Blackwell. Particle swarm optimization, 2007. ISSN 1935-3812.

[182] J Kennedy and R Eberhart. Particle swarm optimization. In *Neural Networks, 1995. Proceedings., IEEE International Conference on*, volume 4, pages 1942–1948 vol.4, 1995. ISBN VO - 4. doi: 10.1109/ICNN.1995.488968.

[183] Darrell Whitley. A genetic algorithm tutorial. *Statistics and Computing*, 4(2): 65–85, 1994. ISSN 09603174. doi: 10.1007/BF00175354.

[184] Abhishek Kumar, Wolfgang Drexler, and Rainer a Leitgeb. Subaperture correlation based digital adaptive optics for full field optical coherence tomography. *Optics Expres*, 21(9):10850–10866, 2013. doi: 10.1364/OE.21.010850.

Appendix A

Mirao 52-E specifications

Dimensions	64 x 64 x 23 mm
Weight	0.49 kg
Pupil diameter	15 mm
Number of actuators	52
Inter-actuator voltage	$\pm$ 1 V max in each actuator Sum of absolute voltage values $<$ 25 V
Input intensity	0.65 A max in each actuator
Coating	Protected silver
Reflectivity	λ in [410 nm, 560 nm] : $>$ 95 % λ in [560 nm, 800 nm] : $>$ 98 %
Rise time[1]	$\leq$ 6 ms
Hysteresis	$<$ 2 %
Linearity	$>$ 95 %
Wavefront quality in active flat configuration	0.02 μm RMS[2]

Table A.1: Specifications of the Mirao-52e

Dimensions	230 x 245 x 90 mm
Weight	3 kg
Main input voltage	100 to 240 V AC
Main input frequency	50 to 60 Hz
Actuator output voltage	$\pm$ 1 V max in each of the 52 channels. Sum of absolute voltage values $<$ 25 V
TTL trigger output voltage	TTL 3.3 V
TTL trigger signal duration	1 ms
Working temperature	15° to 35°C
Fuses	Two fuses 240 V / 4 A / ϕ 5 mm / L 20 mm
Impulse withstand (overvoltage) category	Cat. II
Compliance to international standards	IEC 61010-1:2001 (EN 61010:2001) IEC 61326-1:2005 (EN 61326-1:2006)

Table A.2: Specifications of the electronic control unit for Mirao-52e

		11	19	27	35		
	5	12	20	28	36	43	
1	6	13	21	29	37	44	49
2	7	14	22	30	38	45	50
3	8	15	23	31	39	46	51
4	9	16	24	32	40	47	52
	10	17	25	33	41	48	
		18	26	34	42		

Table A.3: Actuator layout of the Mirao-52e

Appendix B

SLD data sheet

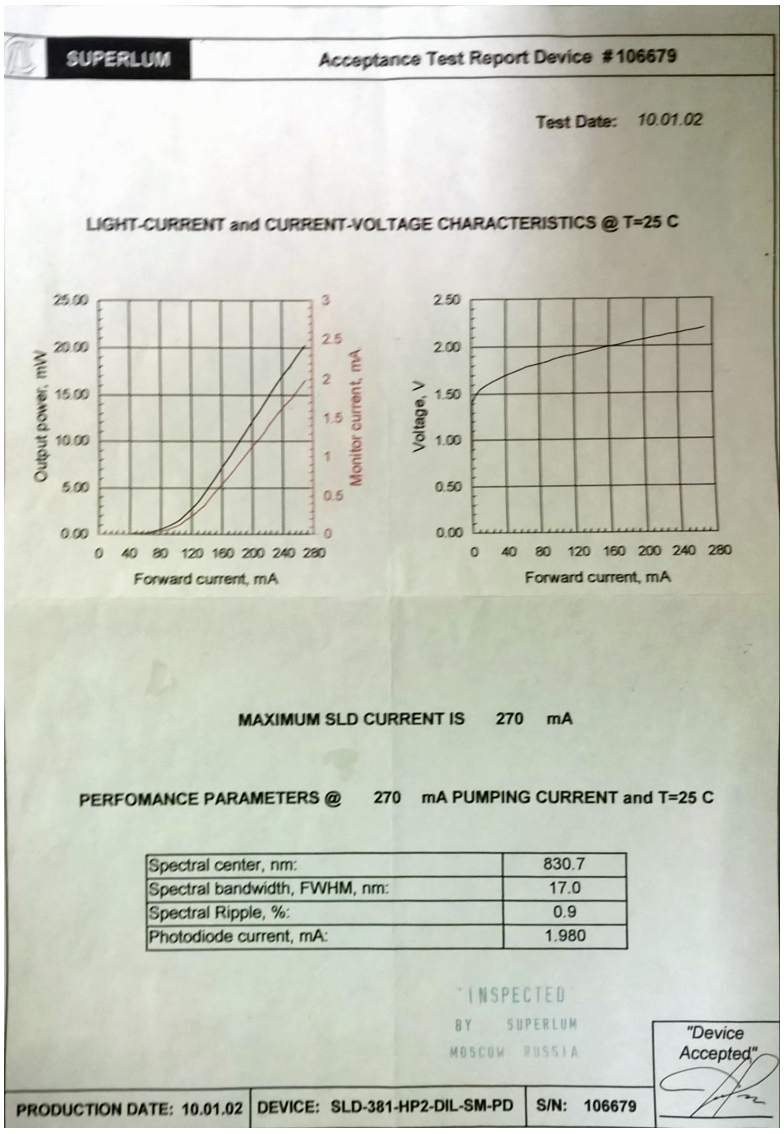

SUPERLUM

Acceptance Test Report Device #106679

Test Date: 10.01.02

LIGHT-CURRENT and CURRENT-VOLTAGE CHARACTERISTICS @ T=25 C

MAXIMUM SLD CURRENT IS 270 mA

PERFOMANCE PARAMETERS @ 270 mA PUMPING CURRENT and T=25 C

Spectral center, nm:	830.7
Spectral bandwidth, FWHM, nm:	17.0
Spectral Ripple, %:	0.9
Photodiode current, mA:	1.980

INSPECTED BY SUPERLUM MOSCOW RUSSIA

"Device Accepted"

PRODUCTION DATE: 10.01.02	DEVICE: SLD-381-HP2-DIL-SM-PD	S/N: 106679

FIGURE B.1: Specifications of SLD emitting light with central wavelength 830 nm.

Appendix C

LabVIEW implementation of the genetic algorithm

This appendix provides a diagrammatic overview of the LabVIEW code implementation of the genetic algorithm as discussed in chapter 8. The caption for each figure gives a brief description of the function for each snippet of LabVIEW code.

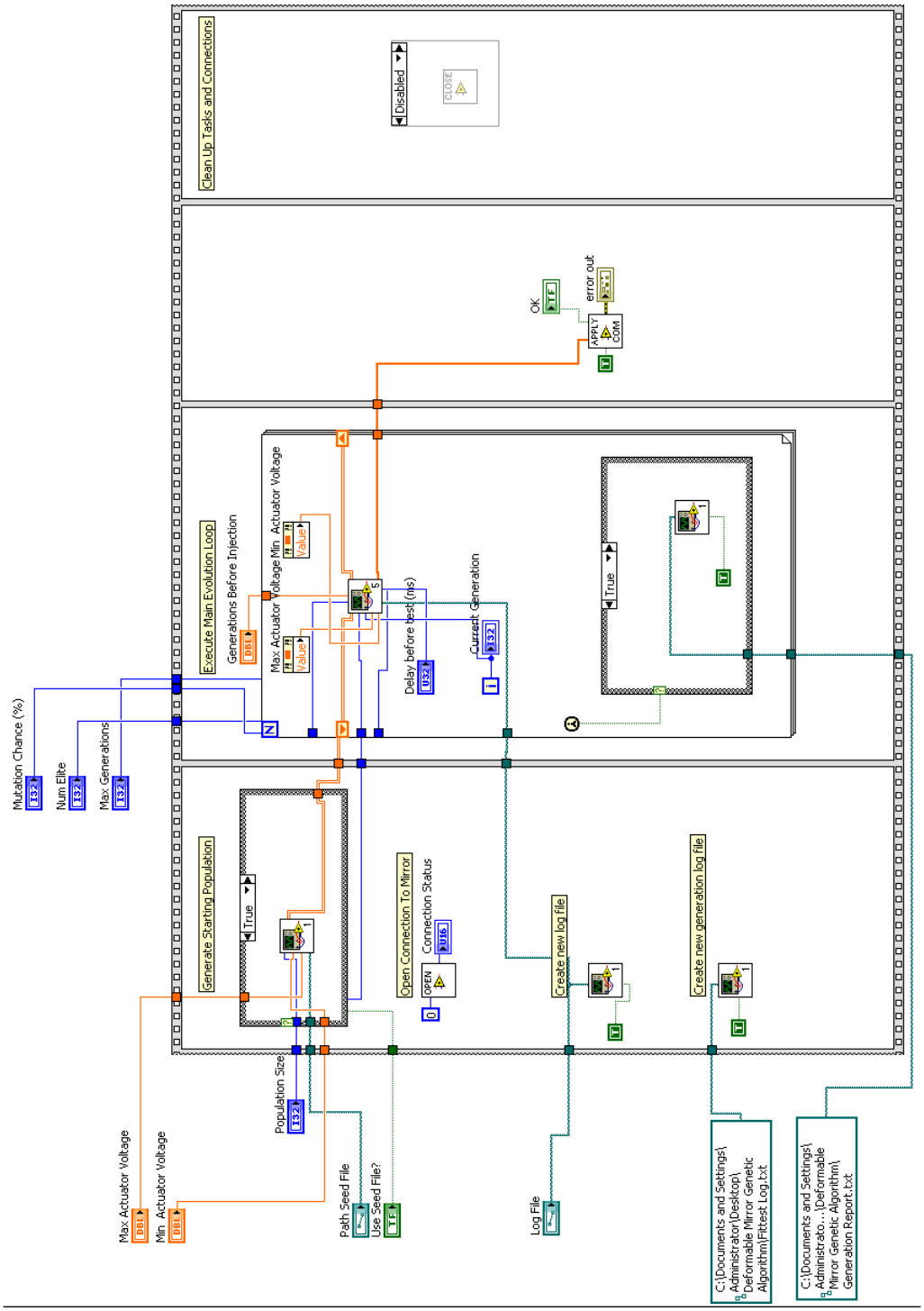

FIGURE C.1: Start Evolution.VI is the primary VI to execute when running the GA. This VI is responsible for setting the starting parameters of the GA, opening communications with the DM, creating log files and the random starting population from a seed file.

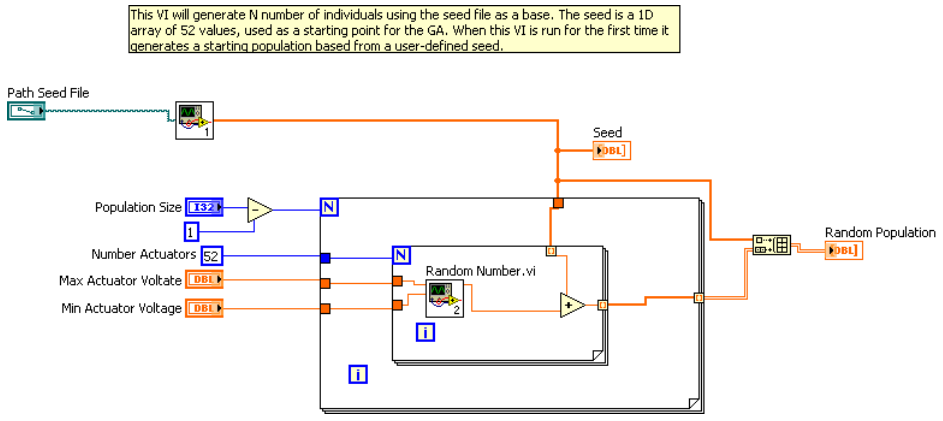

FIGURE C.2: Generate Random Population From Seed.VI will import an XML file acquired from CASAO. This file contains a set of command values that determine the voltages applied to each actuator in the DM. The VI will generate a number of 52-length 1D arrays equal to Population Size by adding random numbers to the seed file.

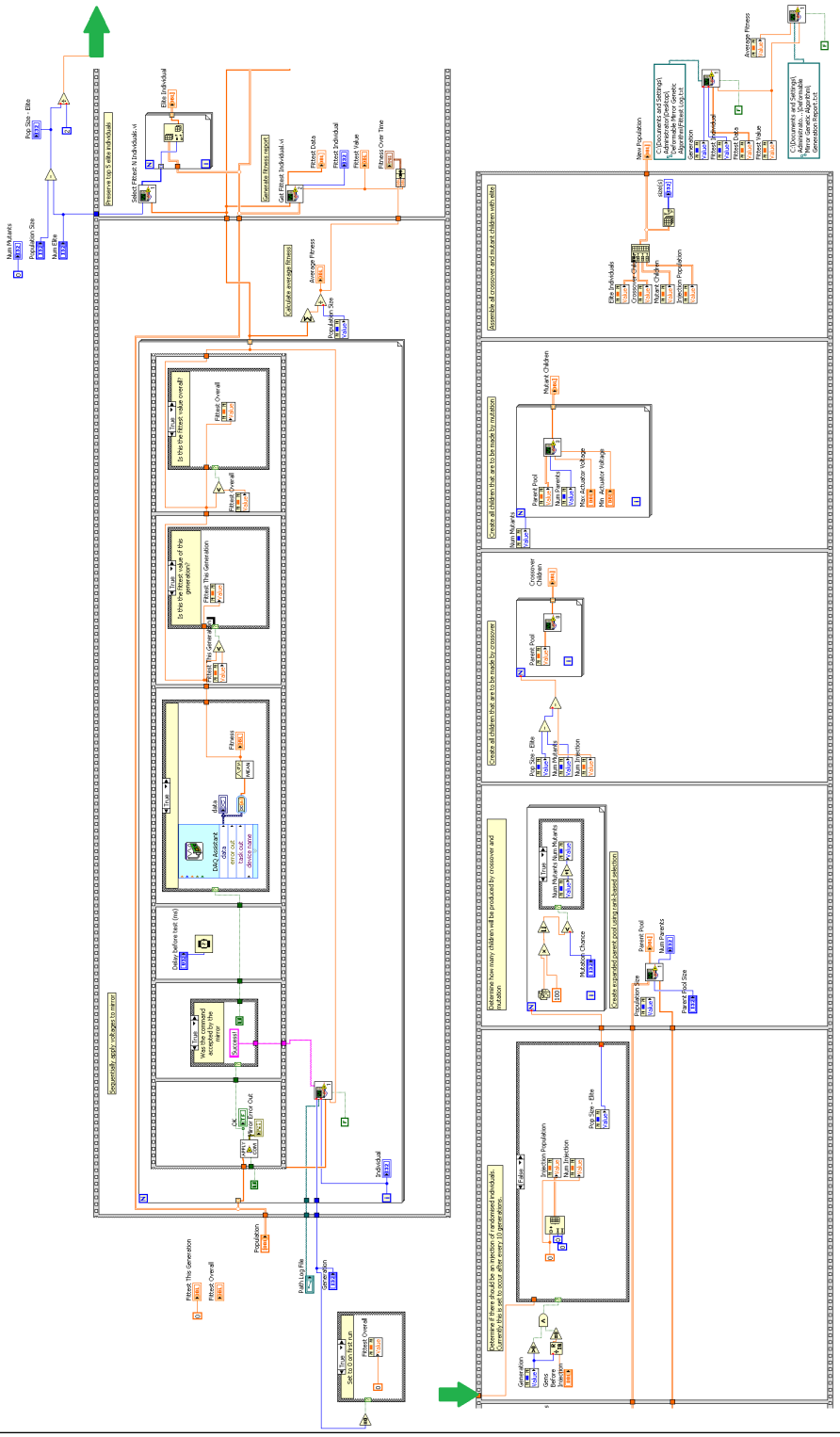

FIGURE C.3: Main Loop.VI is where the majority of the GA functionality occurs. This VI will remain active until the GA terminates. In this VI there are calls to various sub VIs that determine the fitness of a solution and initialise the reproduction cycle. Also seen in this VI are the various code fragments used to generate logs and reports during GA execution.

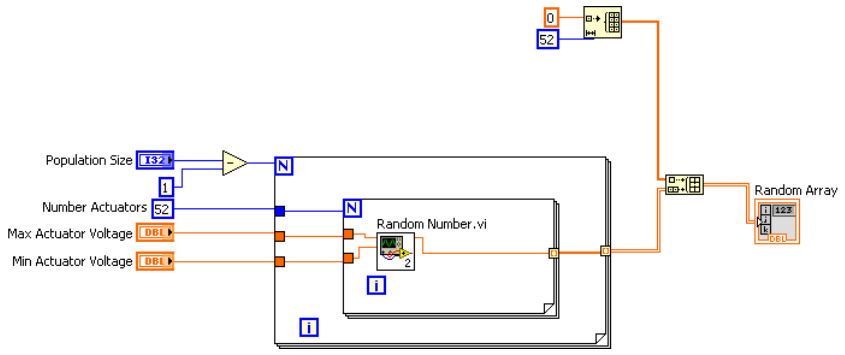

FIGURE C.4: Generate Random Population.VI is similar to Fig. C.2 though it does not require a seed file to generate a random set of individuals.

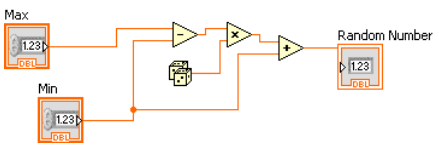

FIGURE C.5: Random Number.VI generates a random number between two given limits and is used for many functions in the GA.

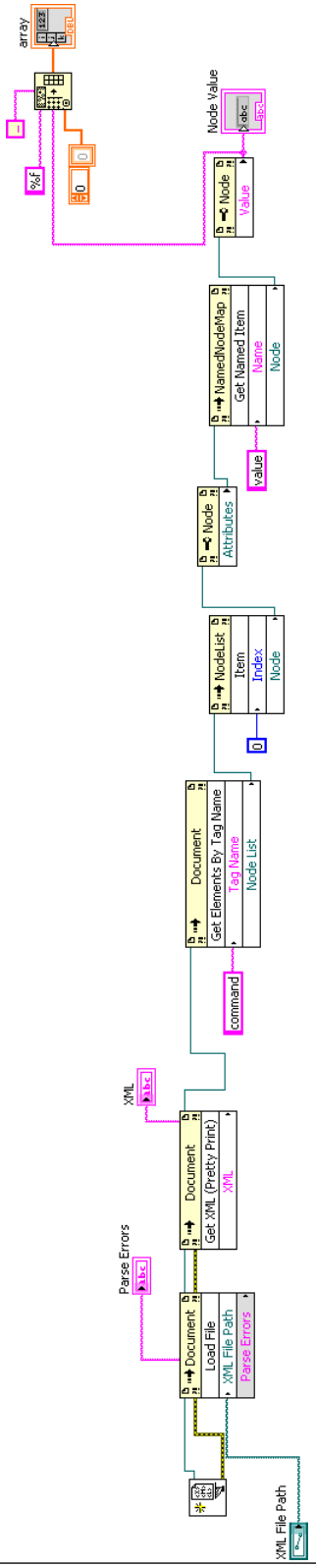

FIGURE C.6: Read CASAO Command Values.VI is responsible for reading the XML files output by the CASAO software. This VI reads through the file to find the tags for the command values, and exports them as an array of doubles.

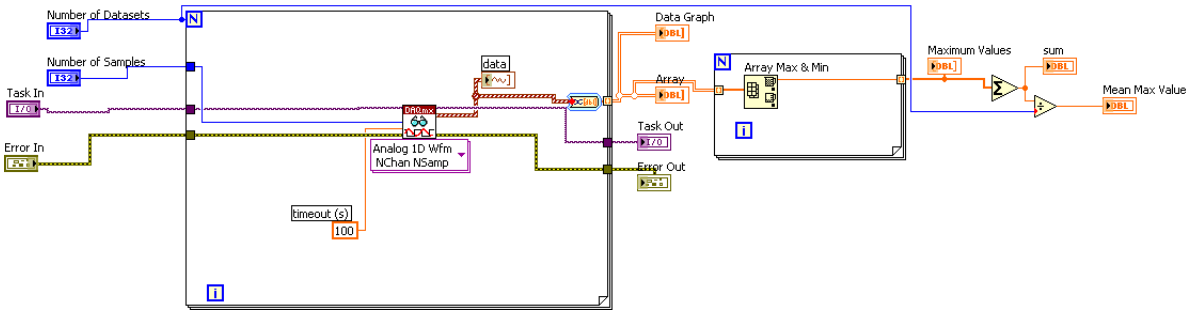

FIGURE C.7: Get individual fitness.VI calculates the fitness value of a given individual.

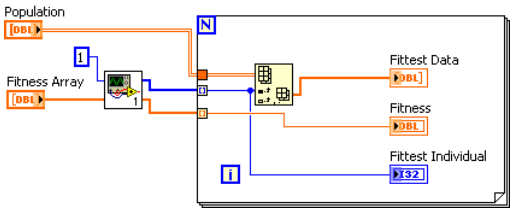

FIGURE C.8: Get Fittest Individual.VI will sort through the population of individuals and select the one with the highest fitness.

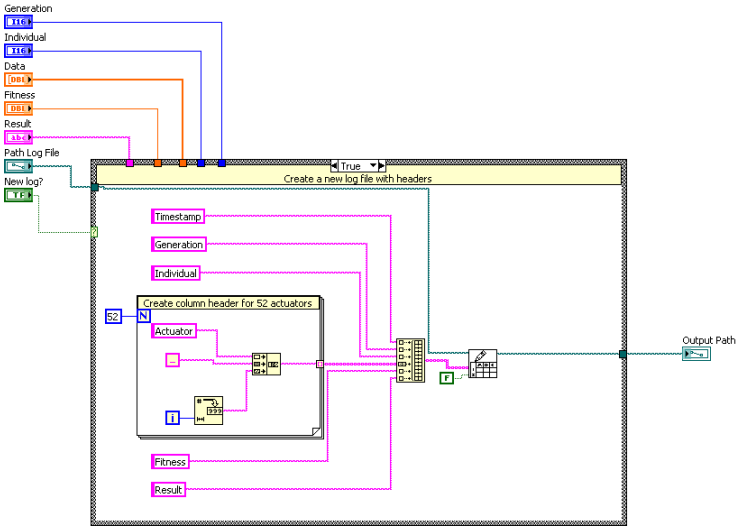

FIGURE C.9: Log Entry.VI will create an entry in the log file for the current individual with all its relevant information, including values and fitness level.

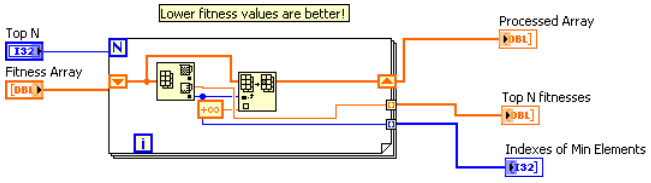

FIGURE C.10: Select Fittest N Individuals.VI will sort through the population and select the top N fittest individuals.

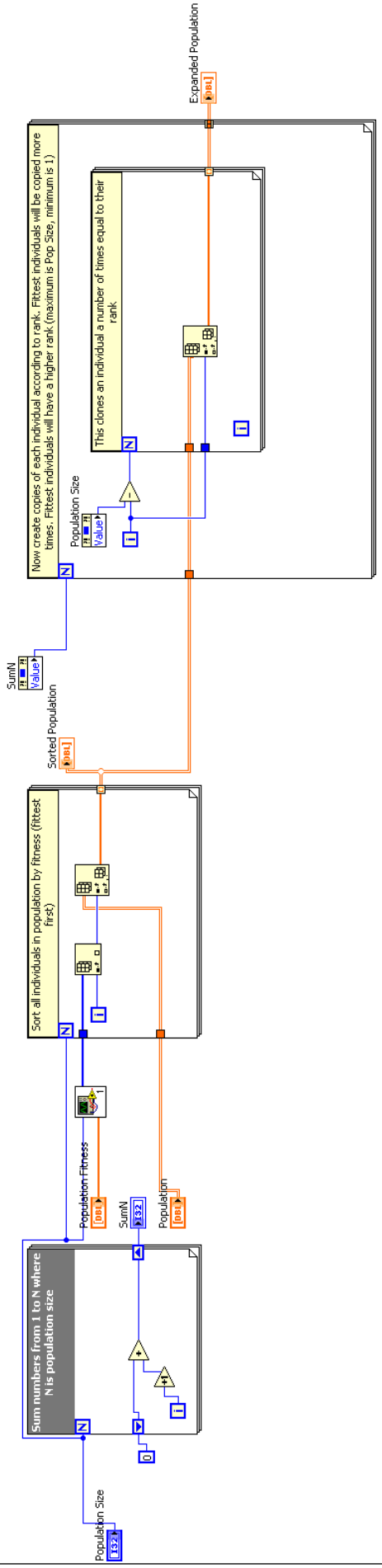

FIGURE C.11: Rank Selection.VI is the method used to select two parents for breeding.

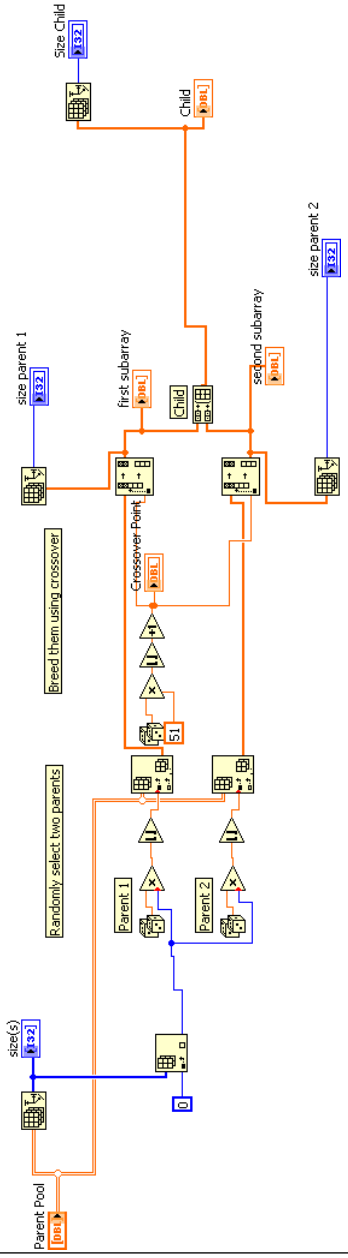

FIGURE C.12: Crossover 1 Point.VI takes two parent individuals, randomly determines a crossover point and then cuts these parents, splicing them together to create a child.

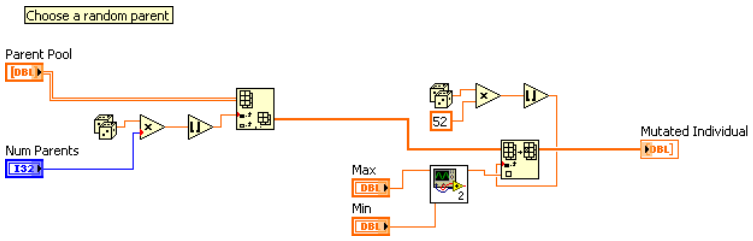

FIGURE C.13: Mutate 1 Point.VI takes a single parent individual and selects a single value in the array to change.

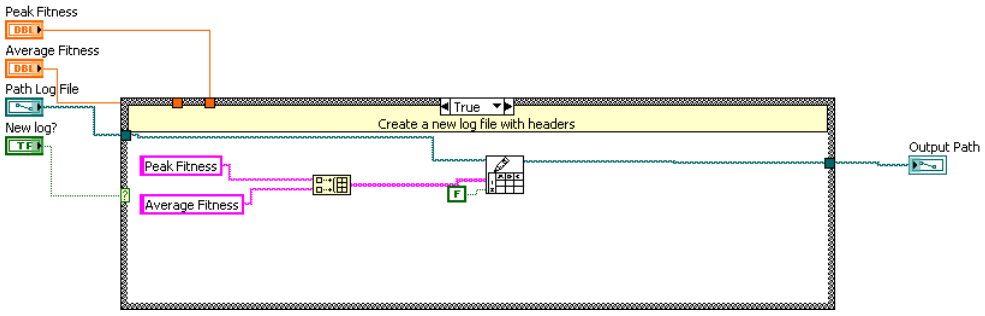

FIGURE C.14: Generation Report.VI provides information for each generation such as time stamp, highest fitness and average fitness.